Si Alloy Negative Electrode Materials for Li-ion Batteries

by

Simeng Cao

Submitted in partial fulfilment of the requirements
for the degree of Doctor of Philosophy

at

Dalhousie University
Halifax, Nova Scotia
March 2021

Table of Contents

List of Tables

List of Figures

Abstract

Si-based negative electrode materials are promising for lithium batteries. However, Si-based negative electrode materials suffer from huge volume change, crystallization effect ($Li_{15}Si_4$ formation), unstable solid electrolyte interface during cycling. Preparing Si/inactive materials and Si/C compounds (especially carbon coated Si materials) are two efficient methods to alleviate these problems mentioned above. This work focuses on designing and developing new Si-transition metal negative electrode materials. Si-Mo, Si-TiN, and Si-Ti-N-O alloys were prepared by Ar milling, N_2 (g) milling, and air milling, respectively. Composition, morphology, and electrochemical performance of Si-Mo, Si-TiN, and Si-Ti-N-O alloys were investigated. Thermal stability of these alloys was also studied, since high thermal stability is an important requirement for preparing carbon coated Si negative electrode materials at high temperature. A preliminary study of high temperature carbon coating preparation for these Si alloys studied in this thesis and related issues were also discussed.

List of Abbreviations Used

a-C	Amorphous Carbon
a-Si	Amorphous silicon
ASI	Area specific impedance
B	Instrumental broadening
BE	Binding energy
BF	Bright field
BSE	Backscattered electron
CCCV	Constant current/constant voltage
CCD	Charge-coupled device
CE	Coulombic efficiency
cr-$Li_{15}Si_4$	Crystalline $Li_{15}Si_4$
cr-Si	Crystalline silicon
CVD	Chemical vapor deposition
d	Distance between lattice planes
DEC	Diethyl carbonate
DF	Dark field
DMC	Dimethyl carbonate
e	Charge of an electron
EC	Ethylene carbonate
EDS	Energy dispersive spectrometer
EMC	Ethyl methyl carbonate

f	The percent active Si in the alloy that forms the cr-$Li_{15}Si_4$ phase during cycling
F	Faraday constant
FWHM	Full width at half maximum
HE-NMC	High energy NMC
HREM	High resolution electron microscopy
HV-spinel	High potential spinel $LiNi_{0.5}Mn_{1.5}O_4$
ICE	Initial coulombic efficiency
IF	Intensity factors
IRC	Irreversible capacity
K	Dimensionless shape factor
LCO	$LiCoO_2$
LFP	$LiFePO_4$
$LiPF_6$	Lithium hexafluorophosphate
LMO	$LiMn_2O_4$
LTO	$Li_4Ti_5O_{12}$
m	Mass
M	Molecular mass
NCA	$LiNi_{0.8}Co_{0.15}Al_{0.05}O_2$
NMC	$LiNi_xMn_yCo_{(1-x-y)}O_2$
NMC111	$LiNi_{1/3}Mn_{1/3}Co_{1/3}O_2$
NMC442	$LiNi_{0.4}Mn_{0.4}Co_{0.2}O_2$

NMC532	$LiNi_{0.5}Mn_{0.3}Co_{0.2}O_2$
NMC622	$LiNi_{0.6}Mn_{0.2}Co_{0.2}O_2$
NMC811	$LiNi_{0.8}Mn_{0.1}Co_{0.1}O_2$
NMP	N-Methyl-2-pyrrolidone
N/P	Negative to positive electrode capacity ratio
q_s	Theoretical specific capacity
q_v	Theoretical volumetric capacity
$ROCO_2Li$	Lithium alkyl carbonates
SAED	Selected area electron diffraction
SDD	A silicon drift detector for energy dispersive spectrometer
SE	Secondary electron
SEI	Solid electrolyte interphase
SEM	Scanning electron microscope
STEM	Scanning transmission electron microscopy
TEM	Transmission electron microscopy
U_s	Specific energy density
U_v	Volumetric energy density
UV	Ultraviolet
XPS	X-ray photoelectron spectroscopy
XRD	X-ray diffraction
θ	Angle between incident X-rays and lattice planes
λ	Wavelength

μ	Chemical potential
$(\mu/\rho)_m$	Mass absorption coefficient of a mixture
ρ	Density
τ	Grain size

Acknowledgements

Firstly, I would like to express my sincere gratitude to my supervisor Dr. Mark Obrovac for giving me the opportunity to be a member in his research group. With his patience, motivation, and immense knowledge, he provided me guidance throughout my research and the writing of this thesis. I would also like to thank my supervisory committee, Dr. Mita Dasog, Dr. Ted Monchesky, and Dr. Peng Zhang for their help and support along the way.

I would like to thank Dr. Timothy Hatchard for helping me in experimental instrument operation and giving me useful advice on my research. I would also like to thank Dr. Jeff Dahn for giving me the access to his laboratory equipment. The Li-ion battery course taught by him widened my knowledge about this research field and is very helpful for my research project. I would like to thank my fellow lab mates for the discussions about our projects and for all the fun we have had in the last five years.

Finally, I would like to thank my husband, my parents, and my friends for supporting and encouraging me over the past five years.

Chapter 1 Introduction

The Nobel Prize in Chemistry 2019 was awarded to John B. Goodenough, M. Stanley Whittingham, and Akira Yoshino, for their outstanding contributions to development of lithium-ion batteries. During the oil crisis in the 1970s, many scientists and engineers worked on developing lithium-ion batteries. At that time, M. Stanley Whittingham tried to explore a new battery system, where TiS_2 and lithium metal were used as the positive and negative electrodes, respectively.[1,2] This is regarded as the starting point for the development of commercial lithium-ion secondary batteries. Unfortunately, lithium dendrite formation on the lithium metal surface during repeated cell cycling could result in serious safety issues because of the generation of thermally unstable high surface area lithium. In 1979/1980 Jahn B. Goodenough et al. used Li_xCoO_2 as the positive electrode for lithium-ion batteries instead of $TiSi_2$, which is significantly important for commercializing lithium-ion batteries.[3,4] Five year later, Akira Yoshino's group experimented using petroleum coke as a lithium battery negative electrode material, which overcame the safety issues of a lithium metal negative electrode.[5,6] Based on these discoveries and developments, Sony was the first to commercialize lithium-ion secondary batteries in 1991, in which a petroleum coke and Li_xCoO_2 were used as the active anode and cathode materials. This marked a revolution in battery industry.[7]

Lithium-ion batteries have high working potential, large energy and power density, and long service life. These outstanding characteristics enable lithium-ion batteries to fulfill

various requirements for electric devices. As a consequence, lithium-ion batteries have extensively been applied to portable information technology devices, powder tools, and hybrid/full electric vehicles.[8,9] If the majority of gasoline powered transportation can be replaced by electric vehicles, greenhouse gas emissions will be greatly reduced.[10] In addition, lithium-ion batteries may also be used in various grid energy storage systems, which can harvest significant amounts of energy form wind, solar, geo-thermal and other renewable sources, making possible a fossil fuel-free society.[8]

With the application of lithium-ion batteries to more fields, lithium-ion batteries should be continuously improved to meet the increasing energy demands. On the aspect of lithium-ion battery negative electrodes, graphite is an excellent negative electrode material and has been commercialized since the 1990s. To further increase energy density of lithium-ion batteries, plenty of studies focus on developing negative electrode materials in recent years.[11–13] Among these studied negative electrode materials, Si-based materials receive much attention, due to silicon's large theoretical capacity and high earth abundance. However, some difficulties are still found with silicon, which make silicon-based negative electrode materials to be unable to meet full commercial requirements. The main difficulties found with silicon are huge volume expansion of silicon during lithiation, crystalline $Li_{15}Si_4$ formation, and unstable solid electrolyte interphase during cell cycling, which can result in low coulombic efficiency and poor cycling performance.[14–21]

This thesis is devoted to developing silicon alloy negative electrode materials that hopefully contribute to wide application of silicon alloys in commercial lithium-ion batteries. Various strategies were shown to alleviate some of the aforementioned problems and they will be the subject of this thesis. As an outline of the thesis: Chapter 2 gives an overview of lithium-ion batteries, including positive electrodes, negative electrodes, and electrolyte. Silicon-based negative electrode materials will be discussed in detail, including their advantages and electrochemical behavior, problems of silicon-based negative electrodes, and efficient solutions to solve these problems. Chapter 3 outlines the experimental tools and theory used throughout this work. Chapter 4 describes phase evolution during ball milling process, thermal stability, and electrochemical characteristics of Si-Mo alloys. Chapter 5 presents a new and cheap method to prepare Si-TiN alloys through nitrogen gas milling, and these Si-TiN alloys were expected to show better electrochemical performance than the conventional Si-TiN alloys made by argon milling. Chapter 6 focuses on thermal stability of Si-TiN alloys prepared by nitrogen gas milling, and a selected sample was further improved by carbon coating at high temperature. Chapter 7 describes electrochemical performance and thermal stability of Si-Ti-N-O alloys synthesized by air milling. Chapter 8 discusses preliminary results of high temperature carbon coating for some Si alloys studied in this thesis and related difficulties. Chapter 9 summarizes the silicon alloy negative electrode materials examined in this thesis and future work in the related area is suggested.

Chapter 2 Background

2.1 Lithium Ion Batteries

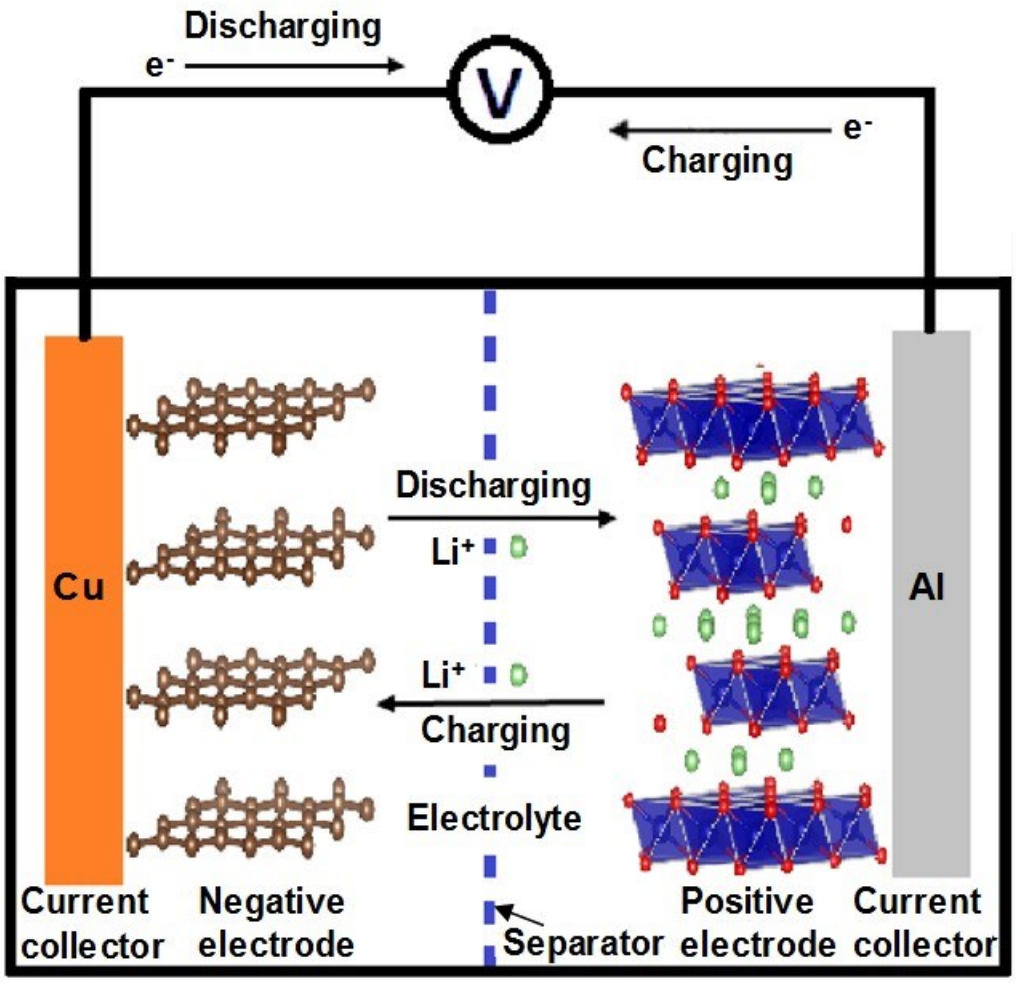

Figure 2.1 Schematic of a Li-ion cell with $LiCoO_2$ as the positive electrode and graphite as the negative electrode. Red, blue, green, and brown spheres represent oxygen ions, cobalt ions, lithium ions, and carbon atoms, respectively.

A lithium-ion battery includes several identical Li-ion cells connected in series and/or parallel. Each Li-ion cell comprises a positive electrode, a negative electrode, electrolyte, porous separator, and a cell can. Positive and negative electrode coatings

typically comprise active material powders, binders, and conductive additives. The positive and negative electrode materials are coated on aluminum foil and copper foil, respectively. The aluminum and copper foils are used as current collectors that provide electrical connection with an external circuit. An electrolyte usually consists of a lithium salt and a nonaqueous organic solvent, which results in an ionically conductive solution, allowing lithium ion transport between positive and negative electrodes.[22] Separators are typically made of porous polyethylene and/or polypropylene, allowing lithium ions to pass through while being electrically insulating.[23] The separator is sandwiched between the positive and negative electrodes to prevent a short circuit. Figure 2.1 shows a schematic diagram of a Li-ion cell with $LiCoO_2$ as the positive electrode and graphite as the negative electrode.

In a Li-ion cell, Li ions move reversibly between positive and negative electrodes during discharging and charging processes, resulting in interconversion between chemical energy and electrical energy. In Figure 2.1, the cycling processes are illustrated. During the discharging process, spontaneous reactions are driven by the chemical potential difference between positive and negative electrodes, causing lithium ions to diffuse into the positive electrode from the negative electrode through the separator. In order to keep charge neutrality, electrons travel to the positive electrode from the negative electrode through an external circuit at the same time. During the charging process, the opposite movements of lithium ions and electrons occur due to an externally applied potential. This results in stored electrical energy in the cell. For both discharging and charging processes, Li-ion diffusion

has a significant effect on the charge/discharge rate of a cell.[24] It is also necessary to maintain electrode structural stability during the insertion and extraction of Li ions so that good cycle life is maintained.[24] For the $LiCoO_2$-graphite cell shown in Figure 2.1, the reactions on the electrodes and the overall reaction are given by

$$LiCoO_2 \leftrightarrow x\ Li^+ + x\ e^- + Li_{1-x}CoO_2 \tag{2.1}$$

$$x\ Li^+ + x\ e^- + y\ C \leftrightarrow Li_xC_y \tag{2.2}$$

$$LiCoO_2 + y\ C \leftrightarrow Li_xC_y + Li_{1-x}CoO_2 \tag{2.3}$$

The open circuit potential of such a cell in volts (V) can be expressed as

$$V = -\frac{\mu_{cathode} - \mu_{anode}}{e} \tag{2.4}$$

where $\mu_{cathode}$ and μ_{anode} are the chemical potentials in electron volts (eV) of the positive and negative electrodes with respect to lithium and e is the charge of an electron.

The amount of lithium stored in active materials is measured in terms of specific and volumetric capacity. The theoretical specific capacity (q_s, mAh/g) of a positive or negative electrode material can be calculated by

$$q_s = \frac{nF}{M} \times \frac{1}{3.6\ \text{C/mAh}} \tag{2.5}$$

Where n is the number of moles of charge transferred during discharging or charging corresponding to one mole active material, F is the Faraday constant (96485.33 C/mol), M is active material molecular weight (g/mol). Theoretical volumetric capacity must be calculated at an active material's full volume expansion, to reflect the space that the material

will ultimately occupy in a real cell. Therefore, theoretical volumetric capacity (q_v, Ah/L) of a positive or negative electrode material can be given by

$$q_v = \frac{q_s \rho}{1+P} \tag{2.6}$$

Where q_s is the corresponding theoretical specific capacity (Ah/kg), ρ is the density of the active material (kg/L), P is the largest volume expansion of the active material during lithiation (if cathode materials are fully lithiated in the initial state, P is equal to 0). Usually, the volume change of positive electrode materials can be negligible during cycling. However, many negative electrode materials typically have significant volume expansion after lithiation, so volume expansion should be considered for theoretical volumetric capacity calculation.

Important metrics for assessing Li-ion cells are: specific energy density (U_s) in watt hours per kilogram (Wh/kg) and volumetric energy density (U_v) in watt hours per liter (Wh/L); and are given by

$$U_s = \frac{\int [V_{(+)} - V_{(-)}] dq}{m} \tag{2.7}$$

$$U_v = \frac{\int [V_{(+)} - V_{(-)}] dq}{v} \tag{2.8}$$

Here [$V_{(+)}$ - $V_{(-)}$] is the working potential of the Li-ion cell in volts (V), q is the total charge quantity in amp hours (Ah), m is the cell mass in kilograms (kg), and v is the cell volume in liters (L).

2.2 Lithium Ion Battery Positive Electrode Materials

A brief introduction of positive electrode materials is given in this section, although positive electrode materials are not the focus in this thesis. Commercial positive electrode materials typically include $LiCoO_2$ (LCO), $LiFePO_4$ (LFP), $LiMn_2O_4$ (LMO), $LiNi_{0.8}Co_{0.15}Al_{0.05}O_2$ (NCA), and $LiNi_xMn_yCo_{(1-x-y)}O_2$ (NMC). Each of these positive electrode materials has advantages and disadvantages. LCO has high energy density, good electrical conductivity, and low self discharge rate.[4,25] The theoretical capacity of LCO is 274 mAh/g when it is fully delithiated. However, an irreversible phase transition can occur if LCO is over delithiated (Li_xCoO_2 ($0 < x < 0.5$)).[26] Therefore, only about half of the theoretical capacity of LCO can be available, which is about 150 mAh/g. The main drawbacks of LCO are toxicity and high cost owing to the use of cobalt. The use of LFP as a positive electrode material was first reported in 1997.[27] Iron is naturally abundant and nontoxic, which make LFP to be cheap and environmental friendly. Also, LFP has excellent thermal stability, good thermal stability, and long cycle life.[28,29] LFP suffers from poor ionic and electronic conductivity, but these difficulties can be overcome through several methods, such as doping metal elements, carbon coating, and nanosizing LFP particles.[30–32] The energy density of a lithium ion cell depends on the cell capacity and the average working potential, according to Equations 2.7 and 2.8. Positive electrode materials with large capacity and high average working potential are most likely to provide high energy density for a full cell. However, LFP has limited volumetric capacity and low average

working potential, which hampers its application in high energy density lithium-ion batteries. LMO was first reported in 1983 and was commercialized by Moli Energy in 1996.[33] LMO is cheap and nontoxic. LMO has 3D lithium ion diffusion network, while some other positive electrode materials have 1D tunnels (like LFP) or 2D pathways (such as LCO, NCA, and NMC) for Li^+ diffusion. The 3D lithium ion diffusion frameworks of LMO contribute to its good rate capability.[29] Difficulties found with this positive electrode material are low capacity (theoretical capacity: 148 mAh/g) and poor cycling performance at high temperarture.[29,34,35] NCA has the largest specific capacity (discharge capacity: ~200 mAh/g) among the currently mature lithium-ion technologies, and it also shows high cycling stability at both room temperature and elevated temperature (60 °C).[29,36] However, NCA is expensive because of its stringent synthesis processes.[37,38] NMC has played an important role for commercial lithium-ion batteries in recent years. The typical commercial NMC materials include $LiNi_{1/3}Mn_{1/3}Co_{1/3}O_2$ (NMC111), $LiNi_{0.4}Mn_{0.4}Co_{0.2}O_2$ (NMC442), and $LiNi_{0.5}Mn_{0.3}Co_{0.2}O_2$ (NMC532). For NMC materials, more nickel contributes to larger capacity at the expense of lower thermal stability and shorter cell lifetime, while higher manganese content gives better cyclability but lower capacity.[39] Compared to LCO, NMC materials have similar or higher specific capacity, similar working potential, and lower cost due to the reduced use of cobalt.[29]

To date, LCO, LFP, LMO, NCA, and NMC positive electrode materials have been successfully utilized in batteries for electric devices and/or electric vehicles. The

production of the positive electrode materials was over 180,000 tons in 2016, and is expected to reach over 400,000 tons in 2025.[29] LCO is mainly used in consumer electronic devices, such as smartphones and laptops. LCO is not a propriate positive electrode material for electric vehicles, due to high cost of cobalt and potential safety risks induced by structure instability in the over delithiated state.[40] LFP, LMO, NCA, and NMC have been used by carmakers, such as Tesla, BMW, BYD, and Nissan. Some other positive electrode materials are under development, such as Ni-rich NMC ($LiNi_{0.6}Mn_{0.2}Co_{0.2}O_2$ (NMC622) and $LiNi_{0.8}Mn_{0.1}Co_{0.1}O_2$ (NMC811)), high energy NMC (HE-NMC), and high potential spinel $LiNi_{0.5}Mn_{1.5}O_4$ (HV-spinel), are promising positive electrode materials for lithium-ion batteries with improved properties.[29]

2.3 Lithium Ion Battery Negative Electrode Materials

2.3.1 Lithium Metal Anodes

Lithium metal has a very high theoretical specific capacity of 3860 mAh/g. In the 1970s, lithium metal was first used as the negative electrode in rechargeable lithium metal batteries, as mentioned in Chapter 1.[1,2] Moli Energy developed the first commercial lithium metal batteries in the late 1980s.[41] Unfortunately, lithium metal negative electrodes suffers from safety problems.[42] This resulted in the cessation of commercial cell production. During charging, rapid electrochemical deposition of Li ions on the lithium metal surface can lead to lithium dendrites, which have a branched structure.[42,43] Lithium dendrites

continuously grow upon repeated charge/discharge , resulting in the formation of highly reactive high surface area lithium. This can lead to a series of safety issues. Lithium dendrites can also make lithium metal detach from the current collector, causing the loss of electric contact and poor cycling performance. In addition, the formation of increased surface area lithium, results in more side reactions between the organic electrolyte and lithium metal, which is detrimental to high coulombic efficiency and long lifetime.[29] In liquid electrolyte systems, these problems found with lithium metal negative electrode are difficult to overcome, and it is necessary to find other negative electrode materials to substitute for lithium metal. In recent years, a lot of research has focussed on the combination of Li metal negative electrodes and solid-state electrolytes, which would be a promising method for commercializing lithium metal negative electrodes.[44–46] However, the application of lithium metal in solid-state electrolytes is not a part of this thesis and will not be discussed here.

2.3.2 Carbonaceous Materials

Carbonaceous materials enabled lithium-ion batteries to become commercially viable around 30 years ago. Carbonaceous materials have been extensively studied in the recent decades.[47–51] As mentioned above, a petroleum coke-based material was used as the negative electrode in the first commercialized lithium-ion battery in 1991.[7] At around the same time, it was found that graphite can reversibly intercalate/deintercalate lithium ions,

when a suitable electrolyte was used.[52] From then on, graphite has become the main negative electrode material used in Li-ion batteries.

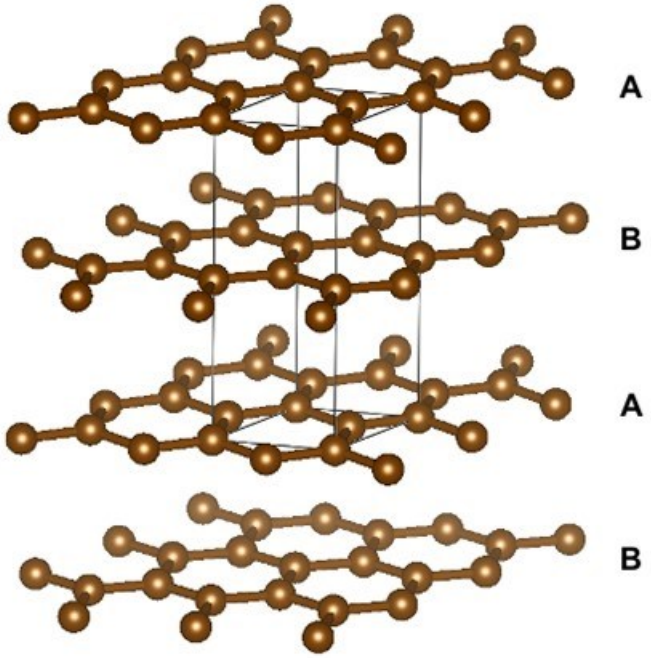

Figure 2.2 A diagram of hexagonal (2H) graphite.

Two types of graphite are used in Li-ion batteries: natural graphite and synthetic graphite. Synthetic graphite is typically prepared through thermal treatment of graphitizable organic precursors (e.g. petroleum pitch), and full graphitization usually occurs at a very high temperature (like ~3000 °C).[53,54] Figure 2.2 illustrates the most common structure of graphite. Within a single layer of graphite, each carbon atom is bonded covalently with three neighboring carbon atoms, forming a honeycomb lattice. Such a single layer is called graphene. Planar graphene layers are parallel to each other, and adjacent layers are connected to each other via weak van der Waals forces. For the graphite structure shown

in Figure 2.2, graphene sheets are stacked in the ABAB sequence. This graphite is called 2H-graphite.[55] "2" indicates that the smallest repeating layer number is 2, and "H" represents a hexagonal structure.

As an important negative electrode material for lithium-ion batteries, graphite can reversibly intercalate/deintercalate Li ions during discharging/charging. One Li ion can be inserted per six carbon atoms in graphite forming LiC_6, which is the full lithiation state of graphite under ambient conditions.[47] In this way, the theoretical specific capacity of graphite is 372 mAh/g, which can be calculated by Equation 2.5. Since Li ions are intercalated into graphite, the spacing between graphene layers is expanded, which leads to a 10% volume expansion of graphite after full lithiation.[47,56] Based on the theoretical specific capacity and the volume expansion, the volumetric capacity of graphite at full lithiation can be obtained using Equation 2.6, and is about 760 Ah/L.

Graphite has low average potential vs. Li^+/Li, high Coulombic efficiency, long service life, and good electronic conductivity. Also, the raw materials for graphite are earth abundant and inexpensive. These advantages make graphite to be extensively used in Li-ion battery negative electrodes. Through several decades of development, graphite is still regarded as one of the most important Li-ion battery negative electrode materials, and significant research has focused on improving the performance of Li-ion batteries with graphite negative electrodes.[57–59] However, with the rapid development of lithium ion

batteries, researchers are pursuing substitutes of graphite for obtaining improved energy density.

2.3.3 $Li_4Ti_5O_{12}$

$Li_4Ti_5O_{12}$ (LTO) has been successfully commercialized as a negative electrode material for lithium-ion batteries. In the potential range of 2.5–1.0 V vs. Li/Li^+, LTO experiences reversible lithiation and delithiation. The theoretical specific capacity of LTO is 175 mAh/g. LTO has a slight volume change of 0.2–0.3% during lithiation/delithiation, so LTO is referred to as a "zero strain" material.[60–62] Based on the theoretical specific capacity of LTO (175 mAh/g) and its negligible volume change during lithiation/delithiation, the theoretical volumetric capacity of LTO can be calculated and is 613 Ah/L. LTO has a high working potential (1.55 V vs. Li/Li^+), which brings some benefits to LTO. It helps to avoid lithium plating, resulting in superior safety performance of LTO. In addition, organic electrolyte is decomposed to form a passivating film on electrode surfaces at a potentials below ~1 V vs. Li^+/Li.[63] The passivating film is called the solid-electrolyte interphase (SEI). Active lithium ions can be consumed owing to SEI formation, which can lead to capacity decrease if lithium ions are limited. However, SEI formation can be avoided during LTO lithiation/delithiation due to its high potential plateau. Besides, the cycle lifetime of LTO is up to 20,000 cycles, which is 10 times longer than that of graphite.[29]

There are still some challenges for LTO, which limit its application in lithium ion batteries. LTO has the highest possible valence for Ti (Ti^{4+}), leading to poor electric conductivity (< 10^{-13} S/cm at room temperature) and limited rate capability.[62,64] Various strategies have been proposed and explored to improve electrochemical performance of LTO, including synthesizing nanosized LTO, doping with metal or non-mental elements, and surface coating using conductive materials.[62,65–68] In fact, nanosized LTO anode materials have been successfully applied for commercial lithium ion batteries. In addition, some side reactions between LTO and the electrolyte do occur during cycling, resulting in gas formation.[69] Preparing carbon-coated LTO can be used to solve this problem, but carbon can also catalyze and accelerate SEI formation, especially at high temperatures.[8,70] In terms of negative electrode materials, large capacity and low working potentials can contribute to high energy density for full cells. Unfortunately, LTO has low specific and volumetric capacity and high working potential, which makes it difficult for LTO to meet the requirements of high energy density cells.

2.3.4 Active Elements

To meet growing energy demand, researchers keep pursuing negative electrode materials with larger capacities. Some elements have reversible electrochemical reactions with lithium, which makes it possible for these elements to be negative electrode materials. Unlike graphite that reversibly inserts Li ions via intercalation processes, the lithiation

processes of the active elements involve breaking and reformation of bonds in the host structure.[71] One mole inserted lithium leads to an approximate 9 mL volume expansion for active elements that alloy with lithium.[71] The reversible reaction of active elements during lithiation/delithiation can be expressed as:

$$xLi^+ + M + xe^- \leftrightharpoons Li_xM \tag{2.10}$$

Where M is an electrochemically active element with lithium, and x is the electron transfer number.

Volumetric capacities and specific capacities of selected active elements are shown in Figures 2.3(a) and (b), respectively. The specific capacity calculations are based on fully lithiated phases of these active elements at room temperature.[13,72–80] Among the active elements shown in Figure 2.3(b), Si has the highest specific capacity of 3579 mAh/g, which is almost ten times that of graphite (372 mAh/g). For most applications, battery volume is much more important than battery weight. Therefore, volumetric capacity is a more meaningful figure of merit for negative electrode materials. The volumetric capacities shown in Figure 2.3(a) are obtained at the state of full lithiation of these discussed active elements. It can be observed that the volumetric capacities of all these elements are much higher than that of graphite.

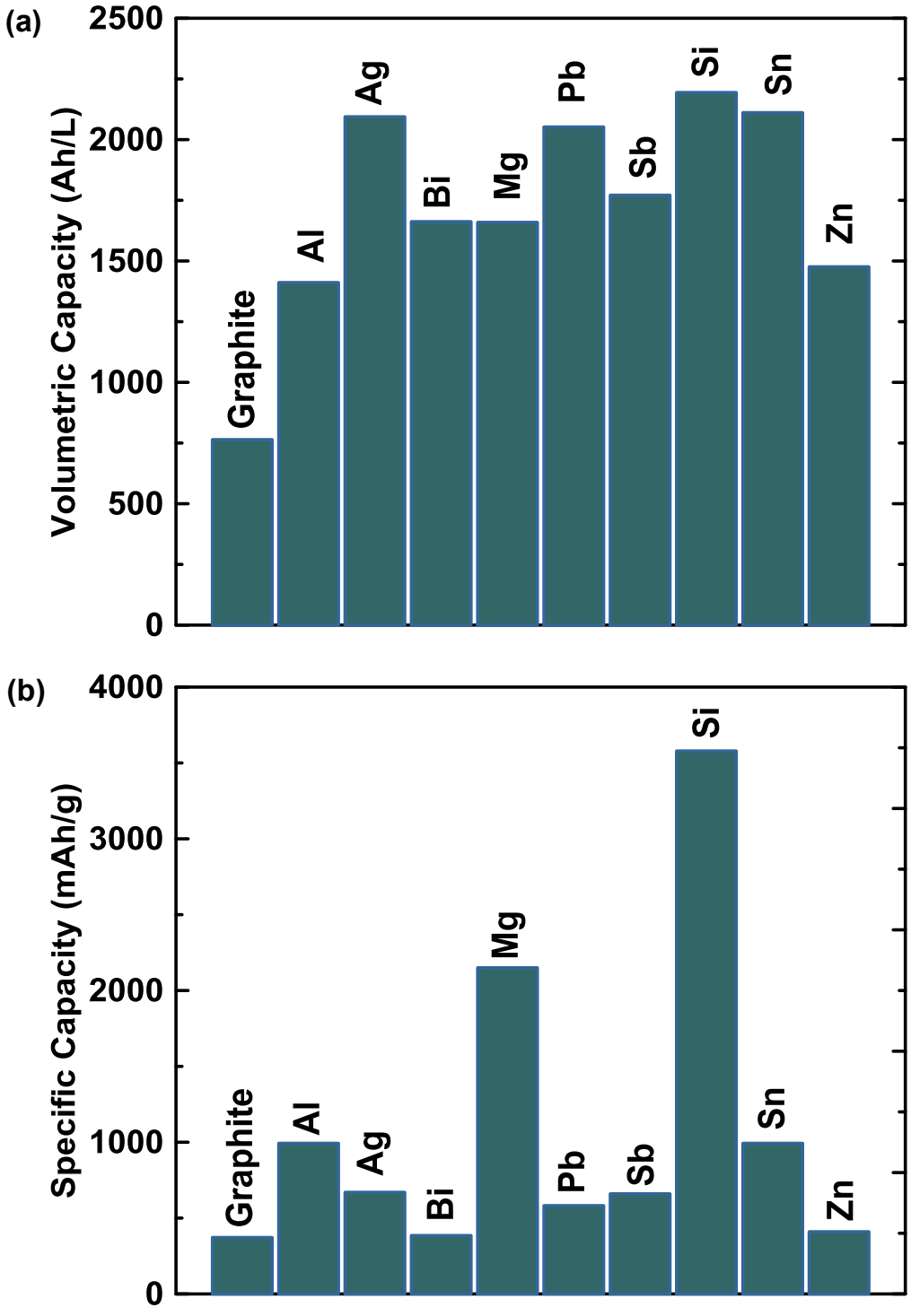

Figure 2.3 (a) Volumetric capacities at the state of full lithiation and (b) specific capacities of graphite and selected active elements

Average potential is another important metric to evaluate negative electrode materials. Figure 2.4 shows the average potentials vs. Li^+/Li of lithium insertion in the selected elements.[13] Mg has a very low average potential vs Li^+/Li, which is not desirable, since this can lead to safety issues induced by lithium deposition during cell cycling. Negative electrode materials with very high average lithiation potentials are also not desirable, such as Bi and Sb. This is because when a positive electrode is chosen, a negative electrode with low (but not too low) average potential can lead to high volumetric energy density of the cell, which is very important for commercial cells.

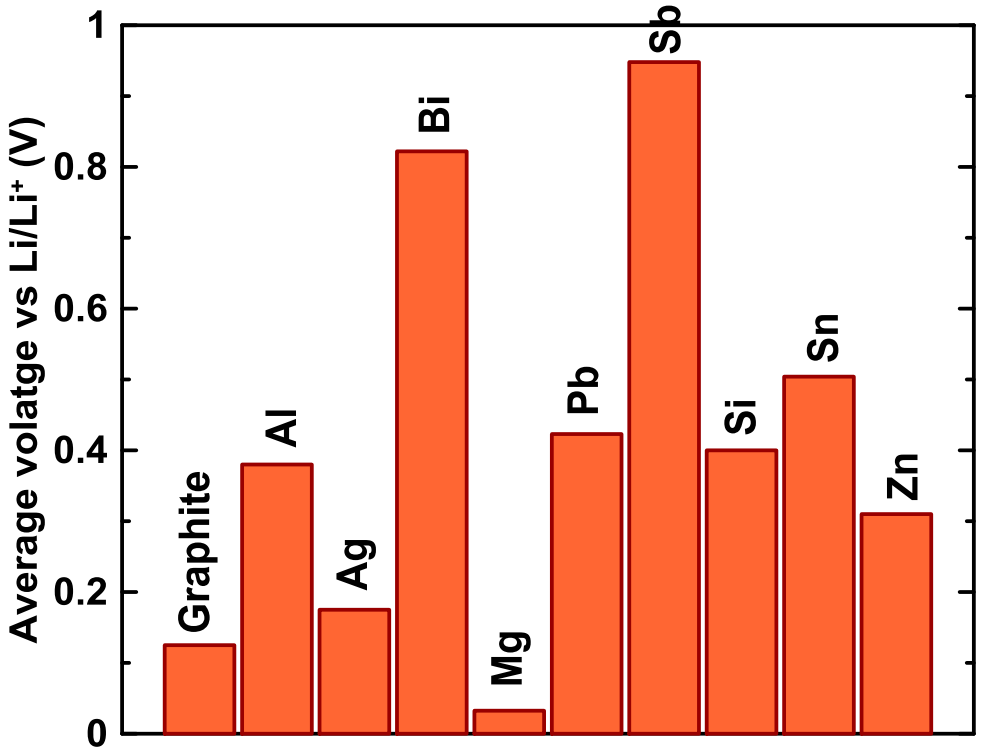

Figure 2.4 Average potential vs Li^+/Li for graphite and selected active elements

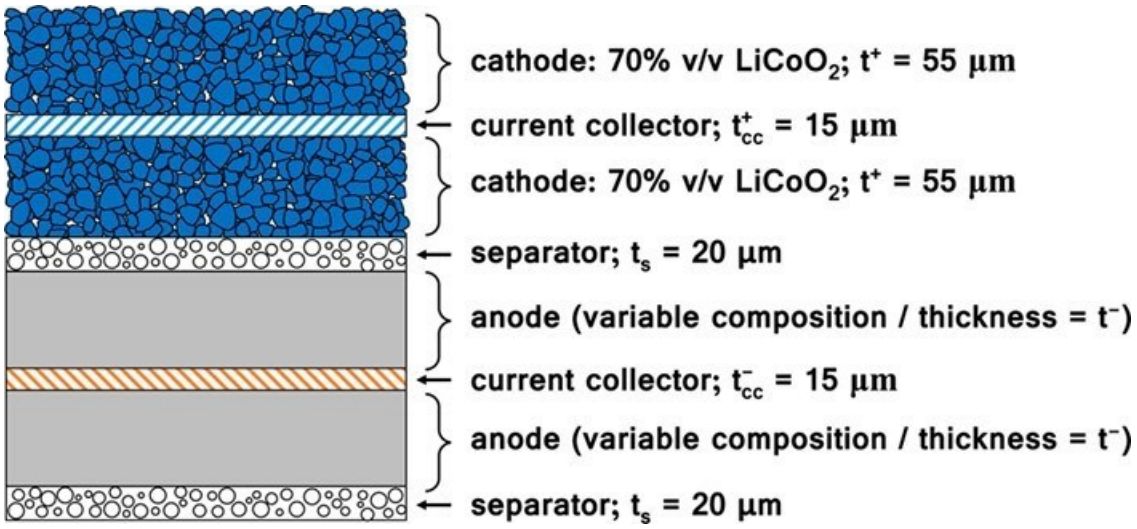

Figure 2.5 Cell stack used to model the impact of different negative electrodes on cell energy density. Reprinted with permission from Reference 13. Copyright 2014 American Chemical Society.

Obrovac et al. proposed a model for evaluating the impact of different negative electrode materials on cell energy density.[13] This model is based on a full cell stack, which is illustrated in Figure 2.5. As shown in Reference 13, cell stack energy density in Wh/L using the cell stack can be expressed as:

$$U_R = \frac{2q_R^+ t^+}{t_{cc}^+ + t_{cc}^- + 2t_s + 2t^+\left[1+\frac{q_R^+}{q_R^-}\left(\frac{N}{P}\right)\right]}\left(V_{avg}^+ - V_{avg}^-\right) \quad (2.11)$$

Where q_R^+ and q_R^- are the volumetric capacities in Ah/L of the positive and negative electrodes, t^+, t_{cc}^+, t_{cc}^-, and t_s are thickness of the positive electrode coating (55 µm), the current collector for the positive electrode (15 µm), the current collector for the negative electrode (15 µm), and the separator (20 µm), respectively, *N/P* is the negative to positive electrode capacity ratio (the value of N/P is about 1.1-1.2 in commercial cells, and N/P of

1.1 is used in this model), and V_{avg}^{+} and V_{avg}^{-} are average potentials of the positive and negative electrodes in V. In order to highlight the effect of the negative electrodes, $LiCoO_2$ was chosen as the positive electrode material in this model, which has a volumetric capacity of 757.5 Ah/L (specific capacity:150 mAh/g; density: 5.05 g/cm^3) and an average potential of 3.9 V. In this model, $LiCoO_2$ accounts for 70% of the volume of the positive electrode coating. Here, the impact of the negative electrode materials shown in Figure 2.4 on cell energy density was studied using the model mentioned above. The negative material in the negative electrode is also assumed account for 70% of the coating volume. Stack energy densities of these negative electrode materials are calculated based on their theoretical volumetric capacities (Figure 2.3(a)) and average potentials (Figure 2.4), and the results are illustrated in Figure 2.6. Compared to graphite, Bi and Sb have much larger volumetric capacities, but just show a little improvement in stack energy density. This is mainly because Bi and Sb have high average potentials, as mentioned above. Excepting Bi and Sb, the other active elements shown in Figure 2.6 contribute to much larger stack energy densities than graphite, and the stack energy densities for Ag, Mg, and Si are higher than the others. However, the average potential of Mg is too low, as discussed above. In addition, Ag is much more expensive than Si. Therefore, Si is of interest and will be discussed in detail in this thesis.

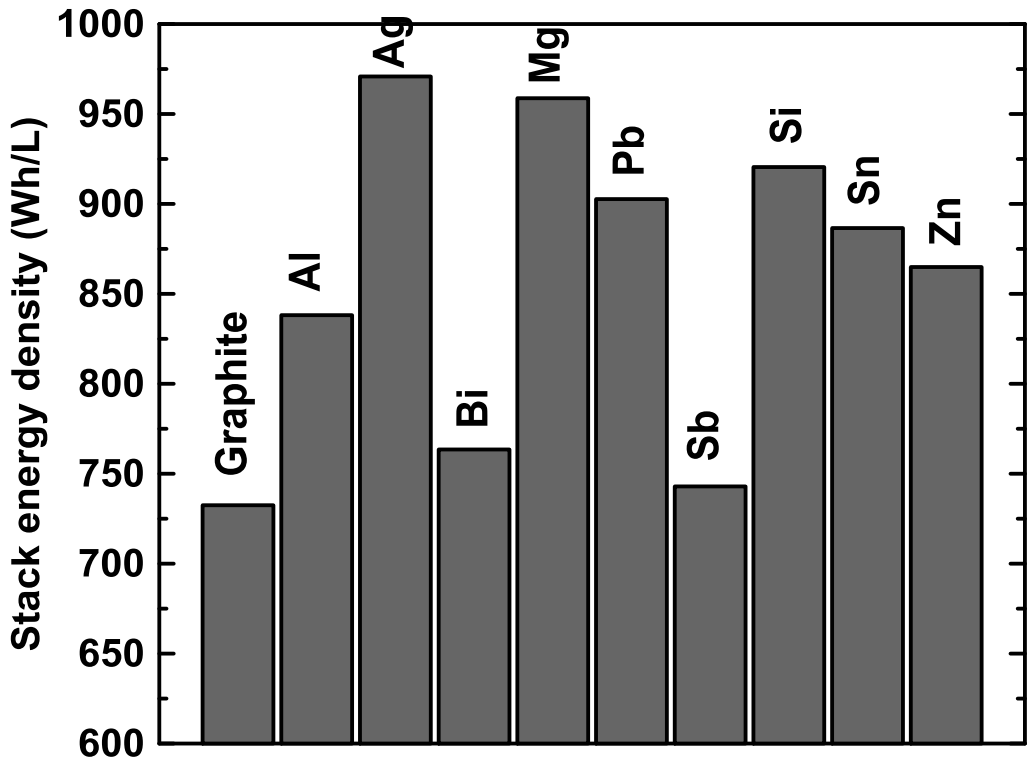

Figure 2.6 Stack energy density for graphite and selected active elements.

2.3.5 Silicon-Based Materials

Silicon is very likely to be extensively applied to next generation negative electrodes in Li-ion batteries. As discussed above, silicon can reversibly react with lithium at an appropriate average potential (~ 0.4 V vs. Li/Li^+) and has very high specific and volumetric capacities (3579 mAh/g and 2194 Ah/L). The use of Si negative electrodes is expected to increase the energy density of Li-ion cells. Besides, Si is plentiful and inexpensive. It has also been shown that lithiated Si has lower reactivity with electrolyte solvents than lithiated graphite.[81] In this section, the electrochemistry of Si during lithiation/delithiation, the challenges of Si negative electrode materials (volume expansion

during lithiation, unstable SEI during cycling, and the effect of two-phase regions), and how to overcome these challenges will be discussed. In recent decades, Si alloy negative electrode materials have received much attention for improved performance. Hence, Si/active and Si/inactive negative electrode materials will also be discussed in detail in this section.

2.3.5.1 Electrochemistry of Silicon during Lithiation/Delithiation

The electrochemical performance of Si negative electrodes is highly susceptible to temperature. At 415 °C, as the amount of inserted Li ions increases, $Li_{12}Si_7$, $Li_{14}Si_6$, $Li_{13}Si_4$ and $Li_{22}Si_5$ form sequentially,[82,83] which is consistent with the Li-Si equilibrium phase diagram.[15] However, the electrochemical behavior of Si negative electrodes is much different at room temperature. The potential-capacity profile of bulk Si powder is shown in Figure 2.7, and some related reactions are as follows.[84]

I and II: $$\text{cr-Si} \xrightarrow{Li} \text{a-Li}_y\text{Si} \xrightarrow{Li} \text{cr-Li}_{15}\text{Si}_4 \ (y = 3.5 \pm 0.2)^{78} \quad (2.12)$$

III: $$\text{cr-Li}_{15}\text{Si}_4 \xrightarrow{-Li} \text{a-Li}_z\text{Si} \xrightarrow{-Li} \text{a-Si} \ (z_{max} = 2.0)^{78} \quad (2.13)$$

IV: $$\text{a-Si} \xrightarrow{Li} \text{a-Li}_{y'}\text{Si} \xrightarrow{Li} \text{a-Li}_{y''}\text{ Si} \quad (2.14)$$

VI: $$\text{a-Li}_{y''}\text{Si} \xrightarrow{Li} \text{cr-Li}_{15}\text{Si}_4 \quad (2.15)$$

For the reactions above, “cr” indicates a crystalline phase and “a” indicates an amorphous phase. During the first lithiation, bulk Si undergoes a two-phase reaction with

Li to form a-Li_ySi (I in Figure 2.7). The fully lithiated phase of Si is $Li_{15}Si_4$ at room temperature (II in Figure 2.7), which corresponds to a specific capacity of 3579 mAh/g. This is contrary to the original knowledge that $Li_{22}Si_4$ is the fully lithiated phase at room temperature, based on the Li-Si phase diagram. In $Li_{15}Si_4$, Si atoms are isolated by Li atoms and reside in equivalent crystallographic sites.[85] Metastable $Li_{15}Si_4$ is not present in the Li-Si equilibrium phase diagram, and turns into other phases at temperatures in the range of 200-350 °C.[86,87] All crystalline phases in the Li-Si equilibrium phase diagram are not formed during room temperature lithiation because their formation is kinetically hindered. During the following delithiation of $Li_{15}Si_4$, a potential plateau at about 0.45 V can be observed in the III region of Figure 2.7, which represents a coexisting phase region (cr-$Li_{15}Si_4$ and a-Li_zSi). Finally, a-Si is produced after full delithiation, which means cr-Si can be amorphized after one complete lithiation/delithiation cycle.[88,89] In the subsequent lithiation, the cut off potential is limited to be above 50 mV. Two amorphous phases are produced and no cr-$Li_{15}Si_4$ forms in this situation (IV in Figure 2.7). However, when the cut off potential is allowed to be below 50 mV, cr-$Li_{15}Si_4$ is present after lithiation (VI in Figure 2.7). For the lithiation of pure Si, it is deemed that $Li_{15}Si_4$ crystallizes below 50 mV.[84]

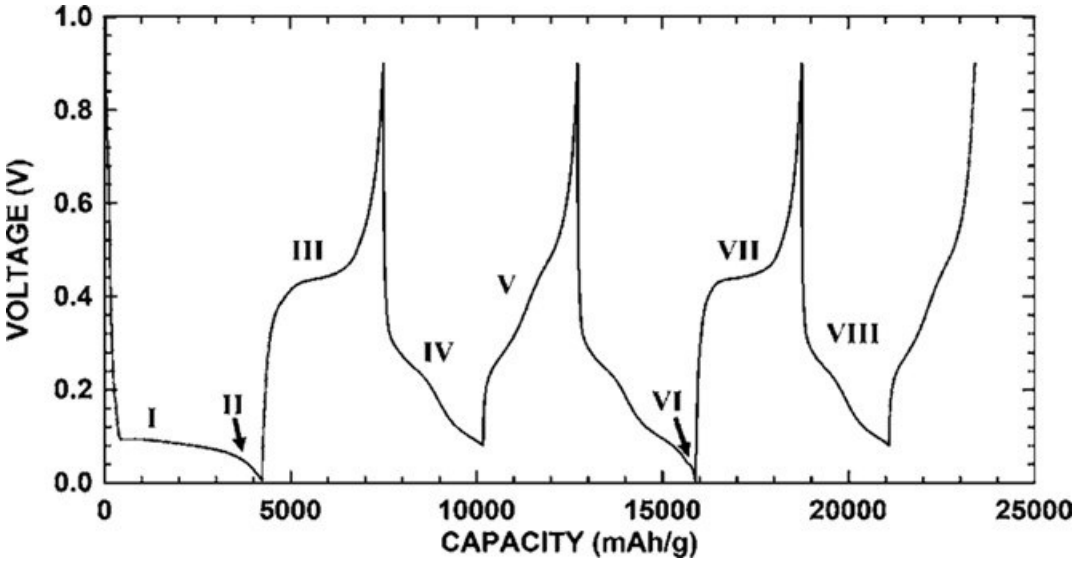

Figure 2.7 Potential-capacity profile of bulk Si powder. Reprinted with permission from Reference 84. Copyright 2007 Electrochemical Society.

2.3.5.2 Challenges of Silicon Negative Electrode Materials and Mitigation Strategies

One main challenge of Si negative electrode materials is Si volume expansion during lithiation. As discussed in section 2.3.4, one mole inserted Li ions causes an increase in volume of 9 mL in active alloying elements. Since the fully lithiated phase of Si is $Li_{15}Si_4$ at room temperature, Si undergoes a huge volume expansion of 280% after full lithiation.[16,71] In commercial cells, the tolerance for negative electrode volume expansion depends on factors such as cell constitution and types of electrolytes. Commercial cells cannot tolerate the huge volume expansion of Si after full lithiation. In addition, the lithiated Si contracts during delithiation. The strain during contraction may cause some active particles to lose electrical contact and, consequently, cell fade.[14,15,90–92] One possible

method to reduce the total volume expansion is to prepare Si/inactive alloys, which will be discussed in section 2.3.5.3.

Two-phase reactions are deemed to be detrimental to cell performance of Si negative electrode materials. As stated in section 2.3.5.1, a two-phase reaction occurs during the initial lithiation of cr-Si (like bulk Si). It has been reported that a very sharp reaction front during cr-Si lithiation was detected by transmission electron microscopy (TEM).[93,94] The reaction front induces high stress on the two-phase (cr-Si and a-Li_ySi) boundary, which was studied by a theoretical model.[95] This may cause active particle pulverization leading to cell fade. Also, a sharp reaction front during the first lithiation of a-Si was still observed, which is similar to that of cr-Si.[96] However, a-Si has a more sloping initial lithiation potential plateau than cr-Si, which suggests lower internal stresses between two phases and less possibility of Si particle fracture. Therefore, a-Si generally has better structure stability than cr-Si during cell cycling.[90] In addition, the delithiation of $Li_{15}Si_4$ also undergoes a two-phase reaction, as discussed in section 2.3.5.1, and is detrimental to cell performance as well.[16–18] Obrovac and Krause introduced a method to cycle cr-Si electrodes in order to avoid 2-phase formation.[84] The cr-Si electrode was first partially lithiated to reach a certain capacity. Then, through several conditioning cycles, more cr-Si was converted to a-Si, but the electrode still consists of cr-Si and a-Si. After these conditioning cycles, the electrode was fully delithiated, and then cycled with a lower potential cutoff above 170 mV. In this way, only a-Si was cycled with no further conversion

from cr-Si to a-Si, and the formation of $Li_{15}Si_4$ can be avoided.[16] With this cycling method, the cr-Si electrode can be cycled for over 100 cycles having stable performance. In addition to limiting the cutoff potential, the formation of $Li_{15}Si_4$ can be suppressed by preparing Si/inactive alloys,[97,98] which will be discussed in section 2.3.5.3.

Irreversible consumption of Li ions is another cause of fade for lithium ion cells with Si negative electrodes. SEI can form on negative electrode surfaces during cell cycling, resulting in lithium ion consumption. Although the SEI leads to some capacity fade, it can protect active materials from further side chemical reactions.[99] Therefore, a stable SEI is crucial for preventing further electrolyte decomposition, so that a long cycle life can be obtained. However, it is difficult to keep a stable SEI at a Si negative electrode during cycling. Because the formed SEI layer is vulnerable to cracking and exfoliation during delithiation (or volume contraction) processes, this can result in fresh electrode surfaces being exposed, leading to more SEI formation at the negative electrode. Applying a carbon coating on Si-based negative electrode materials is regarded as an effective approach to keep a stable SEI, which will be stated in section 2.3.5.3.

2.3.5.3 Silicon/Active and Silicon/Inactive Alloy

Many Si/active alloy negative electrodes have been investigated in Li-ion batteries, such as Si-C,[100,101] Si-Sn,[102–104], Si-Zn,[105] and Si-Ag alloy negative electrodes.[106,107] Si/active alloy negative electrodes have different electrochemical performance from the

parent elements. Among Si/active alloys, Si-C alloys are promising, which combine the high specific and volumetric capacities of Si with the stable structure and good conductivity of C.[108–110] Carbon coated Si-based negative electrode materials have received much attention, as they can avoid the exposure of Si-based particles to electrolyte and keep a stable SEI during cell cycling.[111] Several common methods are applied to prepare carbon coating on Si-based particles, such as chemical vapour deposition,[112] thermal vapour deposition,[113,114] and carbonization of carbon precursors on Si-based particles.[108,115] Liu et al. prepared a Si-C composite with a pomegranate structure.[116] A conductive carbon layer encased a single Si nanoparticle and provided enough space for the nanoparticle to expand and contract during lithiation/delithiation. This special structure has a low overall particle surface area, resulting in low and stable SEI formation. High coulombic efficiency (99.87%) and volumetric capacity (1270mAh/cm^3) were obtained and the reversible capacity reached up to 97% even after 1000 cycles. However, the preparation method of the Si-C composite is very complicated, so it cannot be used in commercial cells.

Si/inactive alloys can be prepared with Si and inactive elements as precursors by ball milling,[117–119] or sputter deposition.[118,120] During the alloying process, silicides are generally produced. Based on thermodynamics, silicides can have displacement-type reactions with Li.[121,122] However, at room temperature, many silicides often are deemed as electrochemically inactive phases in Li-ion cells.[123] Fleischauer et al. suggested that the silicides in sputtered Si-M (M=Cr + Ni, Fe, Mn and Co) films were inactive.[123,124] Of course

there are exceptions. For example, nano-$NiSi_2$ prepared by ball milling has a maximum reversible capacity of 500 mAh/g. The nano-$NiSi_2$ was characterized by in-situ XRD during cycling, and the XRD peaks of $NiSi_2$ disappeared after lithiation, which indicated that nano-$NiSi_2$ is active.[125]

As stated in section 2.3.5.2, alloying Si with inactive elements can be used to suppress the volume expansion during lithiation. In this way, Si is diluted by inactive phases (the inactive elements and produced inactive silicides), so the total volume expansion of the alloys during lithiation is reduced.[71] The formula shown below can be used to calculate the volume percentage of Si in a designed Si/inactive alloy, at a given fully lithiated volume expansion.[71]

$$\%\text{volume Si in alloy } = \frac{\xi_f}{\xi_0} \times 100\% \tag{2.16}$$

Here ξ_f and ξ_0 are the given volume expansion of the alloy and the volume expansion of Si at the state of full lithiation, respectively. When the given full lithiation volume expansion is 100%, the alloy should comprise 36 vol.% Si. Alternative to using an active/inactive alloy to limit volume expansion, the same effect might be achieved by simply limiting the capacity of a pure Si electrode. To compare the effect of these two methods, half cells for pure a-Si and the Si/inactive alloy were made. Figure 2.8 shows the potential profiles of the a-Si (curve A) and the Si/inactive alloy (curve B) half cells. The average potential of the pure a-Si electrode is higher than that of the Si/inactive alloy electrode. Therefore, at a

given volume expansion, a Si/inactive negative electrode can provide a higher volumetric energy density for cells than a pure a-Si negative electrode.

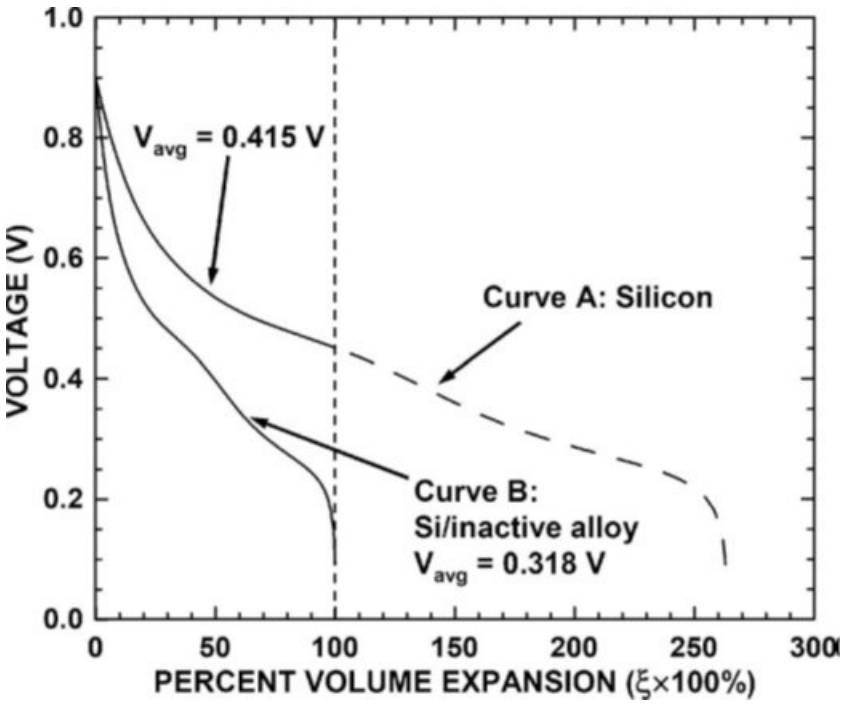

Figure 2.8 Comparison between two methods used to suppress volume expansion to 100%. Reprinted with permission from Reference 71. Copyright 2007 Electrochemical Society.

It is found that nano-structured Si/inactive alloys can suppress $Li_{15}Si_4$ formation,[97,98] as discussed in section 2.3.5.2. Du et al. prepared Si-Ni alloys by sputtering, and the formation of $Li_{15}Si_4$ was suppressed.[126] Similar phenomena were found in sputtered Si-B and S-Fe alloys,[127,128] and ball milled Si-Cu and Si-Ni alloys.[129,130] The possible reason for this is that inactive phases induce high mechanical stresses during Si/inactive alloy volume expansion, which leads to a negative shift of lithiation potential. As stated above, the $Li_{15}Si_4$ crystallization for pure Si is at low potential (about 50mV), so $Li_{15}Si_4$ formation

can be suppressed if the negative shift in lithiation potential is less than ~50 mV. Interestingly, the delithiation potential of Si/inactive alloys usually do not change significantly,[129,130] which is presumably because stress from contraction during delithiation can be released by Si alloy particles fracture.

2.4 Lithium Ion Battery Electrolyte

In a lithium cell, electrolyte plays a key role in transporting lithium ions back and forth between the positive electrode and the negative electrode. The most commonly used electrolyte consists of a mixture of carbonate solvents and a lithium salt. There are many requirements for ideal solvents, such as high salt solubility, low viscosity, and good interfacial stability on negative and positive electrodes. However, no single solvent has been found to meet all the requirements mentioned above. Ethylene carbonate (EC) is the most common electrolyte solvent component for lithium ion cells, which has good salt solubility but high viscosity.[131] Therefore, EC is typically combined with another carbonate solvent with low viscosity, such as diethyl carbonate (DEC), dimethyl carbonate (DMC) and ethyl methyl carbonate (EMC).[22] The most common salt used in lithium ion cells is lithium hexafluorophosphate ($LiPF_6$) due to its good ion conductivity, good solubility, and high chemical stability in carbonate solvents.[22,24] Two main drawbacks have been found when using $LiPF_6$ for lithium cell electrolyte, which are poor thermal stability and moisture

sensitivity.[132–135] $LiPF_6$ can react with traces of water in a lithium cell to produce HF, and HF can corrode passivating films, electrode materials, and other cell parts.[134,135]

As stated above, an SEI forms due to electrolyte decomposition on electrode surfaces during lithium cell cycling, which involves irreversible lithium ion consumption. The SEI has a complex composition, it is mainly made of Li_2CO_3, LiF, Li_2O, lithium alkyl carbonates ($ROCO_2Li$), and nonconductive polymers.[99,136] It is desireable that the SEI has a high ionic conductivity and low electronic conductivity, and passivates against further SEI formation.[104] If the SEI thickens during cell cycling, it could lead to increased impedance and continuous consumption of lithium ions. Using advanced lithium salts and electrolyte additives are good strategies to keep the SEI stable for obtaining improved cell cycling performance.[137,138]

Chapter 3 Experimental Techniques

3.1 Material Synthesis

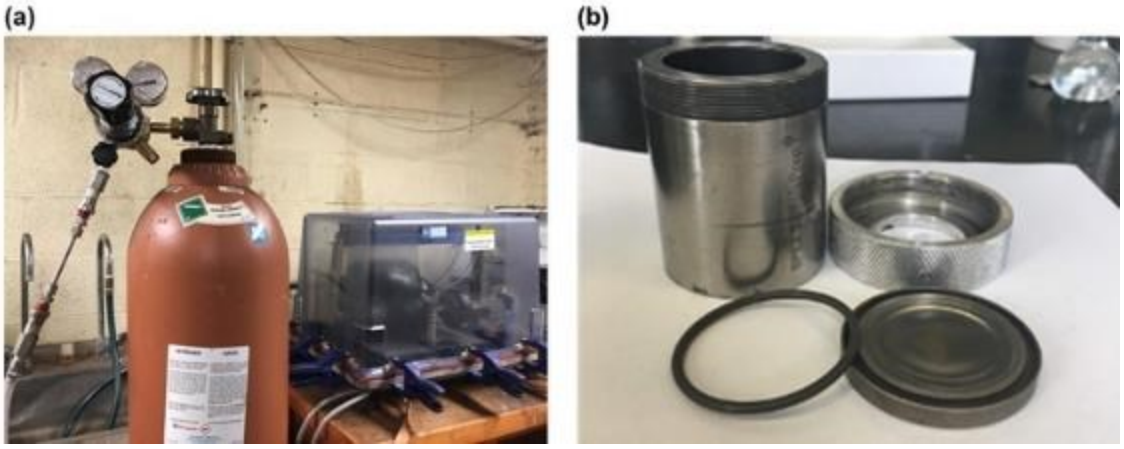

Figure 3.1 (a) A setup for N_2 (g) milling, including a modified ball mill (Spex Mixer Mill Model 8000D), a N_2 (g) cylinder, and a water cooling system. (b) A mill vial for N_2 (g) and air milling.

In this thesis, Si alloys were prepared using mechanical milling. Si powder (Sigma-Aldrich, 325 mesh, 99%) and another powder (such as Mo powder (Alfa Aesar, 250 mesh, 99.9%), Ti powder (Alfa Aesar, 325 mesh, 99%), or TiN (Sigma-Aldrich, < 3 μm)) with different stoichiometric ratios were typically used as starting materials. 0.5 mL total volume of the starting materials was loaded into a mill vial (SPEX CertiPrep, 65 ml, hardened steel) with 180 g stainless steel balls (d = 0.125 inch). A high energy ball mill (Spex Mixer Mill Model 8000D, Spex CertiPrep, Metuchen, NJ) was used to prepare Si alloy samples. The sample preparation conditions described above were optimized in a previous work.[139] The milling atmospheres used for this thesis were Ar, N_2 (g), or air. For

milling in Ar, the milling vials with powders and milling balls were flushed with Ar and sealed in an Ar-filled glovebox. A glovebox filled with N_2 (g) or the setup shown in Figure 3.1(a) was used for N_2 (g) milling. As shown in Figure 3.1(a), the ball mill was modified by enclosing the entire mill in a sealed outer chamber equipped with a gas inlet and outlet. The gas inlet was connected to a compressed nitrogen cylinder via a gas regulator and flowmeter. The gas outlet was connected to an oil bubbler. The mill containers used for N_2 (g) milling were modified as illustrated in Figure 3.1(b). The o-ring seal of the mill container was removed and a 0.125 inch hole was drilled in the container clamping ring. This arrangement allows N_2 (g) to enter the containers freely during milling, but does not allow the escape of the powder contents of the mill. The mill containers with powders and milling medias were flushed with N_2 (g) and Ar before being put in the N_2 (g) glovebox and the setup shown in Figure 3.1 (a), respectively. After the mill container was place in the setup shown in Figure 3.1 (a), the outer chamber was sealed and N_2 (g) was purged through the chamber in order that the air inside was displaced. For air milling, the mill vials used were the same with the ones for N_2 (g) milling, and the sample preparation occurred in air. The milling time is typically 1-16 h. After milling, about 20 mL of ethanol was added into each container and the containers were milled for another 5 min in air. Powder samples were then obtained by collecting the ethanol/powder slurries and drying them at 120°C in air for 20-30 minutes.

For thermal stability investigations, some ball milled samples were heated in a tube furnace under flowing Ar. The temperature of the furnace was increased from room temperature at a heating rate of 10 °C/min, to a target temperature of 600 °C or 800 °C. The target temperature was then maintained for 3 h. The samples were then naturally cooled to room temperature under argon flow.

3.2 X-ray Diffraction

3.2.1 X-ray Diffraction Theory

X-rays are a kind of electromagnetic radiation. Wavelengths of most X-rays are in the range of 0.01 ~ 10 nanometers, which correspond to frequencies ranging from 3×10^{16} to 3×10^{19} Hz and energies ranging from 100eV to 1MeV. The wavelengths of X-rays are between ultraviolet (UV) rays and gamma rays. In fact, there are no obvious boundaries between regions in the electromagnetic spectrum and the so-called boundaries are arbitrary. X-ray diffraction (XRD) is an important application of X-rays, which is a non-destructive analysis technique. It can be used to analyze crystal structures, chemical compositions and other physical properties of solids.

In an XRD instrument, X-rays are produced in a vacuum X-ray tube with an anode, a cathode, and a Wehnelt cylinder. High voltage is maintained between the cathode and the anode (such as Cu, Mo, Ag, and Fe etc.), which can drive electrons toward the anode with very high velocity. The Wehmelt cylinder is in front of the cathode, which is used for

focusing and control of the electron beam. Collision between the electrons and the anode can produce X-rays with different wavelengths, which can form a continuous X-ray spectrum. If the voltage between electrodes is high enough, an electron can be accelerated to quite a high velocity before it reaches the anode. Such an electron with sufficient energy is able to eject an inner shell electron from an atom of the anode, which leads to an exited atom with a hole in the inner shell. During the subsequent de-excitation of the atom, the hole is filled by an outer shell electron. At the same time, an X-ray photon is produced with an energy equal to the difference in electron energy levels, which results in the emission of X-rays with a characteristic wavelength.[140] Based on the name of the filled inner shell, X-rays can be classified as M, L and K.

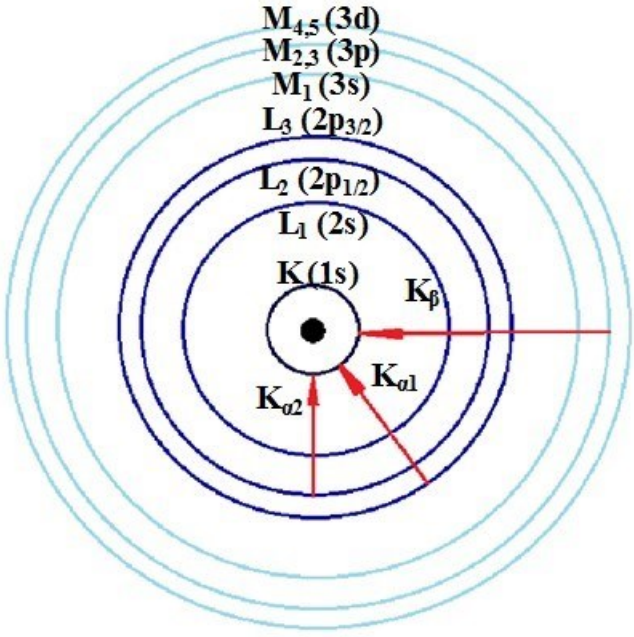

Figure 3.2 Formation processes of Cu K X-rays

When X-rays encounter any substance, they are partly absorbed. The degree of adsorption is proportional to the X-ray wavelength.[141] Since M and L X-rays have longer wavelengths than K X-rays, they are more easily absorbed when passing through materials. Therefore, only K X-rays are typically applied to XRD. Cu is one of the most important targets to produce X-rays, and several formation processes of K X-rays are shown in Figure 3.2. The electron transition from $M_{2,3}$ (3p) to K (1s), L_3 ($2p_{3/2}$) to K (1s) or L_2 ($2p_{1/2}$) to K (1s) can produce a Cu K_β, Cu $K_{\alpha 1}$ or Cu $K_{\alpha 2}$ X-rays, respectively.

Ideally, monochromatic X-rays should be used for XRD. However, the beam produced in X-ray tubes consist of $K_{\alpha 1}$, $K_{\alpha 2}$, K_β, M, L and continuous X-rays. The wavelength of $K_{\alpha 1}$ X-rays is very close to that of $K_{\alpha 2}$ X-rays. These can be difficult to distinguish, so both of them are typically used for XRD. For K_β X-rays, a filter can be employed to reduce their intensities. The filter is made up of a material with an absorption edge between the K_β and K_α wavelength of a target. Such a filter material can absorb a large amount of K_β X-rays and a small amount of K_α X-rays. The atomic number of the filter material is usually one or two less than that of the target material.[141] However, a disadvantage of the filter is that it cannot reduce all continuous X-rays and the transmitted radiation is not very monochromatic. Therefore, single crystal monochromators are often employed. Single crystal monochromators are able to produce transmitted radiation with a narrower wavelength distribution, and are applied in some XRD studies where accuracy is crucial.

Incident X-rays should have a wavelength comparable to lattice plane spacings of a target sample. As shown in Figure 3.3, two beams of X-rays with an identical wavelength can be scattered by two different atoms in the sample. The low beam travels an extra length of 2dsinθ compared to the high beam. If 2dsinθ is equal to an odd multiple of half the wavelength of the X-rays, destructive interference occurs. If 2dsinθ is equal to an integer multiple of the wavelength of the X-rays, constructive interference occurs and Bragg's Law is satisfied:

$$n\lambda = 2dsin\theta \tag{3.1}$$

where λ is the wavelength of the incident X-rays, n is a positive integer, d is a lattice plane spacing of the sample, and θ is the acute angle between the incident X-rays and the lattice planes. In this way, a characteristic peak of the sample typically can be observed in its XRD pattern. Since there are many families of parallel planes with different interplanar distances in a phase, a series of characteristic peaks can be present in its X-ray pattern. The phase can be identified by matching positions of these characteristic peaks with a reference XRD pattern.

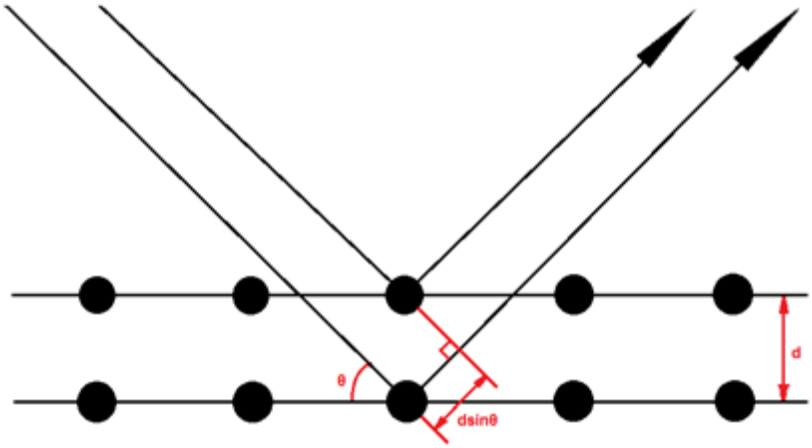

Figure 3.3 Illustration of Bragg's Law of diffraction

Grain sizes of the crystalline phase can be estimated by the Scherrer equation, which is shown below.

$$\tau = \frac{K\lambda}{\sqrt{H^2 - B^2}\cos\theta} \tag{3.2}$$

Here, K is a dimensionless shape factor (0.94 is used for K in this thesis), λ is the X-ray wavelength (0.154 nm in this thesis), H is full width at half maximum (FWHM) of an XRD peak in radians, B is instrumental broadening in radians (0.001745 used here), and θ is angle between the incident X-rays and the lattice planes in radians. Thus, highly crystalline solids have sharp X-ray peaks, while materials with small grain sizes and amorphous solids have broad X-ray peaks.

Different types of detectors are used to determine the intensity of X-ray radiation. Scintillation counters are very sensitive detectors of X-rays. Such detectors comprise a combination of a phosphor screen or scintillator and a photomultiplier tube. When the X-

rays strike the scintillator, it produces visible light. The photomultiplier tube is used to convert the visible light into voltage pulses. Another type of detector is a 1D silicon strip detector. For this type of detectors, silicon strips are arranged in a 1D array with narrow spacing intervals, and can detect diffracted X-rays for different 2θ angles simultaneously.[142] Strip detectors drastically cut down measurement time by increasing active area of capture, and it is an ideal means to characterize a large number of samples in a short time or an in-situ measurement with dynamic conditions. Finally, an XRD pattern of a target sample can be obtained, which is plotted as the intensity as a function of 2θ.

3.2.2 Characterization by X-ray Diffraction

In this thesis, XRD patterns were collected using a Rigaku Ultima IV diffractometer with a Cu Kα X-ray source, a graphite diffracted beam monochromator and a scintillation counter detector. A current of 40 mA and an accelerating voltage of 45 kV were used to generate X-rays. XRD patterns were recorded in the range of 10° to 80° or 20° to 80° 2θ with a step of 0.05° between each measurement. A stainless steel plate (25 mm × 20 mm × 3 mm) and a specifically designed sample holder (Figure 3.4) were used for XRD characterization of air stable samples and air sensitive samples, respectively. The sample holder for air sensitive samples has an arc-shaped aluminized Mylar window, which allows X-rays to get in and out perpendicularly to the window and does not interfere with the detected XRD peak positions. Air sensitive samples were placed and sealed in the special

sample holder in an Ar-filled glovebox so that the samples can be protected under Ar during XRD measurements.

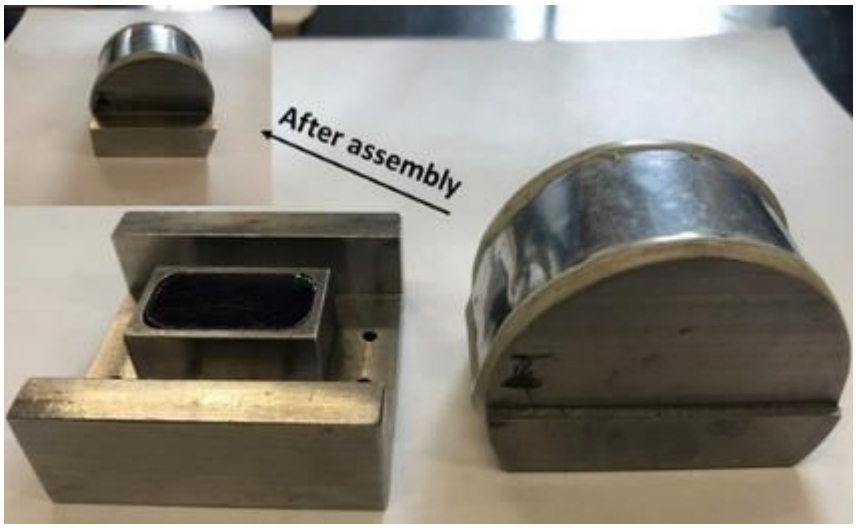

Figure 3.4 XRD sample holders for air sensitive samples.

3.2.3 X-ray Diffraction Quantitative Phase Determination

One approach used for XRD-based quantitative phase analysis involves XRD intensity and intensity factors (*IF*). In a mixture, there is a relationship between the XRD intensity and the weight percentage of each phase, which is shown as follows.[143]

$$I_\alpha = \frac{K_e \sum_1^n K_{\alpha i} X_\alpha}{\rho_\alpha \left(\frac{\mu}{\rho}\right)_m} \tag{3.3}$$

$$K_{\alpha i} = \frac{M_{\alpha i}}{V_\alpha{}^2} |F_{\alpha i}|^2 \left(\frac{1+cos^2 2\theta_{\alpha i}}{sin 2\theta_{\alpha i} cos\theta_{\alpha i}}\right) \tag{3.4}$$

Where I_α is the integrated intensity of phase α, K_e is a constant for a particular XRD instrument, X_α is the weight fraction of phase α, ρ_α is the density of phase α, and $(\mu/\rho)_m$ is the mass absorption coefficient of the mixture, $K_{\alpha i}$ is a constant for each diffraction

reflection i form the crystal structure of phase α, $M_{\alpha i}$ is the multiplicity of diffraction reflection i of phase α, V_α is the volume of unit cell of phase α, $F_{\alpha i}$ is the structure factor of diffraction reflection i of phase α, and $(1+\cos^2 2\theta_{\alpha i})/(\sin 2\theta_{\alpha i}\cos\theta_{\alpha i})$ is the Lorentz polarization correction for the diffractometer, $\theta_{\alpha i}$ is the acute angle between the incident X-rays and the lattice planes for diffraction reflection i of phase α. Here, $K_e\Sigma_1^n K_{\alpha i}/\rho_\alpha$ is a characteristic value for phase α measured with particular XRD conditions and is written as U_α.

The *IF* of phase α (IF_α) is the ratio between U_α and U_s (s indicates an internal standard material). Therefore, an internal standard material is needed to mix with a pure phase α. Since the weight percentages of phase α (X_α) and the internal standard (X_s) are known, IF_α can be calculated by Equation 3.5.

$$IF_\alpha = \frac{U_\alpha}{U_s} = \frac{I_\alpha\left(\frac{\mu}{\rho}\right)_m / X_\alpha}{I_s\left(\frac{\mu}{\rho}\right)_m / X_s} = \frac{I_\alpha X_s}{I_s X_\alpha} \tag{3.5}$$

Where I_α and I_s are the integrated XRD intensity of phase α and the internal standard in the mixture, respectively.

In some cases, pure phase α cannot be obtained to measure the IF_α value directly. If a mixture of phase α and another phase β can be obtained, the problem can be still solved according to Equation 3.3 and 3.4. The weight percentages of phase α (X_α) and phase β (X_β) in the mixture can be calculated as shown below.

$$\frac{I_\alpha}{I_\beta} = \frac{X_\alpha \sum_1^n K_{\alpha i}\ \rho_\beta}{X_\beta\ \sum_1^n K_{\beta i}\ \rho_\alpha} \tag{3.6}$$

$$X_\alpha + X_\beta = 100\% \tag{3.7}$$

Where I_α and I_β are the integrated XRD intensity of phase α and phase β in the mixture, respectively. In this way, the IF_α value can be obtained by adding an internal standard to the mixture of phase α and phase β,

For a target sample with n phases, the IF values of all these phases must be obtained using a fixed internal standard (TiN was used in this thesis). In addition, the total weight percentage of all n phases in the target sample is 100%. Therefore, the weight fraction of each phase j in the sample can be calculated by Equation 3.8.

$$X_j = \frac{X_j}{X_1+X_2+\cdots+X_n} = \frac{{I_j\left(\frac{\mu}{\rho}\right)_m}/{U_j}}{\sum_1^n {I_j\left(\frac{\mu}{\rho}\right)_m}/{U_j}} = \frac{{I_j}/{U_j}}{\sum_1^n {I_j}/{U_j}} = \frac{{I_j}/{IF_j}}{\sum_1^n {I_j}/{IF_j}} \tag{3.8}$$

The calculation process is called the 100% approach.[143,144]

3.2.4 X-ray Diffraction Fitting

As stated above, the 100% approach can be used for XRD quantitative phase analysis. XRD intensity is involved in this calculation method. To obtain XRD intensities a least squares fitting method was employed to fit the XRD pattern of a sample so that intensity (area) of each phase in the sample can be obtained. In this thesis, the background of the XRD patterns of unmilled Si alloys was modeled by a polynomial equation shown in Equation 3.9.

$$y_b = B_{-1}x^{-1} + B_0x^0 + B_1x^1 + B_2x^2 + B_3x^3 \quad (3.9)$$

Where B_{-1}, B_0, B_1, B_2, B_3 are refinable parameters, which are available for all x (or 2θ) values. The background used to fit the XRD pattern of a milled Si sample was the one derived from its corresponding unmilled sample. A Pseudo-Voigt peak shape function was used, as shown in Equation 3.10.

$$I = \gamma \frac{C_0}{H\pi}[1 + C_0X^2] + (1 - \gamma)\frac{{C_1}^{1/2}}{H\pi^{1/2}} exp\,[-C_1X^2] \quad (3.10)$$

Where I is intensity, γ is a mixing parameter, which can be varied between 0 to 1, C_0 and C_1 are equal to 4 and 4ln2, respectively, H is peak FWHM, and X is equal to $(x-x_i)/H$ (x_i is the peak position). The variation in peak FWHM was described by Equation 3.11.[145]

$$H = (Utan^2\theta + Vtan\theta + W)^{1/2} \quad (3.11)$$

Where U, V and W are refinable parameters, which are available for all peaks of one phase, and H can only be positive. In order to reduce variable parameters, all peaks of each phase in an XRD pattern were restricted to have the same relative peak positions and areas of the known XRD pattern of the pure phase. The total fit is the sum of the background and all individual peak fits. During fitting, all refinable parameters were optimized according to the least squares method. In this way, the intensity of each observed phase in a target sample can be gained. The fitting results of a Si-Mo alloy are illustrated in Figure 3.5 as an example.

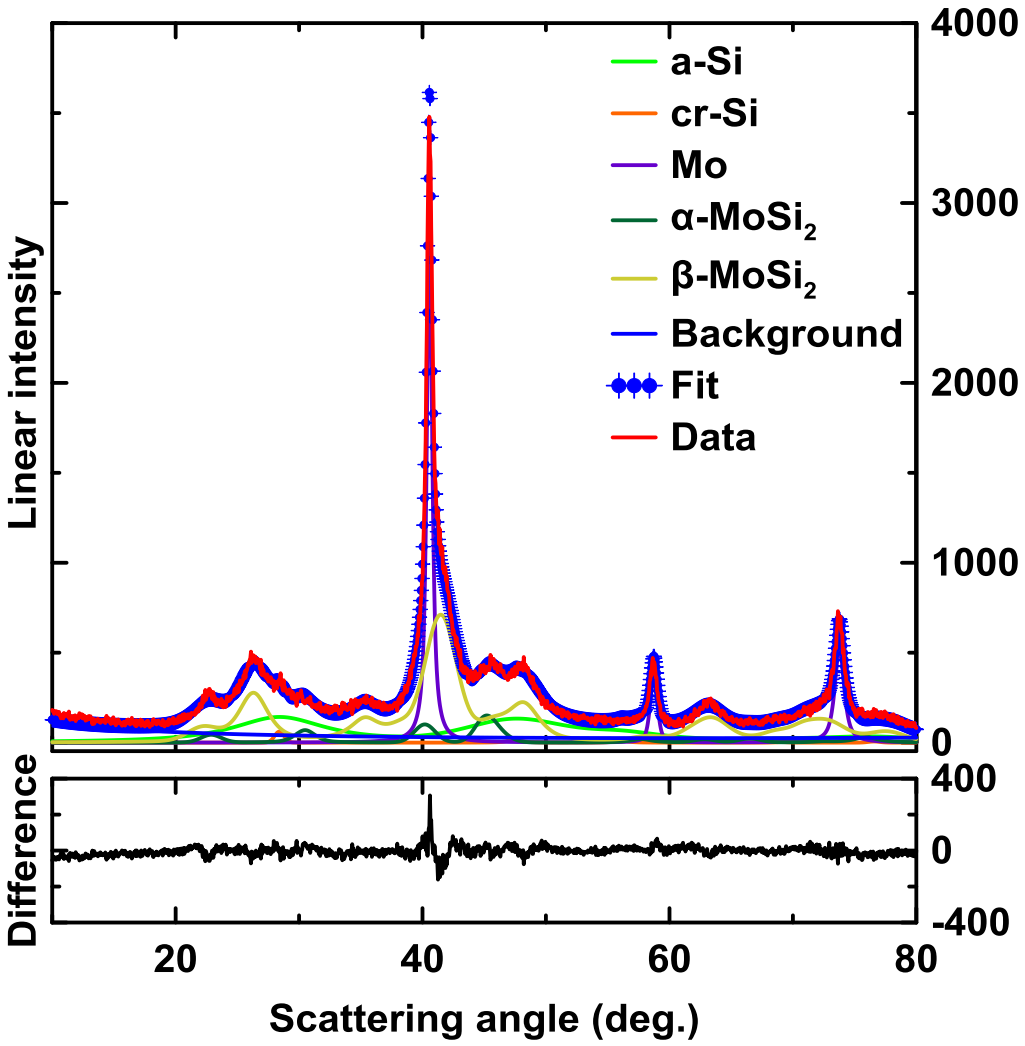

Figure 3.5 XRD fitting results for a Si-Mo alloy.

3.3 Scanning Electron Microscopy

The scanning electron microscope (SEM) is a widely used instrument, which can be used to characterize a sample's microstructure, morphology, and chemical composition. For a microscope, the wavelength of the light source determines the ultimate resolution of the microscope, and shorter wavelengths typically yield higher resolution. Based on this, optical microscopes have a limited resolution of ~ 200 nm. In electron microscopes, high

velocity electrons can be produced, which have much shorter de Broglie wavelengths than visible light. Therefore, electron microscopes have much better resolution than optical microscopes. Image resolution of SEMs are also limited by the electron spot size and the electron beam – specimen interaction volume, where the electron spot size depends on the electron-optical system that produces the electron beam. Usually, the SEM resolution is between 1 and 20 nm.

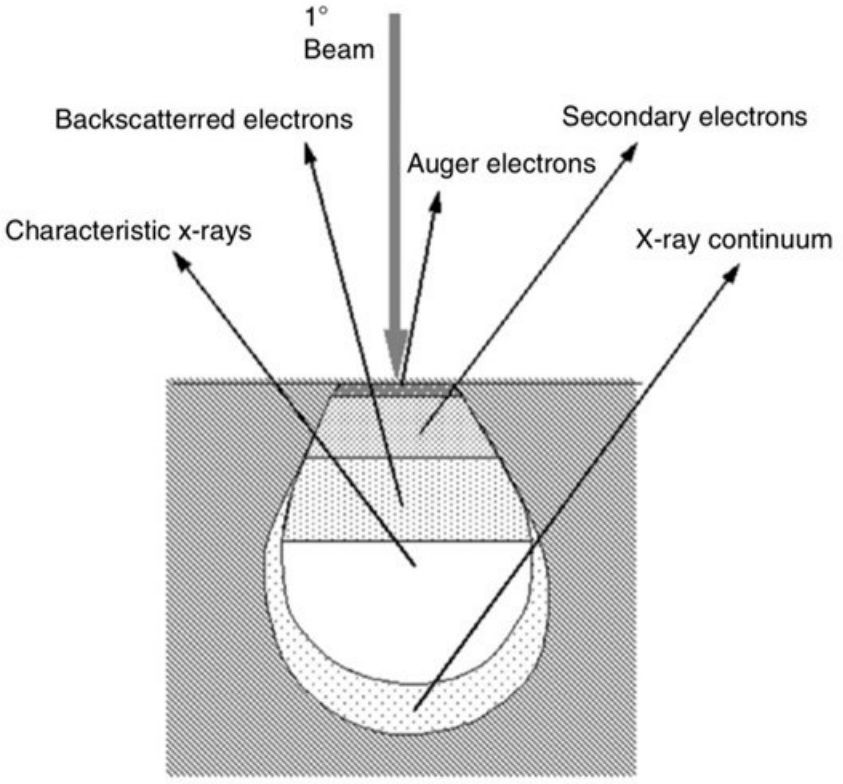

Figure 3.6 Schematic of several signals produced by the electron beam – specimen interaction. Reprinted with permission from Reference 146. Copyright 2007 Springer.

A SEM typically consists of an electron gun, electromagnetic lenses, apertures, a specimen stage, electron beam scanning coils, signal detectors, and signal processing

system.[146] An electron gun is employed to produce and accelerate electrons, and accelerating voltages of between 5-20 kV are typically used.[147] A conventional SEM is usually equipped with an electron gun utilizing a tungsten or lanthanum hexaboride cathode. High temperatures and electric fields at the cathode result in the escape of electrons. Field emission guns are used more frequently in modern SEMs. In a field emission gun, a large electrostatic gradient field is applied to free electrons form the filament. Compared to tungsten and lanthanum hexaboride electron guns, field emission guns can provide enhanced current and lower energy dispersion and have longer lifetime. After electrons are generated and accelerated, electromagnetic lenses and apertures are used to focus and define the electron beam so that a small electron spot can be focused on the specimen. Complex interactions occur between the electron beam and the specimen, and various signals can be produced as shown in Figure 3.6. The signals mainly consist of Auger electrons, secondary electrons (SEs), backscattered electrons (BSEs), characteristic X-rays, etc. SEs are generated by inelastic collisions between the primary electron beam and the specimen atoms. During inelastic collisions, the primary electron beam transfers substantial energy to the specimen atoms, leading to ionization of the specimen atoms and SE generation. SEs have low energy of typically 1-10 eV, so they can only escape from a region within a few nanometers of the specimen surface. Therefore, SEs are mainly used for sample morphology characterization. In addition, BSEs are high energy electrons originating in the electron beam, which have been reflected or backscattered due to elastic

scattering with from the specimen's constituent atoms. BSEs can escape the specimen surface from a deeper and larger region compared to SEs.[146] Sample elements with larger atomic numbers can contribute to generating more BSEs, leading to higher BSE signal and brighter regions in the BSE image. In this way, BSE signal can provide both compositional and morphology information. Furthermore, characteristic X-rays can also be generated by the electron beam – specimen interaction, and the generation mechanism is the same as the one for producing characteristic X-rays for XRD, as described in Section 3.2.1. Chemical information can be obtained through analyzing characteristic X-rays. As mentioned above, the electron beam is focused into a probe spot on the specimen surface to induce various signals. In order to form an image, scanning coils are applied to deflect the electron beam so that it can move from place to place over a rectangular area. Different detectors can be employed to detect different signals produced by the electron beam-material interaction. SE and BSE detectors are used to collect SEs and BSEs, respectively. In addition, a SEM is commonly equipped with an energy dispersive spectrometer (EDS), which can be used for detecting characteristic X-rays for chemical composition characterization. As shown in Figure 3.6, the electron beam – material interaction volume for generating characteristic X-rays is larger than those for SEs and BSEs. Therefore, EDS typically has lower resolution than SE and BSE imaging under the same measurement conditions.

In this thesis, sample morphology and electrode cross sections were characterized using a Schottky field emission SEM (TESCAN MIRA 3 LMU), which was operated at a

5 or 20 kV accelerating voltage. Electrode cross-sections were prepared using a JEOL IB-19530CP cross section polisher. In addition, an EDS system (Oxford instrument X-max 80mm^2) with a silicon drift detector (SDD) was used for semi-quantitative analysis of element content.

3.4 Transmission Electron Microscopy

Transmission Electron Microscope (TEM) is another important tool for microstructural and compositional characterization of materials. In a TEM, a thermionic electron gun with a tungsten or lanthanum hexaboride filament or a field emission gun is used to produce electrons, and the electron generation process is similar to that of an SEM. The voltage employed to accelerate electrons in a TEM is usually in the range of 100-300 kV. The high accelerating voltage contributes to high velocity and short wavelength for the electrons, leading to a typical high resolution of 0.1-0.2 nm for most field emission TEMs. For most conventional TEM imaging modes, a series of electromagnetic lenses and apertures are used to focus the high velocity electrons into a parallel beam. The parallel electron beam passes through a thin specimen, and the electron beam-specimen interaction occurs. The direct beam and the forward scattered diffraction beams are mainly used for imaging. The objective lens is located below the specimen to generate the first intermediate image and the diffraction pattern, as shown in Figure 3.7. The diffraction and projector lenses working together to project either the diffraction pattern (back focal plane of the

objective lens) or an image (image plane of the objective lens) on the recording system. In imaging mode, the objective aperture locates in the back focal plane of the objective lens. When only the direct beam is allowed to pass through the aperture, a bright field (BF) image can be obtained. When one diffracted beams are selected to go through the aperture, a dark field (DF) image can be formed. Also, when the aperture is large, both the direct beam and several diffracted beams are selected for imaging, as illustrated in the left schematic of Figure 3.7. In this way, the direct beam and the diffracted beams interfere with each other in the imaging plane and a high resolution electron microscopy (HREM) image can be obtained. In diffraction mode, the selected area aperture placed in the plane of the first intermediate image is used limit the area of the specimen contributing to the formation of a selected area electron diffraction (SAED) pattern. The final image or diffraction pattern can be viewed on a large fluorescent screen and be acquired by a charge-coupled device (CCD) camera.

Scanning TEM (STEM) is a technique, which combines TEM and SEM. Most modern TEMs can be switched to STEM mode. Conventional TEM uses a parallel electron beam as described above, while STEM, like SEM, uses a small convergent electron beam. For STEM, scanning coils are applied for deflecting the electron beam to scan across a defined specimen area, and a selected detector (like a BF detector) is used to collect the corresponding signal spot by spot, forming an image on a screen pixel by pixel. TEM instruments are usually equipped with an EDS detector, which is an important tool for

chemical composition analysis. In STEM mode, EDS can be employed to form composition maps for showing element distribution.

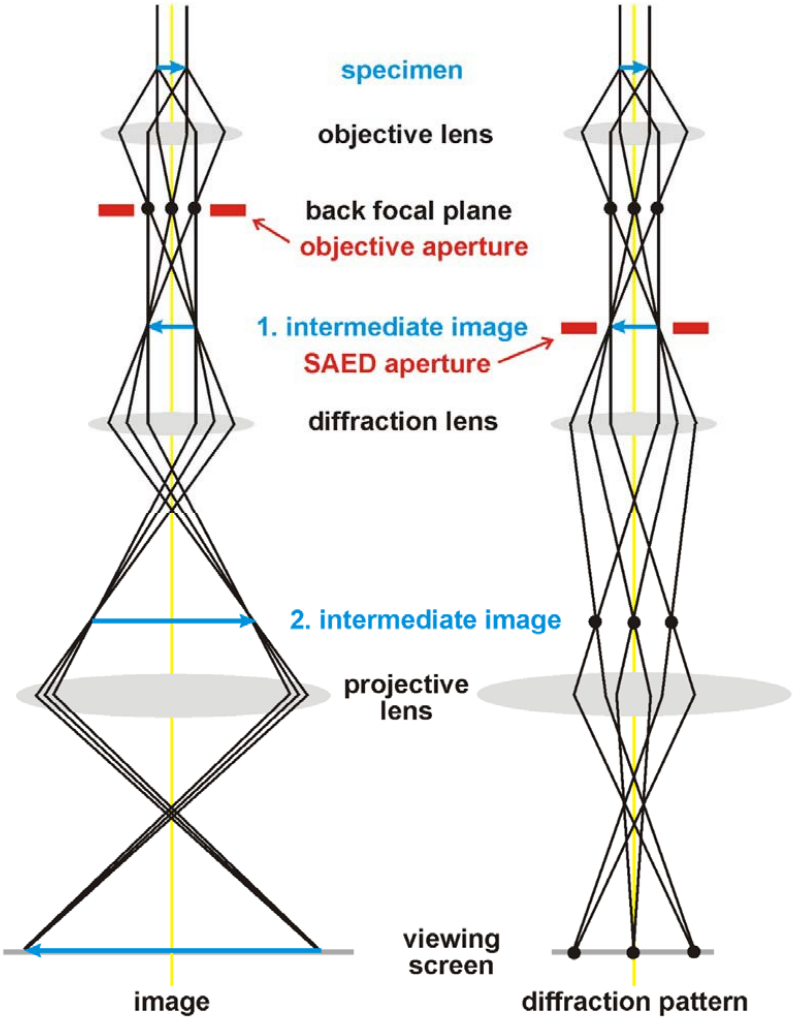

Figure 3.7 Schematic of the beam paths in imaging mode (left) and diffraction mode (right) in a TEM. Reprinted with permission from Reference 183.

In this thesis, a Philips CM30 TEM, which was operated at 250 kV, was used to form BF images, SAED patterns, and HREM images. For TEM specimen preparation, each sample powder was dispersed in methanol by sonicating for 10 min, and a drop of the

mixture was placed onto a lacey carbon coated TEM grid. Element contents in single particles were determined by an EDS system coupled with the TEM instrument having a silicon-lithium detector (Genesis system, EDAX Inc.). Elemental X-ray mappings were performed in STEM mode, which was also used at 250 kV.

3.5 Energy Dispersive X-ray Spectroscopy

As mentioned above, EDS is an analytical technique used for elemental analysis and chemical characterization of a sample. Modern SEM and TEM instruments are typically equipped with EDS. EDS relies on an interaction between an X-ray excitation source and a specimen. In an SEM or TEM instrument, the X-ray excitation source is the electron beam employed for imaging. The incident electron beam with high energy may excite an electron in an inner shell of a target sample, leading to an electron hole where the electron was. Then, an electron in an outer shell fills this hole, and a characteristic X-ray is released simultaneously. The characteristic X-ray generation process is the same as the process used to produce X-rays for XRD (Section 3.2.1). EDS can be employed for measuring intensity and energy of the X-rays emitted from a target sample. The elements present in the sample can be determined by comparing the detected X-ray energies with references in a database. The element contents in the sample can be measured based on the intensities of the characteristic X-rays. In this thesis, EDS is used for semi-quantitatively analyzing element contents and determining element distribution through X-ray mappings.

Some characterization details about EDS used in this thesis can be found in Sections 3.3 and 3.4.

3.6 LECO Analysis

LECO analysis can be applied to determine carbon, hydrogen, nitrogen, oxygen and sulfur contents for a variety of metallic samples and other inorganic materials. Nitrogen and oxygen content measurements are of interest in this thesis, hence the LECO test processes for determining these two element contents will be descried briefly below. A pre-weighted sample is put into a graphite crucible, which is heated in a furnace for fusing the sample. During the fusion, oxygen present in the sample reacts with the graphite crucible to produce CO and/or CO_2. Also, nitrogen present in the sample can be released as N_2 gas. Helium is typically used as a carrier gas in a LECO test system. The formed CO and CO_2 are detected by CO and CO_2 infrared detectors, respectively. Then, the gas passes through a heated reagent (like CuO), where CO is oxidized to form CO_2. Oxygen in the form of CO_2 is detected again through another CO_2 infrared detector with high sensitivity, which is typically for measuring low levels of oxygen. CO_2 is then removed by a scrubber coupled to the high sensitivity CO_2 detector. Following this, nitrogen in the form of N_2 gas is detected by a thermal conductivity detector. In this thesis, nitrogen and oxygen contents of samples were determined through LECO tests by NSL Analytical Services, Inc. According to NSL, for element contents in the range of 10.0 wt.% - 25.0 wt.%, the uncertainty in

reported values is ~2%. For element contents between 3.0 wt.% and 10.0 wt.%, the uncertainty in reported values is ~5%. Any O or N results above ~3 wt.% are automatically run in duplicate with the average composition between the two measurements reported.

3.7 Gas Pycnometer

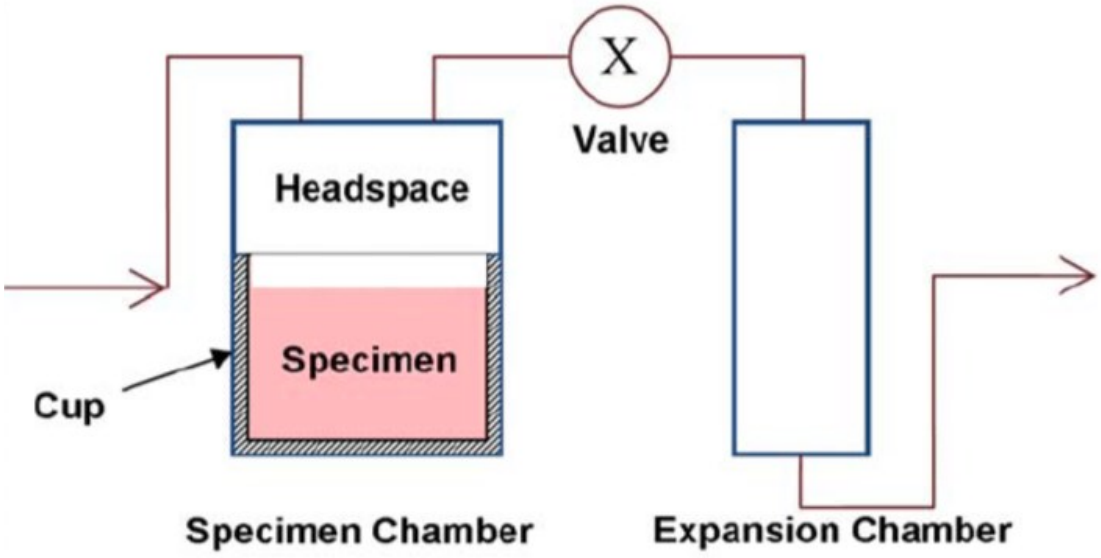

Figure 3.8 Schematic of a gas pycnometer. Reprinted with permission from Reference 149. Copyright 2010 Elsevier.

A gas pycnometer is a device used to measure the density of a sample – or more accurately, the volume of the sample. It employs the gas displacement method, which is non-destructive to measured samples. A schematic of the gas pycnometer is shown in Figure 3.8. It typically consists of a specimen chamber with volume V_1 and an expansion chamber with volume V_2, a valve between the two chambers and a pressure measuring

device (such as a transducer). The gas pycnometer can be applied to a wide variety of solids and slurries. Solids can be directly placed in the specimen chamber. However, an empty disposable cup with known volume is needed for a slurry, which avoids contaminating the specimen chamber. During measurement, the specimen chamber is covered and only a small hole allows an appropriate inert gas (such as helium or nitrogen) to enter. Helium or nitrogen molecules rapidly fill the pores in the measured sample. The pressure (P_1) in the specimen chamber is recorded after equilibrium. Then the gas admission valve (not shown in Figure 3.8) is closed and the valve connected to two chambers is opened. The inert gas in the specimen chamber is discharged into the empty expansion chamber. After equilibrium, the pressure (P_2) in these two chambers is recorded. According to Boyle's Law, the volume of sample can be obtained as:

$$V_s = V_1 + \frac{V_2}{1-\frac{P_1}{P_2}} \tag{3.12}$$

The density of the sample can be calculated by dividing its weight by the determined volume. In this research, a helium pycnometer (AccuPyc II 1340, Micrometritics) was employed to measure sample densities.

3.8 Electrochemical Characterization

Commercial Li cells are typically charged at a constant current to a certain voltage, then the current deceases with the constant voltage until a fixed current is reached. This is called constant current/constant voltage (CCCV) charging. In this thesis, half cells were

made for electrochemical characterization of negative electrode materials. In these half cells, the tested materials and lithium metal are used as positive electrodes and negative electrodes, respectively. This means that CCCV charging in commercial Li cells corresponds to CCCV discharging in half cells with tested negative electrode materials.

Through cycling half cells, potential-capacity curves and capacity-cycle number curves can be obtained. Differential capacity curves (dQ/dV vs. V) can be derived from the corresponding potential-capacity curves. A sharp peak in a dQ/dV curve corresponds to a plateau in the potential-capacity curve, which indicates a two-phase region during cycling.

Electrode materials for Li-ion cells can be evaluated in terms of important electrochemical properties, such as specific and volumetric capacities, irreversible capacity (IRC), coulombic efficiency (CE), average voltage, etc. These important electrochemical properties of electrode materials can be obtained based on their potential-capacity curves and capacity-cycle number curves. In a half cell, specific or volumetric capacity of a target material can be calculated by dividing the total charge after lithiation/delithiation by the mass or the maximum volume during cycling of the electrode material. The IRC is defined as the capacity loss between the first discharge and charge processes. For a negative electrode material, CE is defined as:

$$\eta = \frac{Q_1}{Q_2} \tag{3.13}$$

where Q_1 is the amount of charge during delithiation of the negative electrode material, and Q_2 is the amount of charge during lithiation of the negative electrode materials. Average

voltage can be used to estimate the effect of negative materials on full cell energy density. Potential polarization can be evaluated by the difference between average charging and discharging voltages. Small potential polarization is desired, since polarization arises from irreversible reactions and energy losses.

3.8.1 Electrode Preparation

In this thesis, electrode slurries were made from a mixture of Si alloy, carbon black (Super C, Timcal), a 10 wt% aqueous solution of lithium polyacrylate (LiPAA, made by neutralizing a polyacrylic acid solution (Sigma-Aldrich, average molecular weight ~250,000 g/mole, 35 wt% in H_2O) with $LiOH \cdot H_2O$ (Sigma Aldrich, 98%) in distilled water), a wetting agent (isopropanol, 99.5%), and distilled water, with a Si alloy/carbon black/LiPAA volume ratio of 70/5/25. The electrode slurry was mixed in a planetary ball mill (Retsch PM200) with 3 tungsten carbide balls (7/16 inch (about 11.1 mm) in diameter) at 100 rpm for 1 h. The homogeneous slurry was spread on copper foil (Furukawa Electric, Japan) with a steel coating bar (0.004-inch gap) and dried in air at 120 °C for 1 h. Disk electrodes with a diameter of 13 mm were cut using a circular electrode punch, and were further dried under vacuum at 120 °C for 2 h before cell assembly. Typical electrode loadings were about 2~3 mAh/cm^2.

3.8.2 Coin Cell Fabrication

2325-type coin cells were used in this thesis. The coin cells were assembled and sealed in an Ar-filled glove box. Figure 3.9 illustrates the structure and components of the 2325-type coin cell. A working electrode was assembled with a Li metal (99.9%, Sigma-Aldrich) counter electrode. Two Celgard 2300 separators were sandwiched between the working and counter electrodes, which were used to prevent short circuits. Two copper spacers were used to provide stack pressure and ensure electrical contact. The cells were filled with electrolyte consisting of 1 M $LiPF_6$ (BASF, 98%) dissolved in a solution of ethylene carbonate (EC): diethyl carbonate (DEC): monofluoroethylene carbonate (FEC) (3:6:1 v/v/v, all from BASF).

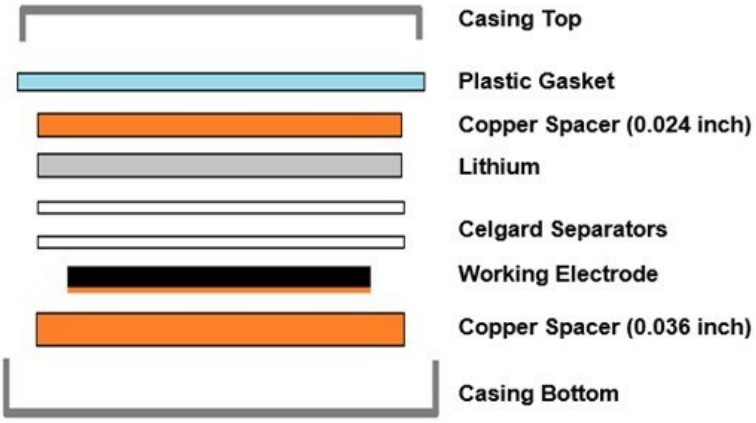

Figure 3.9 Schematic of a 2325-type coin cell.

3.8.3 Coin Cell Cycling

Coin cells were cycled at 30 ± 0.1 °C or 45 ± 0.2 °C between 0.005 V and 0.9 V using a battery testing system (Neware). 30 °C and 45 °C are two commonly used

temperatures for investigating cell performance. C-rate is a measure of the rate at which a cell is being charged or discharged. If a cell is charged or discharged at a 1C rate, the process can be completed after 1 h. To determine C-rate in this thesis, trial cells were cycled at a C/10 or C/20 rate based on the alloy theoretical capacity (assuming that all the Si in the alloy was active with a capacity of 3578 mAh/g). From these trial cells, the actual material capacity was determined. The C-rates of cells used for cycling experiments were calculated from this measured capacity. In cycling experiments, cells were discharged at a C/10 or C/20 rate until the cutoff voltage (5 mV) had been reached. Then, a signature method was used to simulate the potential hold at the end of a CCCV charge cycle in a full cell.[150] Details about the signature method will be described in Sections 4.2 and 5.2. Next, the cells were charged at the C/10 or C/20 rate to 0.9 V. All C-rates were doubled in the following cycles.

Chapter 4 Synthesis, Lithium Insertion and Thermal Stability of Si–Mo Alloys*

4.1 Introduction

Si is a promising negative electrode material for lithium ion batteries owing to its high specific and volumetric capacities (3579 mAh/g and 2194 Ah/L) and proper average potential (~ 0.4 V vs. Li/Li^+).[13] As mentioned in Section 2.3.5.2, there are still some challenges for Si-based negative electrode materials, such as huge volume changes of Si, unstable solid electrolyte interface (SEI), and crstalline-$Li_{15}Si_4$ (cr-$Li_{15}Si_4$) formation during cycling.[16,63,151] Preparing Si/inactive alloys is regarded as an efficient way to reduce the total volume expansion after lithiation and suppress cr-$Li_{15}Si_4$ formation.[71,126,127] In addition, Si-based negative electrode materials can be improved by carbon coating as described in Section 2.3.5.3. Chemical vapor deposition (CVD) is an important method to apply carbon coatings to Si-based negative electrode materials.[152] However, CVD coating is a high temperature process, requiring samples to be heated to at least 800 °C for a pure carbon phase to be deposited. This is problematic for nanostructured Si-based negative

---

* This chapter was adapted with permission from S. Cao, S. Gracious, J. C. Bennett, and M. N. Obrovac. Synthesis, Lithium Insertion and Thermal Stability of Si–Mo Alloys. Journal of The Electrochemical Society. Publication date: 5 October 2020. Copyright 2020, IOP Publishing. S. Cao's contribution includes performing the main experiment and analysis work and writing the manuscript. S. Gracious performed some sample preparation. J. C. Bennett preformed measurements and analysis of TEM and STEM. M. N. Obrovac provided guidance and participated in experimental design and the interpretation of all the data.

electrode materials, since amorphous Si (a-Si) crystallizes at temperatures of 600 °C, resulting in the growth of large crystalline Si (cr-Si) grains. This is detrimental for Si-based negative electrode materials, since it is desirable that active Si be an amorphous phase or a crystalline phase with small grain sizes (e.g. < 150 nm), otherwise fracture of the active Si phase can occur during cycling, resulting in capacity fade.[93,96] Therefore, Si-based negative electrode materials with high thermal stability against grain growth are highly desirable.

In this study, the synthesis, electrochemistry, and thermal stability of Si-Mo alloys were investigated. To the author's knowledge, lithium insertion in these alloys has not been investigated previously. Their propensity to form nanostructured alloys during ball milling was evaluated, as it is commercially important that precursors used for ball milling processes be amenable towards rapid alloy formation. The thermal stability of the resulting nanostructured Si-Mo alloys was also investigated. It was hoped that the high melting point of the $MoSi_2$ inactive phase (2020 °C) would impart thermal stability onto nanostructured Si-Mo alloys, so that these alloys could be compatible with high-temperature post-processing methods (e.g. CVD processing). Finally, an electrochemical investigation of Si-Mo alloys as-milled and after heat treatment was done to study their potential as negative electrode materials.

4.2 Experimental

Si_xMo_{100-x} ($90 \geq x \geq 70$, $\Delta x = 10$) samples were prepared by ball milling Si powder (Sigma-Aldrich, 325 mesh, 99%) and Mo powder (Alfa Aesar, 250 mesh, 99.9%) in Ar for 1-16 h. The details of the preparation processes can be found in Section 3.1. In addition, Si, Mo, and α-$MoSi_2$ (Sigma-Aldrich, 7.5 μm, 99.8%) powders were ball milled under the same conditions for 2 h, respectively. Here TiN (Alfa Aesar, 200 mesh, 99.5%) was used as an internal standard to mix with the as-milled Si, Mo, and α-$MoSi_2$ (consists of α-$MoSi_2$ and β-$MoSi_2$), respectively. The intensity factors (IFs) of Si, Mo, α-$MoSi_2$, and β-$MoSi_2$ were calculated as described in Section 3.2.3. These phases were ball milled, so that they had similar structures and properties as the phases in the Si-Mo samples. The IF value of each phase was obtained through a series of standard mixtures with different TiN weight ratios. In some instances, caking of the sample on the inner wall of the mill container occurred. When this occurred, the caked portion of the sample was collected by milling with ethanol and several 1/4 inch (6.35mm) stainless steel balls. In addition, selected ball milled Si_xMo_{100-x} (1, 4 and 16 h) samples were heated at 600 °C or 800 °C for 3 h, and the heat treatment processes were the same as described in Section 3.1.

Table 4.1 Cell cycling procedure (CC_DChg: constant current discharge, CC_Chg: constant current charge).

Step ID	Step name	Time (hh:m:ss:ms)	Voltage (V)	Current (mA)
1	Rest	00:00:05:000	-	-
2	CC_DChg	-	0.005	C/20
3	Rest	00:10:00:000	-	-
4	CC_DChg	-	0.005	C/30
5	Rest	00:10:00:000	-	-
6	CC_DChg	-	0.005	C/40
7	CC_Chg	-	0.9000	C/20
8	Rest	00:15:00:000	-	-
9	CC_DChg	-	0.005	C/10
10	Rest	00:10:00:000	-	-
11	CC_DChg	-	0.005	C/15
12	Rest	00:10:00:000	-	-
13	CC_DChg	-	0.005	C/20
14	CC_Chg	-	0.9000	C/10
15	Cycle	Begin ID: 8	Times: 49	

Selected Si-Mo samples were characterized with a Schottky field emission scanning electron microscope (SEM, TESCAN MIRA 3 LMU) using a 20.0 kV accelerating voltage. Si-Mo sample densities were measured with a Micromeritics AccuPyc II 1340 gas pycnometer. Bright field (BF) images, selected area electron diffraction (SAED) patterns, and high-resolution electron microscopy (HREM) images were collected

using a Philips CM30 transmission electron microscopy (TEM) with an operating voltage of 250 kV. Element (Si and Mo) distributions in single particles of Si-Mo samples were investigated by elemental mapping. The data was collected in scanning TEM (STEM) mode. A nominal analytical beam diameter of 1 nm was used at 200 kV, where the dwell time was 100 μs. X-ray diffraction (XRD) patterns of Si-Mo alloys were collected using a Rigaku Ultima IV diffractometer in the 2θ range of 10° ~ 80°.

Electrode preparation and cell assembly for Si-Mo samples were as described in Sections 3.8.1 and 3.8.2. Half cells were cycled between 0.005 – 0.9 V at 30.0 ± 0.1 °C using a battery testing system (Neware). The cell cycling procedure is listed in Table 4.1. During the first cycle, cells were discharged (alloy lithiation) at a constant C/20 rate (the method to determine C-rates can be found in Section 3.8.3) to 0.005 V. After that, the cells were also discharged at C/30 and C/40 rates with a 10 min open-circuit period between current steps once the cutoff potential (0.005 V) had been reached, in order to simulate constant current constant voltage (CCCV) discharging. In the following cycles, all the steps were the same, excepting the currents used were two times larger than those in the first cycle.

4.3 Results and Discussion

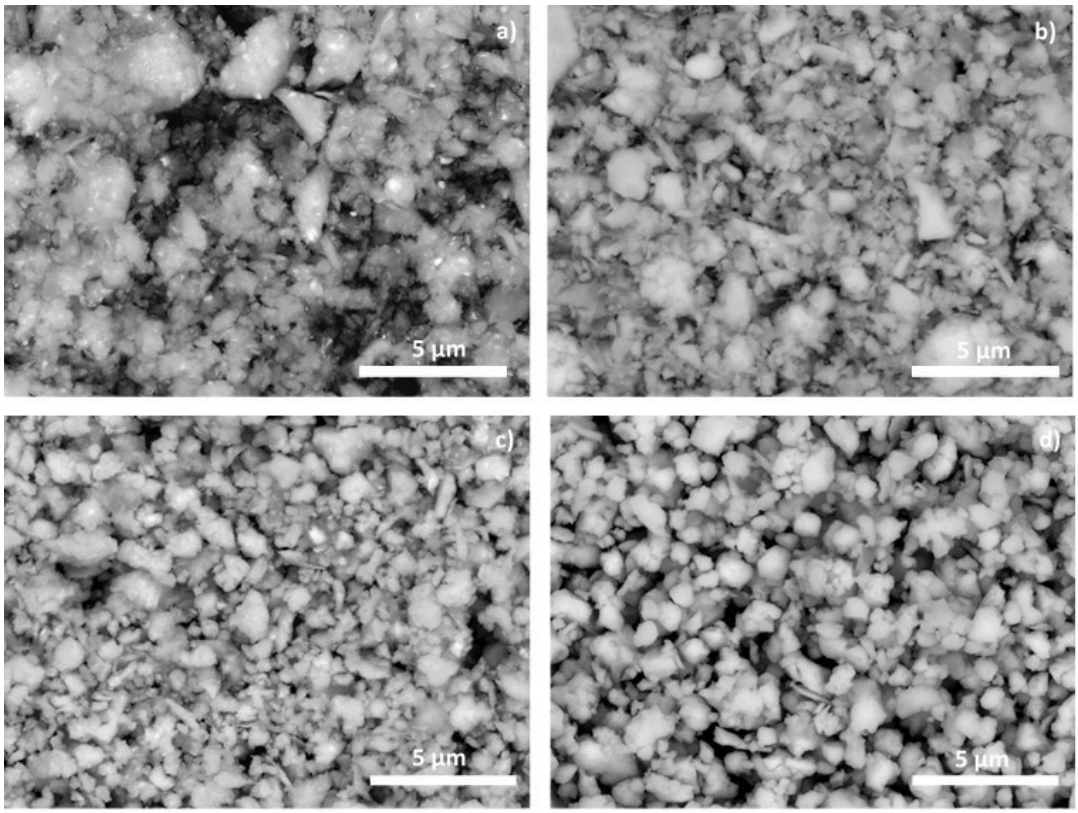

Figure 4.1 BSE images: (a) $Si_{90}Mo_{10}$ 1 h; (b) $Si_{90}Mo_{10}$ 16 h; (c) $Si_{70}Mo_{30}$ 1 h; (d) $Si_{70}Mo_{30}$ 16 h.

Backscattered electron (BSE) images of several Si-Mo samples ($Si_{90}Mo_{10}$ 1 h, $Si_{90}Mo_{10}$ 16 h, $Si_{70}Mo_{30}$ 1 h, and $Si_{70}Mo_{30}$ 16 h) are shown in Figure 4.1. Bright spots in the samples milled for 1 h indicate the presence of unmilled Mo particles. The samples become more homogeneous as milling time is increased. No Mo particles are present after 16 h milling. XRD patterns of Si_xMo_{100-x} alloys ($90 \geq x \geq 70$, $\Delta x = 10$, milling time: 1- 16 h) are shown in Figure 4.2. These Si-Mo alloys are composed of cr-Si, a-Si, Mo, and nanocrystalline α and β-$MoSi_2$ phases. The large width of the a-Si peaks makes them

difficult to discern in some XRD patterns. Mo and cr-Si peaks are significant at low milling times, but their peaks decrease in intensity as Mo and Si react during milling to form $MoSi_2$. According to the Si-Mo equilibrium phase diagram,[153] α-$MoSi_2$ is the low temperature form of this phase, with an α-$MoSi_2$/Si 2-phase region present below 1400 °C. Above 1900 °C the α-$MoSi_2$ phase converts to β-$MoSi_2$. It is interesting that the high-temperature β-$MoSi_2$ phase was the main silicide produced during milling. Only a small amount of α-$MoSi_2$ formed. This illustrates that ball milling is a non-equilibrium process that often produces metastable phases.

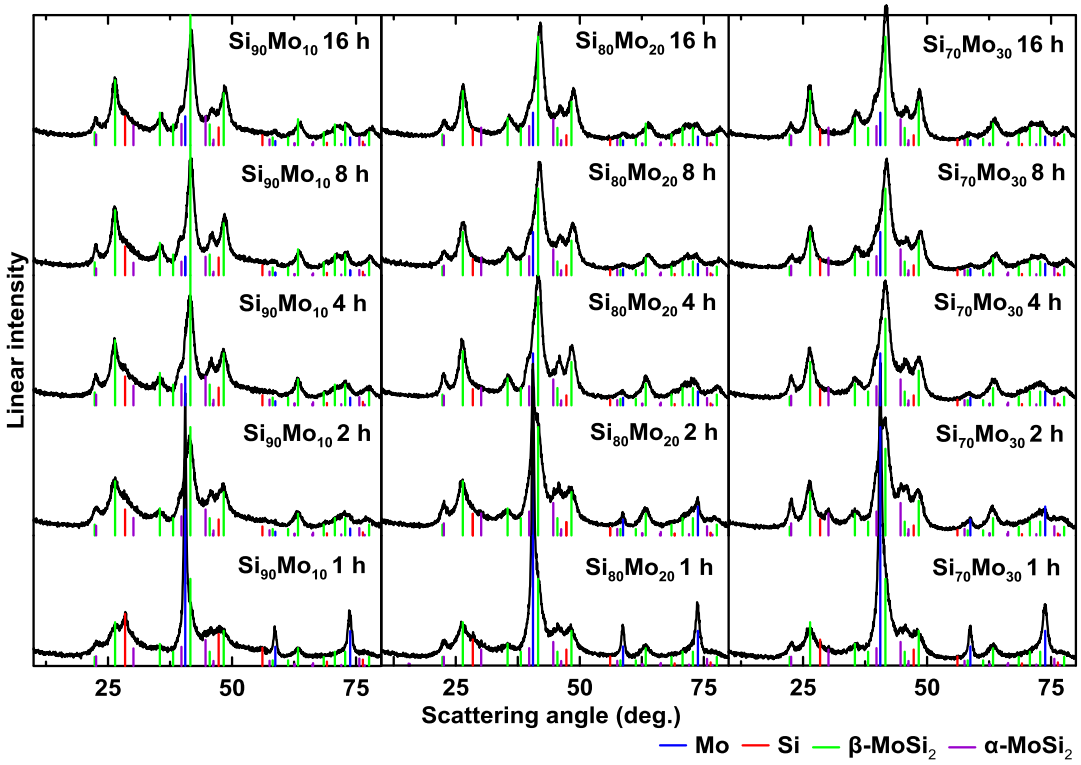

Figure 4.2 XRD patterns of Si_xMo_{100-x} alloys made with different compositions and milling times.

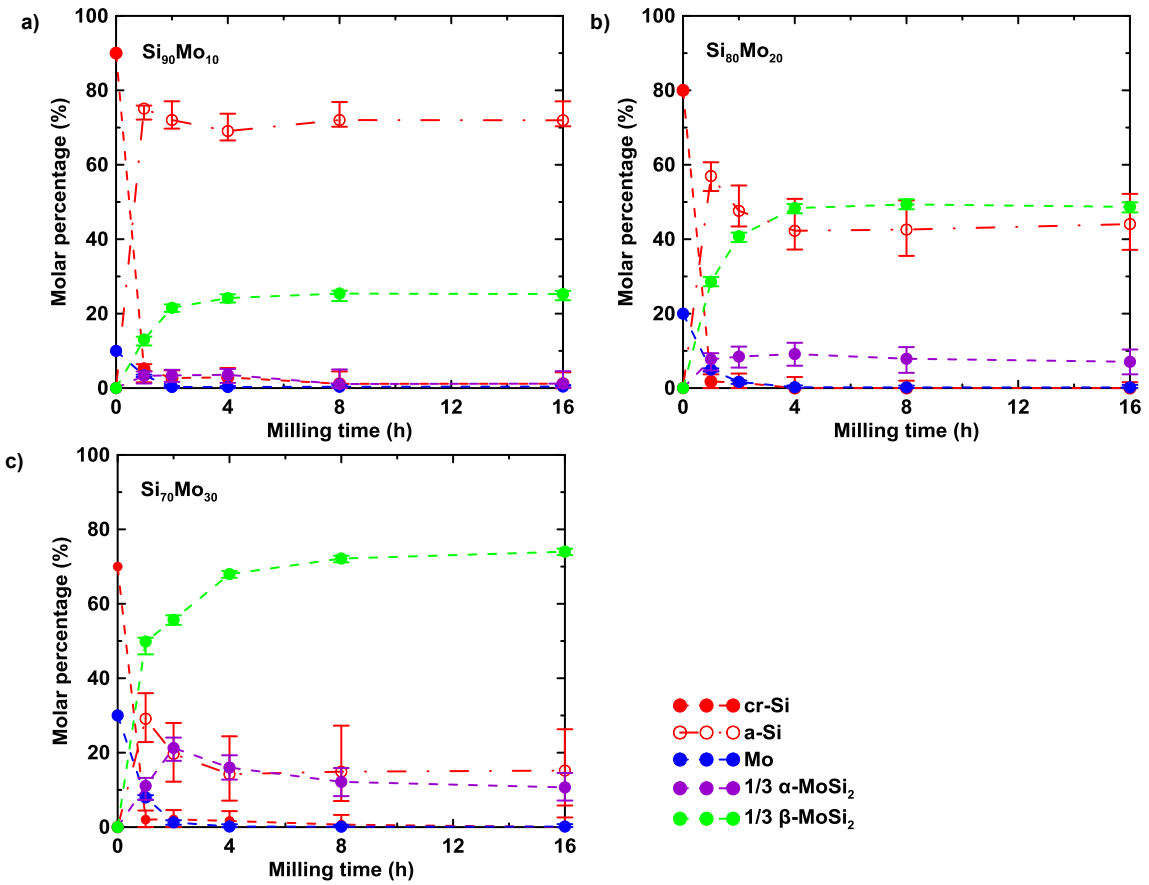

Figure 4.3 Phase composition analysis of Si-Mo alloys made with different milling times: (a) $Si_{90}Mo_{10}$; (b) $Si_{80}Mo_{20}$; (c) $Si_{70}Mo_{30}$. All molar percentages are calculated on a per atom basis. To determine error bars, the integrated intensity of each phase in the fit was changed until there was a ±10% change in the goodness of fit.

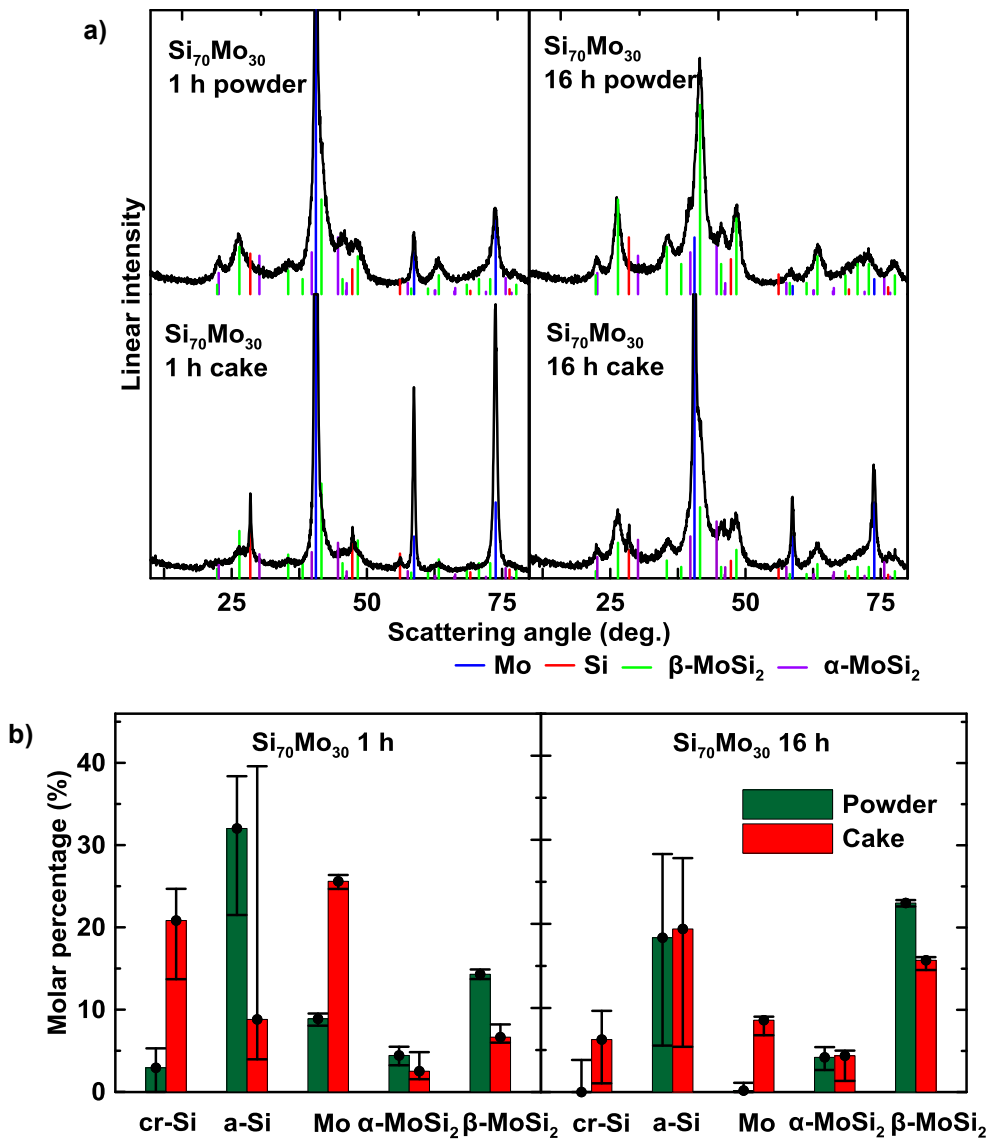

Figure 4.4 (a) XRD patterns and (b) composition analysis of loose powder and cake for $Si_{70}Mo_{30}$ 1 h and 16 h samples. To determine error bars, the integrated intensity each phase in the fit was changed until there was a ±10% change in the goodness of fit.

The evolution of the phase compositions of the Si-Mo alloys during ball milling was determined quantitatively from XRD measurements, as described in Sections 3.2.3 and 3.2.4, and the results are shown in Figure 4.3. For all the samples, cr-Si converts to a-Si

within 1 h of milling. Concurrently, Si reacts with Mo to form α-$MoSi_2$ or β-$MoSi_2$. This reaction is slower and takes about 4 h to reach completion. However, nearly all of the Mo was consumed after only about 2 h, which conflicts with the completed reaction time (4 h), as indicated by when the reaction reaches steady-state. The rapid disappearance of Mo in the XRD patterns is likely due to it adhering to the wall of the milling vial, as is discussed below. Alloys with more Mo content produced a higher fraction of α-$MoSi_2$ during milling. Some of the α-$MoSi_2$ converted into β-$MoSi_2$ with longer milling time. Based on the Scherrer equation shown in Section 3.2.1, the grain size of the β-$MoSi_2$ phase was estimated to be about 3 nm in size for all samples as it was initially formed and increased to 4 nm with longer milling time. It is possible that as more β-$MoSi_2$ is formed, there is a greater chance of aggregation of this phase and therefore a greater chance of producing larger grains.

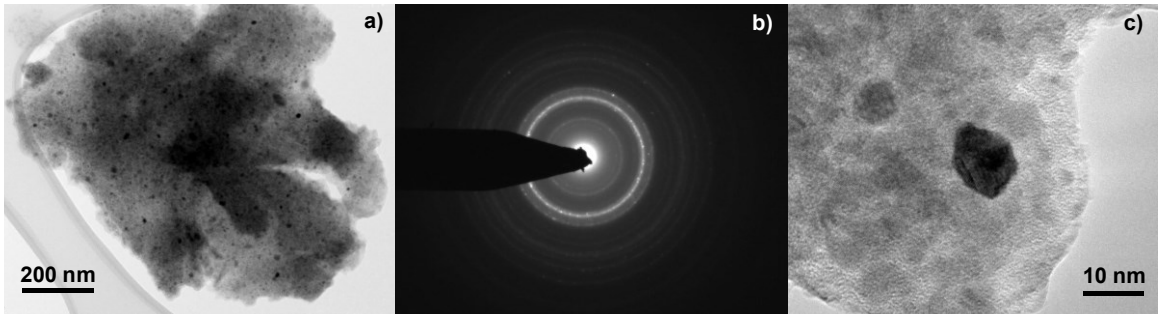

Figure 4.5 TEM images of $Si_{80}Mo_{20}$ 8 h: (a) BF image, (b) SAED pattern, and (c) HREM image.

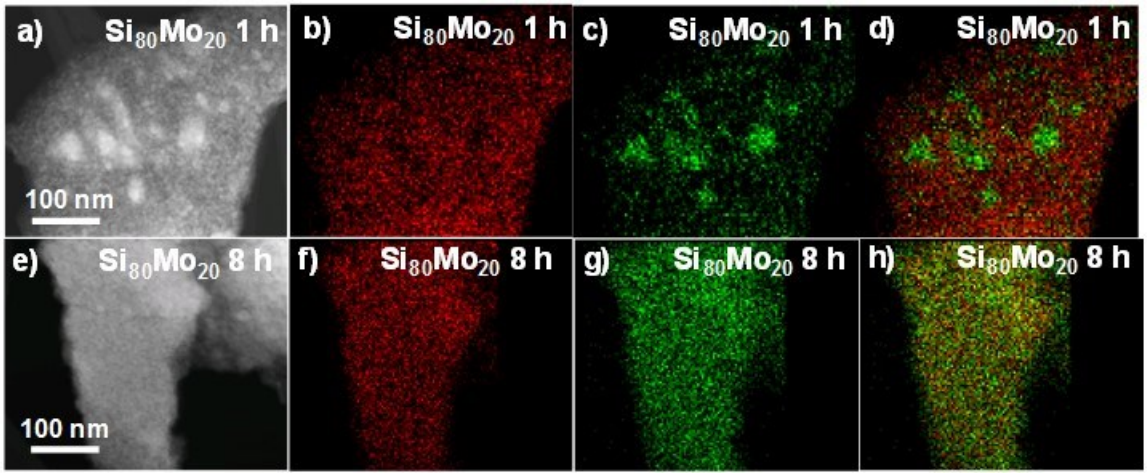

Figure 4.6 STEM images, Si maps, Mo maps, and Si-Mo substitution overlays, respectively, of $Si_{80}Mo_{20}$ alloy made with 1 h milling time (a-d) and 8 h milling time (e-h). (red = Si, green = Mo).

All TEM results for Si-Mo alloys with complete reactions are generally the same. TEM images of the $Si_{80}Mo_{20}$ 8 h alloy are shown in Figure 4.5, including a BF image (Figure 4.5(a)), a SAED pattern (Figure 4.5(b)), and a HREM image (Figure 4.5(c)). All the diffraction rings observed in Figure 4.5(b) correspond to the lattice spacings of β-$MoSi_2$. The rings are fairly continuous and intense, indicating a significant amount of nanocrystalline β-$MoSi_2$ is present in this alloy, consistent with the most intense phase observed in XRD patterns. The diffuse rings in the SAED pattern are typical of a-Si. Based on TEM images, the Si-Mo alloys consist of β-$MoSi_2$ with small particle/grain sizes (1~14 nm for the size range and 4 nm for the average size based on 50 random particles/grains) that are homogeneously embedded in an a-Si matrix.

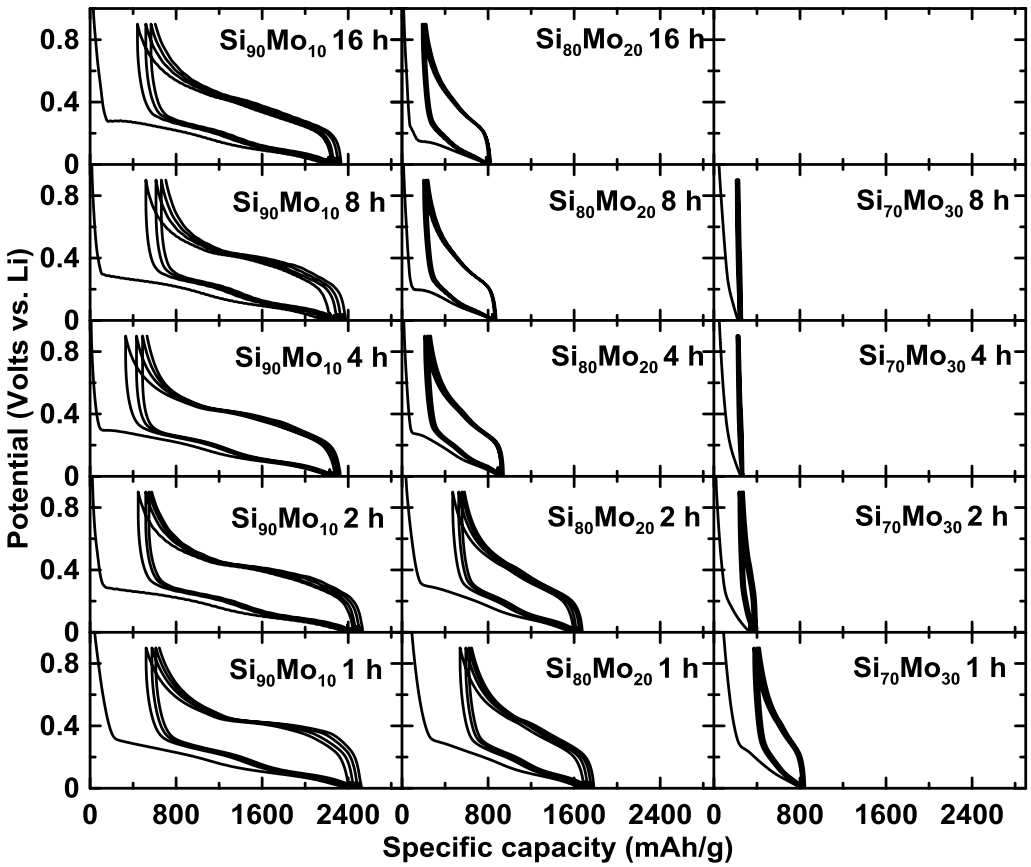

Figure 4.7 Potential profiles of Si_xMo_{100-x} ($90 \geq x \geq 70$, $\Delta x = 10$, 1-16 h) alloy electrodes vs. Li.

Si and Mo distributions in single particles of the $Si_{80}Mo_{20}$ 1 h and 8 h samples were investigated by X-ray compositional mapping. STEM images, Si maps, Mo maps, and Si-Mo substitution overlays are exhibited in Figure 4.6(a and e), (b and f), (c and g), and (d and h), for the 1 h and 8 h milled samples, respectively. The substitution overlays are employed to show a combination of Si and Mo elements, where only the element with the higher intensity at each pixel is displayed. The results indicate that the $Si_{80}Mo_{20}$ 8 h alloy

has a more homogeneous Si-Mo distribution than the $Si_{80}Mo_{20}$ 1 h alloy. This phenomenon is typical of all the Si-Mo samples with different Si-Mo stoichiometric ratios studied here.

The first four cycles of the Si_xMo_{100-x} ($90 \geq x \geq 70$, $\Delta x = 10$, 1-16 h) half-cell potential profiles are shown in Figure 4.7. Generally, the potential profiles of $Si_{90}Mo_{10}$ (1-16 h), $Si_{80}Mo_{20}$ (1-16 h), and $Si_{70}Mo_{30}$ (1 h) samples have characteristics typical of a-Si, namely two sloping plateaus during the lithiation processes.[155] A plateau at about 0.45 V can also be observed in the delithiation potential profiles of $Si_{90}Mo_{10}$ (1-8 h), which is from cr-$Li_{15}Si_4$ delithiation and indicates cr-$Li_{15}Si_4$ formation during lithiation.[84] The reversible specific capacities and irreversible specific capacities and initial columbic efficiencies (ICEs) of the Si_xMo_{100-x} samples are shown in Figure 4.8. Also shown are the percent volume expansions of these alloys, based on the reversible capacities and calculated according to Reference 71. As expected, increasing the Mo content results in lower capacity because of the formation of the β-$MoSi_2$ and α-$MoSi_2$ phases, which were found to be inactive as described below. Reversible and irreversible capacities generally decrease with milling time from 1 h to 4 h and then stabilize after 4 h. This suggests that the reaction between Si and Mo to produce inactive silicides is complete after 4 h milling, which is in accordance with the results of the phase composition analysis of Si-Mo alloys during milling. In addition, Figure 4.8 indicates that the ICEs of the $Si_{90}Mo_{10}$ and $Si_{80}Mo_{20}$ alloys are in the range of 68.7% – 84.9% and that total volume expansion of the Si-Mo samples is reduced as the inactive phases increase.

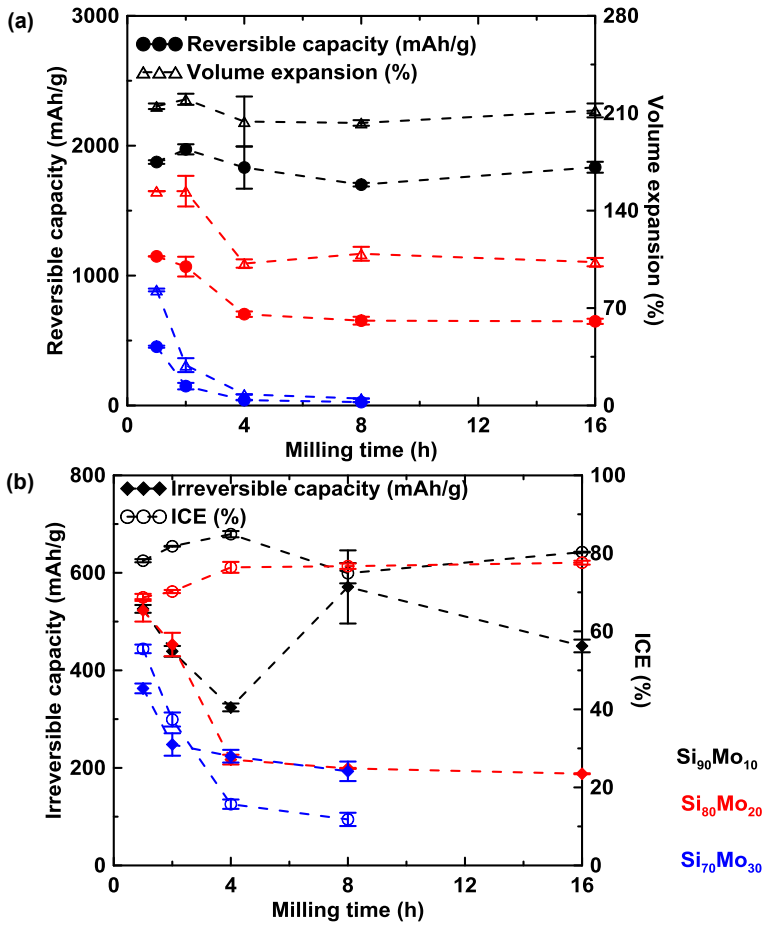

Figure 4.8 (a) Reversible capacities, percent volume expansions, (b) irreversible capacities, and ICEs, and of Si_xMo_{100-x} ($90 \geq x \geq 70$, $\Delta x = 10$, 1-16 h) vs. Li (for each sample, the error bars were calculated based on 3 duplicate cells).

To confirm if nanocrystalline β-$MoSi_2$ and α-$MoSi_2$ were inactive, a sample comprising nanocrystalline α-$MoSi_2$ and β-$MoSi_2$ was made by milling crystalline α-$MoSi_2$ for 2 h. This sample had no electrochemical activity (Figure 4.9(a)) and no change in its XRD pattern was detected after discharging to 5 mV (Figure 4.9(b)). Therefore, both nanocrystalline α-$MoSi_2$ and β-$MoSi_2$ were found to be electrochemically inactive with lithium during cycling at room temperature.

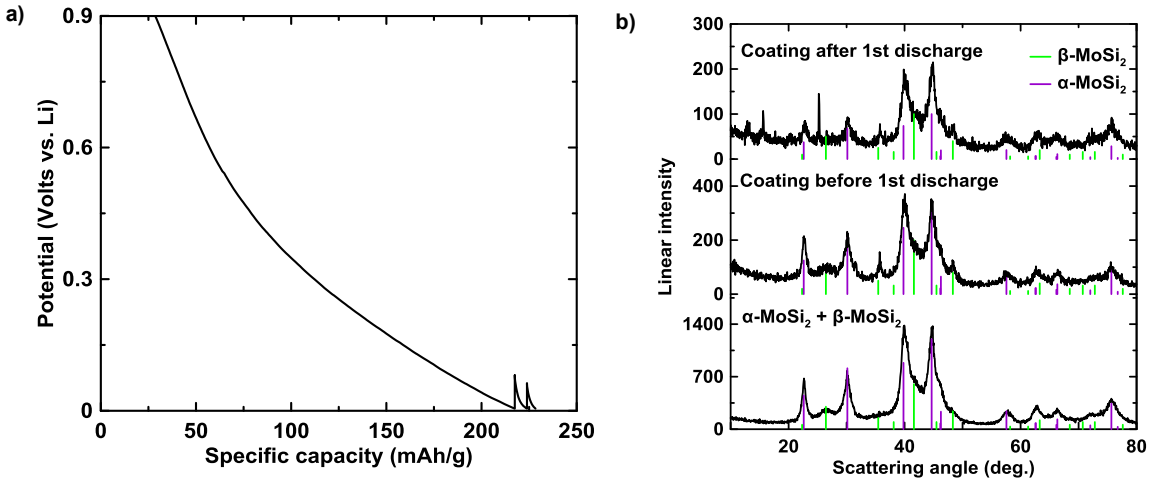

Figure 4.9 (a) Potential profile of a sample comprising nanocrystalline α-$MoSi_2$ and β-$MoSi_2$. (b) XRD patterns of the sample, the electrode coating of the sample before, and after fully lithiation.

Figure 4.10 shows the 1st, 2nd, 10th and 30th cycle differential capacity (dQ/dV) curves of the Si_xMo_{100-x} electrodes. Sharp peaks observed during the first lithiation indicate a nucleation and growth process during the initial lithiation step.[127] In general, two broad peaks are present in the subsequent lithiation processes, which is typical of a-Si. Sharp peaks at about 0.45 V during delithiation can be clearly observed for $Si_{90}Mo_{10}$ (1-16 h) and $Si_{80}Mo_{20}$ (1 h), which corresponds to the delithiation of cr-$Li_{15}Si_4$, indicating its formation at full lithiation.[84] Broad peaks at about 0.4 V during delithiation also exist in the dQ/dV curves of the $Si_{90}Mo_{10}$ (1-16 h) alloys. This behavior was also observed in Si-Fe-Mn alloys and it was speculated that the two peaks arise from the different environments of $Li_{15}Si_4$ at the $Li_{15}Si_4$/metal silicide contact region compared to $Li_{15}Si_4$ within the bulk of the $Li_{15}Si_4$ grains.[156]

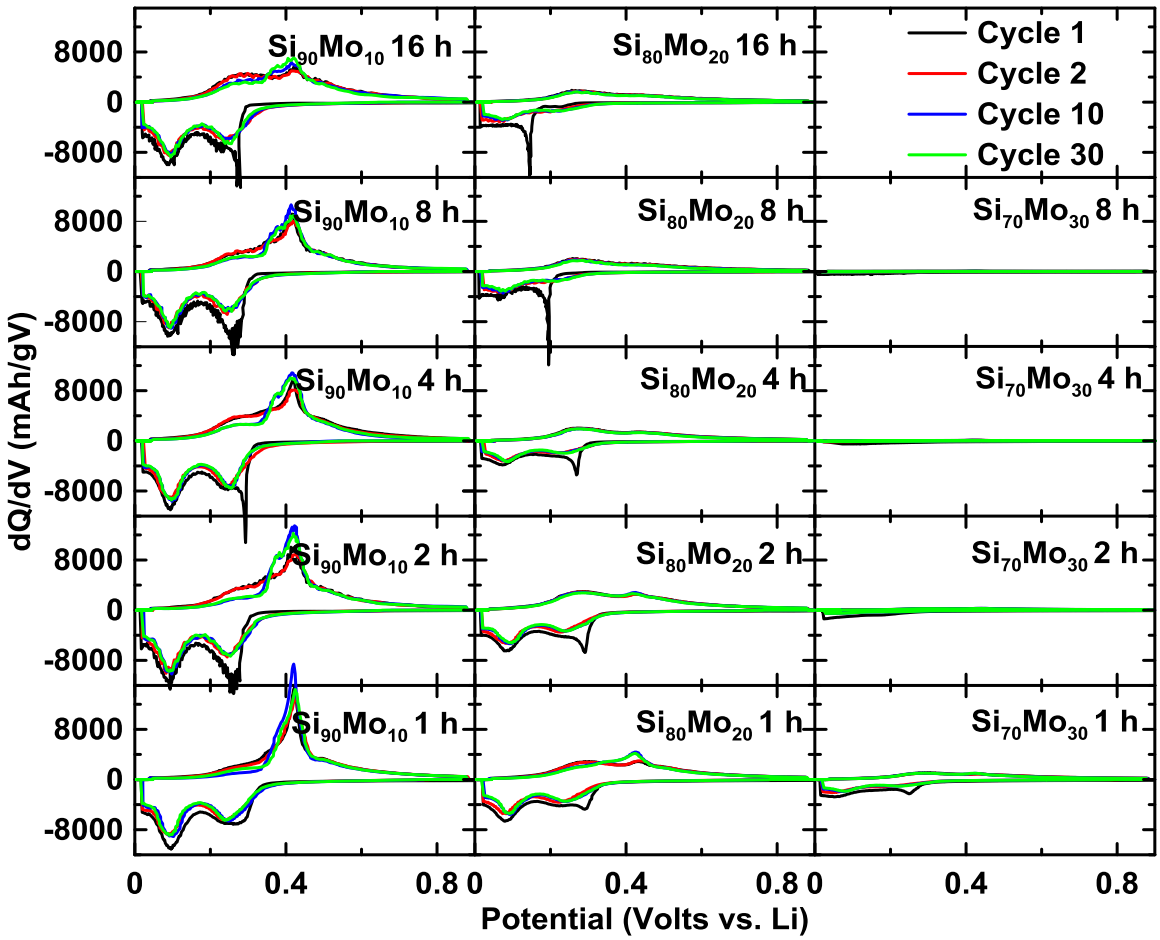

Figure 4.10 Differential capacity curves of Si_xMo_{100-x} ($90 \geq x \geq 70$, $\Delta x = 10$, 1-16 h) alloy electrodes vs. Li.

The amount of cr-$Li_{15}Si_4$ formed during cycling was quantified as the ratio between the delithiation capacity in the 0.36-0.48 V range and the total delithiation capacity, as described in Reference 156. This ratio is about 0.2 for no cr-$Li_{15}Si_4$ formation and about 1 if all the Si forms cr-$Li_{15}Si_4$ after full lithiation. Therefore, the percent active Si in the alloy that forms the cr-$Li_{15}Si_4$ phase during cycling (*f*) is:

$$f = \frac{\left(\frac{Q_{0.36-0.48\,V}}{Q_{tot}} - 0.2\right)}{1-0.2} \times 100\% \qquad (4.1)$$

Where $Q_{0.36-0.48\ V}$ is the delithiation capacity in the 0.36-0.48 V range and Q_{tot} is the total delithiation capacity. Figure 4.11 shows the amount of active Si that forms cr-$Li_{15}Si_4$ during cycling vs. cycle number for all the $Si_{90}Mo_{10}$ (1-16 h) and $Si_{80}Mo_{20}$ (1-16 h) half cells shown in Figure 4.10. Data for the $Si_{70}Mo_{30}$ samples are not shown because they are essentially inactive. It can be seen in Figure 4.11 that the Si-Mo alloys with longer milling time and more Mo content show better cr-$Li_{15}Si_4$ suppression. This is shown more clearly in Figure 4.12, which shows the maximum value of *f* plotted as a function of milling time. The enhanced cr-$Li_{15}Si_4$ suppression arises presumably because long milling time and high Mo content contribute to fine grain structure (homogenous Si-Mo distribution) as illustrated in Figure 4.6. This is consistent with earlier studies, as increasing milling time reduces Si grain size and increases the Si/inactive phase contact area, while increasing the inactive phase has been shown to suppress the formation of cr-$Li_{15}Si_4$ by shifting the potential profile to lower potentials.[126,127] Indeed, this was found to be the case here, as the average lithiation potentials of the alloys were found to generally decrease with increasing milling time (Figure 4.13).

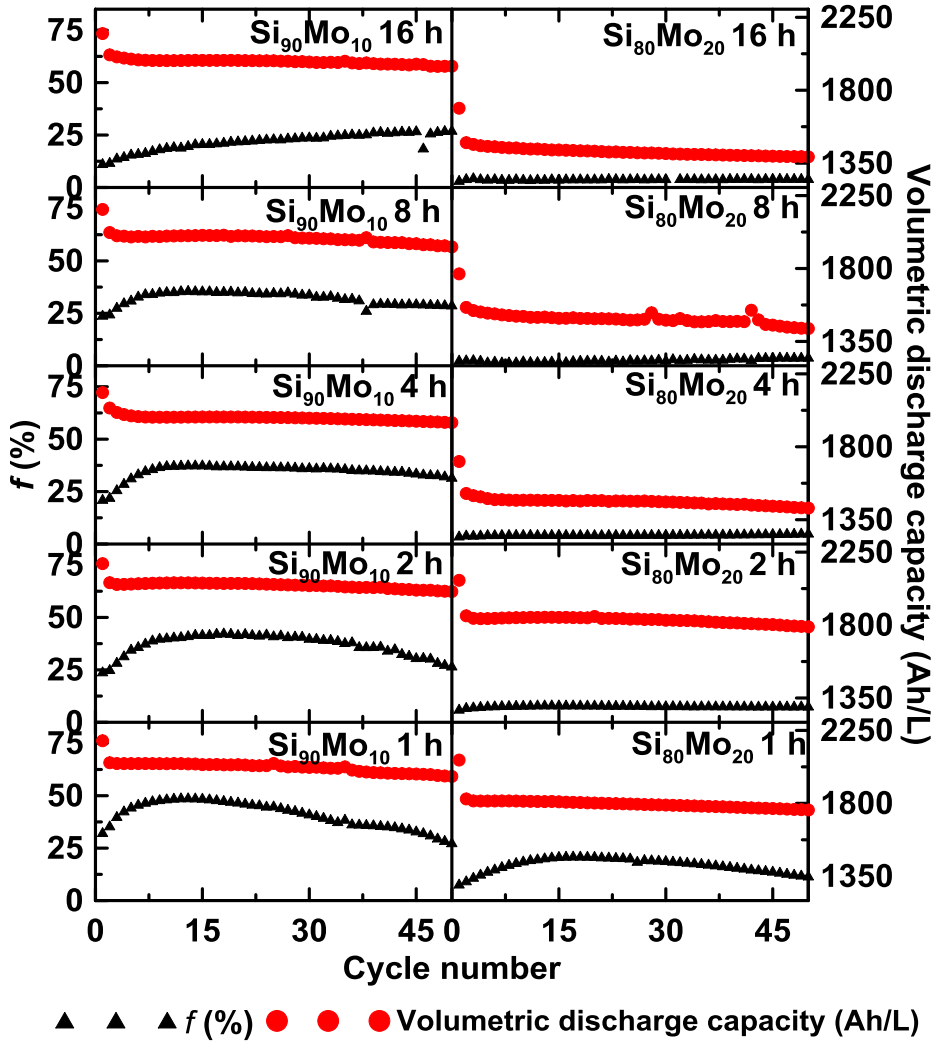

Figure 4.11 Plots of the percent active Si that forms cr-$Li_{15}Si_4$ at full lithiation (*f*) vs. cycle number and volumetric capacity vs. cycle number of $Si_{90}Mo_{10}$ and $Si_{80}Mo_{20}$ alloy electrodes.

Figure 4.11 also shows the cycling performance of $Si_{90}Mo_{10}$ and $Si_{80}Mo_{20}$ alloys in terms of volumetric capacity. In addition, the specific capacity of $Si_{90}Mo_{10}$, $Si_{80}Mo_{20}$, and $Si_{70}Mo_{30}$ alloys and the volumetric capacity of $Si_{70}Mo_{30}$ alloys are shown in Figure 4.14. As milling time increases more Si is consumed to form the inactive $MoSi_2$ phases, reducing capacity, as mentioned above. The relation between milling time and first cycle

capacity is shown in Figure 4.15, which also confirms that a steady-state has been reached after 4 h milling. After this reaction is completed (i.e. for samples milled 4 h or more) the capacity remains constant. For these samples both specific and volumetric capacities decrease with increasing Mo. However, the volumetric capacity decreases much less dramatically, since the addition of Mo also increases density.

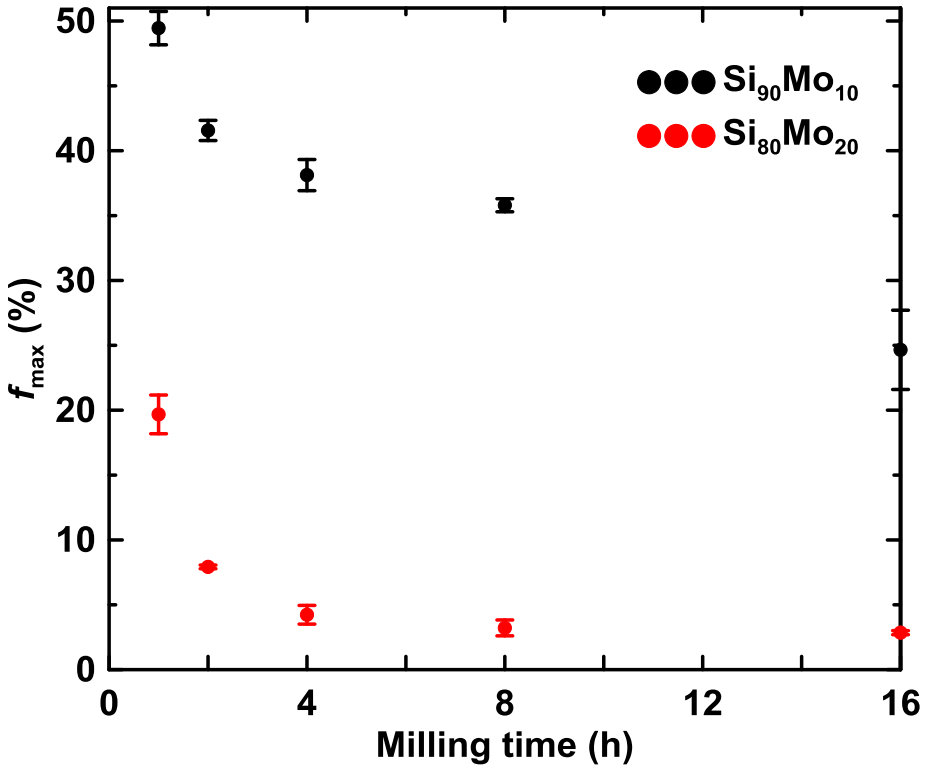

Figure 4.12 Maximum value of *f* observed during cycling plotted as a function of milling time for $Si_{90}Mo_{10}$ and $Si_{80}Mo_{20}$ alloys (for each sample, the error bar was calculated based on 3 duplicate cells).

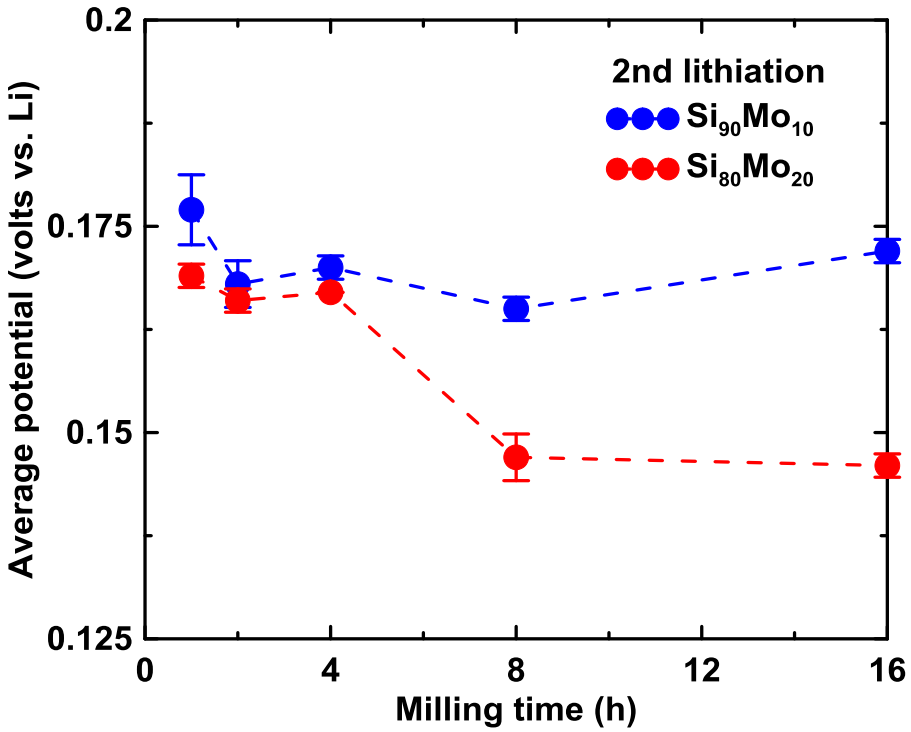

Figure 4.13 Average 2nd lithiation potentials vs. Li of $Si_{90}Mo_{10}$ and $Si_{80}Mo_{20}$ electrodes as a function of ball milling time (for each sample, the error bar was calculated based on 3 duplicate cells).

As shown in Figures 4.11 and 4.14, all samples milled 4 h or longer show good cycling stability during the 50 cycles tested, excepting the $Si_{90}Mo_{10}$ samples, which are the samples that also exhibited cr-$Li_{15}Si_4$ formation during cycling. Relationships between cr-$Li_{15}Si_4$ formation, reversible capacity (1st delithiation capacity) and capacity fade are illustrated in Figure 4.16(a-d). As shown in Figure 4.16(a), the capacity fade of the high capacity $Si_{90}Mo_{10}$ alloys is highly correlated to cr-$Li_{15}Si_4$ formation during cycling. This indicates that these high volume expansion alloys are susceptible to internal fracture when cr-$Li_{15}Si_4$ formation is not suppressed during cycling. In contrast, the lower capacity/volume expansion $Si_{80}Mo_{20}$ alloys have much smaller *f* values and show no such

correlation (Figure 4.16(b)). The high capacity $Si_{90}Mo_{10}$ alloys all show higher levels of fade (Figure 4.16(c)) than the $Si_{80}Mo_{20}$ alloys (Figure 4.16(d)). This higher level of fade is likely related to mechanical disconnection from the electrode during cycling the high capacity alloys. As the capacity becomes lower in the $Si_{80}Mo_{20}$ alloys with greater milling time, the fade correspondingly becomes smaller.

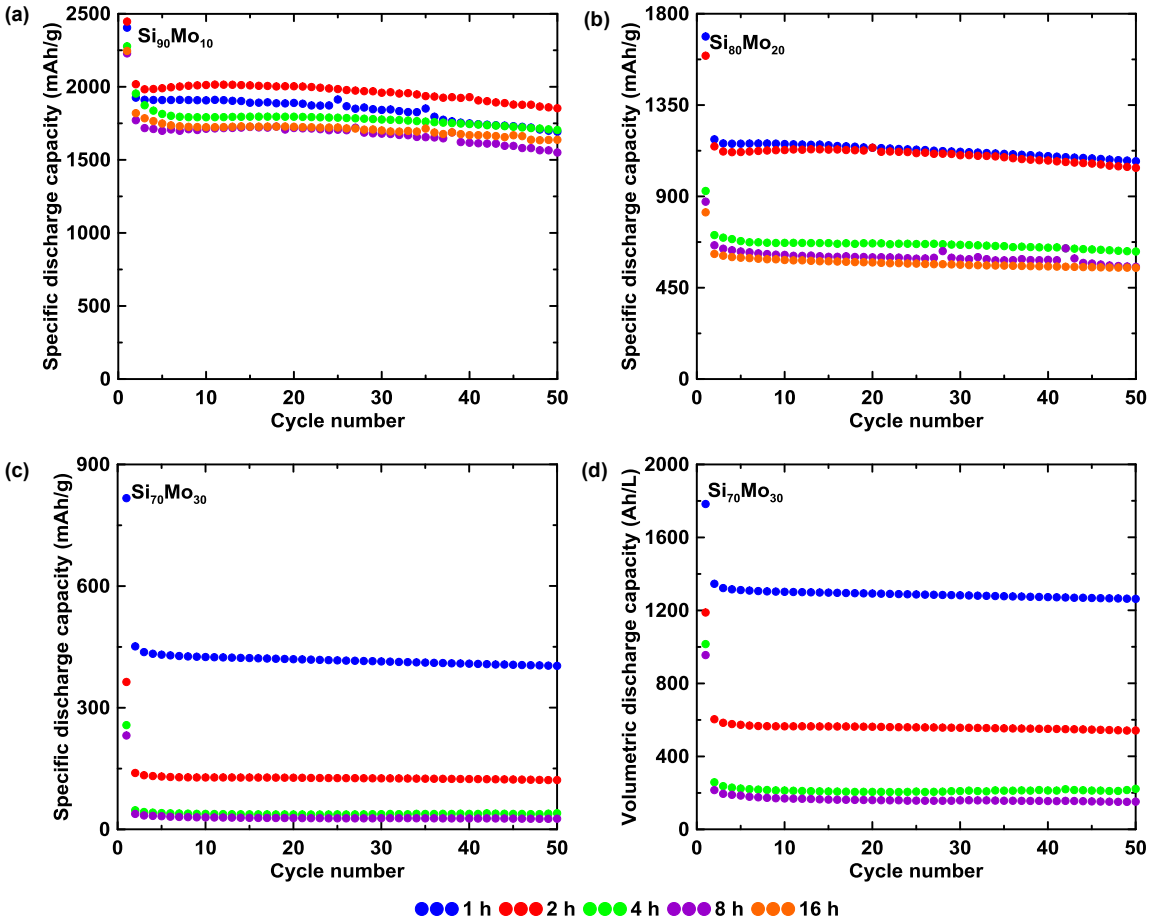

Figure 4.14 Specific capacity vs. cycle number of (a) $Si_{90}Mo_{10}$, (b) $Si_{80}Mo_{20}$, and (c) $Si_{70}Mo_{30}$ and (d) volumetric capacity vs. cycle number of $Si_{70}Mo_{30}$.

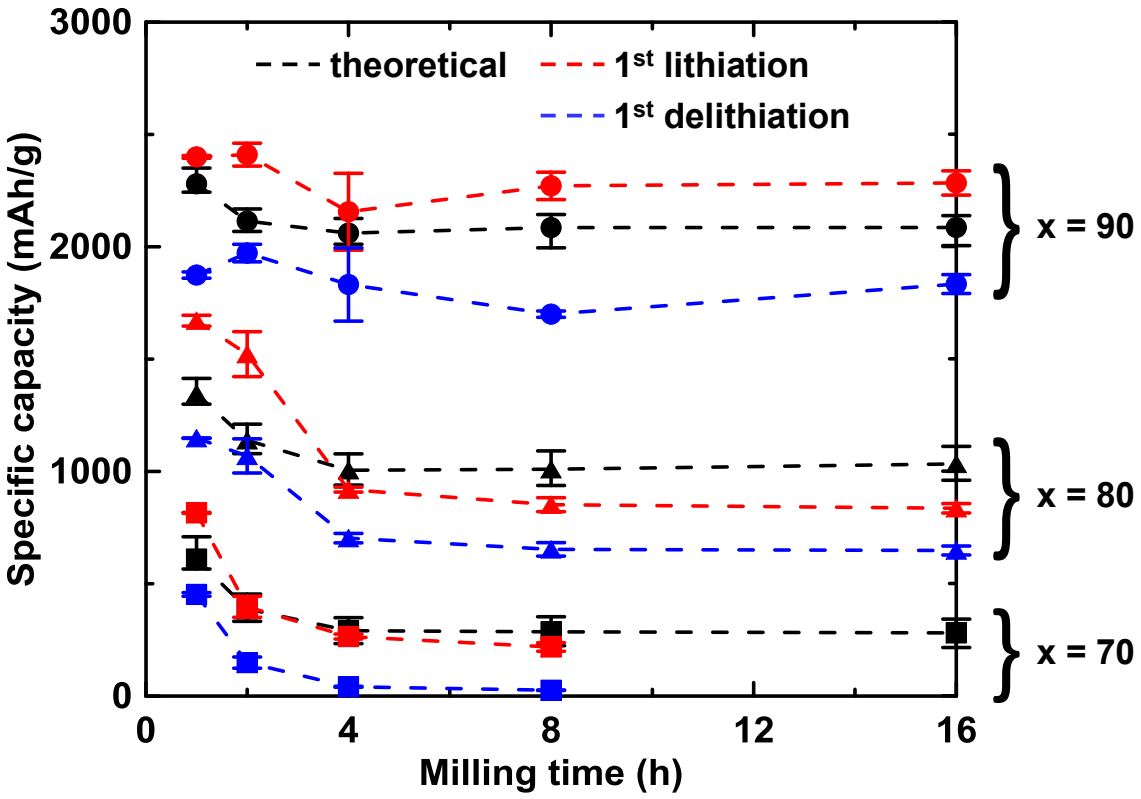

Figure 4.15 Comparison between the theoretical capacities, 1st lithiation capacities, and 1st delithiation capacities of Si_xMo_{100-x} ($90 \geq x \geq 70$, $\Delta x = 10$, 1-16 h) alloys (for each sample, the error bars were calculated based on 3 duplicate cells).

Figure 4.15 shows the first lithiation capacities, the first delithiation capacities and the theoretical capacities based on quantitative XRD analysis, assuming that only the Si phase is active, of the Si_xMo_{100-x} ($90 \geq x \geq 70$, $\Delta x = 10$, 1-16 h) samples. For the $Si_{90}Mo_{10}$ 1-16 h, $Si_{80}Mo_{20}$ 1-2 h, and $Si_{70}Mo_{30}$ 1 h samples, the theoretical capacities have values between the 1st lithiation and 1st delithiation capacities, as expected. For the $Si_{80}Mo_{20}$ 4-16 h and $Si_{70}Mo_{30}$ 2-8 h samples, the measured capacities are less than predicted theoretically, indicating incomplete lithiation of the active Si phase. This may be due to the

encapsulation of some active Si by the larger amount of inactive phase, as shown in Figure 4.6.

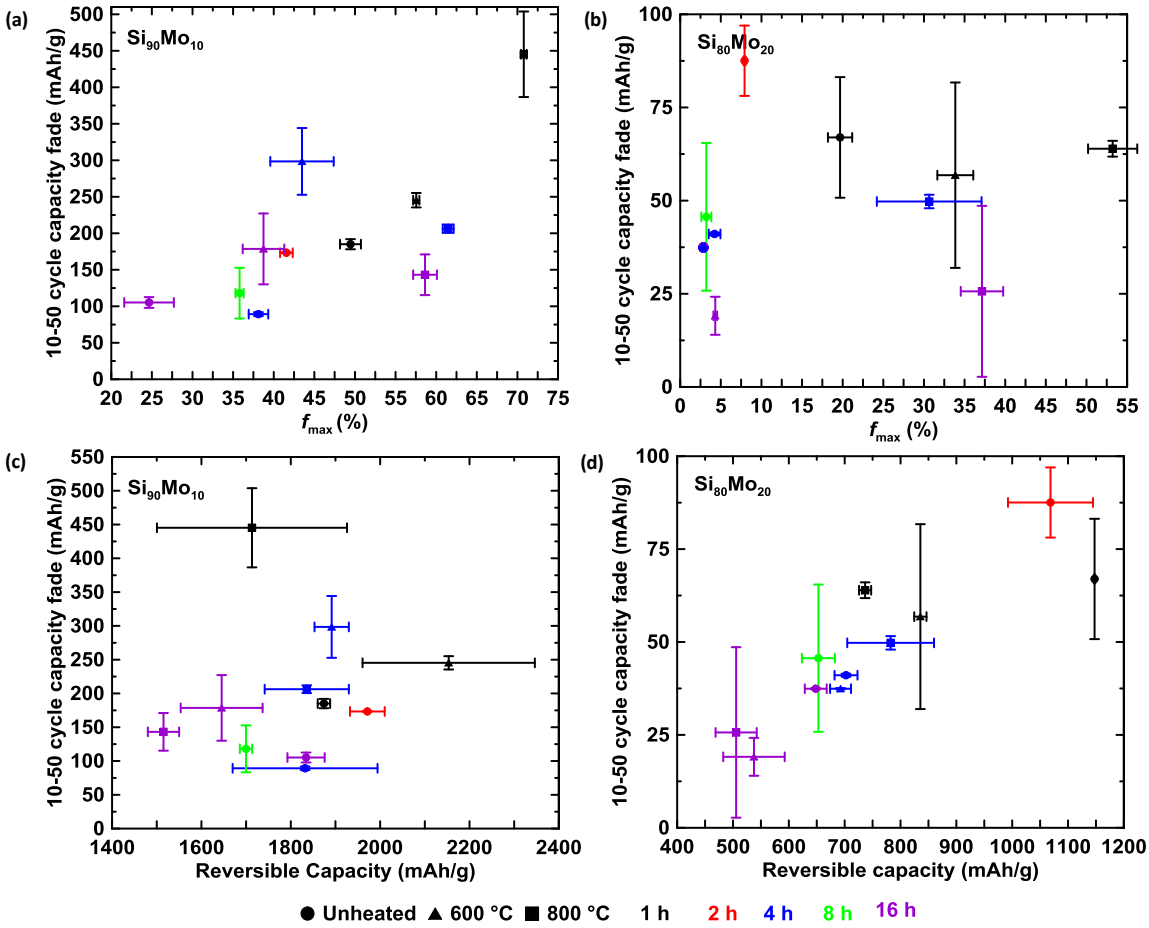

Figure 4.16 Capacity fade during 10-50 cycles vs. maximum value of *f* for (a) $Si_{90}Mo_{10}$ and (b) $Si_{80}Mo_{20}$, and capacity fade during 10-50 cycles vs. reversible capacity (1st charge capacity) for (c) $Si_{90}Mo_{10}$ and (d) $Si_{80}Mo_{20}$ (for each sample, the error bars were calculated based on 3 duplicate cells).

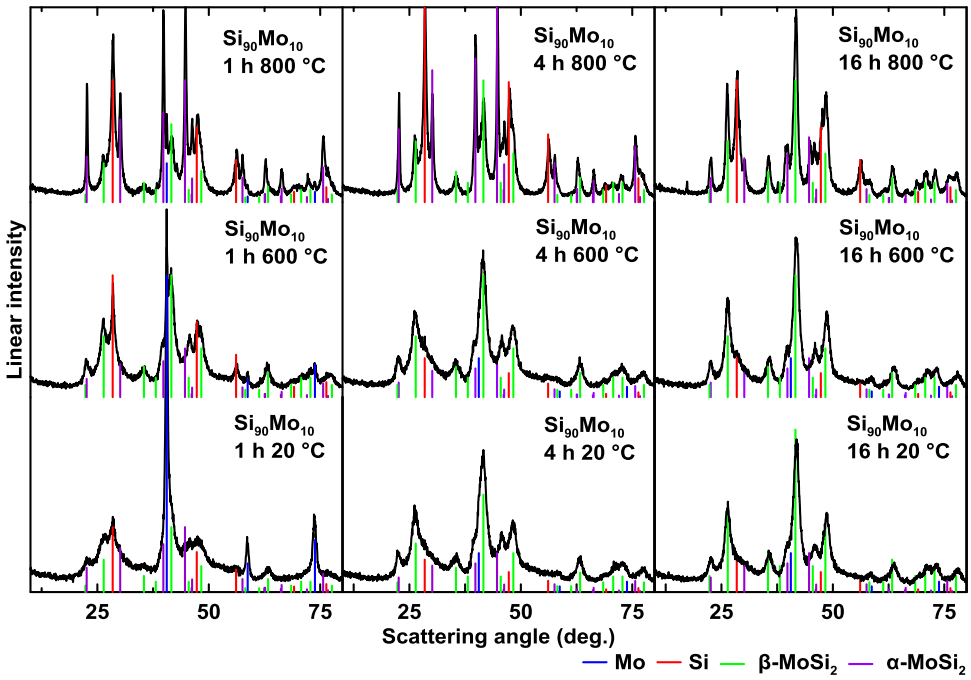

Figure 4.17 XRD patterns of $Si_{90}Mo_{10}$ alloys with different milling times and heat treatment temperatures.

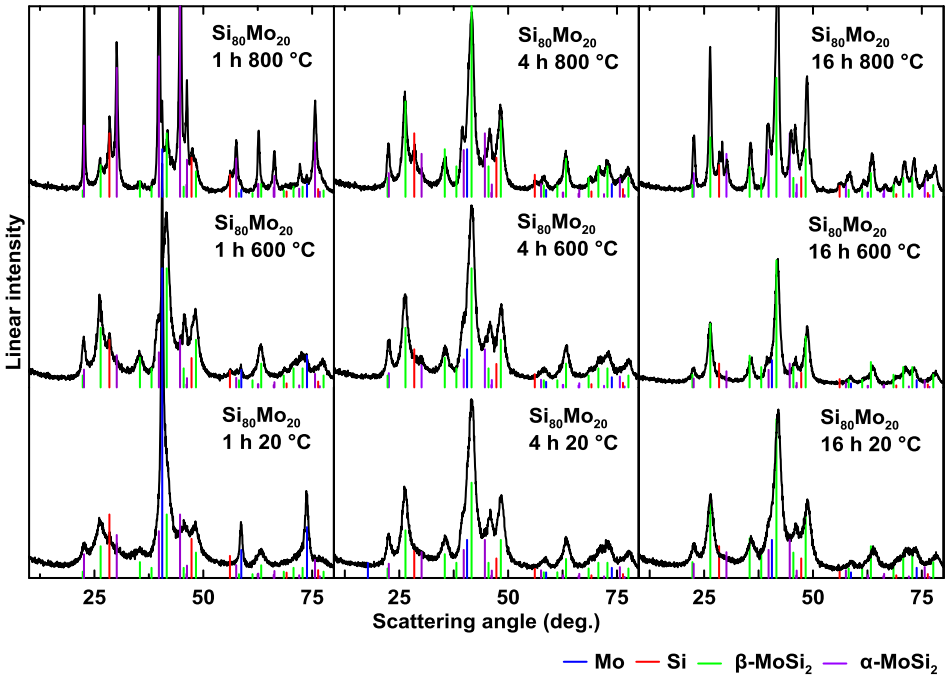

Figure 4.18 XRD patterns of $Si_{80}Mo_{20}$ alloys with different milling times and heat treatment temperatures.

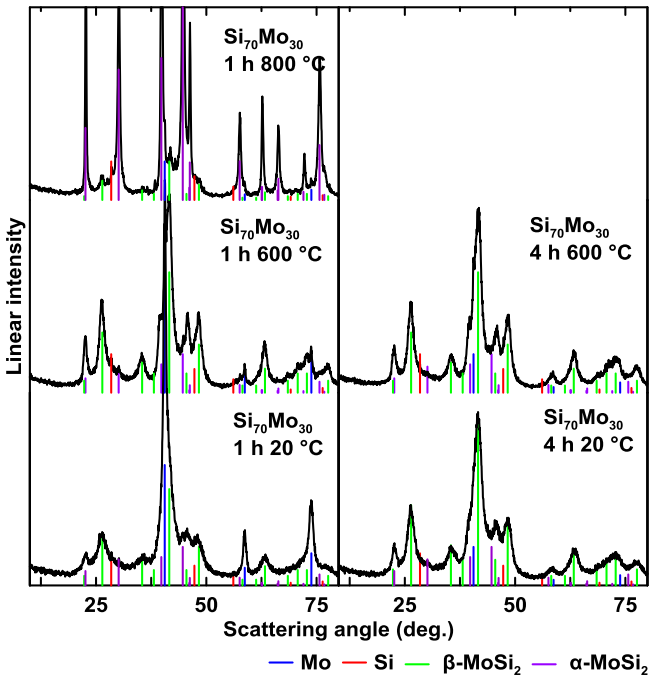

Figure 4.19 XRD patterns of $Si_{70}Mo_{30}$ alloys with different milling times and heat treatment temperatures.

Selected Si-Mo alloys were heated at 600 and 800 °C to study their thermal stability. XRD patterns of selected $Si_{90}Mo_{10}$, $Si_{80}Mo_{20}$, and $Si_{70}Mo_{30}$ alloys before and after heating are shown in Figures 4.17, 4.18 and 4.19, respectively. In general, alloy crystallization, indicated by sharpening XRD peaks, was slight at 600 °C, but became readily evident at 800 °C. The phase evolution during heating is shown in Figure 4.20. During heating the Si-Mo 1 h samples, the Mo content decreased, which is indicative of its reaction with Si to produce $MoSi_2$. This shows that after 1 h ball milling, the reaction is not complete. In contrast, the phase behavior of the 4 h and 16 h samples are similar, confirming that the ball milling reaction between Si and Mo is complete after only 4 h. After heating

at 800 °C, the crystallization of a-Si occurred in all Si-Mo alloys. In addition, the β-$MoSi_2$ phase converts to the α-$MoSi_2$ during heating at 600 and 800 °C, which is consistent with the Si-Mo equilibrium phase diagram where α-$MoSi_2$ is the stable phase of $MoSi_2$ below 1900 °C.

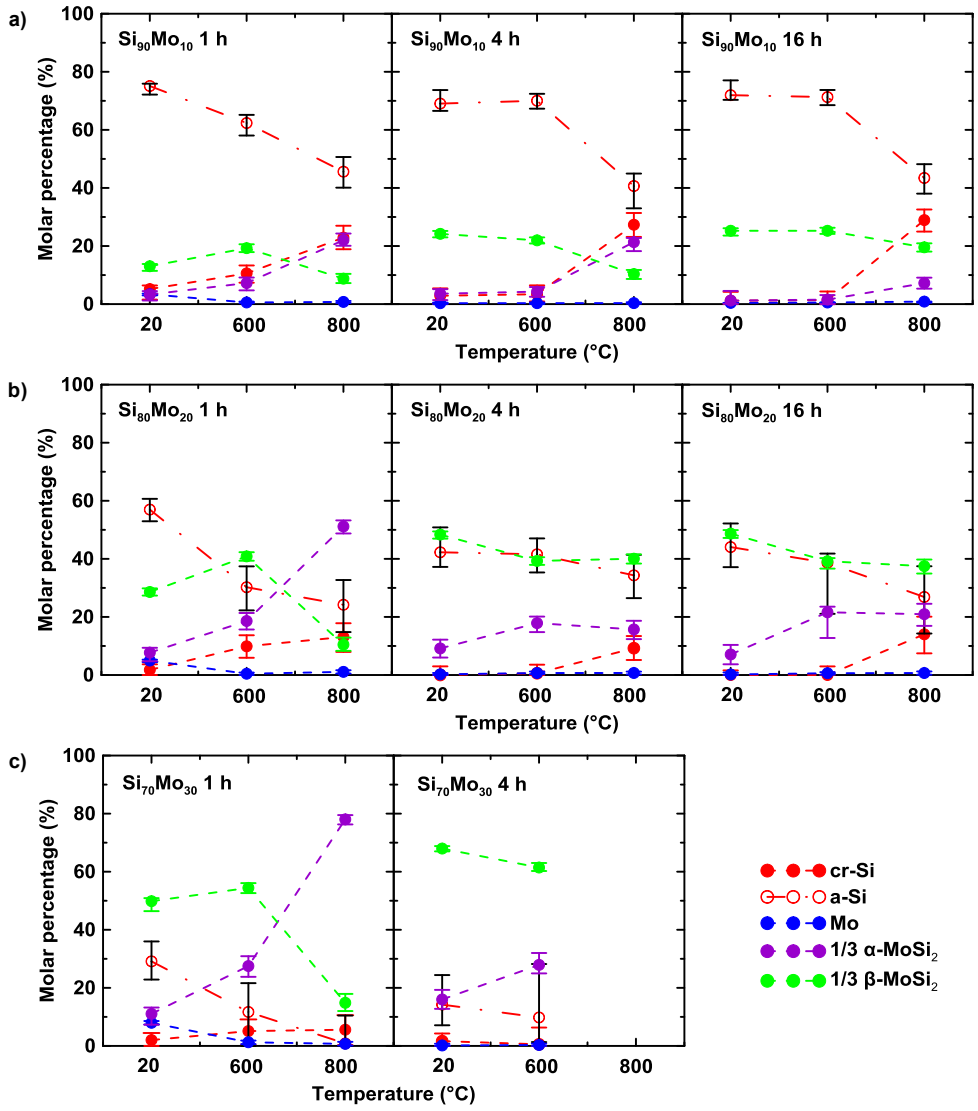

Figure 4.20 Composition analysis of selected Si-Mo alloys before and after heat treatment: (a) $Si_{90}Mo_{10}$; (b) $Si_{80}Mo_{20}$; (c) $Si_{70}Mo_{30}$. All molar percentages are calculated on a per atom basis. To determine error bars, the integrated intensity each phase in the fit was changed until there was a ±10% change in the goodness of fit.

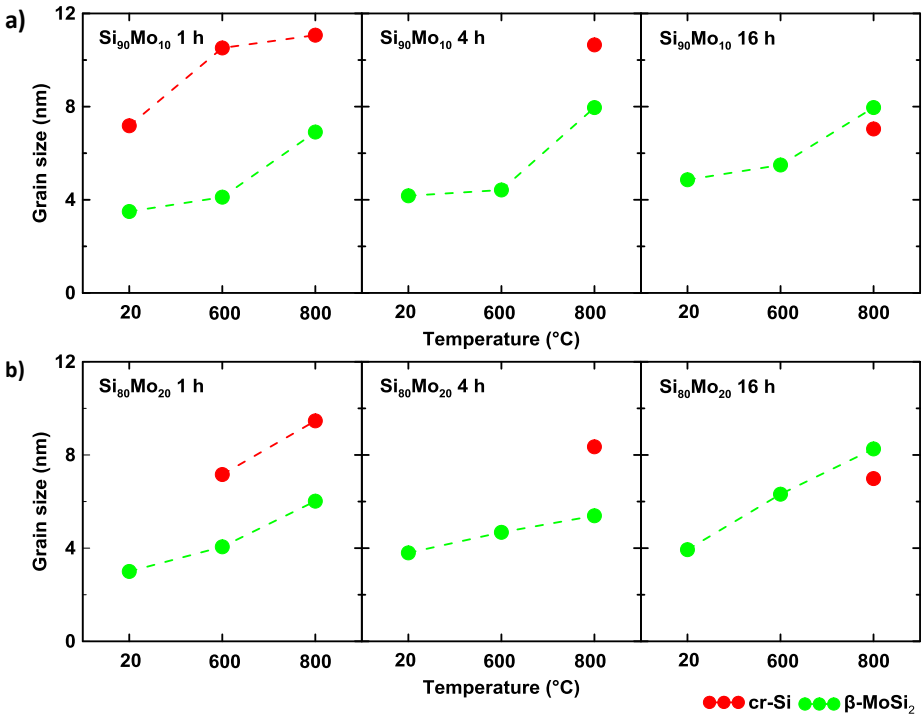

Figure 4.21 Grain sizes of cr-Si and β-$MoSi_2$ before and after heat treatment: (a) $Si_{90}Mo_{10}$ and (b) $Si_{80}Mo_{20}$.

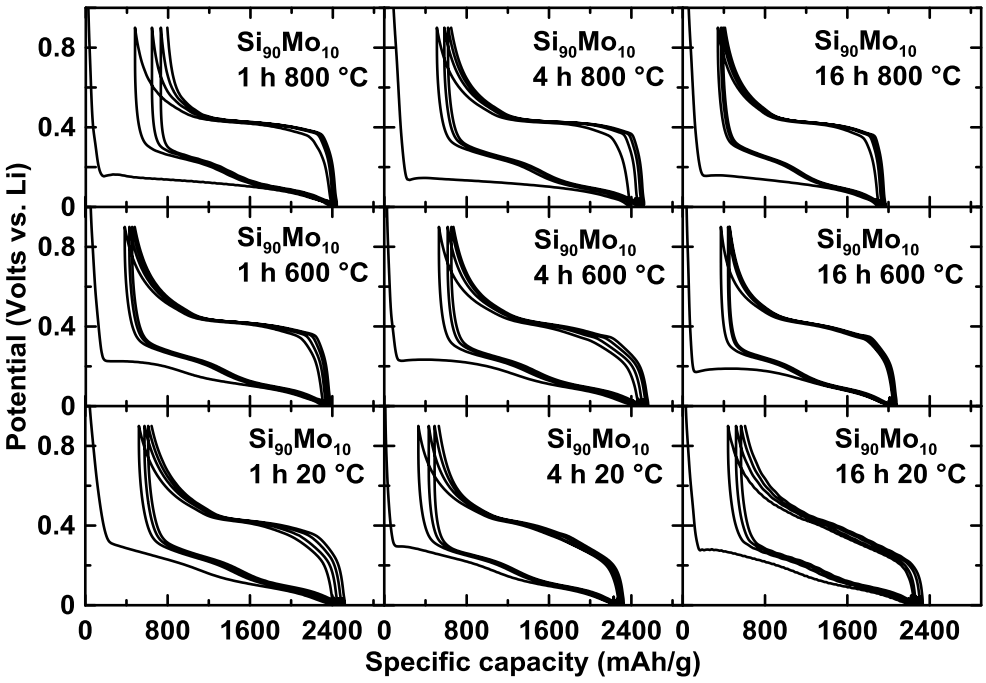

Figure 4.22 Potential profiles of selected $Si_{90}Mo_{10}$ alloy electrodes with different heat treatment temperatures.

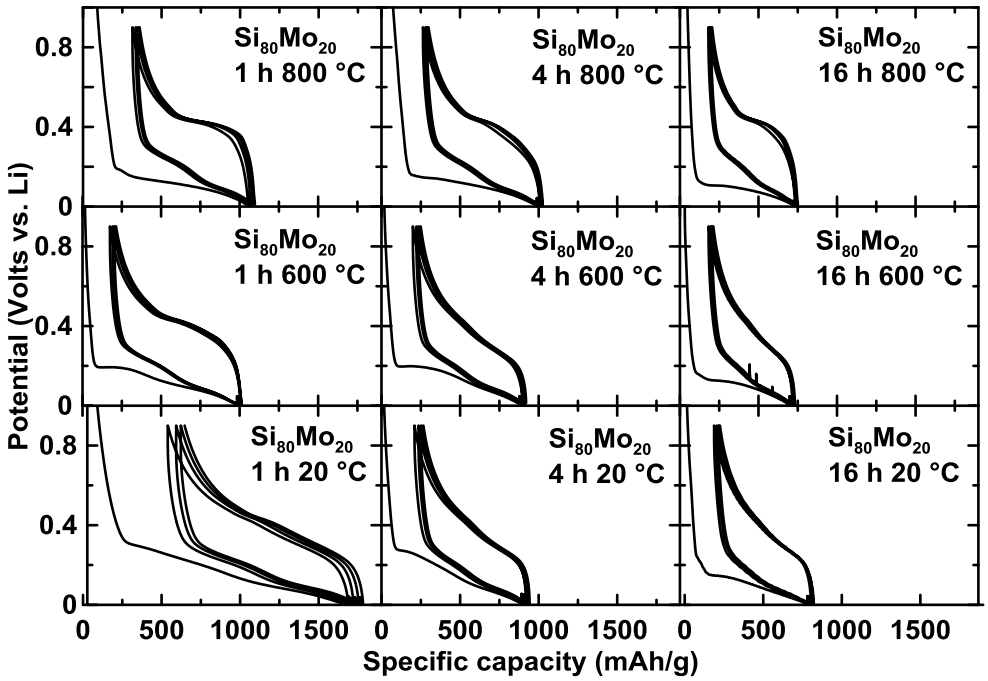

Figure 4.23 Potential profiles of selected $Si_{80}Mo_{20}$ alloy electrodes with different heat treatment temperatures.

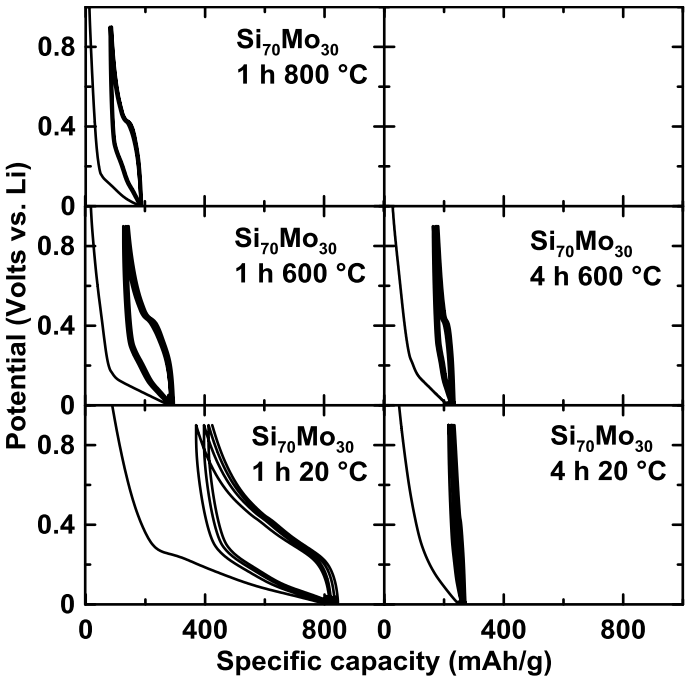

Figure 4.24 Potential profiles of selected $Si_{70}Mo_{30}$ alloy electrodes with different heat treatment temperatures.

The grain sizes of the cr-Si and β-$MoSi_2$ phases in all the Si-Mo samples were calculated based on the Scherrer equation shown in Section 3.2.1 and are plotted in Figure 4.21 as a function of heating temperature. The grain size of the β-$MoSi_2$ phase grows with heating temperature for all alloys regardless of composition and milling time. For the $Si_{90}Mo_{10}$ or $Si_{80}Mo_{20}$ samples shown in Figure 4.21, the cr-Si phase that appears at 800°C has lower grain size when the sample is milled longer. This may result from better dispersion of the Si phase in the alloy (shown in Figure 4.1 and Figure 4.6). However, Figures 4.17-4.21 clearly show that $MoSi_2$ fails to suppress Si crystallization at temperatures greater than 600°C and even more readily crystalizes itself, despite its high melting point.

Figures 4.22-4.24 show the potential profiles (for the first four cycles) of the Si-Mo alloys before and after heat treatment at different temperatures. The consequences of their crystallization during heating are readily apparent. Compared to the unheated Si-Mo alloys, a more pronounced delithiation potential plateau at about 0.45 V is present for the heated sample, indicating a greater degree of cr-$Li_{15}Si_4$ formation. This is likely because of the growth of Si and $MoSi_2$ grains during heating, resulting in Si disconnection from the inactive phase and, subsequently, a lack of the suppression of cr-$Li_{15}Si_4$ formation.[157] This can be seen more clearly in Figure 4.25(a) and (b), which shows the cycling performance (volumetric capacity) and the degree of cr-$Li_{15}Si_4$ formation (*f*) as a function of cycle number for $Si_{90}Mo_{10}$ and $Si_{80}Mo_{20}$, respectively. The reversible and irreversible specific

capacities, ICEs, and percent volume expansions of the Si-Mo samples after heat treatment can be found in Figure 4.26. Based on Figures 4.8 and 4.26, the Si-Mo 4 h and 16 h samples typically show similar reversible and irreversible specific capacities, ICEs, and the percent volume expansions before and after heat treatment. Furthermore, both the $Si_{90}Mo_{10}$ 16 h and $Si_{80}Mo_{20}$ 16 h samples before and after heat treatment have comparable cycling performance, which shows that these Si-Mo alloys have high temperature tolerance. The heated $Si_{90}Mo_{10}$ 16 h samples have high reversible specific capacities of about 1500-1700 mAh/g and large reversible volumetric capacities of about 1900-2000 Ah/L. The heated $Si_{80}Mo_{20}$ 16 h samples have much lower reversible specific capacities about 500-600 mAh/g, but they still have high volumetric capacities of about 1300-1400 Ah/L, since these alloys have larger density than $Si_{90}Mo_{10}$ samples.

Figure 4.16(a-d) show the relationships between cr-$Li_{15}Si_4$ formation, reversible capacity and 10-50 cycle capacity fade of all heated and unheated $Si_{90}Mo_{10}$ and $Si_{80}Mo_{20}$ alloys. The same general trends found for the unheated alloys remain present for the heated alloys. Figure 4.16(a) and (c) suggest that the 10-50 cycle capacity fade of the large capacity $Si_{90}Mo_{10}$ alloys largely depends on the cr-$Li_{15}Si_4$ formation fraction during cycling, which is related to internal particle fracture. For the lower capacity $Si_{80}Mo_{20}$ alloys, the capacity fade during 10-50 cycles is less and increases with increasing reversible capacity. This shows that in these lower expansion alloys, fade is mostly affected by the structural integrity of the electrode, rather than particle fracture. Because of this property, good

cycling can be achieved in these alloys as long as the reversible capacity is not excessive. This is illustrated in the 16 h milled $Si_{80}Mo_{20}$ alloys heated to 800 ºC. Despite being highly crystalline (Figure 4.18) and exhibiting large amounts of cr-$Li_{15}Si_4$ formation during cycling (40%), the capacity fade of this sample is the lowest of all of the alloys measured (~13 mAh/g or 0.8% / cycles 10-50).

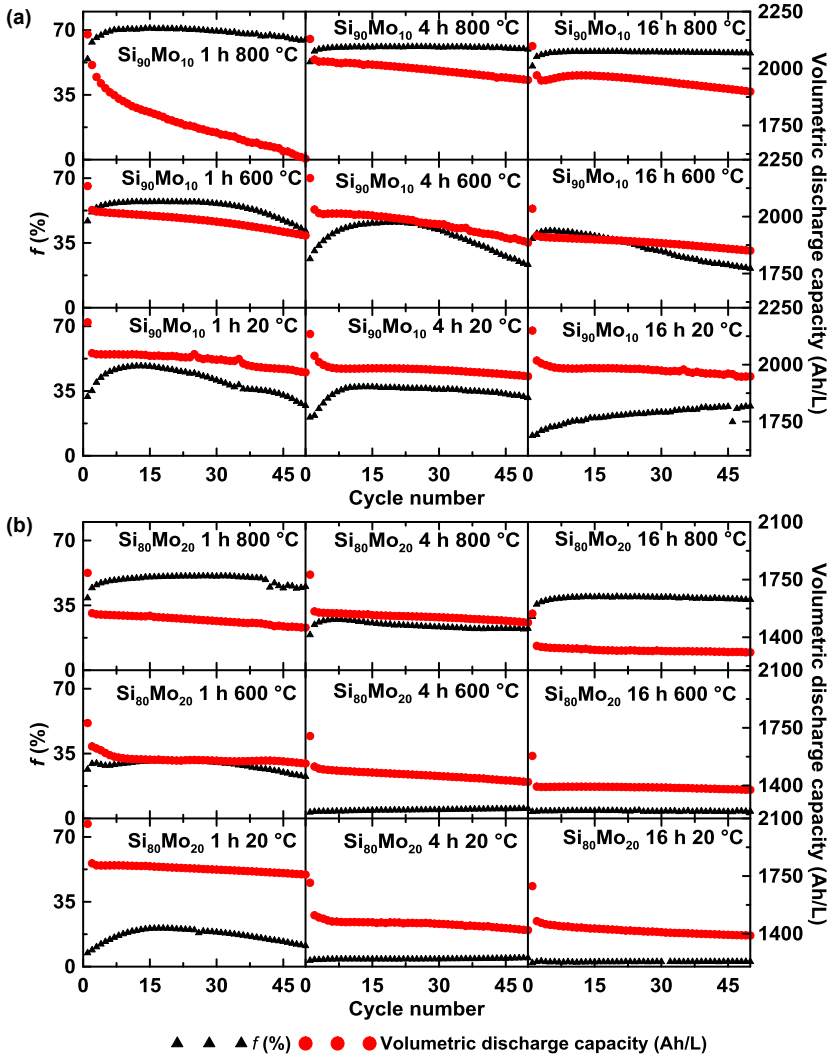

Figure 4.25 Plots of the percent active Si that forms cr-$Li_{15}Si_4$ at full lithiation (*f*) vs. cycle number and volumetric capacities vs. cycle number of (a) $Si_{90}Mo_{10}$ and (b) $Si_{80}Mo_{20}$ alloys with different heat treatment temperatures.

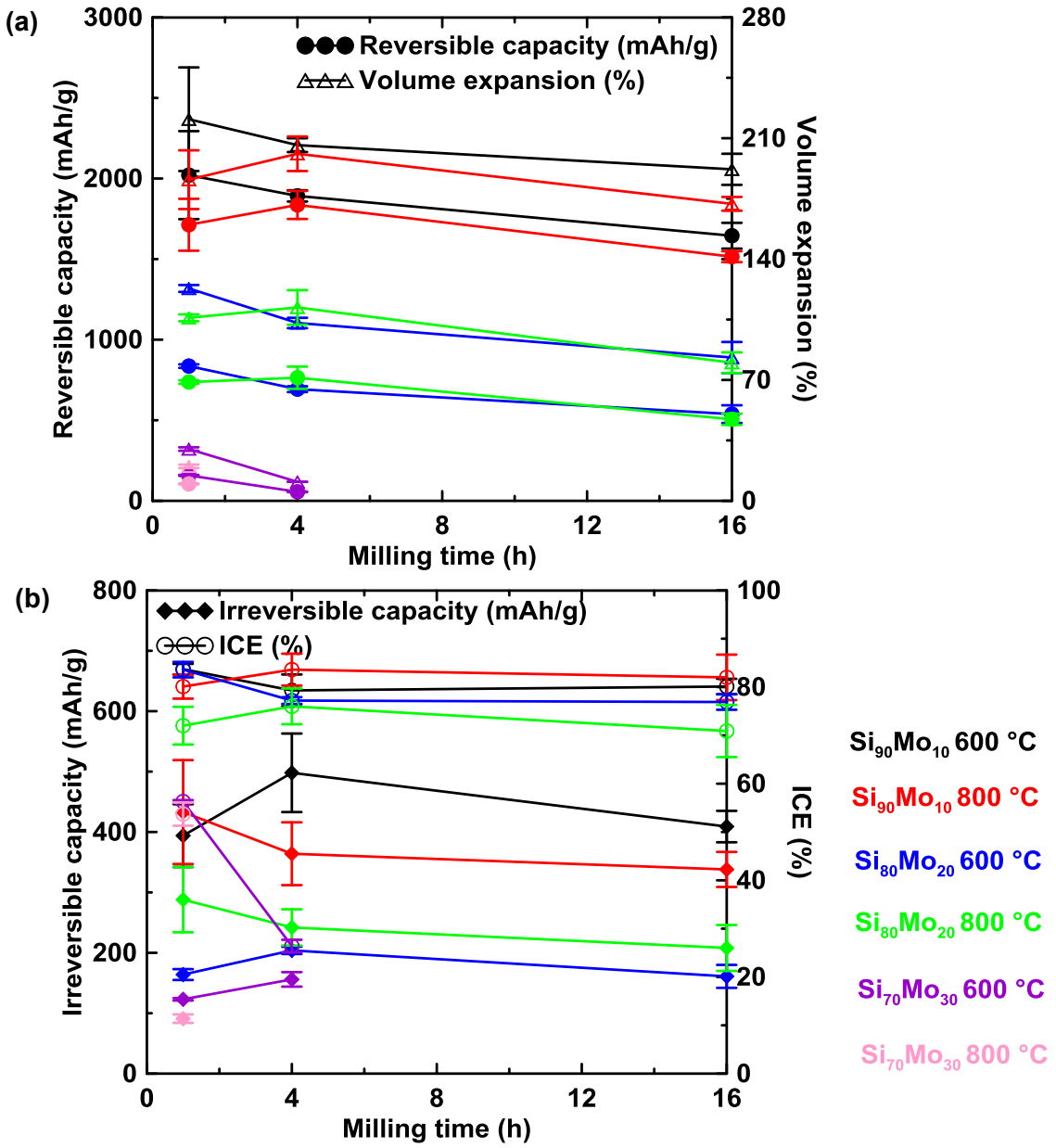

Figure 4.26 (a) Reversible capacities, percent volume expansions, (b) irreversible capacities, and ICEs of Si_xMo_{100-x} ($90 \geq x \geq 70$, $\Delta x = 10$, 1-16 h) with different heat treatment temperatures vs. Li (for each sample, the error bars were calculated based on 3 duplicate cells).

4.4 Conclusions

The phase evolution during ball milling, electrochemical properties, and thermal stability of Si-Mo alloys were studied. It was found that Si-Mo can rapidly form nanostructured a-Si/$MoSi_2$ alloys by ball milling within 4 h. However, caking of Mo on the walls of the ball mill occurred during ball milling, especially for high-Mo content alloys, which could be detrimental to manufacturing processes. These alloys were found to have similar thermal stability as other Si-transition metal alloys, with the crystallization of the a-Si phase occurring at about 600 °C and crystallization of the $MoSi_2$ phase occurring at even lower temperatures. This crystallization resulted in a high degree of $Li_{15}Si_4$ formation during cycling. However, surprisingly, this was not found to be detrimental to cycling for the samples heated at 800 °C. Such samples seemed to be able to maintain electrical contact to the active Si phase despite $Li_{15}Si_4$ formation. As a result, Si-Mo alloys can provide good cycling performance at high temperatures despite not being especially thermally stable. The $Si_{90}Mo_{10}$ 16 h and $Si_{80}Mo_{20}$ 16 h alloys after heat treatment at 800 °C also have high reversible volumetric capacities of about 1900 Ah/L and 1300 Ah/L, respectively. The compatibility of these alloys with the high temperatures required for the carbon coating process make them good candidates as compositions for highly engineered Li-ion battery negative electrode materials.

Chapter 5 Si-TiN Alloy Li-ion Battery Negative Electrode Materials Prepared by Reactive N_2 Gas Milling*

5.1 Introduction

As mentioned in Sections 2.3.5.3 and 4.1, adding inactive phases to Si is an efficient way to reduce the total volume expansion and suppress crystalline $Li_{15}Si_4$ (cr-$Li_{15}Si_4$) formation during lithiation.[16,126,127] In 2000, Kim et al. selected TiN as an inactive phase, and used high-energy mechanical milling to prepare Si-TiN negative electrode materials for Li cells.[158] TiN is an attractive inactive phase, since it has high electrical conductivity and it is also highly stable towards reactions with electrolyte at low potentials.[159,160] However, apart from Kim et al.'s early studies and other studies on Si-TiN and Si-TiN-C alloys,[161,162] Si-TiN negative electrode materials have received little attention. One possible reason for this is the high cost of TiN.[163] Recently, Wang et al. have reported a simple and inexpensive method to synthesize Si-TiN alloys by ball milling Ti and excess Si in N_2 (g).[163] During this process, $TiSi_2$ is formed as an intermediate during milling. As

---

* This chapter was adapted with permission from S. Cao, J. C. Bennett, Y. Wang, S. Gracious, M. Zhu, and M. N. Obrovac. Si-TiN alloy Li-ion battery anode materials prepared by reactive N_2 gas milling. Journal of Power Sources. Publication date: 31 October 2019. Copyright 2019, Elsevier B.V. S. Cao's contribution includes performing the main experiment and analysis work and writing the manuscript. J. C. Bennett preformed measurements and analysis of TEM and STEM. Y. Wang provided ideas about experimental design. S. Gracious performed some sample preparation. M. N. Obrovac provided guidance and participated in experimental design and the interpretation of all the data.

milling progresses further, the $TiSi_2$ phase undergoes a displacement reaction with N_2 (g) and converts to TiN and Si. This result is surprising, since Calka et al. found mechanical milling Si in nitrogen gas at room temperature could produce Si_3N_4,[164] and thermodynamic equilibrium would also predict Si-Si_3N_4-$TiSi_2$ coexistence for the Si-rich region of the N-Si-Ti system. Therefore the formation of TiN must be kinetically favored over the formation of Si_3N_4. It has been confirmed that Si_3N_4 forms only very slowly if Si is ball milled in a N_2(g) environment under the conditions used by Wang. The resulting Si-TiN negative electrode materials are impressive, since they can be inexpensively produced and have good cycling stability even at high Si contents.

Here, a systematic and detailed study is presented of the microstructure and nanostructure of $Si_x(TiN)_{100-x}$ ($85 \geq x \geq 60$, $\Delta x = 5$) alloys prepared by N_2 (g) reactive milling or conventional inert gas ball milling of Si + TiN. These properties are then related to their electrochemical performance in Li cells.

5.2 Experimental

$Si_x(TiN)_{100-x}$ ($85 \geq x \geq 60$, $\Delta x = 5$) alloys were synthesized by reactive gas milling in N_2 (g) for 16 h with Si powder (Sigma-Aldrich, 325 mesh, 99%) and Ti powder (Alfa Aesar, 325 mesh, 99%) as precursors. These alloys are referred to here as Si-TiN (N_2). Si-TiN alloys were also prepared by conventional inert gas (Ar was used in this study) milling for 16 h using Si and TiN (Sigma-Aldrich, < 3 μm) powders as raw materials. Such alloys

are referred to here as Si-TiN (Ar). The sample preparation conditions and processes were as described in Section 3.1.

Morphology of Si-TiN alloys and electrode cross sections were characterized using a Schottky field emission scanning electron microscope (SEM, TESCAN MIRA 3 LMU) with a 20 kV accelerating voltage. An SEM energy dispersive spectroscopy (EDS) system (Oxford instrument X-max 80mm^2) was used for semi-quantitative analysis of Si, Ti, and Fe contents. For each sample, three regions with area of about 0.2 mm^2 ~ 1.8 mm^2 were chosen randomly for the semi-quantitative analysis, and the analysis results from the three regions were almost identical. X-ray diffraction (XRD) patterns of Si-TiN alloys were collected using a Rigaku Ultima IV diffractometer in the 2θ range of 10° ~ 80°. O and N contents of selected Si-TiN (N_2) samples were obtained by LECO analysis (NSL Analytical Services, Inc, Cleveland OH). A Multilab 2000 Multitechnique Surface Analysis Instrument (Thermo VG Scientific) was used for X-ray photoelectron spectroscopy (XPS) characterization, with a non-monochromatic Mg Kα X-ray source (1253.6 eV) and operated at a power of 280 W at 14 kV. The standard C 1s binding energy (BE, 284.8 eV) was used to calibrate binding energy for all XPS data. XPS spectra of Si-TiN samples were fitted using CasaXPS software. In the fitting, the background was removed with a nonlinear Shirley-type model, and a Gaussian-Lorentzian line shape (GL(30)) was used. Bright field (BF), selected area electron diffraction (SAED), and high resolution electron microscopy (HREM) images were obtained using a Philips CM30 transmission electron microscopy

(TEM), which was operated at 250 kV. Ti and Si contents in single Si-TiN particles were determined by an EDS system coupled with the TEM instrument. Elemental mappings were used to grain element (Si and Ti) distributions in single particles of Si-TiN. The data was collected in a scanning TEM (STEM) mode. A nominal analytical beam diameter of 15 nm was used at 250 kV, where the dwell time was 200 μsec. Sample densities were measured with a helium pycnometer (AccuPyc II 1340, Micrometrics).

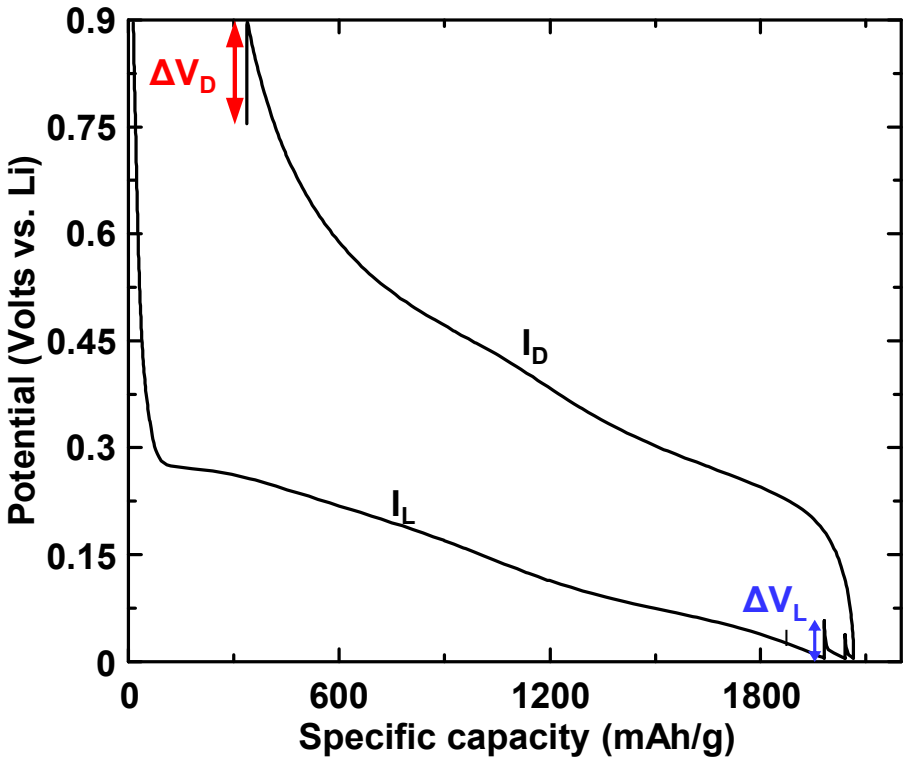

Figure 5.1 Potential curve illustrating the change in voltage during 10 min rest after lithiation half-cycle and 15 min rest after delithiation half-cycle used to calculate lithiation and delithiation ASI values.

Electrode preparation and half cell assembly of Si-TiN (N_2 and Ar) alloys were as described as Sections 3.8.1 and 3.8.2, respectively. The half cells were cycled at 30 ± 0.1 °C or 45 ± 0.2 °C between 0.005 V and 0.9 V using a battery testing system (Neware). In the first cycle, a C/10 rate was used for discharging and charging the cells and C/20 and C/30 rates were applied to simulate a trickle at a constant voltage for obtaining a constant current constant voltage (CCCV) type cycling. In the following cycles, the currents used were two times larger than those in the first cycle (i.e. simulating CCCV cycling at a C/5 rate). The half cells were cycled for 50 or 100 cycles. The method to determine C-rates and the other parts of the cycling procedure can be found in Sections 3.8.3 and 4.1, respectively. Area specific impedance (ASI) values were calculated using the change in voltage during each 10 min rest after lithiation half-cycle and each 15 min rest after delithiation half-cycle, as shown in Figure 5.1. The ASI was calculated according to the equation:

$$ASI = \frac{\Delta \mathrm{V} \times \mathrm{A}}{I} \tag{5.1}$$

Where ΔV (ΔV_L or ΔV_D) is the voltage change during the 10 or 15 min rest step, A is the geometric area of the electrode (1.33 cm^2), and I is the current used before the rest step.

5.3 Results and Discussion

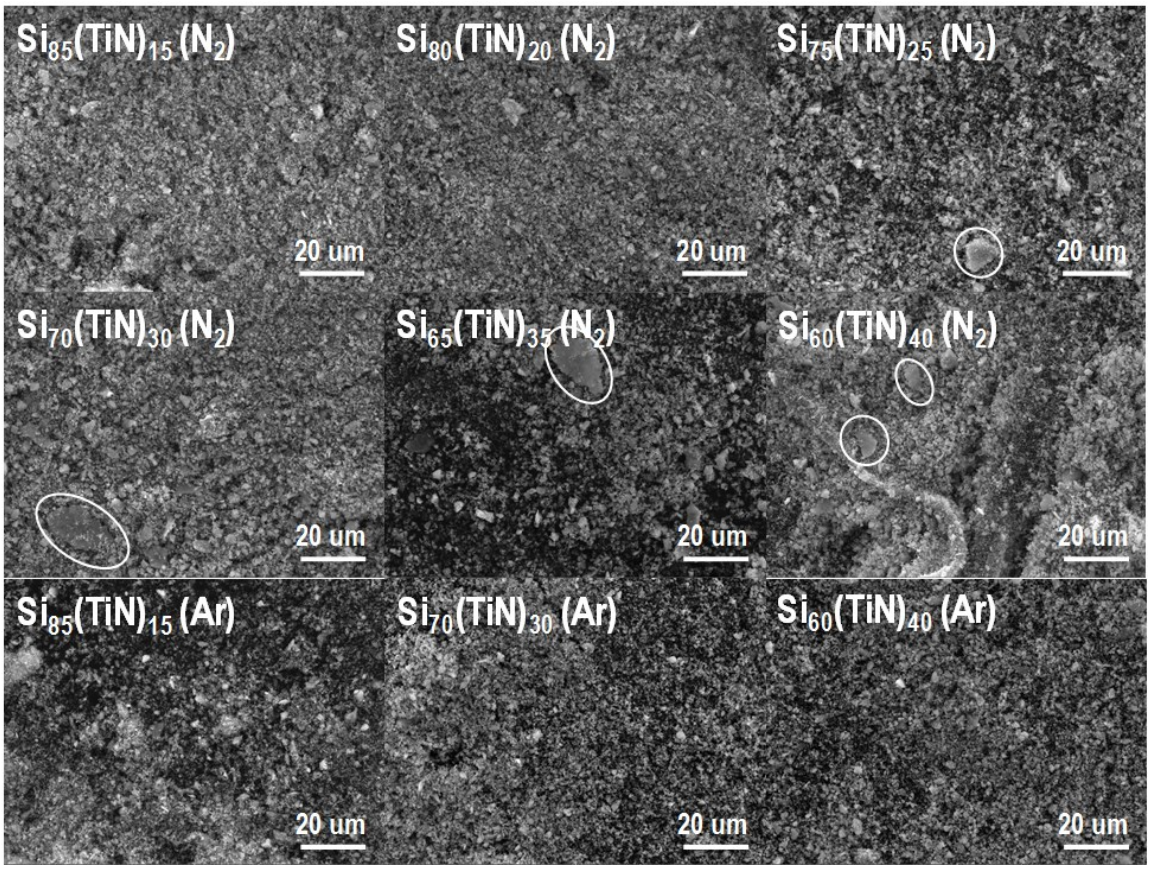

Figure 5.2 SEM images of $Si_x(TiN)_{100-x}$ ($85 \geq x \geq 60$, $\Delta x = 5$, N_2) and $Si_x(TiN)_{100-x}$ ($x = 85$, 70, and 60, Ar) alloys.

SEM images of $Si_x(TiN)_{100-x}$ ($85 \geq x \geq 60$, $\Delta x = 5$, N_2) and $Si_x(TiN)_{100-x}$ ($x = 85$, 70, and 60, Ar) alloys are shown in Figure 5.2. An SEM BSE image of the cross section of a $Si_{85}(TiN)_{15}$ (N_2) electrode before cell cycling is shown in Figure 5.3. Cross-section images of electrodes of the other $Si_x(TiN)_{100-x}$ (N_2 and Ar) alloys appear identical. Generally, all these alloys have almost identical morphology having an average particle size of ~1 μm (based on 50 random particles of $Si_{70}(TiN)_{30}$ (N_2) and 50 random particles of $Si_{70}(TiN)_{30}$

(Ar)). However, several large flakes of about 10-20 μm in extent can be observed in the Si-TiN (N_2) samples with high Ti contents, as indicated by white circles. It is known that during ball milling, ball-powder-ball collisions can lead to both fracturing and cold welding, with cold welding resulting in flake formation.[165] For samples containing ductile materials (like Ti and Fe), cold welding could play a dominant role. Therefore, the Si-TiN (N_2) samples, which have ductile Ti as a precursor, form flakes while the Si-TiN (Ar) samples, which only have brittle precursors, do not.

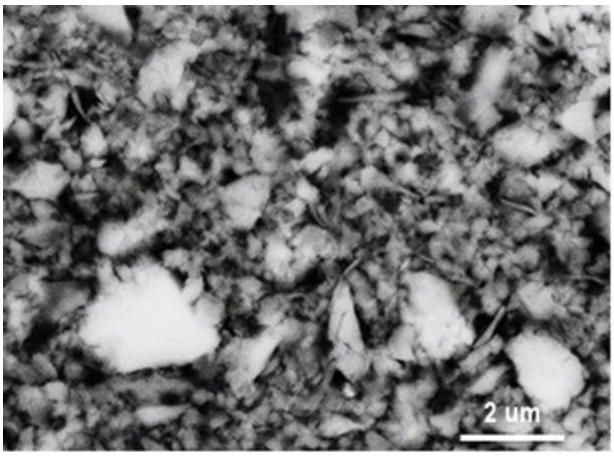

Figure 5.3 BSE image of cross section of $Si_{85}(TiN)_{15}$ (N_2) electrode before cell cycling.

Table 5.1 lists the relative Si, Ti, and Fe contents of the Si-TiN (N_2 and Ar) samples as determined by SEM EDS analysis. The results show that the Si-Ti atomic ratios of these samples are consistent with those of their precursors. All of the samples contained a small Fe impurity of 1.1-1.8 at.% for the Si-TiN (N_2) alloys and 0.7-2.6 at.% for the Si-TiN (Ar) alloys. Fe is likely to be an impurity introduced from ball milling with steel balls and steel milling vials. The Si-TiN (Ar) alloys likely have a larger Fe impurity as a

consequence of milling with abrasive TiN precursor powder. The $Si_{85}(TiN)_{15}$ (N_2) and $Si_{60}(TiN)_{40}$ (N_2) samples were selected for LECO tests to determine the O and N contents in these samples. Based on LECO and SEM EDS results, the compositions of the two samples were calculated and are listed in Table 5.2. For the $Si_{85}(TiN)_{15}$ (N_2) alloy, the N content (15.1 at.%) is slightly higher than the Ti content (12.2 at.%). Combined with the XRD results as shown in Figure 5.4, this suggests that a nearly complete reaction of Ti with N_2 to form TiN. In contrast, the $Si_{60}(TiN)_{40}$ (N_2) sample had slightly lower N content (24.6 at.%) than Ti (27.3 at.%). This implies an incomplete reaction of Ti with N_2. This might be due to the ductility of the added Ti, which resulted in the formation of large flakes and may have limited the Ti-N_2 reaction. The O contents of the $Si_{85}(TiN)_{15}$ (N_2) and $Si_{60}(TiN)_{40}$ (N_2) alloys are about 5.6 at.% and 5.5 at.%, respectively. The Si precursor powder used has an O impurity of about 8 at.%,[166] whereas the Ti precursor powder has almost no O (about 0.4 at.%). Therefore all of the oxygen in the samples can be accounted for as a consequence of the oxygen impurity in the precursor Si powder.

Table 5.1 Compositions of Si-TiN (N_2 and Ar) alloys based on SEM EDS analysis (for each powder sample, the uncertainties were calculated based on 5 random regions) .

Sample	Composition (atomic %)		
	Si	Ti	Fe
$Si_{85}(TiN)_{15}$ (N_2)	83.5 ± 0.3	15.4 ± 0.2	1.1 ± 0.1
$Si_{80}(TiN)_{20}$ (N_2)	78.4 ± 0.0	20.2 ± 0.2	1.4 ± 0.2
$Si_{75}(TiN)_{25}$ (N_2)	73.9 ± 0.4	24.9 ± 0.4	1.2 ± 0.1
$Si_{70}(TiN)_{30}$ (N_2)	68.8 ± 0.2	29.8 ± 0.3	1.4 ± 0.1
$Si_{65}(TiN)_{35}$ (N_2)	64.5 ± 0.2	34.4 ± 0.1	1.1 ± 0.1
$Si_{60}(TiN)_{40}$ (N_2)	59.1 ± 1.0	39.1 ± 1.0	1.8 ± 0.1
$Si_{85}(TiN)_{15}$ (Ar)	83.9 ± 0.5	15.7 ± 0.7	0.7 ± 0.3
$Si_{70}(TiN)_{30}$ (Ar)	68.4 ± 0.3	29.1 ± 0.4	2.5 ± 0.1
$Si_{60}(TiN)_{40}$ (Ar)	58.8 ± 0.6	38.6 ± 0.5	2.6 ± 0.2

Table 5.2 Compositions of $Si_{85}(TiN)_{15}$ (N_2) and $Si_{60}(TiN)_{40}$ (N_2) samples based on SEM EDS and LECO analysis (the uncertainties of Si, Ti, and Fe contents are shown in Table 5.1; the uncertainties for N and O contents are shown in Section 3.6).

Sample	Composition (atomic %)				
	Si	Ti	Fe	N	O
$Si_{85}(TiN)_{15}$ (N_2)	66.2	12.2	0.9	15.1	5.6
$Si_{60}(TiN)_{40}$ (N_2)	41.3	27.3	1.3	24.6	5.5

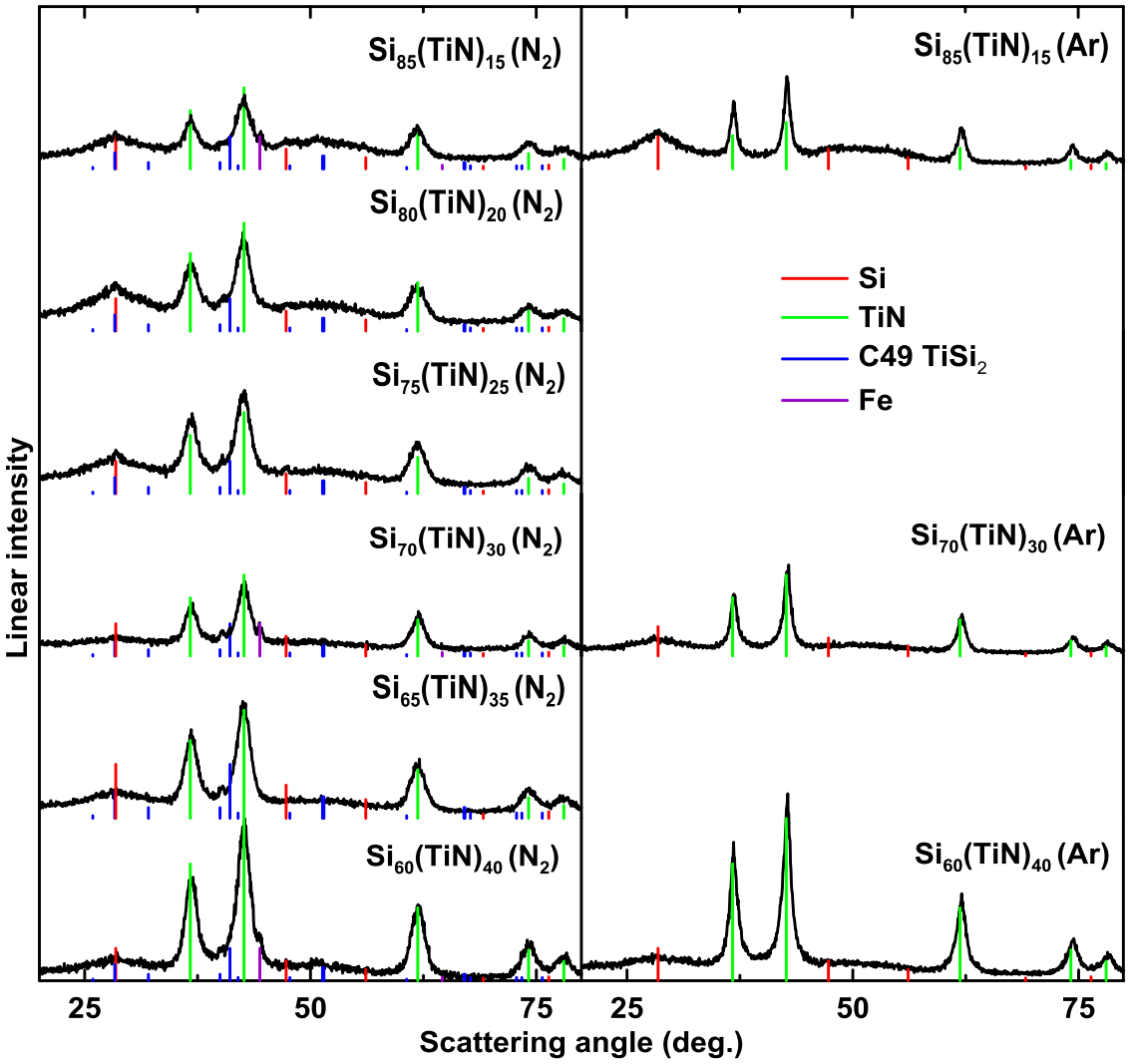

Figure 5.4 XRD patterns of $Si_x(TiN)_{100-x}$ ($85 \geq x \geq 60$, $\Delta x = 5$, N_2) and $Si_x(TiN)_{100-x}$ (x = 85, 70, and 60, Ar) alloys.

XRD patterns of $Si_x(TiN)_{100-x}$ ($85 \geq x \geq 60$, $\Delta x = 5$, N_2) and $Si_x(TiN)_{100-x}$ (x = 85, 70 and 60, Ar) samples are shown in Figure 5.4. The XRD patterns of all the Si-TiN alloys are similar. All the alloys consist of amorphous Si (a-Si) and nanocrystalline TiN phases. A small peak at about 44°, corresponding to the (110) reflection Fe, can be observed for the $Si_{85}(TiN)_{15}$, $Si_{70}(TiN)_{30}$ and $Si_{60}(TiN)_{40}$ N_2 samples, corresponding to the Fe impurity

found by SEM EDS. As shown in reference 163, C49-$TiSi_2$ is an intermediate product during ball milling Si and Ti powders in N_2 (g). Therefore, small impurity peaks found at about 41.1° and 42.0° in the XRD patterns of the Si-TiN (N_2) samples were identified to be from the (131) and (150) reflections of C49-$TiSi_2$, respectively. In addition, it can be found in Figure 5.4 that TiN peaks of the Si-TiN (N_2) alloys are smaller and broader than the corresponding TiN peaks of the Si-TiN (Ar) alloys, which indicates that the Si-TiN (N_2) samples have smaller TiN grain sizes. According to the Scherrer equation (Equation 3.2), all of the Si-TiN (N_2) alloys have a TiN grain size of about 5 nm, while the TiN grain sizes of the Si-TiN (Ar) samples are larger and are about 7-10 nm.

In order to identify chemical states of elements in Si-TiN alloys prepared by reactive gas milling and conventional inert gas milling methods, the $Si_{70}(TiN)_{30}$ (N_2) and $Si_{70}(TiN)_{30}$ (Ar) alloys were selected for XPS analysis. Figure 5.5(a) shows Si 2p XPS spectra of these two samples and their fitting results. Each Si 2p spectrum was fitted with two pairs of Si $2p_{3/2}$ and Si $2p_{1/2}$ peaks with an area ratio of 2:1 and with a spin-orbit splitting of 0.6 eV. The fitting results indicate that at low BEs two peaks at 99.3 eV and 99.9 eV are present in both the $Si_{70}(TiN)_{30}$ (N_2) and $Si_{70}(TiN)_{30}$ (Ar) Si 2p spectra. These peaks are typically from the $2p_{3/2}$ and $2p_{1/2}$ contributions from elemental Si.[167] The two remaining peaks in the $Si_{70}(TiN)_{30}$ (Ar) Si 2p spectrum are at 103.1 eV and 103.7 eV, and are most likely from Si $2p_{3/2}$ and $2p_{1/2}$ in SiO_2.[167] In contrast, the two remaining peaks in the Si 2p spectrum of the $Si_{70}(TiN)_{30}$ (N_2) sample are at lower BEs of 102.4 eV and 103.0 eV, and

are probably generated by Si $2p_{1/2}$ and $2p_{3/2}$ in SiO_xN_y based on some previous XPS studies.[168,169] Therefore, both the Si-TiN (N_2 and Ar) alloys have two different chemical states for Si: elemental Si and either SiO_2 for $Si_{70}(TiN)_{30}$ (Ar) or SiO_xN_y for $Si_{70}(TiN)_{30}$ (N_2).

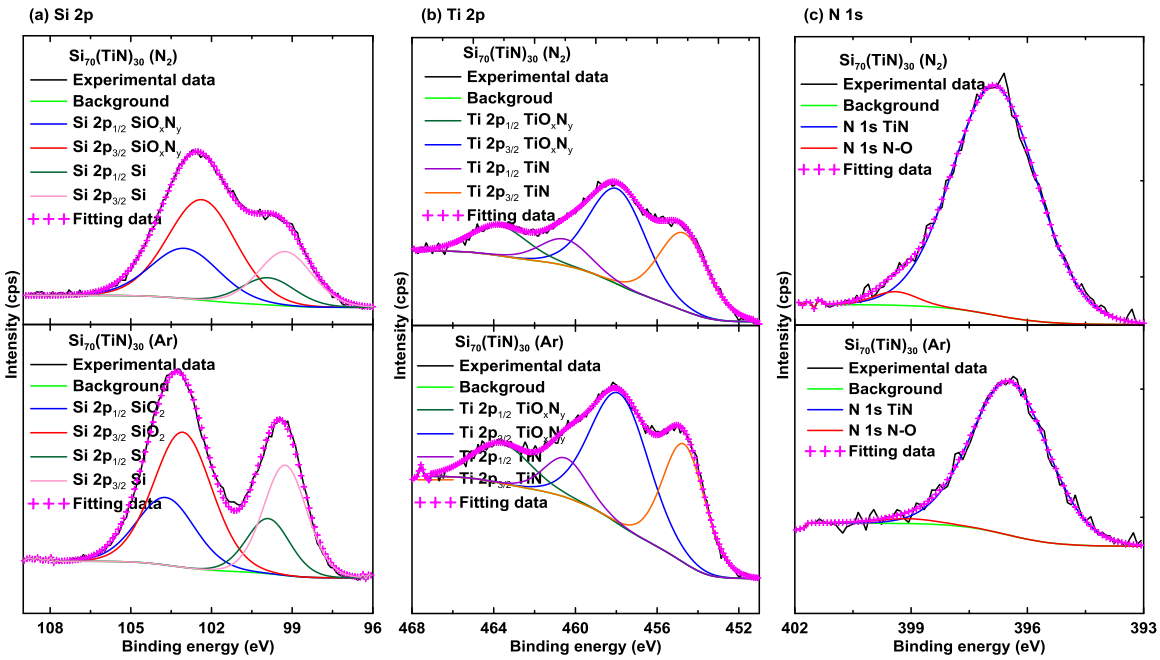

Figure 5.5 XPS spectra of $Si_{70}(TiN)_{30}$ (N_2) and $Si_{70}(TiN)_{30}$ (Ar) alloys: (a) Si 2p spectra, (b) Ti 2p spectra, and (c) N 1s spectra.

Ti 2p XPS spectra and fitting results of $Si_{70}(TiN)_{30}$ (N_2) and $Si_{70}(TiN)_{30}$ (Ar) are shown in Figure 5.5(b). Here each Ti 2p spectrum was fitted with two pairs of Ti $2p_{3/2}$ and Ti $2p_{1/2}$ peaks with a spin-orbit split of 5.8 eV. The four fitting peaks from high to low BE in the $Si_{70}(TiN)_{30}$ (N_2) Ti 2p spectrum are at 463.7 eV, 460.5 eV, 457.9 eV, and 454.7 eV. For $Si_{70}(TiN)_{30}$ (Ar), the corresponding peaks have almost the same BEs, at 463.6 eV, 460.5 eV, 457.8 eV, and 454.7 eV. These peaks can be associated with Ti $2p_{1/2}$ in TiO_xN_y, Ti $2p_{1/2}$

in TiN, Ti $2p_{3/2}$ in TiO_xN_y, and Ti $2p_{3/2}$ in TiN.[170,171] This indicates that Ti has similar chemical states in both samples.

Figure 5.5(c) shows N 1s spectra of the $Si_{70}(TiN)_{30}$ (N_2 and Ar) samples. Both N 1s spectra can be fitted by assuming peaks from two chemical states of N at 399.4 eV and 396.8 eV in the $Si_{70}(TiN)_{30}$ (N_2) N 1s spectrum and at 399.1 eV and 396.5 eV in the counter example N 1s spectrum. For each sample, the main N 1s peak (at 396.8 eV or 396.5 eV) can be attributed to N 1s in TiN,[171,172] while the smaller component at higher BE is presumably produced by N 1s in N-O bonds.[173] To sum up, the XPS results demonstrate that chemical states of the elements in Si-TiN (N_2) are consistent with those in Si-TiN (Ar): Si-TiN (N_2) comprising mostly Si, TiN, SiO_xN_y ; and Si-TiN (Ar) comprising mostly Si, TiN, and SiO_2.

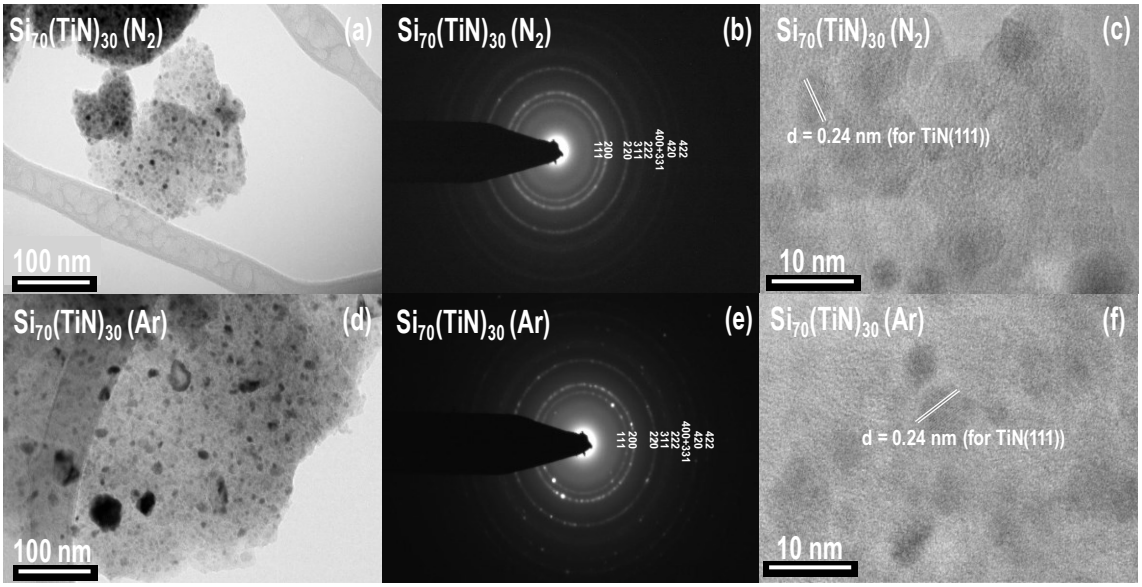

Figure 5.6 TEM images of $Si_{70}(TiN)_{30}$ (N_2) and $Si_{70}(TiN)_{30}$ (Ar): (a and d) BF images, (b and e) SAED patterns, and (c and f) HREM images.

TEM images of the $Si_{70}(TiN)_{30}$ (N_2) and $Si_{70}(TiN)_{30}$ (Ar) samples are shown in Figure 5.6, including BF images (Figure 5.6(a) and (d)), SAED patterns (Figure 5.6(b) and (e)), and HREM images (Figure 5.6(c) and (f)). The BF image shows that $Si_{70}(TiN)_{30}$ (N_2) comprises nanoparticles of about 1~9 nm (average size: 3 nm, based on 50 random particles) in extent that are embedded in an amorphous matrix. The $Si_{70}(TiN)_{30}$ (Ar) sample also comprises amorphous regions but contains larger nanoparticles that range in size from about 1 nm to 40 nm, with most being about 4 nm in extent. In the SAED patterns of the $Si_{70}(TiN)_{30}$ (N_2 and Ar) samples, strong and spotty diffraction rings observed correspond to the lattice spacings of TiN. The SAED patterns also contain diffuse rings corresponding to a-Si. Some very bright spots can be found on the TiN diffraction rings in the $Si_{70}(TiN)_{30}$ (Ar) SAED pattern. This suggests that some large TiN crystals are present in the Si-TiN (Ar) sample, which is consistent with the XRD results. Based on the fine lattice fringes and/or Moire fringes shown in the HREM images, it can be deemed that TiN nanocrystallites (about 5~10 nm) are distributed in a-Si for both samples. In summary, the TEM results show that the $Si_{70}(TiN)_{30}$ (N_2 and Ar) samples are composed of TiN particles/grains dispersed in an a-Si matrix, where the TiN particles/grains are more evenly sized (1~9 nm) for the $Si_{70}(TiN)_{30}$ (N_2) sample compared to the $Si_{70}(TiN)_{30}$ (Ar) sample (1~40 nm).

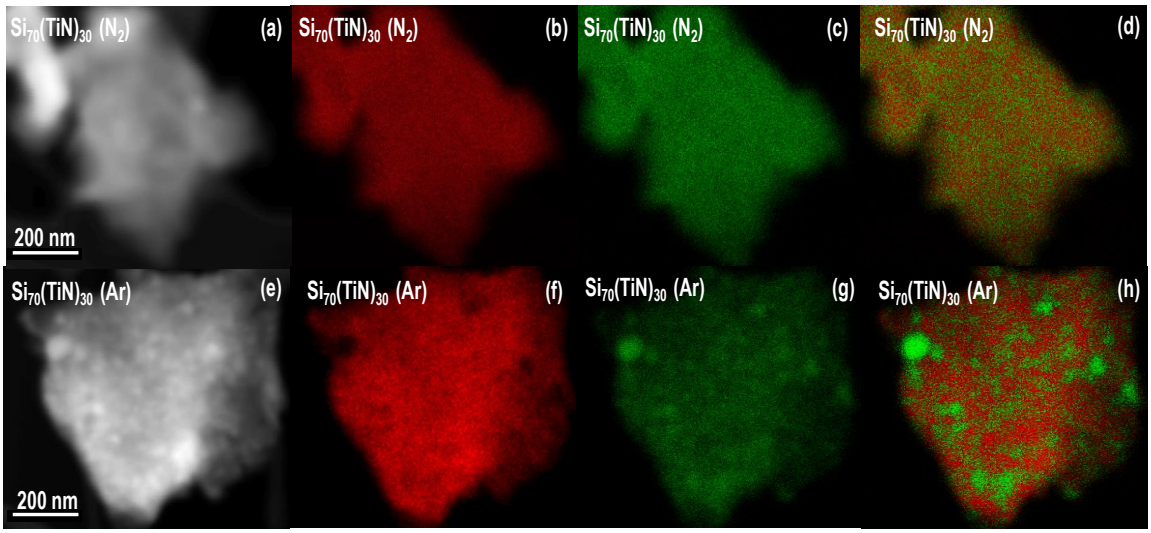

Figure 5.7 STEM images of $Si_{70}(TiN)_{30}$ (N_2) and $Si_{70}(TiN)_{30}$ (Ar): (a and e) STEM images, (b and f) Si maps, (c and g) Ti maps, and (d and h) Si-Ti substitution overlays (Si: red, Ti: green).

Si and Ti distributions in single particles of the $Si_{70}(TiN)_{30}$ (N_2) and $Si_{70}(TiN)_{30}$ (Ar) samples were investigated by X-ray mapping. For each sample, 3~5 particles were used for the analysis, and the results are generally the same. In addition, the Si-Ti atomic ratio of each analyzed particle was about 70:30, as determined by an EDS system coupled with the TEM instrument, in agreement with the target composition. Figure 5.7 shows STEM images (Figure 5.7(a) and (e)), Si maps (Figure 5.7(b) and (f)), Ti maps (Figure 5.7(c) and (g)), and Si-Ti substitution overlays (Figure 5.7(d) and (h)) for the $Si_{70}(TiN)_{30}$ (N_2 and Ar) samples. The substitution overlays show a combination of Si and Ti elements, where only the element with the higher intensity at each pixel is displayed. The Si-Ti distribution in the $Si_{70}(TiN)_{30}$ (N_2) sample is homogeneous within the resolution of the

instrument. In contrast, larger Ti and Si regions can be observed for the $Si_{70}(TiN)_{30}$ (Ar) sample, which are due to larger TiN grains or TiN clusters, as observed by TEM.

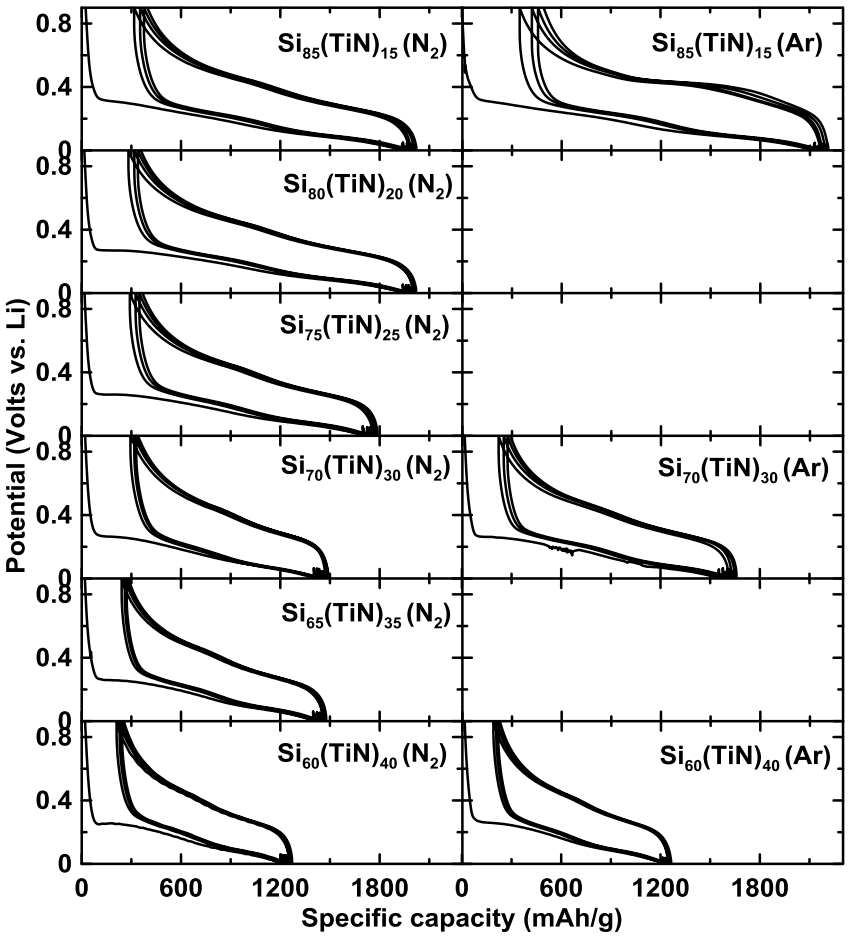

Figure 5.8 Potential-capacity curves of the first four cycles of Si-TiN (N_2 and Ar) electrodes versus lithium metal during 30 °C cell cycling.

Figures 5.8 and 5.9 show potential-capacity curves (for the first four cycles) and their differential capacity (dQ/dV)-potential curves for Si-TiN (N_2 or Ar) versus lithium metal during 30 °C cell cycling. All samples, excepting those with composition $Si_{85}(TiN)_{15}$ have a voltage plateau at about 0.32 V and a corresponding sharp peak in their dQ/dV curves during the first lithiation, which has been ascribed to a nucleation and growth

process for the lithiation of Si.[127] The voltage plateau and the sharp peak shift to lower voltage for the samples with more inactive TiN. This suggests that the nucleation and growth process may be blocked by inactive TiN. For all the Si-TiN alloys, excepting $Si_{85}(TiN)_{15}$ (Ar), a pair of sloping plateaus in the potential curves and a corresponding pair of broad peaks in the dQ/dV curves are characteristic of the lithiation/delithiation of a-Si without cr-$Li_{15}Si_4$ formation.[126] In the case of $Si_{85}(TiN)_{15}$ (Ar), a sharp anodic peak at about 0.45 V in the dQ/dV curve can be observed, corresponding to the delithiation of cr-$Li_{15}Si_4$. Therefore, cr-$Li_{15}Si_4$, which has been associated with fade in Si-based alloys, forms in this sample during cycling.

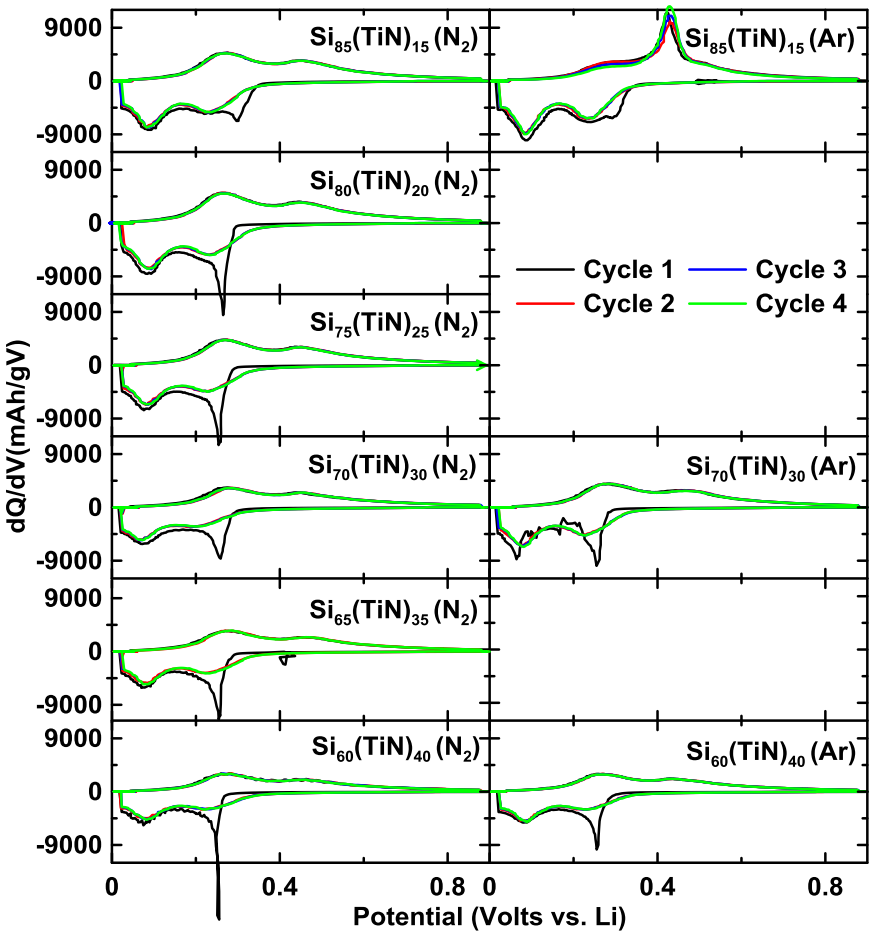

Figure 5.9 Differential capacity curves of the first four cycles of Si-TiN (N_2 and Ar) electrodes versus lithium metal during 30 °C cell cycling.

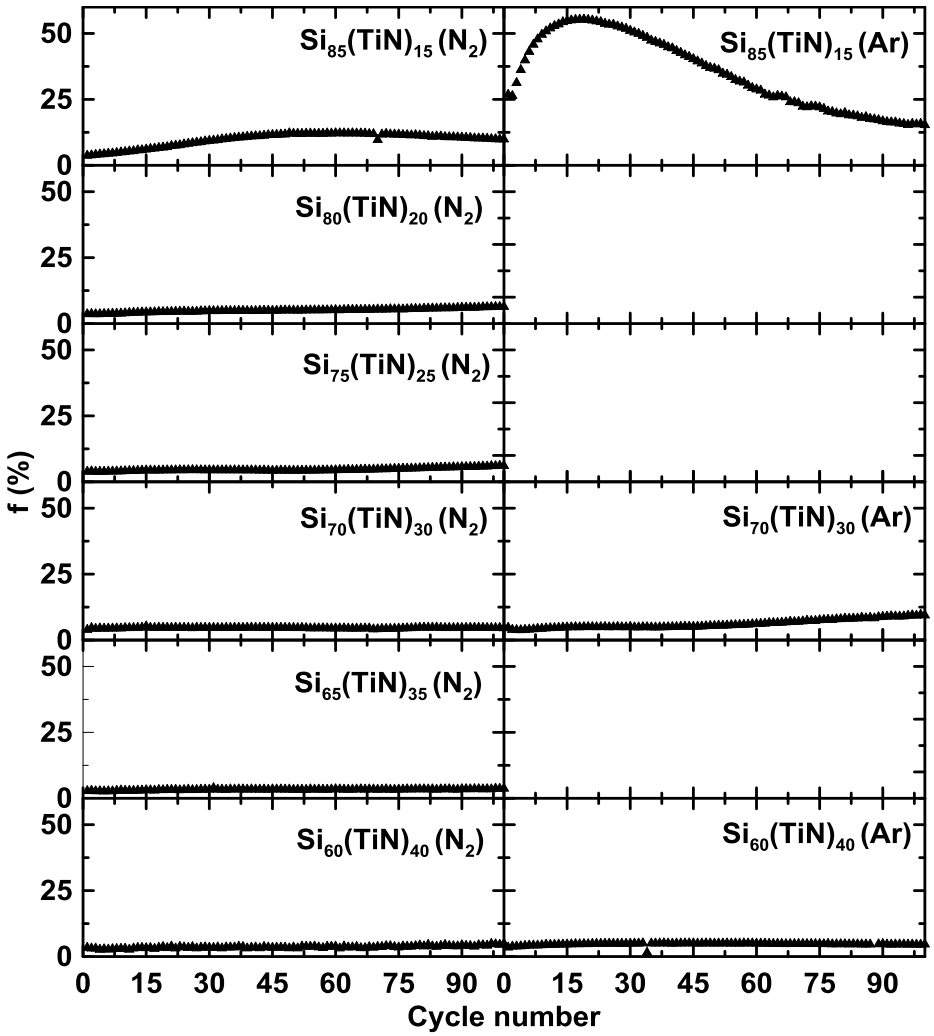

Figure 5.10 Plots of the percent active Si that forms $Li_{15}Si_4$ at full lithiation (*f*) vs. cycle number of Si-TiN (N_2 and Ar) during 30 °C cell cycling.

The amount of $Li_{15}Si_4$ formed during cycling was quantified with the method described in Section 4.3. Figure 5.10 shows the amount of active Si that forms $Li_{15}Si_4$ during cycling plotted as a function of cycle number for all the Si-TiN (N_2 and Ar) cells shown in Figure 5.9. All samples, excepting $Si_{85}(TiN)_{15}$ (Ar), do not form significant amounts of $Li_{15}Si_4$ during cycling. In the case of $Si_{85}(TiN)_{15}$ (Ar), the amount of active Si

that forms $Li_{15}Si_4$ during cycling increases rapidly during cycling, reaching a peak at about 55% after 17 cycles. This indicates that significant structural changes occur in this sample during cycling. For instance, the formation of $Li_{15}Si_4$ during cycling has been associated with the disconnection of Si from a supporting matrix and can indicate internal fracturing of the alloy particle.[17] The decrease in *f* after 17 cycles can be attributed to an increase in impedance in this sample during cycling, as discussed below.

The dQ/dV curves and *f* values for $Si_x(TiN)_{100-x}$ (x = 85, 70, and 60) N_2 and Ar samples were also measured at 45 °C and the results are shown in Figure 5.11(a) and (b) respectively. No $Li_{15}Si_4$ delithiation peaks can be observed in the dQ/dV curves of the Si-TiN (N_2) alloys and the $Si_{60}(TiN)_{40}$ (Ar) sample. Accordingly, these alloys have insignificant $Li_{15}Si_4$ formation during cycling, as shown in Figure 5.11(b). However, the $Si_{85}(TiN)_{15}$ (Ar) and $Si_{70}(TiN)_{30}$ (Ar) samples, form up to 55% and 34% $Li_{15}Si_4$ during cycling. The results suggest that the Si-TiN (N_2) alloys can suppress $Li_{15}Si_4$ formation better than the Si-TiN (Ar) alloys even at 45 °C. This indicates more stable microstructure of the Si-TiN (N_2) negative electrode materials during cycling.

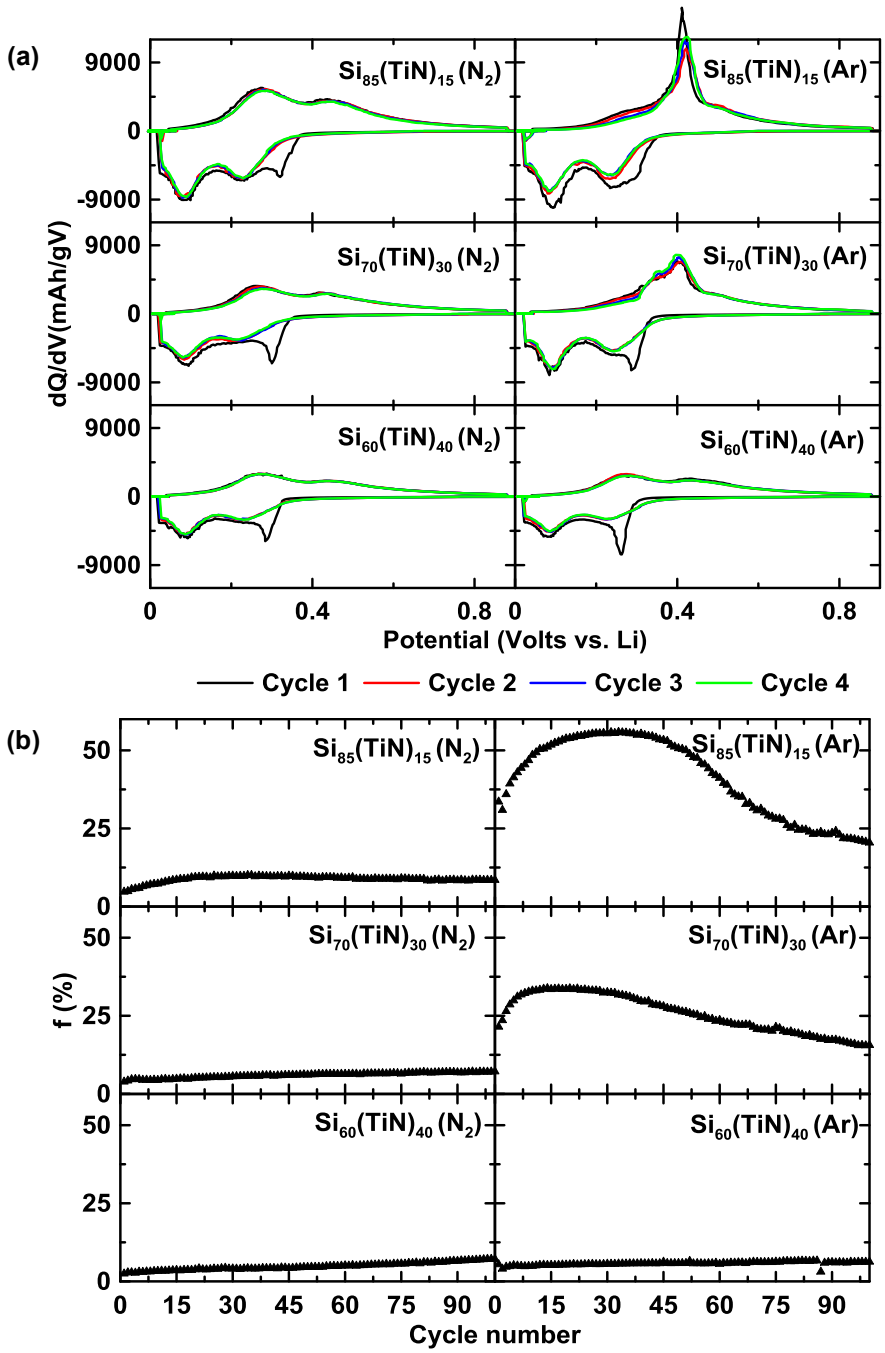

Figure 5.11 (a) Differential capacity curves (the first four cycles shown) and (b) plots of the percent active Si that forms $Li_{15}Si_4$ at full lithiation (*f*) vs. cycle number of $Si_x(TiN)_{100-x}$ (x = 85, 70 and 60, N_2 and Ar) samples during 45 °C cell cycling.

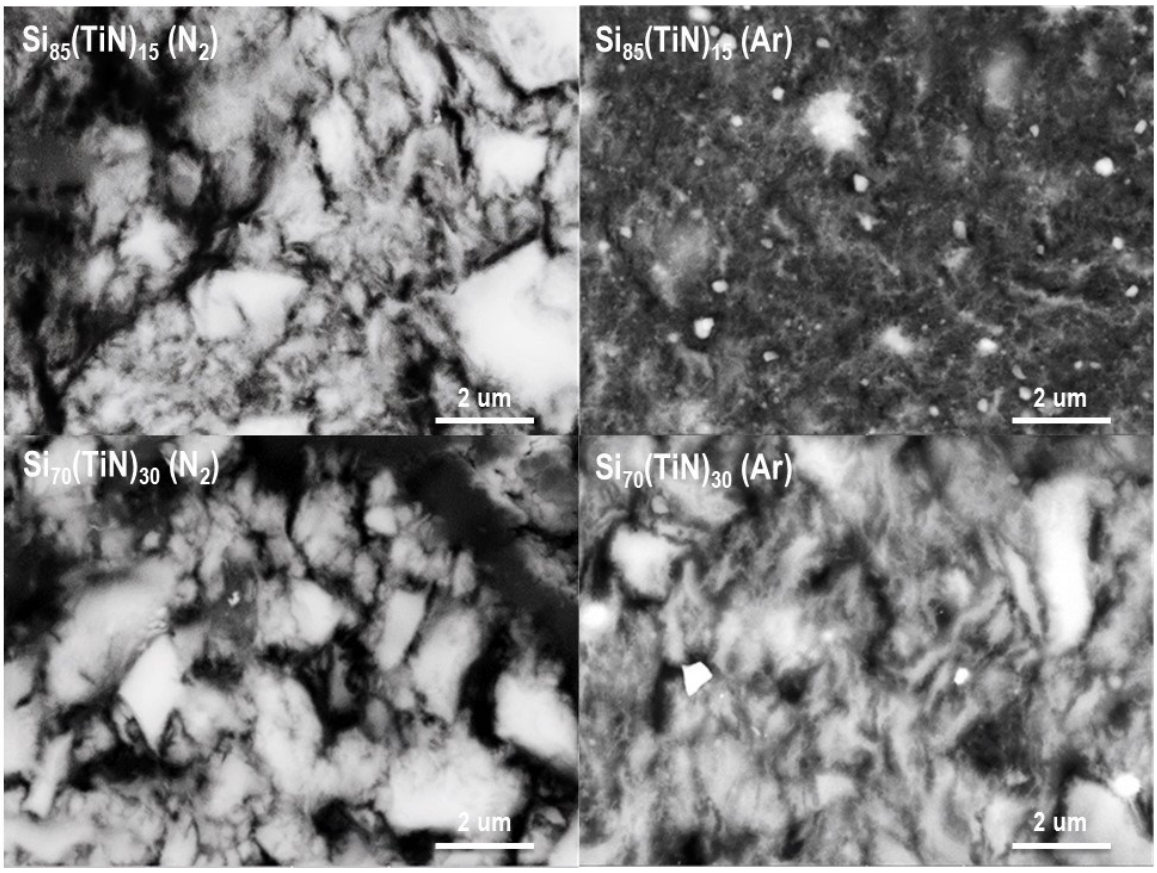

Figure 5.12 BSE images of cross section of selected Si-TiN (N_2 and Ar) electrodes after 50 cycles (30 °C cell cycling).

To confirm if particle fracture is co-incident with the formation of $Li_{15}Si_4$ during cycling of the $Si_x(TiN)_{100-x}$ (Ar) samples, SEM BSE images were taken of cross sections of $Si_{85}(TiN)_{15}$ and $Si_{70}(TiN)_{30}$ (N_2 and Ar) electrodes after 50 cycles (30 °C cell cycling). These images are shown in Figure 5.12. The $Si_{85}(TiN)_{15}$ and $Si_{70}(TiN)_{30}$ (N_2) electrodes, which exhibited no/low $Li_{15}Si_4$ during cycling show relatively minor changes, compared to their pristine state (Figure 5.3). Large particles (> 2 μm) are still apparent with distinct edges. However, smaller alloy particles have become more diffuse, which is evidence of

surface erosion, as has been observed previously for Si-alloys.[19] The resulting surface area increase causes increased electrolyte reactivity and a corresponding build-up of electrolyte decomposition products. This is likely the origin of fade in these electrodes. In contrast, the $Si_{85}(TiN)_{15}$ (Ar) and $Si_{70}(TiN)_{30}$ (Ar) electrodes are much more greatly deteriorated. The surfaces of all the alloy particles comprising the $Si_{70}(TiN)_{30}$ (Ar) electrode, which also had little $Li_{15}Si_4$ formation during cycling, are very indistinct, indicating a high degree of surface erosion and electrolyte decomposition at the surface. We suspect the coarser grain structure of the Si-TiN (Ar) alloys likely results in the enhanced surface erosion effect, as larger reactive Si grains will be exposed at the alloy surface. The $Si_{85}(TiN)_{15}$ (Ar) alloy appears to have completely disintegrated during cycling. This alloy showed significant $Li_{15}Si_4$ during cycling, as shown in Figure 5.10, which is associated with particle fracture. We believe this to be the cause of the severe disintegration of this alloy during cycling.

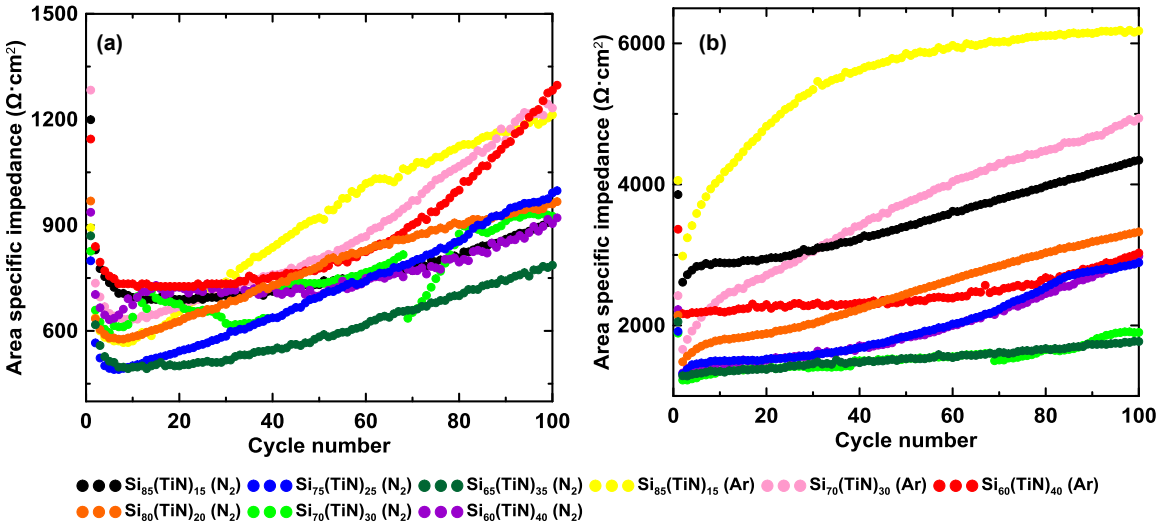

Figure 5.13 (a) Plots of lithiation and (b) delithiation ASI (30 °C cell cycling) vs. cycle number of Si-TiN (N_2 and Ar) alloys.

Figures 5.13(a) and (b) show the ASI of Si-TiN (N_2 and Ar) samples during lithiation and delithiation at 30 °C, respectively. Here only relative changes in ASI during cycling are significant because of variations in electrode loading and surface area. During lithiation, all Si-TiN (N_2 and Ar) samples show a general ASI growth during 100 cycles. This trend may be due to continual SEI formation on the alloy particles, disconnection/fracture of the alloy particles or continually increasing impedance on the Li counter electrode during cycling. However, the Si-TiN (Ar) samples typically have larger ASI growth rates during lithiation and delithiation than their corresponding Si-TiN (N_2) samples. As mentioned above, we believe that the increased ASI growth rate of the Si-TiN (Ar) samples is due to increased surface erosion during cycling caused by their coarser grain structure, resulting in SEI growth and particle disconnection. This would in turn result in a higher effective current density on the remaining connected particles. In the case of $Si_{85}(TiN)_{15}$ (Ar) impedance growth is particularly severe. This is consistent with Figure 5.12, which shows that this electrode has completely disintegrated during cycling, which we believe is correlated with the formation of $Li_{15}Si_4$ phase as discussed above. When $Li_{15}Si_4$ forms it can cause particle fracture, due to volume mismatch of the Li_xSi-$Li_{15}Si_4$ 2-phase region. This would lead to more disconnection of active Si from the lattice, more $Li_{15}Si_4$ formation and more fracture. However, when a cell's impedance becomes very high, $Li_{15}Si_4$ will no longer form, since its equilibrium formation potential (~50 mV) will become shifted below 0 V.[97] This accounts for the decrease in the fraction of $Li_{15}Si_4$ formed for this

cell shown in Figure 5.10. Therefore these results are consistent with the $Si_{85}(TiN)_{15}$ (Ar) sample fracturing during cycling, causing cell fade (as shown below) and the formation of $Li_{15}Si_4$. Continual fracturing during subsequent cycling results in further fade, increasing impedance, which eventually suppresses the $Li_{15}Si_4$ formation.

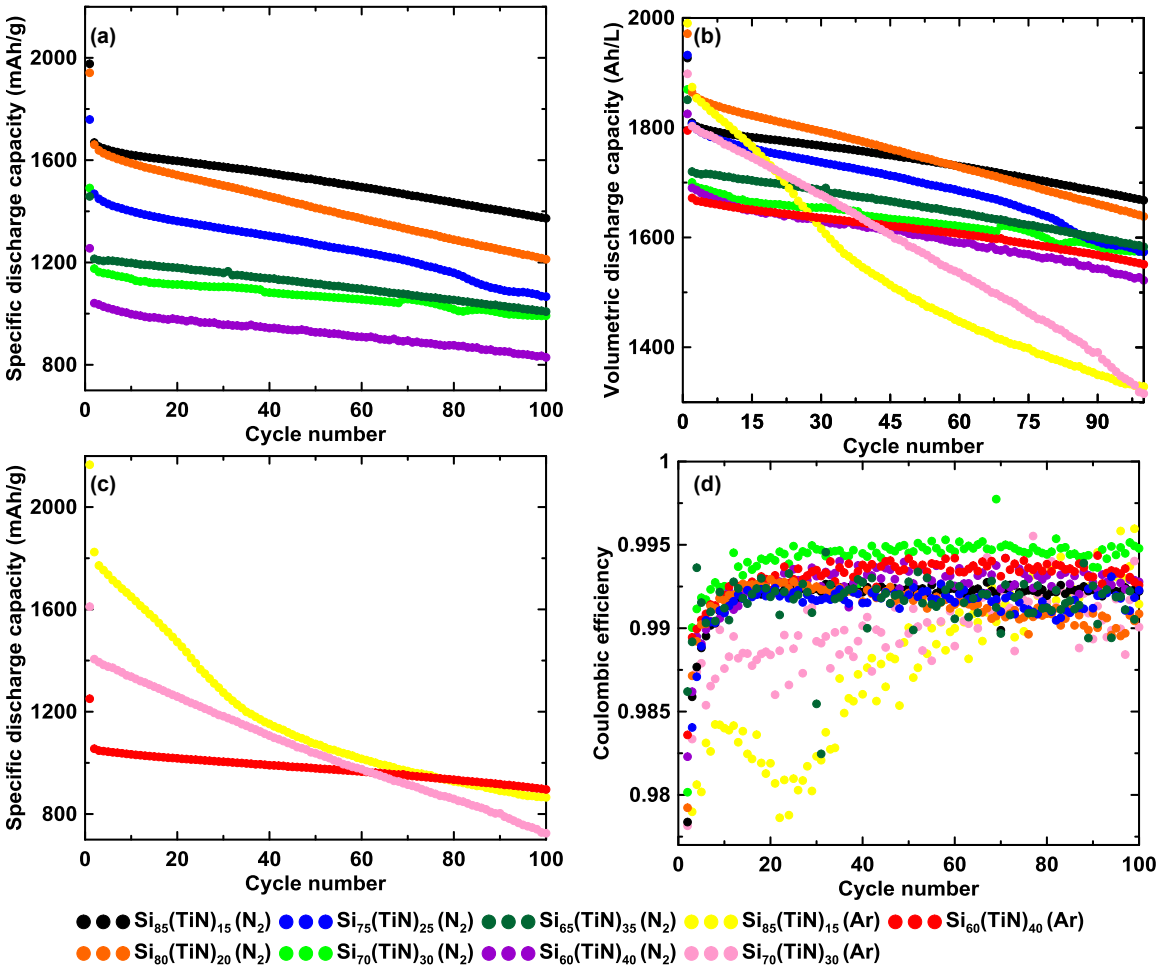

Figure 5.14 The specific discharge capacity vs. cycle number of (a) Si-TiN (N_2) and (b) Si-TiN (Ar) alloys. (c) The volumetric discharge capacity and (d) the coulombic efficiency of Si-TiN (N_2 and Ar) alloys (30 °C cell cycling).

Figure 5.14(a) and (b) show the specific discharge capacity – cycle number curves of Si-TiN (N_2 and Ar) alloys, respectively. All of the Si-TiN (N_2) samples have similar cycling performance, with generally increasing capacities with Si content. In contrast, for the Si-TiN (Ar) samples, only the lowest capacity $Si_{60}(TiN)_{40}$ (Ar) sample has comparable capacity retention to the Si-TiN (N_2) samples. The other Si-TiN (Ar) samples with higher Si contents suffer from rapid capacity fade. Both of these samples show evidence of $Li_{15}Si_4$ formation during 30°C or 45°C cycling. The fade is especially large for the $Si_{85}(TiN)_{15}$ (Ar) sample, which suffered from severe $Li_{15}Si_4$ formation and a rapid rise in impedance during cycling, characteristic of particle/composite degradation. These effects are again ascribed to the larger grain sizes and less homogeneous particle morphologies of the Si-TiN (Ar) samples. The volumetric discharge capacities of all the Si-TiN alloys are shown in Figure 5.14(c). The reversible capacities of these alloys are all over double that of graphite and are in the range of about 1650 Ah/L to 1900 Ah/L. The coulombic efficiencies of the cells are shown in Figure 5.14(d). All alloys have coulombic efficiencies greater than 99%, excepting the high Si content Si-TiN (Ar) samples, which suffered from poor cycling characteristics, as discussed above.

Based on the results of SEM EDS, LECO tests, XRD, and XPS, it can be deemed that phase compositions of the Si-TiN (N_2) samples are comparable with those of the Si-TiN (Ar) samples. However, the Si-TiN (N_2 and Ar) samples exhibit different performance in Li cells, with the Si-TiN (Ar) samples generally having inferior electrode structural

stability, more capacity fade, $Li_{15}Si_4$ formation during cycling and higher impedance growth rate, especially for the alloys with high Si content. This degradation in cell performance most likely results from their different microstructures. According to the TEM and STEM results, the Si-TiN (N_2 and Ar) samples may be represented schematically as shown in Figure 5.15. Figure 5.15(a) represents a Si-TiN (N_2) particle, in which 5-10 nm inactive TiN grains are homogenously distributed in an a-Si matrix. Figure 5.15(b) represents a Si-TiN (Ar) particle, in which, TiN grains with a non-uniform size ranging from 10-50 nm are distributed in a-Si. In this sample some large TiN grains and clusters of small TiN grains are present. Such Si-TiN (Ar) particles have a lower TiN/a-Si contact area. Therefore, during lithiation the expansion of Si can impart a larger areal stress on the Si/TiN interface, compared to the Si-TiN (N_2) particles. This may result in the fracturing of the Si/TiN interface, with the unbound Si, no longer under constraint, now able to form $Li_{15}Si_4$ during lithiation.[17] Furthermore, the Si-TiN (Ar) particles have larger Si and TiN regions. As a result, particle cracking and pulverization may be induced by non-uniform volume changes within a particle. This can lead to electric disconnection among active Si grains during cycling, which may contribute to ASI growth and capacity fade. Finally, active Si on the alloy particle surfaces can react with electrolyte, resulting in surface erosion, increased surface area, and correspondingly increased SEI formation. This is true of all of the alloys here; however, it is most severe for the Si-TiN (Ar) alloys, which have coarser grain structure and therefore larger active Si grains exposed at the alloy surfaces.

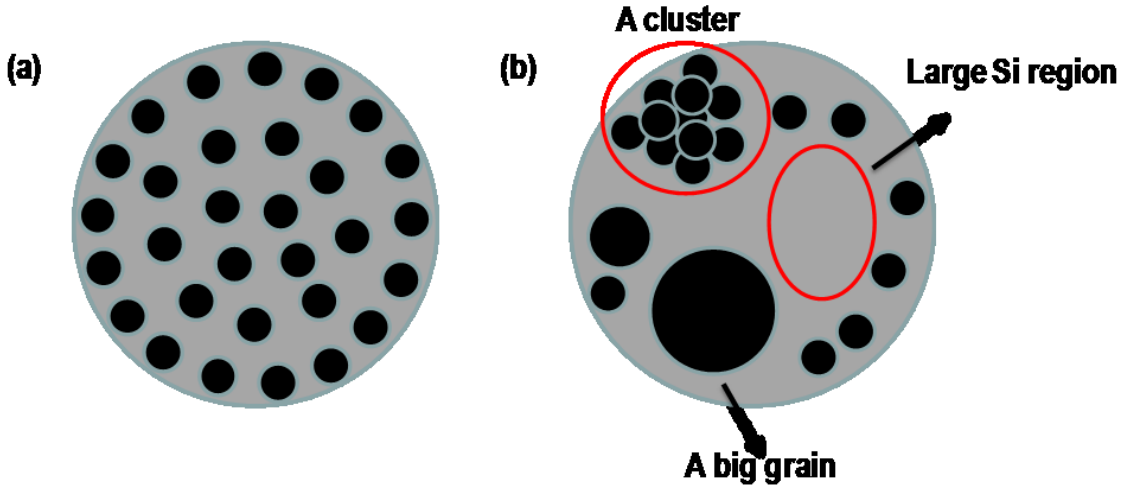

Figure 5.15 Schematic drawings of the (a) Si-TiN (N_2) and (b) Si-TiN (Ar) microstructures. (grey: Si, and black: inactive TiN).

Regardless of the mechanism, it is apparent that the Si-TiN (N_2) alloys have a highly homogeneous nanostructure that results in superior electrochemical performance in Li cells compared to conventionally made Si-TiN (Ar) alloys. In addition, N_2 reactive gas milling may be a less expensive milling method that introduces less contamination during ball milling.

5.4 Conclusions

In this study, Si-TiN negative electrode materials prepared by reactive gas milling of Si and Ti powders in N_2 (g) and by a conventional method (Si and TiN ball milled directly in an inert gas) were studied. In comparison with the conventional method, the reactive N_2 gas milling method is a significantly less costly synthesis route, since no TiN precursor is

needed. The reactive N_2 gas milling method also introduced less iron contamination, since no abrasive TiN precursor was present during milling. Through SEM EDS, LECO, XRD, and XPS characterization, it was found that the Si-TiN alloys prepared by reactive gas milling and conventional milling all had similar phase compositions. However, the microstructures of the alloys differed significantly, depending on the milling method. The Si-TiN (N_2) sample particles comprise 5-10 nm inactive TiN grains homogenously distributed in an a-Si matrix. In contrast, the Si-TiN (Ar) sample particles comprise TiN grains with non-uniform sizes ranging from 10-50 nm that are less homogeneously distributed in an a-Si matrix. The Si-TiN (N_2) alloys had better cycling performance in Li cells and showed no evidence of $Li_{15}Si_4$ formation during cycling. The Si-TiN (Ar) samples with high Si content had severe capacity fade, increasing ASI, and significant $Li_{15}Si_4$ formation during cycling. The improved cycling performance of the Si-TiN (N_2) alloys was attributed to their homogeneous nanostructure. These alloys have high volumetric capacities in the range of 1650 Ah/L to 1900 Ah/L and are also attractive from a manufacturing standpoint. Further improvements to the Si-TiN (N_2) alloys (e.g. by carbon coating to reduce surface erosion) are needed to increase their cycle life (e.g. to 80% retention at ~1000 cycles) to make them attractive for use in consumer electronics.

Chapter 6 Thermal Stability Study of Si-TiN Alloys Prepared by Reactive N_2 Gas Milling

6.1 Introduction

As described in Chapter 5, Si-TiN alloys prepared by reactive N_2 gas milling have finer grain structure and better cell performance compared to Si-TiN alloys synthesized by conventional inert gas milling. In this chapter, thermal stability of Si-TiN alloys synthesized under N_2 gas milling was studied. High temperature tolerance is a precondition for further improving cycle life by high temperature carbon coating as mentioned in Section 4.1. These Si-TiN alloys were expected to have high thermal stability, due to their fine microstructure and high melting point of TiN (~3300 °C).[174] Electrochemical investigation was performed for Si-TiN samples before and after heat treatment and carbon coating. Si-TiN alloys prepared by conventional Ar milling were used as reference samples, and their thermal stability was also studied in this chapter.

6.2 Experimental

$Si_x(TiN)_{100-x}$ (x = 85, 70, 60) alloys were prepared by N_2 gas milling and Ar milling. The sample synthetization was as described in Section 5.2. These Si-TiN samples were heated at 800 °C for 3 h using the heat treatment method shown in Section 3.1. Here the Si-TiN alloys synthesized by N_2 and Ar milling after heat treatment are referred to as Si-TiN (N_2, 800 °C) and Si-TiN (Ar, 800 °C), respectively. Carbon coating was performed by

mixing the alloy powder with a phenolic resin (3M RPR1, resole phenol-formaldehyde resin, having phenol to formaldehyde ratio of 1.5–2.1/1, catalyzed with 2.5 percent potassium hydroxide, ~75% solution in water, 3M Co.)/N-Methyl-2-pyrrolidone (NMP, Sigma-Aldrich, anhydrous 99.5%) solution, so that the alloy-phenolic resin mass ratio was 1:0.45. The suspension was mixed using planetary mill (Retsch PM200) with 3 tungsten carbide balls (d = 12.7 mm) at 100 rpm for 30 min and was dried at 120 °C in air overnight. Then, the sample was collected and heated at 800 °C for 1 h. Other heating conditions can be found in Section 3.1.

X-ray diffraction (XRD, Rigaku Ultima IV diffractometer) and transmission electron microscopy (TEM, Philips CM30) were used for sample characterization. In addition, energy dispersive spectroscopy (EDS) X-ray elemental mappings were collected using scanning TEM (STEM) mode. The median filtered element maps were used in this study. The XRD, TEM, and elemental X-ray mapping details are as described in Section 5.2. Electrode cross sections were characterized using a Schottky field emission scanning electron microscope (SEM, TESCAN MIRA 3 LMU), which was operated at an accelerating voltage of 20 kV. For the selected Si-TiN (N_2) sample for carbon coating, the sample morphology before and after carbon coating was also characterized by SEM, which was operated at 5 kV. True sample densities and specific surface areas were measured with a helium pycnometer (AccuPyc II 1340, Micrometrics) and a surface area analyzer (Micromeritics FlowSorb II 2300), respectively.

Electrode preparation and half cell assembly were as described in Sections 3.8.1 and 3.8.2, respectively. The half cells were cycled using a battery testing system (Neware) at 30 ± 0.1 °C or 45 ± 0.2 °C between 0.005 V and 0.9 V. The details of the cell cycling procedure can be found in Section 5.2.

6.3 Results and Discussion

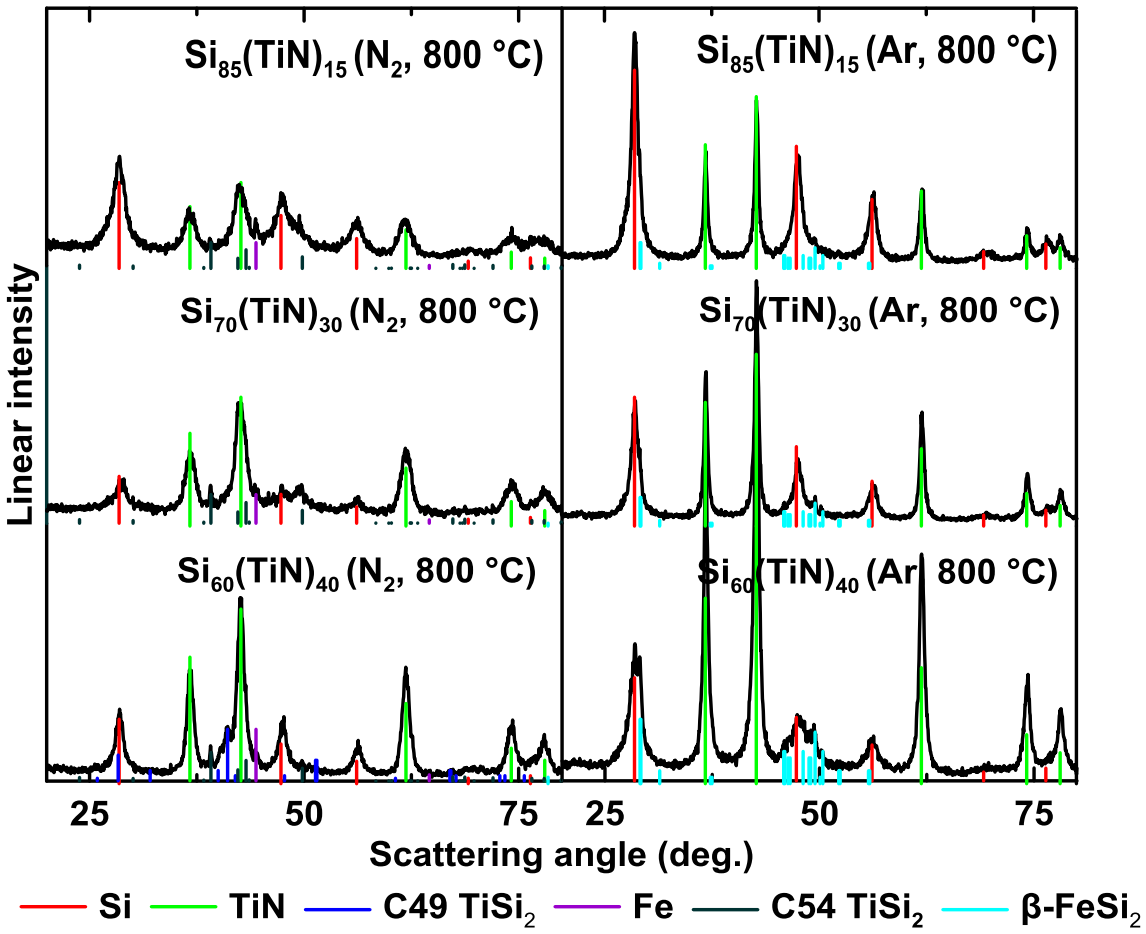

Figure 6.1 XRD patterns of $Si_x(TiN)_{100-x}$ (x = 85, 70, 60, N_2 and Ar, 800 °C) alloys.

Figure 6.1 displays XRD patterns of $Si_x(TiN)_{100-x}$ (x = 85, 70, and 60, N_2 and Ar, 800 °C) alloys, which show that these alloys mainly consist of nanocrystalline Si and TiN phases. As mentioned in Chapter 5, the Si-TiN (N_2 and Ar) samples before heat treatment are typically made of amorphous Si (a-Si) and nanocrystalline TiN phases (TiN Scherrer grain sizes: 5 nm for Si-TiN (N_2) and 7-10 nm for Si-TiN (Ar)). Si and TiN grain sizes of Si-TiN (N_2 and Ar, 800 °C) were also estimated by the Scherrer equation (Equation 3.2). The results indicate that the Si-TiN (N_2, 800 °C) alloys have Si grains of 6-8 nm and TiN grains of 6-9 nm, while Si and TiN grain sizes of the Si-TiN (Ar, 800 °C) samples are larger, which are typically 7-10 nm and 15-17 nm, respectively. It can be found that a-Si converted into crystalline Si (cr-Si), and the TiN grain sizes grew during heating the Si-TiN (N_2 and Ar) samples at 800 °C. However, the Si-TiN (N_2, 800 °C) alloys show less crystallization of Si and TiN compared to the Si-TiN (Ar, 800 °C) alloys, which is probably due to the finer microstructure of Si-TiN (N_2) before heat treatment as described in Chapter 5. Among these three Si-TiN (N_2, 800 °C) alloys shown in Figure 6.1, $Si_{70}(TiN)_{30}$ (N_2, 800 °C) has the smallest and broadest Si XRD peaks, indicating that this sample has the highest temperature tolerance. In addition, some other tiny peaks can be observed in Figure 6.1. Small impurity peaks at about 41.1° and 42.0° present in the XRD pattern of $Si_{60}(TiN)_{40}$ (N_2, 800 °C) probably correspond to the (131) and (150) reflections of C49-$TiSi_2$, respectively. C49-$TiSi_2$ (metastable phase of $TiSi_2$ at room temperature) is an intermediate product during ball milling Si and Ti powders in N_2 (g), as described in Chapter 5. A small

amount of C49-$TiSi_2$ was found to be present in the $Si_x(TiN)_{100-x}$ (x = 85, 70, and 60, N_2) samples before heat treatment, also as described in Chapter 5. In addition, tiny peaks at about 39.1° and 49.8° can be observed in the XRD patterns of $Si_x(TiN)_{100-x}$ (x = 85, 70, and 60, N_2, 800 °C), which are identified to be from the (311) and (331) reflections of C54-$TiSi_2$ (thermodynamically stable phase of $TiSi_2$ at room temperature). Since C54-$TiSi_2$ was not observed in the Si-TiN (N_2) samples before heat treatment, it is likely that C49-$TiSi_2$ converted into C54-$TiSi_2$ during heat treatment at 800 °C, which is consistent with the Si-Ti phase diagram. Fe and β-$FeSi_2$ may also be present in the Si-TiN (N_2, 800 °C) and Si-TiN (Ar, 800 °C) alloys, respectively, as shown in Figure 6.1. Fe impurities are likely to be introduced from the steel balls and steel milling vials used for sample preparation as discussed in Chapter 5.

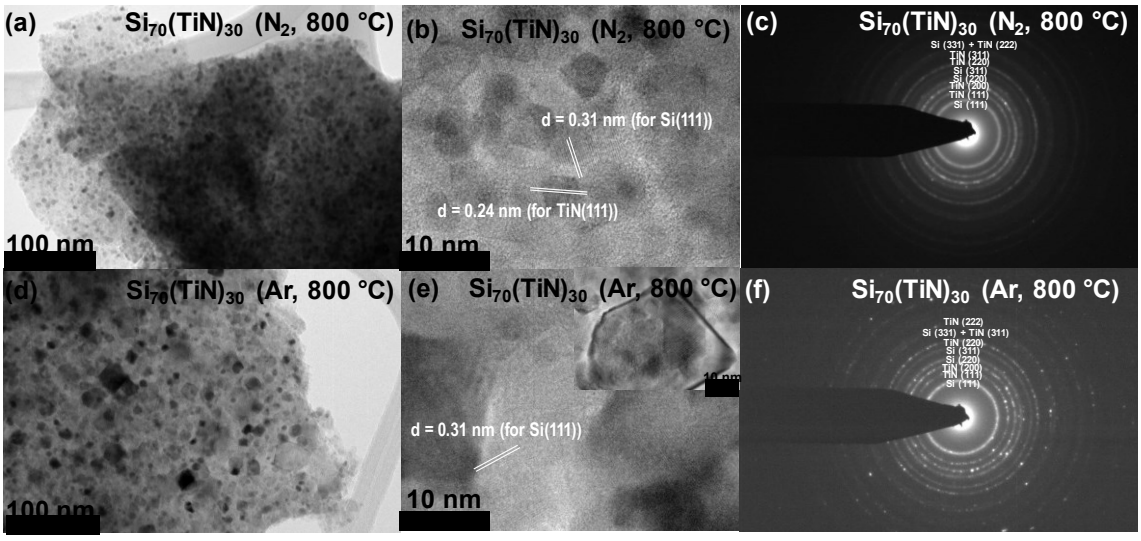

Figure 6.2 TEM images of $Si_{70}(TiN)_{30}$ (N_2 and Ar, 800 °C): (a and d) BF images, (b and e) HREM images, and (c and f) SAED patterns.

TEM images of the $Si_{70}(TiN)_{30}$ (N_2 and Ar, 800 °C) samples are shown in Figure 6.2, including bright field (BF) images (Figures 6.2(a) and (d)), high resolution electron microscopy (HREM) images (Figures 6.2(b) and (e)), and selected area electron diffraction (SAED) patterns (Figures 6.2(c) and (f)). Figure 6.2(a) indicates that TiN nanoparticles (the size range is 1~11 nm and the average size is 4 nm based on 50 random particles) are homogeneously distributed in the $Si_{70}(TiN)_{30}$ (N_2, 800 °C) alloy. In Figure 6.2(b), the small grains (~10 nm) with a rectangular profile and very fine fringes are most likely to be TiN grains, while the irregular grains (~10 nm) with wider fringes are cr-Si grains. Regions with mottled contrast are a-Si regions. In addition, strong diffraction rings shown in Figure 6.2(c) (crystalline Si and TiN) are present in the $Si_{70}(TiN)_{30}$ (N_2, 800 °C) sample, indicating polycrystallinity. Weak diffuse intensity rings can also be seen, which is associated with a-Si. Based on Figures 6.2(a-c), the grain structure of the $Si_{70}(TiN)_{30}$ (N_2, 800 °C) sample consists of TiN particles/grains (1~11 nm) uniformly embedded in a polycrystalline Si (~10 nm) / a-Si matrix. In contrast to the $Si_{70}(TiN)_{30}$ (N_2, 800 °C) alloy, the $Si_{70}(TiN)_{30}$ (Ar, 800 °C) alloy comprises Si and TiN nanocrystals having larger and more uneven grain/particles sizes. The Si grain size of $Si_{70}(TiN)_{30}$ (Ar, 800 °C) is about 10~20 nm, as evidenced by the lattice fringes throughout matrix shown in Figure 6.2(e). Figure 6.2(d) and the insert of Figure 6.2(e) show that TiN particles/grains in the $Si_{70}(TiN)_{30}$ (Ar, 800 °C) sample are typically faceted with particle/grain sizes ranging from 1~76 nm (average size: 7 nm, based on 50 random particles). Continuous Si diffraction rings and spotty TiN

diffraction rings observed in the SAED pattern of $Si_{70}(TiN)_{30}$ (Ar, 800 °C) (Figure 6.2(f)) also suggest polycrystalline Si and large TiN grains are present in this sample. As described in Chapter 5, before heat treatment, the $Si_{70}(TiN)_{30}$ (Ar) alloy has a coarse grain structure (about 1~37 nm TiN grains/particles are inhomogeneously distributed in a-Si), while the $Si_{70}(TiN)_{30}$ (N_2) alloy has a uniform distribution of a-Si and TiN crystallites (1~9 nm). The $Si_{70}(TiN)_{30}$ (Ar) alloy shows a much coarser grain structure after heat treatment. In contrast, the $Si_{70}(TiN)_{30}$ (N_2) alloy generally keeps its fine grain structure during heat treatment at 800 °C, although the Si and TiN grain sizes increase slightly.

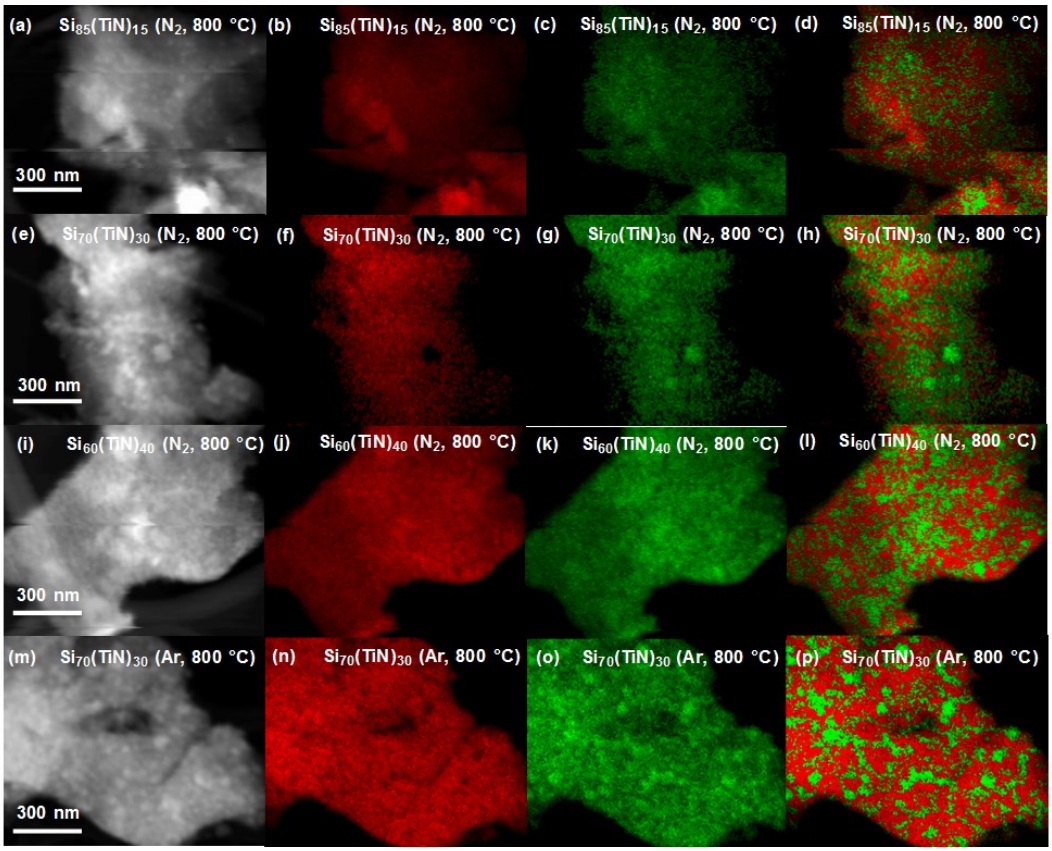

Figure 6.3 (a, e, i, and m) STEM images, (b, f, j, and n) Si maps, (c, g, k, and o) Ti maps, and (d, h, l, and p) Si-Ti substitution overlays (Si: red, Ti: green) of $Si_x(TiN)_{100-x}$ (x = 85, 70, 60, N_2, 800 °C) and $Si_{70}(TiN)_{30}$ (Ar, 800 °C)

Si and Ti distributions in single particles of $Si_x(TiN)_{100-x}$ (x = 85, 70, and 60, N_2, 800 °C) and $Si_{70}(TiN)_{30}$ (Ar, 800 °C) were studied by elemental X-ray mapping. Several particles of each alloy were used for this characterization, and the results were generally the same. In addition, the Si-Ti atomic ratio of each analyzed particle was in agreement with the target composition, as determined by an EDS system coupled with the TEM instrument. Figure 6.3 shows STEM images (Figures 6.3(a), (e), (i), and (m)), Si maps (Figures 6.3(b), (f), (j), and (n)), Ti maps (Figures 6.3(c), (g), (k), and (o)), and Si-Ti substitution overlays (Figures 6.3(d), (h), (l), and (p)) for Si-TiN (N_2 and Ar, 800 °C) samples, as indicated. A substitution overlay shows a combination of Si and Ti elements, where only the element with the higher intensity at each pixel is displayed. As shown in Figure 6.3, the Si-TiN (N_2, 800 °C) samples generally show uniform Si-Ti distribution within the instrument resolution. However, Si rich regions are larger in $Si_{85}(TiN)_{15}$ (N_2, 800 °C) and $Si_{60}(TiN)_{40}$ (N_2, 800 °C) compared to those in $Si_{70}(TiN)_{30}$ (N_2, 800 °C), based on Figures 6.3(d), (h), and (l). This is a well-understood phenomenon for $Si_{85}(TiN)_{15}$ (N_2, 800 °C), since it has the highest Si content among these three Si-TiN (N_2, 800 °C) samples. For the $Si_{60}(TiN)_{40}$ (N_2, 800 °C) alloy with the highest Ti content among these three samples, the Si-Ti mixing during ball milling may be hindered by a large amount of ductile Ti, contributing to large Si rich regions present in this sample. It can be believed that an appropriate initial Ti content (neither too low nor too high) could contribute to obtaining a homogenous Si-Ti distribution for Si-TiN (N_2) alloys. Compared to $Si_{85}(TiN)_{15}$ (N_2, 800 °C)

and $Si_{60}(TiN)_{40}$ (N_2, 800 °C), $Si_{70}(TiN)_{30}$ (N_2, 800 °C) has smaller Si rich regions and lower Si crystallization (as shown in Figure 6.1), which is probably because this sample has more appropriate initial Ti content. In comparison, the relative distributions of Si, Ti, and Si-Ti in $Si_{70}(TiN)_{30}$ (Ar, 800 °C) are much more inhomogeneous, as illustrated in Figure 6.3.

Figures 6.4(a) and (b) show potential-capacity curves of the first four cycles of Si-TiN (N_2 and Ar, 800 °C) half cells during 30 °C cell cycling and the corresponding differential capacity (dQ/dV)-potential curves. During the first lithiation, a sharp peak at about 0.13 V in the dQ/dV curves can be observed for most of the Si-TiN (N_2 and Ar, 800 °C) samples, which is characteristic of cr-Si lithiation.[126] During the following lithiation, a pair of sloping plateaus in the potential curves and a corresponding pair of broad peaks in the dQ/dV curves are present for all these Si-TiN (N_2 and Ar, 800 °C) alloys shown in Figure 6.4, which are characteristic of a-Si lithiation.[126] This is consistent with the lithiation and delithiation behavior of cr-Si. In addition, excepting $Si_{70}(TiN)_{30}$ (N_2, 800 °C), all the Si-TiN (N_2 and Ar, 800 °C) samples studied here display a sharp anodic peak at about 0.45V in their dQ/dV curves, suggesting that crystalline $Li_{15}Si_4$ (cr-$Li_{15}Si_4$) formed after full lithiation for these Si-TiN (N_2 and Ar, 800 °C) samples.[2] cr-$Li_{15}Si_4$ is regarded as being detrimental for Si-based negative electrode materials as mentioned in Section 2.3.5.2. Based on Figure 6.4, only $Si_{70}(TiN)_{30}$ (N_2, 800 °C) shows almost no cr-$Li_{15}Si_4$ formation during cycling.

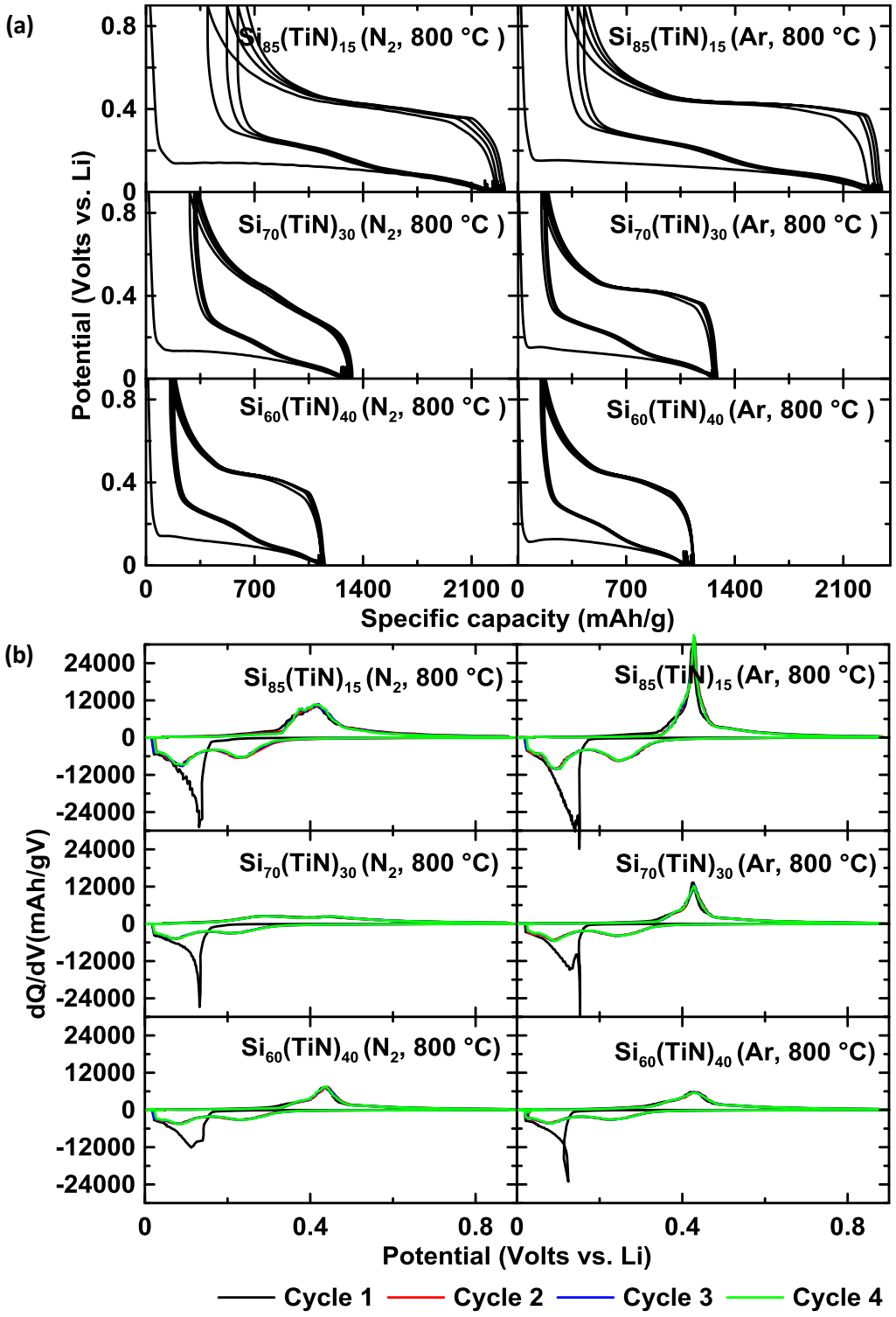

Figure 6.4 (a) Potential-capacity curves of the first four cycles of Si-TiN (N_2 and Ar, 800 °C) vs. lithium metal at 30 °C, and (b) their corresponding dQ/dV-potential curves.

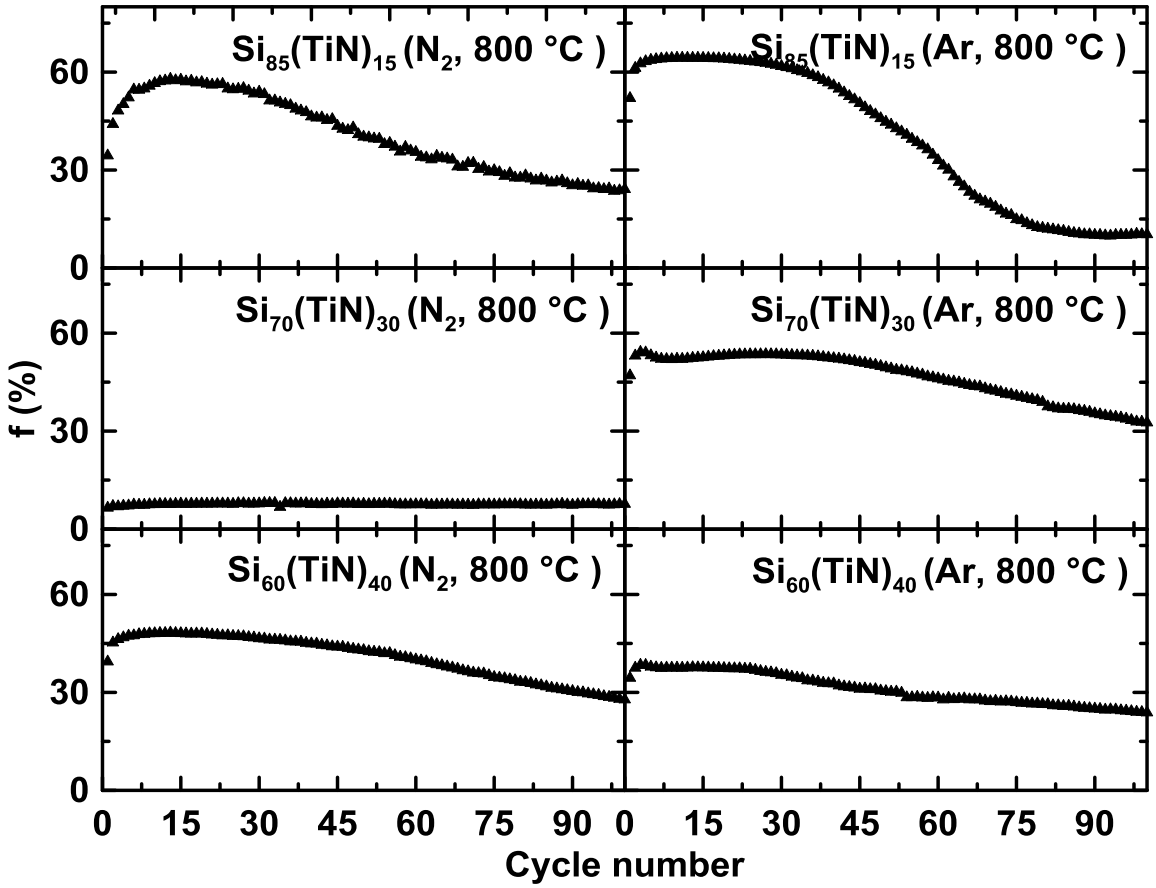

Figure 6.5 Plots of the percent active Si that forms $Li_{15}Si_4$ at full lithiation (*f*) vs. cycle number of Si-TiN (N_2 and Ar, 800 °C).

The formation of cr-$Li_{15}Si_4$ during cycling for the $Si_x(TiN)_{100-x}$ (x = 85, 70, and 60, N_2 and Ar, 800 °C) alloys was quantitively analyzed, as described in Section 4.3. The percent active Si that forms $Li_{15}Si_4$ at full lithiation (*f*) for the Si-TiN (N_2 and Ar, 800 °C) samples is illustrated in Figure 6.5. Excepting $Si_{70}(TiN)_{30}$ (N_2 and Ar, 800 °C), all the Si-TiN (N_2 and Ar, 800 °C) samples shown in Figure 6.5 show significant cr-$Li_{15}Si_4$ formation during cycling, suggesting significant structural changes may occur in these samples. For these Si-TiN (N_2 and Ar, 800 °C) samples with cr-$Li_{15}Si_4$ formation during cycling, the cr-

$Li_{15}Si_4$ formation fraction generally grows with cycle number to reach the maximum value, and then drops with longer cycling. As explained in Section 5.3, cr-$Li_{15}Si_4$ formation could result in Si-based particle fracture and disconnection of active Si from inactive phases, which can contribute to more cr-$Li_{15}Si_4$ formation and more fracture. At the same time, more active particle fracture may lead to a continuous increase in cell impedance during cycling. When cell impedance reaches a certain high value, the high impedance causes the equilibrium potential (~50 mV) of cr-$Li_{15}Si_4$ formation to shift negatively.[175] In this way, cr-$Li_{15}Si_4$ formation can be suppressed when the equilibrium potential shifts below 0 V. As shown in Figure 6.5, only $Si_{70}(TiN)_{30}$ (N_2, 800 °C) shows low and stable *f* values of about 7% during 100 cycles, implying that this sample may have good structural stability during cycling. $Si_{70}(TiN)_{30}$ (N_2, 800 °C) has the best cr-$Li_{15}Si_4$ suppression among these samples shown in Figure 6.5, which is presumably because this sample has the finest microstructure as illustrated in Figure 6.3.

The $Si_{70}(TiN)_{30}$ (N_2 and Ar, 800 °C) alloys were selected for 45 °C cell cycling. Figures 6.6(a) and (b) show dQ/dV curves of the first four cycles and cr-$Li_{15}Si_4$ formation fraction during cycling for these two samples vs. lithium metal at 45 °C, respectively. The $Si_{70}(TiN)_{30}$ (N_2, 800 °C) alloy has cr-$Li_{15}Si_4$ formation of about 5%-13% during 50 cycles. In the contrary, the $Si_{70}(TiN)_{30}$ (Ar, 800 °C) alloy forms up to 50% cr-$Li_{15}Si_4$ during cycling. The results indicate that $Si_{70}(TiN)_{30}$ (N_2, 800 °C) has good cr-$Li_{15}Si_4$ suppression and high structural stability during 45 °C cell cycling.

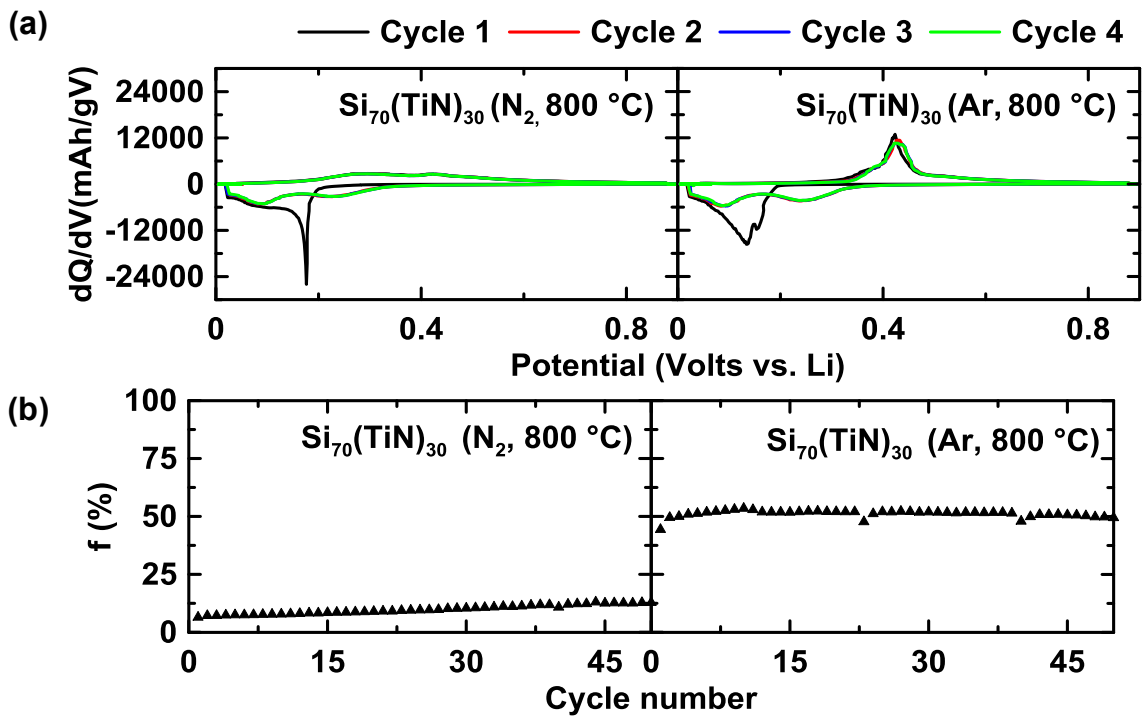

Figure 6.6 (a) Differential capacity curves (for the first four cycles) and (b) plots of the percent active Si that forms $Li_{15}Si_4$ at full lithiation (*f*) vs. cycle number of $Si_{70}(TiN)_{30}$ (N_2 and Ar, 800 °C) vs. lithium metal at 45 °C.

Figures 6.7(a-d) display SEM backscattered electron (BSE) images of cross sections of the fresh $Si_{70}(TiN)_{30}$ (N_2, 800 °C) electrode, the $Si_{70}(TiN)_{30}$ (N_2, 800 °C) electrode after 50 cycles at 30°C, the fresh $Si_{70}(TiN)_{30}$ (Ar, 800 °C) electrode, and the $Si_{70}(TiN)_{30}$ (Ar, 800 °C) electrode after 50 cycles at 30°C, respectively. Cycled $Si_{70}(TiN)_{30}$ (N_2, 800 °C) shows tiny morphology differences from its pristine state. A main difference could be that the cycled $Si_{70}(TiN)_{30}$ (N_2, 800 °C) sample has less clear particle edges compared to the fresh one. This suggests that $Si_{70}(TiN)_{30}$ (N_2, 800 °C) experienced surface erosion during cycling, which was also observed for the Si-TiN (N_2 and Ar) alloys before heat treatment, as described in Chapter 5. Some bright spots can be found in the SEM BSE

images of the fresh and cycled $Si_{70}(TiN)_{30}$ (Ar, 800 °C) electrode cross sections, which are attributed to tungsten impurities probably from the tungsten carbide balls used for electrode slurry preparation. Tungsten impurity content (W/(W+Si+Ti)) for these two samples is about 1.5 at.%, which was determined by SEM EDS. Based on Figures 6.7(c) and (d), morphology changes of $Si_{70}(TiN)_{30}$ (Ar, 800 °C) are significant after 50 cycles, which are associated with the coarse grain structure of this sample (Figure 6.3(n-p)) and high cr-$Li_{15}Si_4$ formation during cycling (Figure 6.5). A gray material covering the $Si_{70}(TiN)_{30}$ (Ar, 800 °C) particles formed during cycling, suggesting severe surface erosion. As mentioned above, both the $Si_{70}(TiN)_{30}$ (N_2 and Ar, 800 °C) alloys experienced surface erosion during cycling, resulting in surface area growth and increased surface electrolyte interface (SEI) formation. However, it is obvious that $Si_{70}(TiN)_{30}$ (N_2, 800 °C) shows less morphology changes compared to $Si_{70}(TiN)_{30}$ (Ar, 800 °C) after 50 cycles, which can be attributed to its finer grain structure (Figure 6.3) and better cr-$Li_{15}Si_4$ suppression (Figure 6.5).

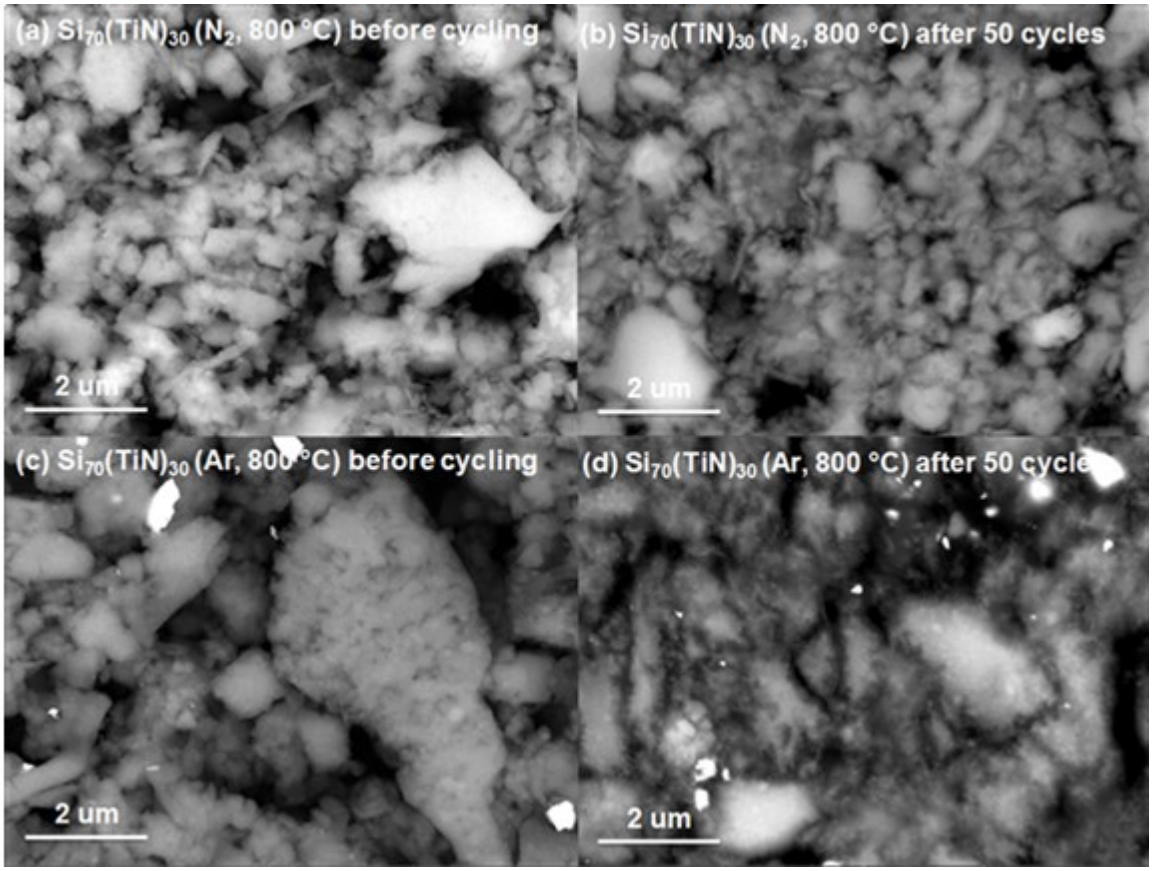

Figure 6.7 SEM BSE images of cross sections of (a) the fresh $Si_{70}(TiN)_{30}$ (N_2, 800 °C) electrode, (b) the $Si_{70}(TiN)_{30}$ (N_2, 800 °C) electrode after 50 cycles at 30°C, (c) the fresh $Si_{70}(TiN)_{30}$ (Ar, 800 °C) electrode, and (d) the $Si_{70}(TiN)_{30}$ (Ar, 800 °C) electrode after 50 cycles at 30°C.

Figures 6.8(a-c) show specific discharge capacity, volumetric discharge capacity, and columbic efficiency (CE) for the Si-TiN (N_2 and Ar, 800 °C) alloys during 30 °C cell cycling, respectively. The $Si_{85}(TiN)_{15}$ (N_2, 800 °C) and $Si_{70}(TiN)_{30}$ (N_2, 800 °C) samples show larger initial capacity fade than their corresponding Ar milling samples. This maybe because $Si_{85}(TiN)_{15}$ (N_2, 800 °C) and $Si_{70}(TiN)_{30}$ (N_2, 800 °C) have larger surface area compared to their reference examples ($Si_{85}(TiN)_{15}$ (N_2, 800 °C) vs. $Si_{85}(TiN)_{15}$ (Ar, 800 °C):

14.0 ± 0.1 m^2/g vs. 11.9 ± 0.2 m^2/g; $Si_{70}(TiN)_{30}$ (N_2, 800 °C) vs. $Si_{70}(TiN)_{30}$ (Ar, 800 °C): 13.1 ± 0.2 m^2/g vs. 7.2 ± 0.5 m^2/g; for each specific surface area shown here, the uncertainty was determined based on the values obtained from adsorption and desorption processes of BET surface area analysis), probably resulting from lower crystallization and less particle aggregation during thermal treatment. The larger surface areas of $Si_{85}(TiN)_{15}$ (N_2, 800 °C) and $Si_{70}(TiN)_{30}$ (N_2, 800 °C) could contribute to more SEI formation and larger capacity fade during the first cycle. In addition, both $Si_{85}(TiN)_{15}$ (N_2 and Ar, 800 °C) samples show fast capacity fade during cycling. However, $Si_{85}(TiN)_{15}$ (N_2, 800 °C) has larger capacity retention than $Si_{85}(TiN)_{15}$ (Ar, 800 °C). $Si_{70}(TiN)_{30}$ (N_2, 800 °C) and $Si_{60}(TiN)_{40}$ (N_2, 800 °C) display similar cycling stability with their corresponding Si-TiN (Ar, 800 °C) alloys. Although $Si_{70}(TiN)_{30}$ (N_2, 800 °C) better suppressed cr-$Li_{15}Si_4$ formation during cycling compared to $Si_{70}(TiN)_{30}$ (Ar, 800 °C), the former shows no improved cycling performance. However, CEs of $Si_{70}(TiN)_{30}$ (N_2, 800 °C) are larger than those of $Si_{70}(TiN)_{30}$ (Ar, 800 °C) after about 30 cycles. As shown in Figure 6.7, severe surface erosion occurred in $Si_{70}(TiN)_{30}$ (Ar, 800 °C) during cycling, but no obvious particle pulverization can be observed. It can be believed that cr-$Li_{15}Si_4$ formation could contribute to Si-based particle fracture for $Si_{70}(TiN)_{30}$ (Ar, 800 °C), but did not result in significant electrical disconnection of active Si. Therefore, the $Si_{70}(TiN)_{30}$ (Ar, 800 °C) sample displays no fast capacity fade, although significant cr-$Li_{15}Si_4$ formed during cycling. However, in $Si_{70}(TiN)_{30}$ (Ar, 800 °C), continuous Si-based particle fracture resulting from cr-$Li_{15}Si_4$

formation can cause more active Si to be exposed to electrolyte and increased surface erosion, leading to more SEI formation. In contrast, $Si_{70}(TiN)_{30}$ (N_2, 800 °C) with almost no cr-$Li_{15}Si_4$ formation has better particle structural stability and less surface erosion (Figure 6.7), resulting in less SEI formation. In this way, $Si_{70}(TiN)_{30}$ (N_2, 800 °C) shows a greater advantage in CE compared to $Si_{70}(TiN)_{30}$ (Ar, 800 °C) as cycle number increases, as illustrated in Figure 6.8(c). The $Si_{60}(TiN)_{40}$ (N_2 and Ar, 800 °C) samples with similar ability to restrict $Li_{15}Si_4$ formation show similar cycling performance.

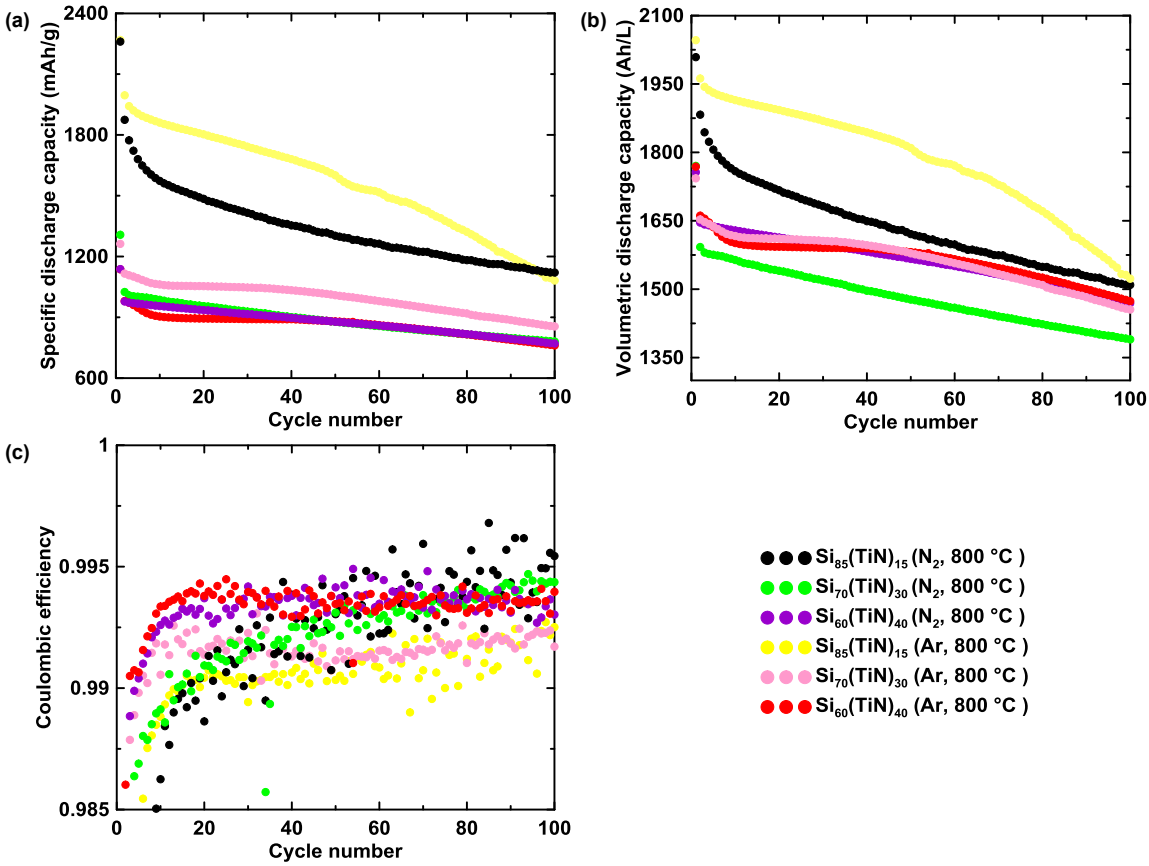

Figure 6.8 (a) Specific discharge capacity vs. cycle number, (b) volumetric discharge capacity vs. cycle number, and (c) CE of Si-TiN (N_2 and Ar, 800 °C) alloys during 30 °C cell cycling.

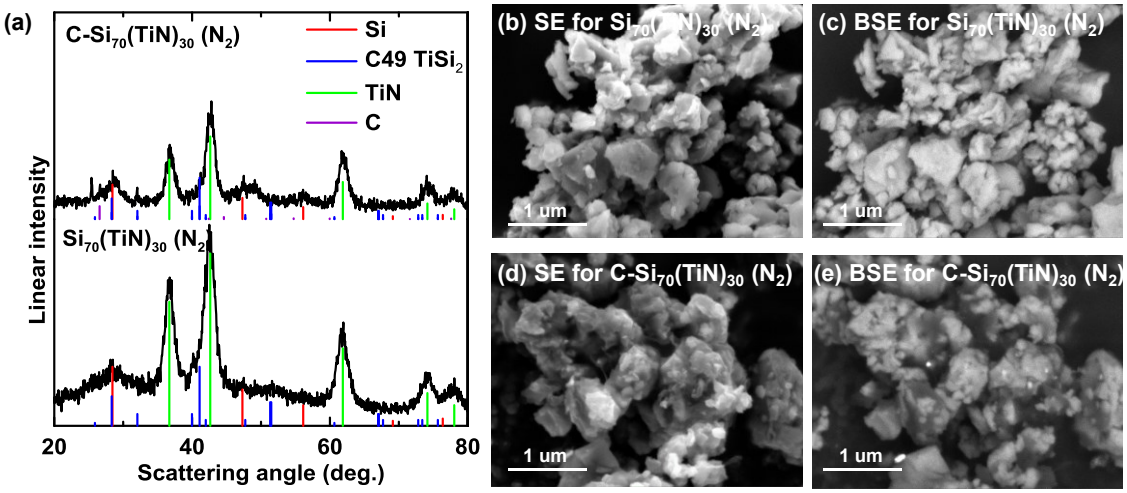

Figure 6.9 (a) XRD patterns of $Si_{70}(TiN)_{30}$ (N_2) and C-$Si_{70}(TiN)_{30}$ (N_2), (b) SEM SE and (c) SEM BSE images of $Si_{70}(TiN)_{30}$ (N_2), and (d) SEM SE and (e) SEM BSE images of C-$Si_{70}(TiN)_{30}$ (N_2).

As discussed above, the $Si_{70}(TiN)_{30}$ (N_2) alloy shows high temperature tolerance, such as low Si crystallization, fine grain structure, and good cr-$Li_{15}Si_4$ suppression during cycling after heat treatment. Here, $Si_{70}(TiN)_{30}$ (N_2) was selected for high temperature carbon coating. The carbon coated $Si_{70}(TiN)_{30}$ (N_2) (C-$Si_{70}(TiN)_{30}$ (N_2)) sample was prepared by heating a $Si_{70}(TiN)_{30}$ (N_2)/phenolic resin mixture at 800 °C for 1 h. XRD patterns, SEM SE images, and SEM BSE images of $Si_{70}(TiN)_{30}$ (N_2) before and after carbon coating are illustrated in Figure 6.9. C-$Si_{70}(TiN)_{30}$ (N_2) and $Si_{70}(TiN)_{30}$ (N_2) samples have similar XRD patterns. In the XRD patten of C-$Si_{70}(TiN)_{30}$ (N_2), a tiny broad XRD reflection is present at 26.6°, probably responding to amorphous C (a-C) produced during carbon coating preparation. In addition, C-$Si_{70}(TiN)_{30}$ (N_2) shows quite low Si crystallization, evidenced by broad Si XRD peaks. As shown in Figures 6.9(b) and (d), C-$Si_{70}(TiN)_{30}$ (N_2)

exhibits a different sample morphology from $Si_{70}(TiN)_{30}$ (N_2). The C-$Si_{70}(TiN)_{30}$ (N_2) particles show less distinct edges, suggesting that most of the $Si_{70}(TiN)_{30}$ (N_2) particles are coated with carbons. In the SEM BSE image of the C-$Si_{70}(TiN)_{30}$ (N_2) sample (Figure 6.9(e)), dark parts can be observed on the surface of Si alloy particles, supporting that the $Si_{70}(TiN)_{30}$ (N_2) particles are surrounded by carbon. Based on Figure 6.9, it can be believed that the $Si_{70}(TiN)_{30}$ (N_2) particles are generally carbon coated through the method described above without obvious crystallization or phase composition change during high temperature carbon coating. The average thickness of the carbon coating was determined by the carbon coating volume per unit C-Si70(TiN)30 (N2) volume/the volumetric surface area of Si70(TiN)30 (N2), where the carbon coating volume per unit C-Si70(TiN)30 (N2) volume was estimated based on the measured densities of Si70(TiN)30 (N2), C-Si70(TiN)30 (N2), and assuming the density of the carbon coating was 1.6 g/mL. According to this calculation, the average carbon coating thickness was 2 nm. However, a uniform coating so thin should not be visible by the SEM measurements used. This indicates that the coating does not uniformly cover the alloy surface. This is consistent with the SEM images, where various shades of grey in the images correspond to varying thicknesses of carbon coating. Figures 6.10(a-e) illustrate the first four cycle dQ/dV curves, the percent active Si that forms $Li_{15}Si_4$ at full lithiation (*f*), volumetric capacity, normalized capacity (all the capacities were normalized to the 10th delithiation capacity), and CE for C-$Si_{70}(TiN)_{30}$ (N_2 vs. lithium metal at 30 °C, respectively. The data from $Si_{70}(TiN)_{30}$ (N_2)

(from Chapter 5) and $Si_{70}(TiN)_{30}$ (N_2, 800 °C) are also shown in Figure 6.10(c) and (d). Based on Figures 6.10(a) and (b), it can be found that only 4%-7% cr-$Li_{15}Si_4$ formed during cycling for the C-$Si_{70}(TiN)_{30}$ (N_2) sample, which suggests good cr-$Li_{15}Si_4$ suppression. C-$Si_{70}(TiN)_{30}$ (N_2) has a lower ICE (72.0%) compared to $Si_{70}(TiN)_{30}$ (N_2) (80.3%) and $Si_{70}(TiN)_{30}$ (N_2, 800 °C) (78.4%). This is presumably because C-$Si_{70}(TiN)_{30}$ (N_2) has much higher surface area (138 m^2/g, ~11 times larger than $Si_{70}(TiN)_{30}$ (N_2) and $Si_{70}(TiN)_{30}$ (N_2, 800 °C)), probably resulting from high porosity generated during phenolic resin carbonization. The large surface area (138 m^2/g) could lead to a large amount of SEI formation and low ICE. In addition, the C-$Si_{70}(TiN)_{30}$ (N_2) sample has a lower reversible volumetric capacity (1490 Ah/L) than $Si_{70}(TiN)_{30}$ (N_2) and $Si_{70}(TiN)_{30}$ (N_2, 800 °C), which can be attributed to introduced a-C that typically has very low reversible capacity. The 50-cycle capacity retention of C-$Si_{70}(TiN)_{30}$ (N_2) is 94%, which is higher than those of $Si_{70}(TiN)_{30}$ (N_2) (89%) and $Si_{70}(TiN)_{30}$ (N_2, 800 °C) (85%). Also, compared with $Si_{70}(TiN)_{30}$ (N_2) and $Si_{70}(TiN)_{30}$ (N_2, 800 °C), C-$Si_{70}(TiN)_{30}$ (N_2) shows comparable CEs (Figure 6.10 (e)) but displays better cycling stability (Figure 6.10(d)). A carbon coated $Si_{70}(TiN)_{30}$ (N_2) sample with further improved cell performance can be expected if an optimized carbon coating method is applied.

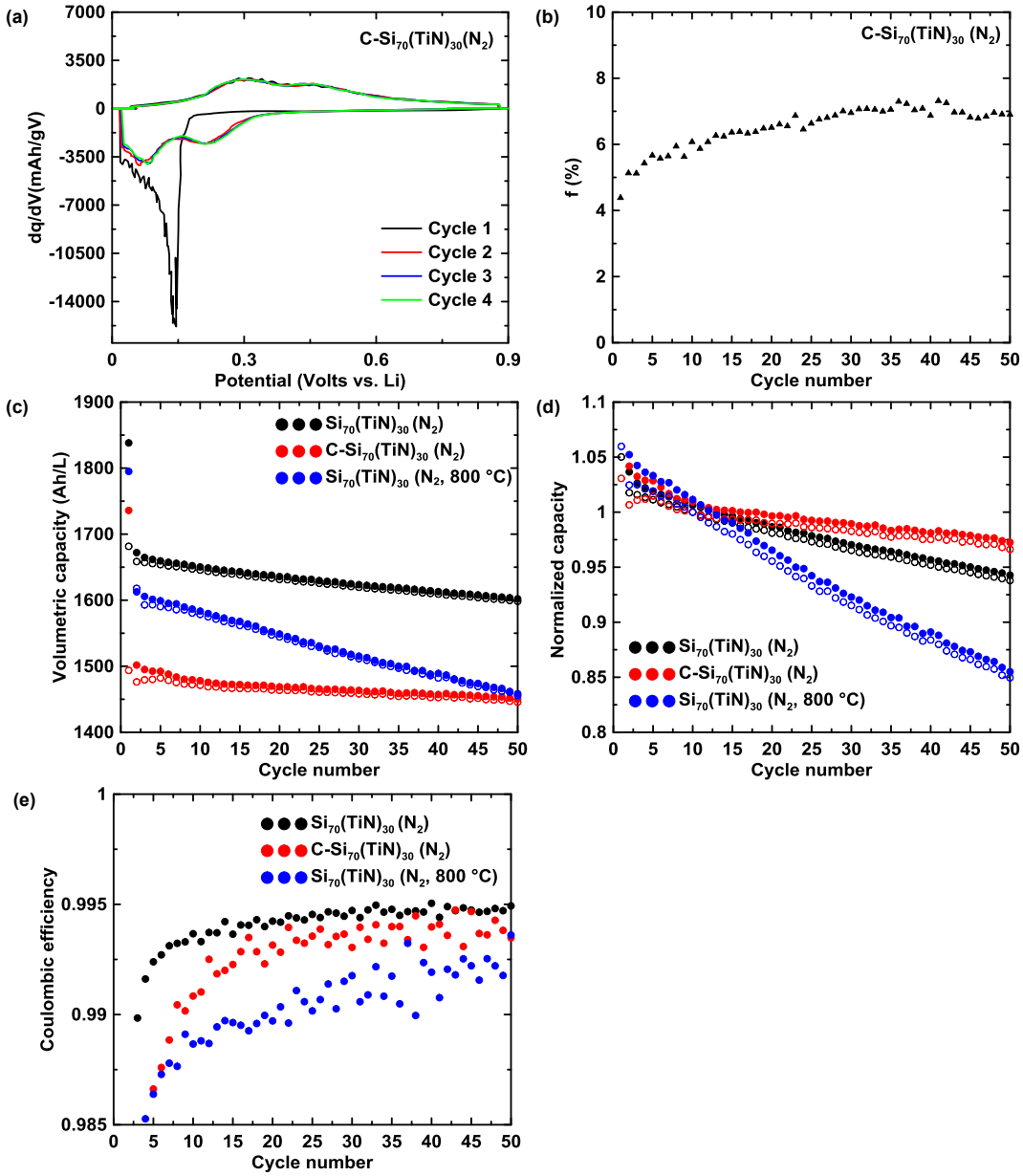

Figure 6.10 (a) The first four cycle dQ/dV curves, (b) plot of the percent active Si that forms $Li_{15}Si_4$ at full lithiation (*f*) of C-$Si_{70}(TiN)_{30}$ (N_2) vs. lithium metal at 30 °C, (c) volumetric capacity (discharge: solid circle; charge: hollow circle), (d) normalized capacity (For each sample, all the capacities were normalized to the 10th delithiation capacity. Solid circle for discharge and hollow circle for charge), and (e) CE of $Si_{70}(TiN)_{30}$ (N_2), C-$Si_{70}(TiN)_{30}$ (N_2), and $Si_{70}(TiN)_{30}$ (N_2, 800 °C) vs. lithium metal at 30 °C.

6.4 Conclusions

In this chapter, thermal stability of Si-TiN (N_2 and Ar) alloys was investigated. The Si-TiN (N_2 and Ar) alloys show no obvious phase composition change during heating, and the Si-TiN (N_2 and Ar) alloys after heat treatment mainly consist of nanocrystalline Si and TiN. The Si-TiN (N_2, 800 °C) samples display lower crystallization and finer microstructure than the Si-TiN (Ar, 800 °C) samples. Among $Si_x(TiN)_{100-x}$ (x = 85, 70, and 60, N_2, 800 °C), $Si_{70}(TiN)_{30}$ (N_2, 800 °C) shows the lowest Si crystallization and the finest grain structure, probably due to an appropriate initial Ti content of this sample (higher ductile Ti content may hinder Si-Ti mixing during milling). $Si_{70}(TiN)_{30}$ (N_2, 800 °C) shows good resistance to cr-$Li_{15}Si_4$ formation during cycling and insignificant morphology changes after cycling, presumably owing to its fine microstructure. $Si_{70}(TiN)_{30}$ (N_2) was selected for high temperature carbon coating. The C-$Si_{70}(TiN)_{30}$ (N_2) sample with a reversible volumetric capacity of 1490 Ah/L shows a higher 50-cycle capacity retention (94%) compared to $Si_{70}(TiN)_{30}$ (N_2) (89%) and $Si_{70}(TiN)_{30}$ (N_2, 800 °C) (85%). Unfortunately, the C-$Si_{70}(TiN)_{30}$ (N_2) sample has a large specific surface area, generated during phenolic resin carbonization, probably leading to a large amount of SEI formation and low CEs. In a future work, a more proper carbon coating method will be explored for obtaining a carbon coated $Si_{70}(TiN)_{30}$ (N_2) sample with further improved cell performance.

Chapter 7 Si-Ti-N-O Alloy Li-ion Battery Negative Electrode Materials Prepared by Air Milling

7.1 Introduction

As discussed in Section 2.3.5, there are still some difficulties to fully commercialize silicon-based negative electrodes, such as huge volume changes and crystalline $Li_{15}Si_4$ (cr-$Li_{15}Si_4$) formation during cycling. In recent years, extensive research has has been carried out to improve Si-based negative electrode materials performance, mainly focusing on Si-M (M = transition metal) alloys,[13,166,176] Si/C composites,[108,177,178] and SiO_x (typically $x \leq 1$).[179–182] SiO_x, an important silicon-based negative electrode material, has already been commercialized in lithium batteries. Silicon monoxide can be generated by simultaneous evaporation of silicon and silicon dioxide in vacuum at approximately 1400 °C, as shown below.[183]

$$Si(s) + SiO_2(s) \rightarrow 2SiO(g) \quad (7.1)$$

Solid amorphous silicon monoxide (a-SiO) can be obtained by quenching. Up to now, the atomic structure of solid a-SiO has not been clarified clearly, and many models proposed for a-SiO microstructure are still controversial. These models mainly include a random bonding model (all intermediate compositions between Si and SiO_2 can be formed, and the two atom species are blended on an atomic scale),[184] a random mixture model (disproportionation into two separated phases Si and SiO_2),[185] and an interface clusters

mixture model.[183] Figure 7.1 illustrates the interface clusters mixture model, in which Si and SiO_2 nanoclusters are surrounded by a Si-suboxide matrix.[183] Unfortunately, SiO_x usually has a low initial coulombic efficiency (ICE), which is attributed to inactive Li_4SiO_4 formation during the first lithiation of SiO_x.[181] Cao et al. prepared SiO_x by simply ball milling Si powder in air, and a resulting sample ($SiO_{0.37}$) showed some improvements compared to commercial SiO, such as a larger volumetric capacity (1800 Ah/L vs. 1400 Ah/L) and a higher ICE (70% vs. 55%).[186]

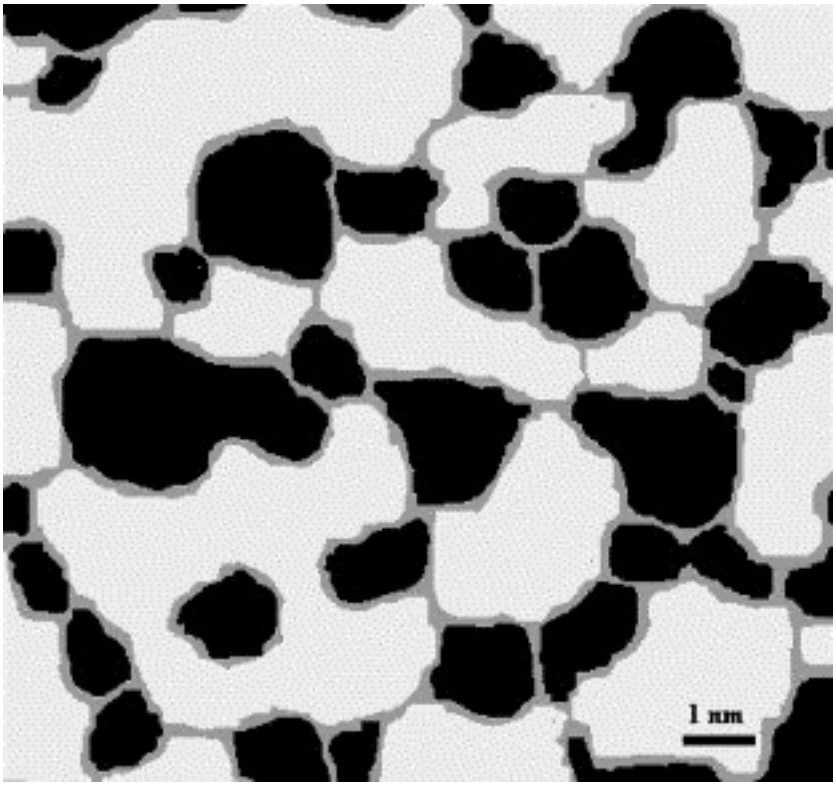

Figure 7.1 An interface clusters mixture model for a-SiO microstructure (black: silicon; light gray: silicon dioxide; and gray: silicon suboxide). Reprinted with permission from Reference 183. Copyright 2003 Elsevier.

High thermal stability is a prerequisite when silicon-based negative electrode materials need to be further improved by high-temperature post-processing methods (e.g. high temperature carbon coating). However, the microstructure of silicon-based negative electrode materials can change during thermal treatment, which may affect their cell performance. The effect of heat treatment on SiO_x microstructure has not been completely known. Park et al. indicated that Si nanocrystals were produced and uniformly dispersed in a SiO_x matrix during heating SiO_x.[187] It has been shown that heat treatment is an efficient approach to improve cycling performance of SiO_x.[186,187] However, heat treatment could be detrimental for some other silicon-based negative electrode materials (e.g. Si-Mo alloys (Chapter 4) and Si-TiN (N_2 and Ar) alloys (Chapters 5 and 6)). Worse cell performance could be gained after thermal treatment, which is not desirable.

Here, Si-Ti-N-O alloys were prepared by simply mechanical milling Si and Ti powders in air. Phase composition, sample morphology, electrochemical performance, and thermal stability of these Si-Ti-N-O alloys were studied in this chapter.

7.2 Experimental

Si-Ti-N-O alloys were prepared by mechanical milling. The raw materials used were Si powder (Sigma-Aldrich, 325 mesh, 99%) and Ti powder (Alfa Aesar, 325 mesh, 99%). Si_xTi_{100-x} ($70 \leq x \leq 85$, $\Delta x = 5$) samples were milled in air for 8 h or 16 h. Other details about sample preparation can be found in Section 3.1. To study the thermal stability

of Si-Ti-N-O alloys, samples were heated at 800 °C for 3 h, using the heating procedure described in Section 3.1.

Sample morphology and electrode cross sections were characterized using a Schottky field emission scanning electron microscope (SEM, TESCAN MIRA 3 LMU) with an accelerating voltage of 20 kV. An energy dispersive spectroscopy (EDS) system (Oxford instrument X-max 80mm^2) was employed for semi-quantitative analysis of Si, Ti and Fe contents. O and N contents were determined by LECO analysis (NSL Analytical Services, Inc, Cleveland OH). X-ray diffraction (XRD) patterns were collected using a Rigaku Ultima IV diffractometer. Transmission electron microscopy (TEM) images were obtained with a Philips CM30 TEM operated at a voltage of 250 kV. EDS X-ray mappings were collected in a scanning TEM (STEM) mode, which was also operated at 250 kV. True sample densities were measured with a helium pycnometer (AccuPyc II 1340, Micrometrics).

Electrode preparation and half cell assembly were as described in Sections 3.8.1 and 3.8.2, respectively. Cells were cycled at 30 ± 0.1 °C using a Neware battery testing system in a voltage window of 0.005V-0.9 V. Other cell cycling conditions were the same as described in Section 5.2.

7.3 Results and Discussion

XRD patterns of Si_xTi_{100-x} ($70 \leq x \leq 85$, $\Delta x = 5$, 8 h and 16 h in air) are shown in Figure 7.2. For Si_xTi_{100-x} ($75 \leqslant x \leqslant 85$, $\Delta x = 5$, 8 h in air), the XRD peaks are identified to be mainly from amorphous Si (a-Si), TiN, and C49 $TiSi_2$. The samples with longer air milling time (Si_xTi_{100-x} ($70 \leqslant x \leqslant 85$, $\Delta x = 5$, 16 h in air)) typically consist of a-Si and TiN. No obvious C49 $TiSi_2$ XRD peaks can be observed for these samples, suggesting that C49 $TiSi_2$ was consumed during air milling probably via a displacement reaction. Therefore, the formation of TiN follows a 2-step reaction:

Step 1: $2Si + Ti \rightarrow C49\text{-}TiSi_2$

Step 2: $2C49\ TiSi_2\ (s) + N_2\ (g) \rightarrow 2TiN\ (s) + 4Si\ (s)$

This 2-step reaction has been observed previously for the reactive gas ball milling of Ti and Si in N_2(g).[163] The XRD results of the Si-Ti (8 h in air) alloys indicate that a higher Ti content contributes to a larger C49 $TiSi_2$-N_2 (g) reaction rate to produce TiN and Si. A small XRD peak at about 44° can be observed for some alloys shown in Figure 7.2, which could be attributed to Fe impurity introduced from the stainless steel balls and stainless steel vials during ball milling. SEM images of the Si_xTi_{100-x} (x = 85 and 70, 8 h and 16 h in air) alloys are exhibited in Figure 7.3, suggesting these Si-Ti-N-O samples have similar sample morphology; that is irregularly shaped particles with an average particle size of ~1 μm (based on 50 random particles for each sample shown in Figure 7.3)

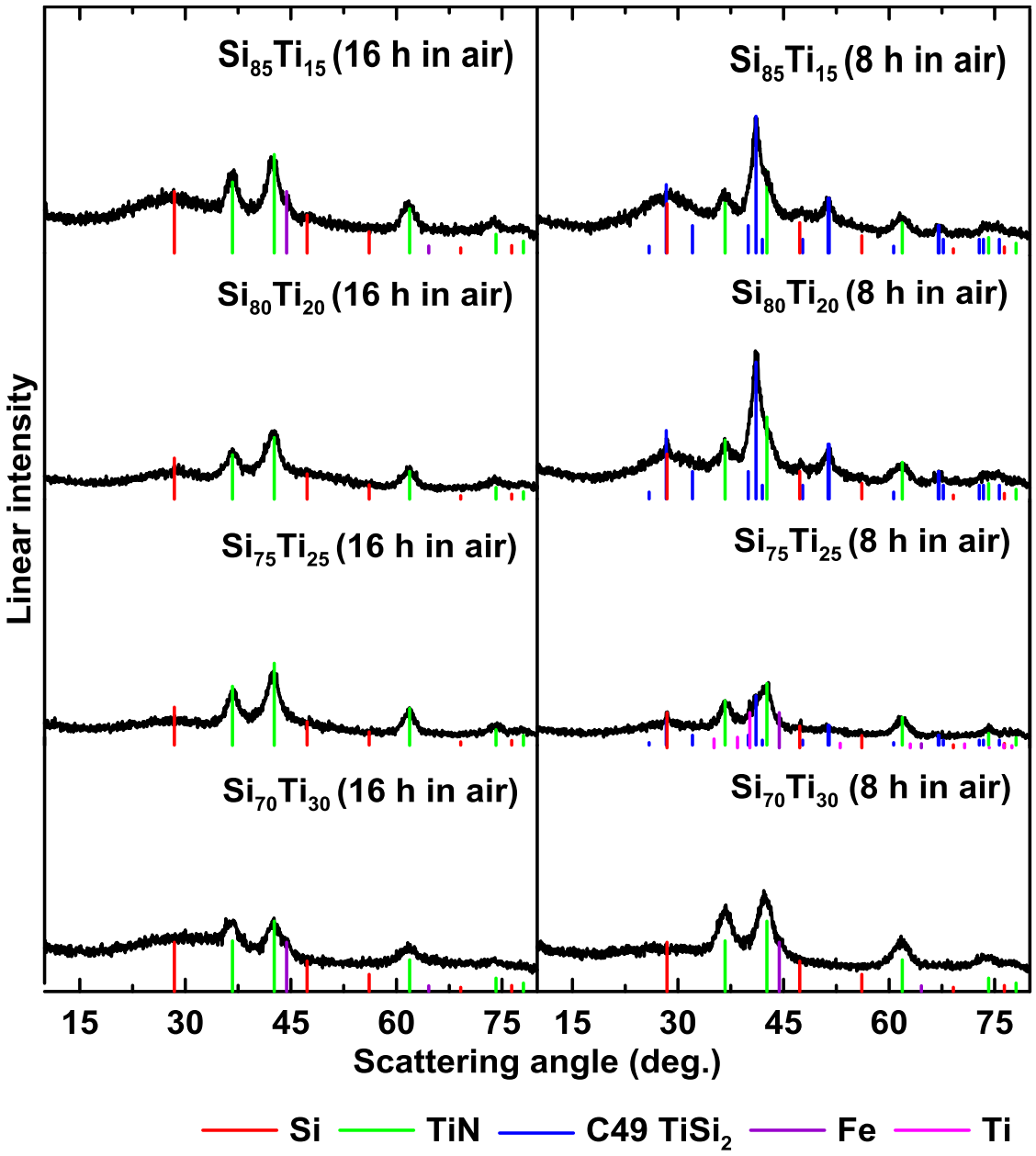

Figure 7.2 XRD patterns of Si_xTi_{100-x} ($70 \leq x \leq 85$, $\Delta x = 5$, 8 h and 16 h in air).

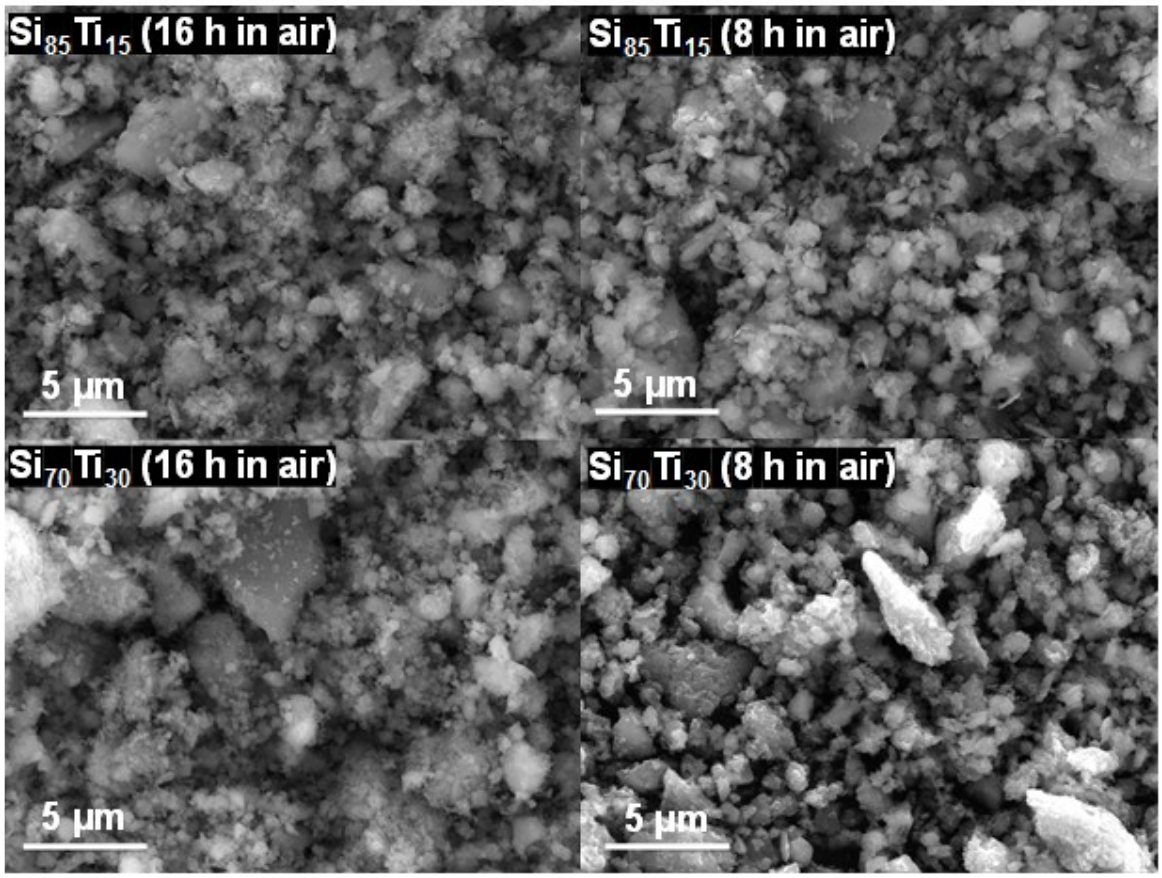

Figure 7.3 Sample morphology of some selected Si-Ti-N-O alloys.

Table 7.1 lists Si, Ti, Fe, N, and O contents for the Si_xTi_{100-x} ($70 \leq x \leq 85$, $\Delta x = 5$, 8 h and 16 h in air) alloys, as determined by SEM EDS and LECO analysis. The results show that Fe contamination is in the range of 0.7 at.%-3.1 at.%. Generally, it can be found that longer milling time and higher Ti content contribute to an increase in Fe impurity content, which could be detrimental to industrial manufacturing processes. In addition, the Si-Ti-N-O samples with longer air milling time and higher Ti content typically have larger N and O contents, as shown in Figure 7.4. For each Si-Ti-N-O sample listed in Table 7.1, a large amount of O exists in the sample and N content is higher than Ti content. This

indicates that in addition to the a-Si, TiN, and C49 $TiSi_2$ phases observed in the XRD patterns shown in Figure 7.2, other phases (such as Si-O and Si-N compounds) are also likely to be present in the Si-Ti-N-O alloys. However, these possible phases cannot be detected in the XRD patterns, as they are likely X-ray amorphous.

Possible phase compositions of the Si-Ti-N-O samples are proposed here for the 16 h samples, based on the XRD results, atomic composition analysis, and results of previous studies of reactive ball milling of Si in air[186] and Ti with N_2,[163] according to the following model:

1. Si and Ti react to make $TiSi_2$, which then fully reacts with nitrogen to make TiN + Si.
2. any remaining N reacts with Si to make Si_3N_4.
3. O is assumed to react with the remaining Si to produce SiO_x, which reacts with lithium to form Li_4SiO_4 after the first full lithiation/delithiation.

In this model, the Fe is not assumed to take part in the reaction, but instead is assumed to remain as Fe metal (as observed by XRD). This is because it cannot be determined if the FeSi, $FeSi_2$ phases or a combination of these are also present, since these phases may be amorphous and therefore difficult to detect by XRD. Since the Fe content is small, the assumption that Fe remains as elemental metal should not cause large error.

Table 7.1 Element contents of Si-Ti-N-O samples based on SEM EDS and LECO analysis (for each powder sample, the uncertainties of Si, Ti, and Fe contents were calculated based 5 random regions, which are typically 0.5 at.%, 2.0 at.%, and 4.0 at.%, respectively; the uncertainties for N and O contents are shown in Section 3.6).

Sample	Composition (atomic %)				
	Si	Ti	Fe	N	O
$Si_{85}Ti_{15}$ (16 h in air)	49.7	9.1	1.6	20.8	18.8
$Si_{85}Ti_{15}$ (8 h in air)	61.3	11.0	1.1	12.6	14.1
$Si_{80}Ti_{20}$ (16 h in air)	41.9	10.7	2.7	26.4	18.3
$Si_{80}Ti_{20}$ (8 h in air)	54.4	14.0	0.7	16.2	14.7
$Si_{75}Ti_{25}$ (16 h in air)	36.0	14.8	3.1	27.2	18.9
$Si_{75}Ti_{25}$ (8 h in air)	43.9	20.1	1.4	19.3	15.3
$Si_{70}Ti_{30}$ (16 h in air)	30.7	12.6	2.8	33.7	20.3
$Si_{70}Ti_{30}$ (8 h in air)	41.2	17.2	2.1	22.6	16.9

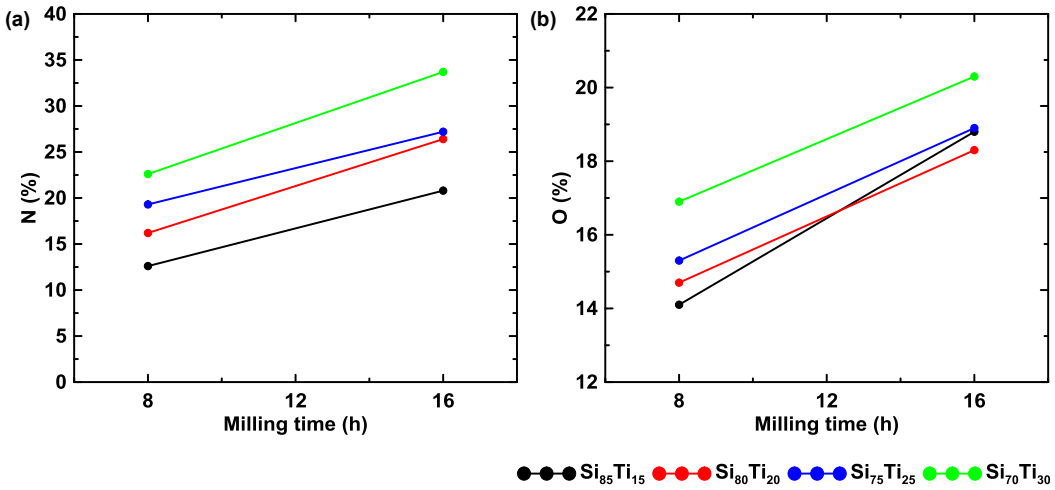

Figure 7.4 (a) N and (b) O contents of Si-Ti-N-O alloys as a function of air milling time.

The predicted phase compositions from this analysis are listed in Table 7.2 and their theoretical reversible capacities are listed, based on Li insertion into any elemental Si present to form $Li_{15}Si_4$. The formation of Si-N phases (assumed here to be Si_3N_4) were the only way that the large nitrogen content in these samples could be accounted for. The formation of such phases is surprising, since Si-N compounds were not found to form during reactive gas milling of Ti and Si in pure N_2(g), which only resulted in the formation of Si + TiN.[163] Furthermore, no nitrogen compounds were observed to form during the reactive ball milling of pure Si in air.[186] Therefore, the high nitrogen content of these samples can only be accounted for by some synergistic reaction between Si, O, N and Ti; perhaps indicating the formation of ternary Si-O-N or quaternary Si-Ti-O-N compounds. Similarly, according to table 7.1, the O/Si ratio of the 16 h samples increases from 0.38 to 0.66 with increasing Ti content. This ratio is higher than for Si ball milled in air under the same conditions, which reaches a maximum value of 0.37.[186] Again this may indicate synergistic behavior between these elements and the formation of ternary or quaternary species.

Table 7.2 Possible phase compositions (after the first full lithiation/delithiation cycle) and the corresponding reversible capacities for Si_xTi_{100-x} (16 h in air) samples.

Sample	Possible phase composition	Capacity (mAh/g)
$Si_{85}Ti_{15}$ (16 h in air)	$Si_{36.2}(TiN)_{9.1}(Si_3N_4)_{2.9}(Li_4SiO_4)_{4.7}Fe_{1.6}$	1449
$Si_{80}Ti_{20}$ (16 h in air)	$Si_{25.6}(TiN)_{10.7}(Si_3N_4)_{3.9}(Li_4SiO_4)_{4.6}Fe_{2.4}$	1026
$Si_{75}Ti_{25}$ (16 h in air)	$Si_{22.0}(TiN)_{14.8}(Si_3N_4)_{3.1}(Li_4SiO_4)_{4.8}Fe_{3.1}$	904
$Si_{70}Ti_{30}$ (16 h in air)	$Si_{9.8}(TiN)_{12.6}(Si_3N_4)_{5.3}(Li_4SiO_4)_{5.1}Fe_{2.8}$	407

Figures 7.5(a) and (b) show the first four cycle potential-capacity curves and the corresponding differential capacity (dQ/dV)-potential curves for half cells of Si-Ti-N-O alloys. As shown in Figure 7.5, the $Si_{70}Ti_{30}$ 16 h air sample was almost inactive, presumably due to low the active Si content in this sample, as predicted in Table 7.2. During the first lithiation of all the other alloys, a plateau at about 0.45 V in the potential curve and a corresponding peak in the dQ/dV curve can be observe. A similar phenomenon has been observed during the first lithiation of SiO_x, which is deemed to be associated with the irreversible reaction of Li with oxygen in the sample.[186] During the following lithiation/delithiation, a pair of sloping plateaus in the potential curve and a corresponding pair of broad peaks in the dQ/dV curve can be observed for these Si-Ti-N-O alloys shown in Figure 7.5, which are characteristic of a-Si lithiation/delithiation without $Li_{15}Si_4$ formation.[16] ICEs of the Si-Ti-N-O alloys shown in Figure 7.5 are listed in Table 7.3. Most

of the Si-Ti-N-O samples listed in Table 7.3 typically show higher ICEs than commercial SiO (55%) and $SiO_{0.37}$ prepared by air milling (70%),[186] but lower than Si-TiN alloys prepared by N_2 (g) milling (usually > 80%).[18] The O/(active Si) ratios (active Si include free Si and Si in SiO before cycling) were calculated for Si_xTi_{100-x} ($70 \leqslant x \leqslant 85$, $\Delta x = 5$, 16 h in air) based on the proposed phase compositions listed in Table 7.2. For most of the Si-Ti-N-O (16 h in air) samples, the O/(active Si) ratio increases with more Ti present in the sample, which could lead to a lower ICE due to the irreversible reaction between Li and O in the sample. $Si_{85}Ti_{15}$ (16 h in air) has a lower ICE than expected, considering its low oxygen content. This may be due to mechanical failure in this electrode during the initial cycle owing to high Si content and its associated high volume expansion.

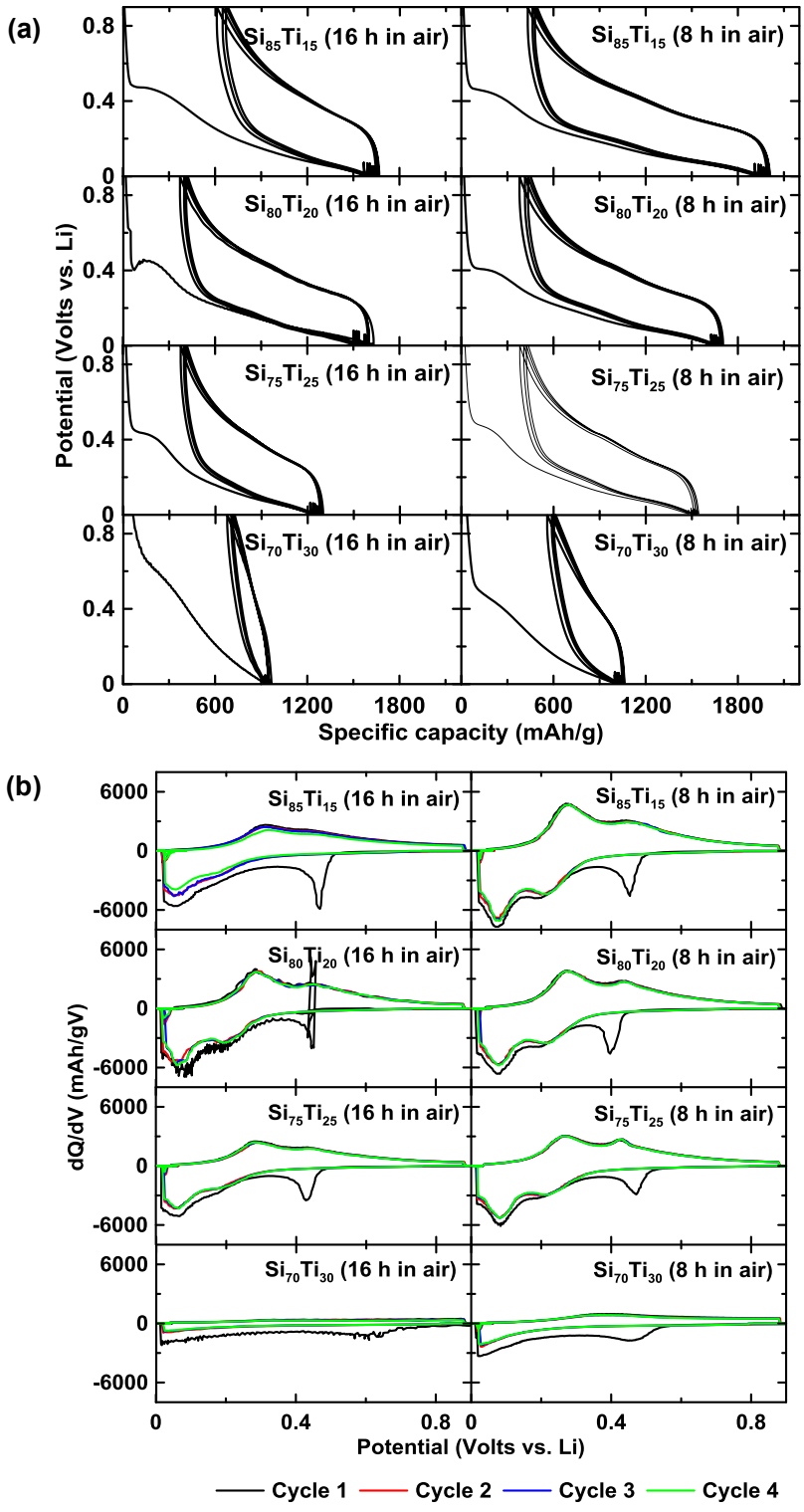

Figure 7.5 (a) The first four cycle potential curves and (b) the corresponding dQ/dV curves of Si-Ti-N-O alloy half cells.

Table 7.3 ICEs (for each sample, the uncertainty was calculated based on 3 duplicate cells) and O/(active Si) ratios of Si-Ti-N-O samples. The O/(active Si) ratios (active Si include free Si and Si in SiO before cycling) are only calculated for some Si-Ti-N-O samples with generally complete C49-$TiSi_2$-N_2 (g) reaction based on the phase compositions shown in Table 7.2.

Sample	ICE (%)	O/(active Si)
$Si_{85}Ti_{15}$ (16 in air)	62.8 ± 0.7	0.46
$Si_{85}Ti_{15}$ (8 h in air,)	76.9 ± 2.2	-
$Si_{80}Ti_{20}$ (16 in air)	77.8 ± 0.5	0.61
$Si_{80}Ti_{20}$ (8 in air)	77.6 ± 0.5	-
$Si_{75}Ti_{25}$ (16 in air)	70.9 ± 0.4	0.71
$Si_{75}Ti_{25}$ (8 in air)	75.2 ± 0.4	-
$Si_{70}Ti_{30}$ (16 in air)	29.8 ± 0.5	1.36
$Si_{70}Ti_{30}$ (8 in air)	47.7 ± 0.3	-

Cr-$Li_{15}Si_4$ formation after full lithiation is most easily characterized by its associated ~0.45 V delithiation dQ/dV peak.[16] In Figure 7.5(b), no obvious 0.45 V sharp peak during delithiation can be observed, suggesting almost no cr-$Li_{15}Si_4$ formation for all these samples during the first four cycles. The amount of active Si that forms $Li_{15}Si_4$ during cycling (f%) (the calculation method is as described in Section 4.3) and cycling performance in terms of volumetric capacity for the Si-Ti-N-O alloys shown in Figure 7.5 are shown in Figure 7.6. The corresponding specific capacity is shown in Figure 7.7(a).

The *f* values of $Si_{70}Ti_{30}$ (16 h in air) are not shown, since this sample has low active Si content and its *f* values may be significantly affected by side relations. Based on Figures 7.6 and 7.7(a), all these Si-Ti-N-O alloys studied here exhibit little cr-$Li_{15}Si_4$ formation (4~6%) during 100 cycles and relatively stable cycling performance. Figure 7.7(b) displays CEs of the Si-Ti-N-O samples studied here, showing that the Si_xTi_{100-x} ($75 \leq x \leq 85$, $\Delta x = 5$, 16 in air) and $Si_{70}Ti_{30}$ (8 h in air) alloys typically have higher CEs of about 99.6% than the other Si-Ti-N-O samples. Calculated reversible capacities based on the modelled compositions for the 16h alloys are listed in Table 7.2. These calculated reversible capacities and the measured 1st discharge and 1st charge capacities of the Si-Ti-N-O (16 h in air) samples are compared shown in Figure 7.8. The agreement is very good. This indicates that at least the amount of active Si predicted by the compositional model is close to what is observed.

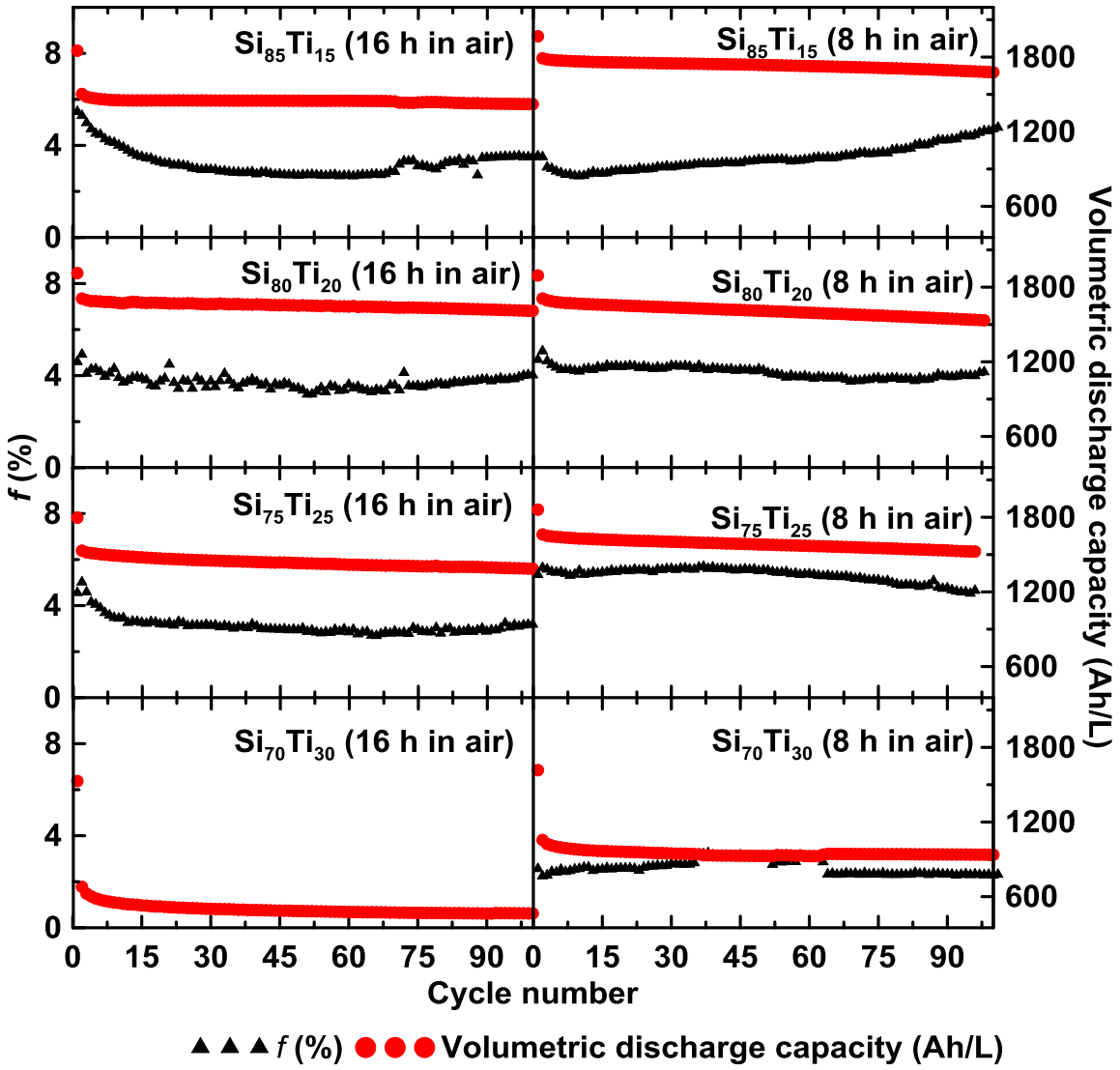

Figure 7.6 Plots of the percent active Si that forms $Li_{15}Si_4$ at full lithiation (*f*) vs. cycle number (the left axis) and volumetric capacity vs. cycle number curves (the right axis) of Si-Ti-N-O alloys vs. lithium metal.

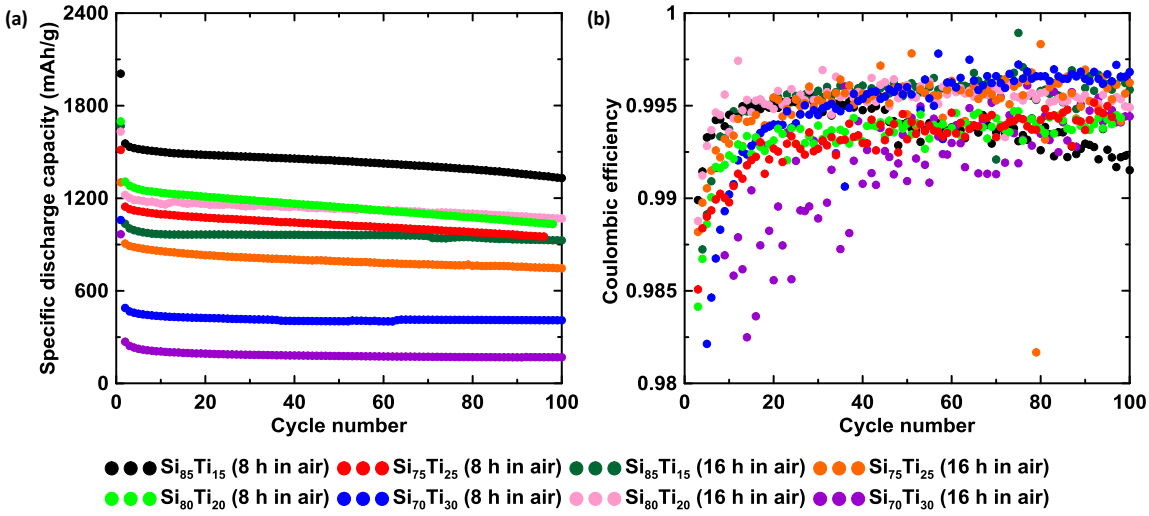

Figure 7.7 (a) Specific discharge capacity and (b) CE of Si-Ti-N-O alloys.

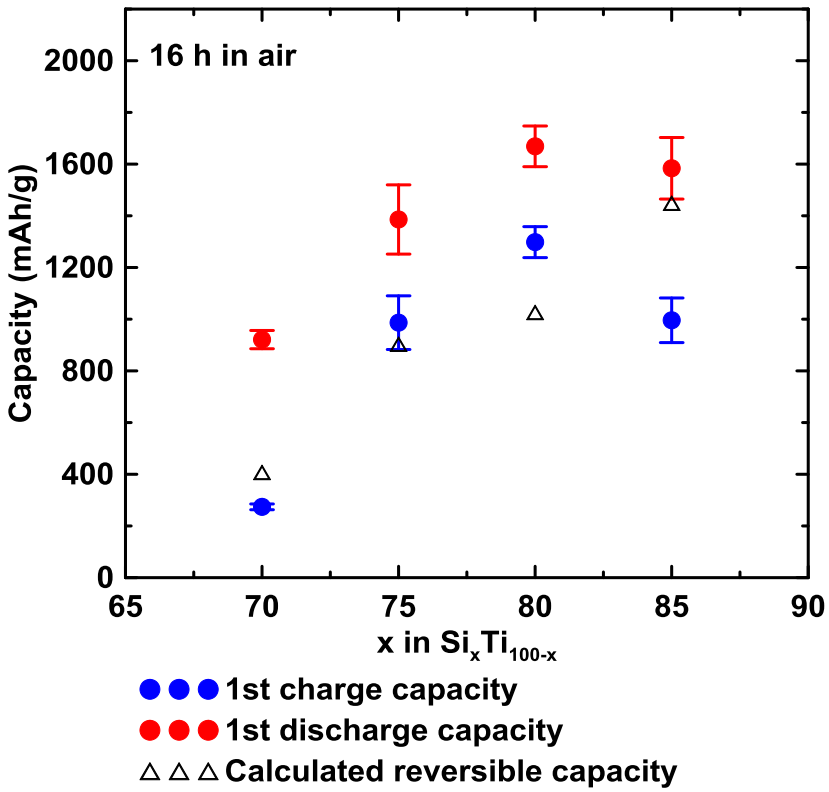

Figure 7.8 Comparison between the calculated reversible capacities (Table 7.2) and the measured first cycle capacities for Si-Ti-N-O (16 h in air) alloys (for each sample, the error bars were calculated based on 3 duplicate cells).

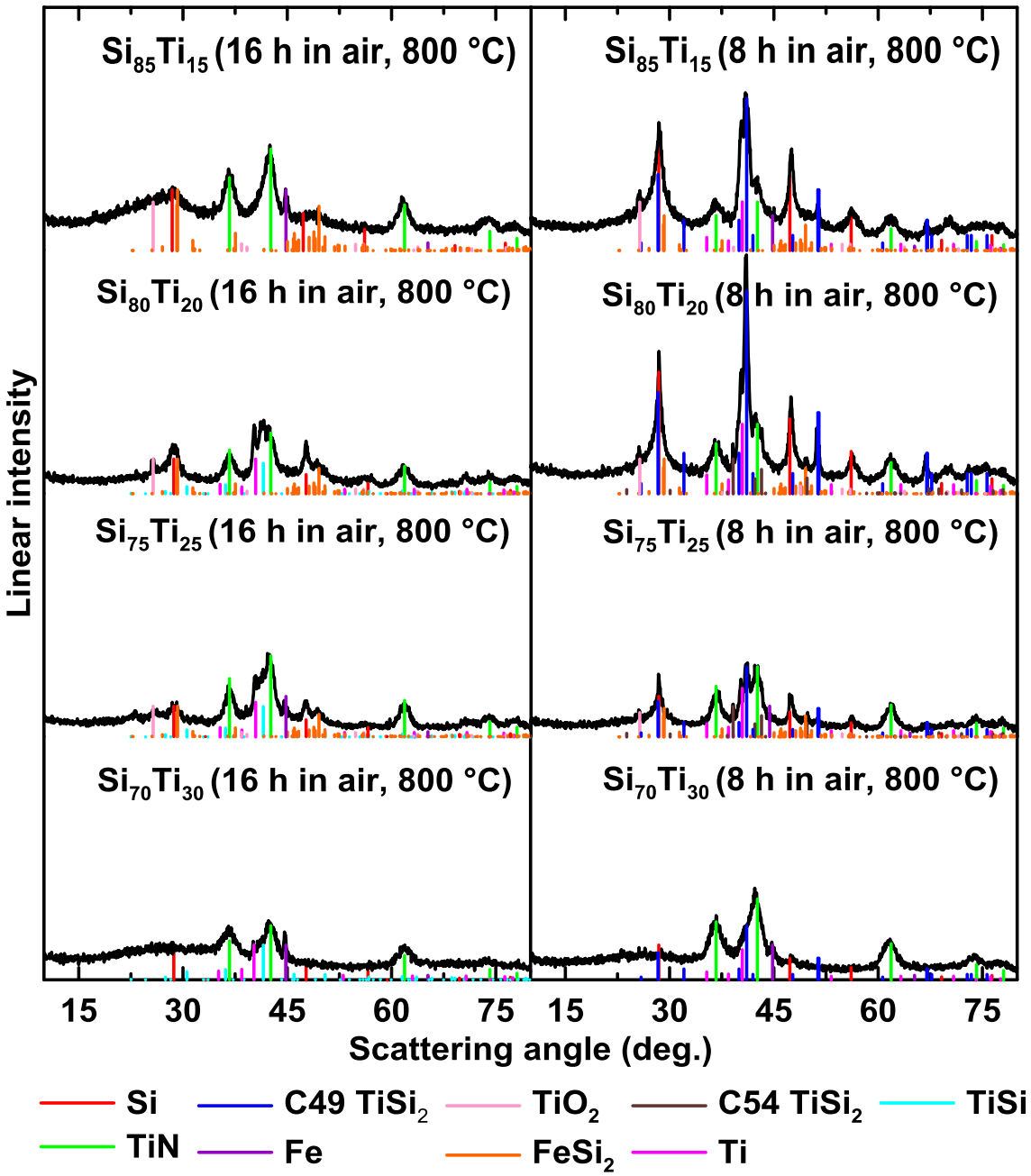

Figure 7.9 XRD patterns of Si-Ti-N-O samples after thermal treatment.

The XRD patterns of the Si_xTi_{100-x} ($70 \leq x \leq 85$, $\Delta x = 5$, 8 h and 16 h in air) samples after heat treatment are shown in Figure 7.9. Si, C49 $TiSi_2$, and TiN can be observed in the heated Si-Ti-N-O samples with a short air milling time (8 h), while Si and TiN are typically

present in the heated Si-Ti-N-O samples with a long air milling time (16 h). These observed phases are generally consistent with those of the Si-Ti-N-O samples before heat treatment shown in Figure 7.2. However, additional peaks can also be found in the XRD pattern of each heated Si-Ti-N-O sample studied here, probably resulting from unexpected side reactions during thermal treatment or crystallization of impurity phases produced during milling. Possible phases corresponding to these additional XRD peaks are Fe, $FeSi_2$, TiSi, Ti, C54 $TiSi_2$, and TiO_2; which are identified in Figure 7.9. Si and C49 $TiSi_2$ XRD peaks of Si_xTi_{100-x} (x = 85 and 80, 8 h in air, 800 °C) are much sharper than those of the samples before heat treatment (Figure 7.2), indicating that significant crystallization of Si and C49 $TiSi_2$ occurred during heat treatment. In contrast, the Si-Ti-N-O alloys with more Ti or a longer air milling time (16 h) show much less crystallization during heating, which suggests that increased Ti content and longer air milling time contribute to higher thermal stability for these Si-Ti-N-O alloys.

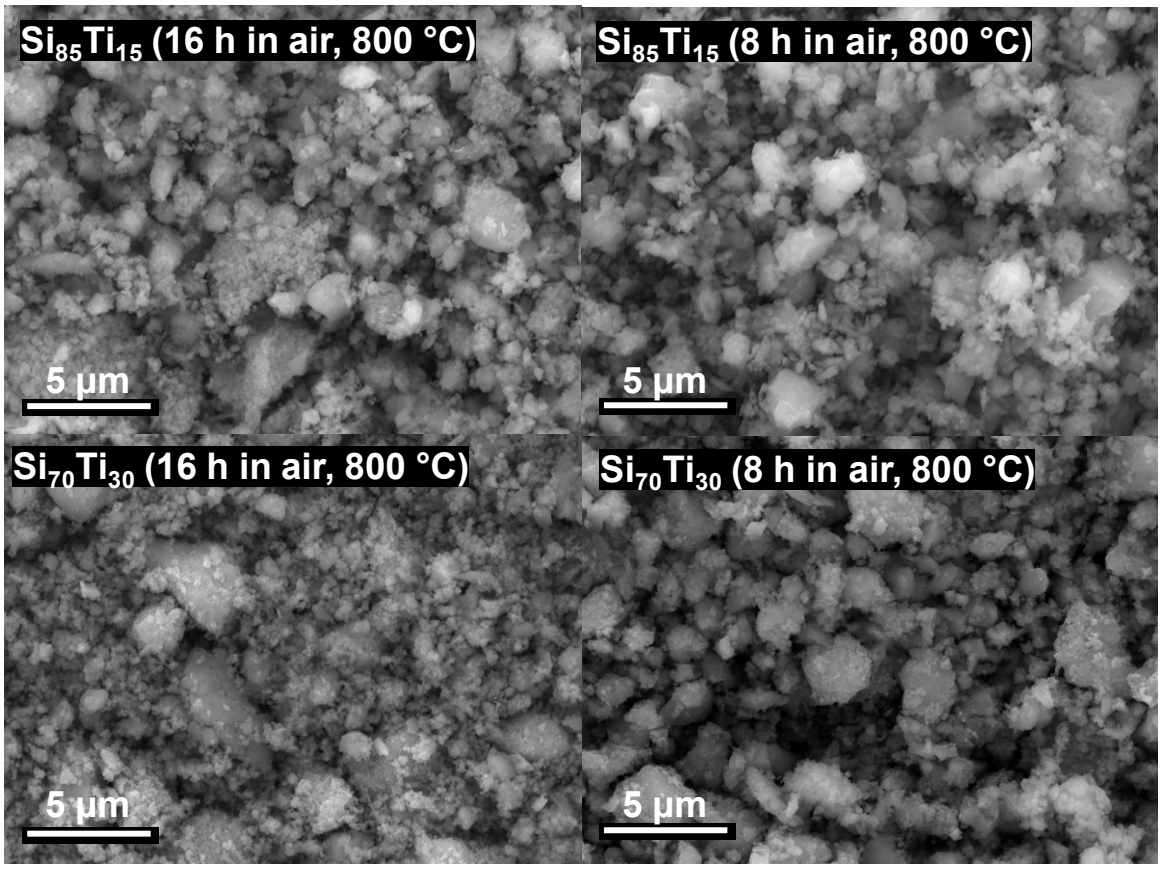

Figure 7.10 Sample morphology of some selected Si-Ti-N-O alloys after thermal treatment.

Sample morphology of Si_xTi_{100-x} (x = 85 and 70, 8 h and 16 h in air, 800 °C) is shown in Figure 7.10. The Si_xTi_{100-x} (x = 85 and 70, 8 h and 16 h in air) alloys before and after heat treatment show no obvious sample morphology change, as shown in Figures 7.3 and 7.10. The internal microstructure of $Si_{85}Ti_{15}$ (8 h in air, 800 °C) and $Si_{75}Ti_{25}$ (16 h in air, 800 °C) was observed by TEM, and the results are displayed in Figure 7.11 (bright field (BF) images (Figures 7.11(a) and (b)), selected area electron diffraction (SAED) patterns (Figures 7.11(c) and (d)), and high resolution electron microscopy (HREM) images (Figures 7.11(e) and (f)). In the SAED pattern of $Si_{85}Ti_{15}$ (8 h in air, 800 °C), spotty

diffraction rings are identified to be probably from polycrystalline Si, C49 $TiSi_2$, and TiN, and some weak diffuse intensity may be associated with a-Si. In the SAED pattern of $Si_{70}Ti_{30}$ (16 h in air, 800 °C), diffuse diffraction rings, strong diffraction rings, and some extra bright spots correspond to a-Si, TiN nanocrystals, and a few large C49 $TiSi_2$ grains, respectively. The phase compositions of $Si_{85}Ti_{15}$ (8 h in air, 800 °C) and $Si_{70}Ti_{30}$ (16 h in air, 800 °C) observed in the SAED patterns are consistent with those detected by XRD (Figure 7.9). In addition, for $Si_{85}Ti_{15}$ (8 h in air, 800 °C) or $Si_{75}Ti_{25}$ (16 h in air, 800 °C), crystalline phases present in the sample have an average grain/particle size of ~10 nm, and the grains/particles s are embedded in an a-Si matrix, based on the BF (50 random particles of each sample was used for the analysis) and HREM images (based on the lattice fringes).

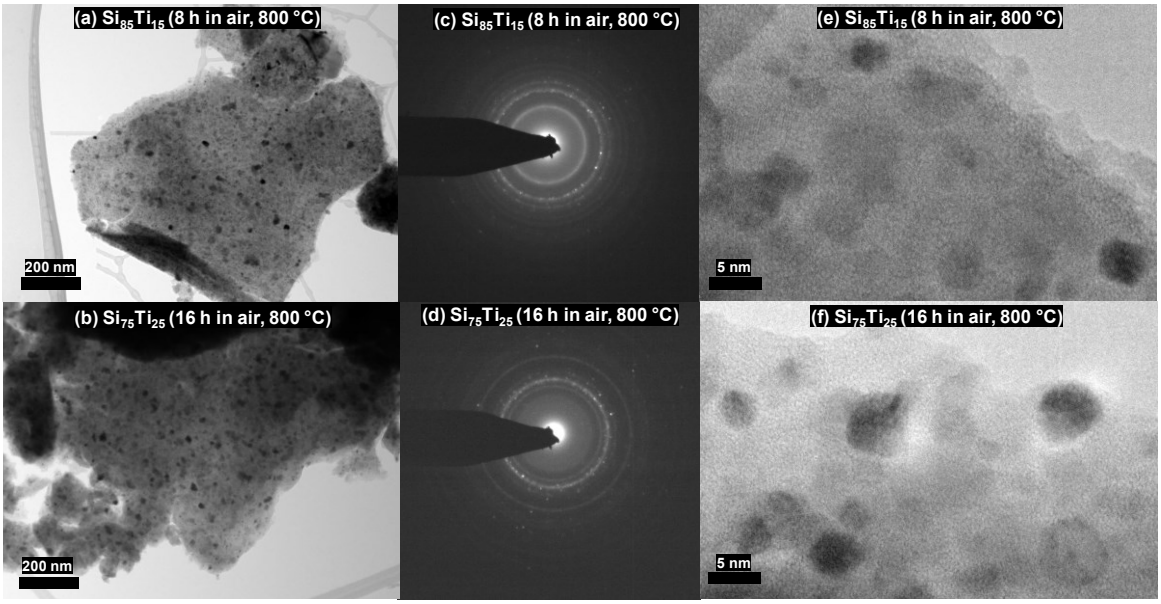

Figure 7.11 TEM images of $Si_{85}Ti_{15}$ (8 h in air, 800 °C) and $Si_{75}Ti_{25}$ (16 h in air, 800 °C): (a and b) BF images, (c and d) SAED patterns, and (e and f) HREM images.

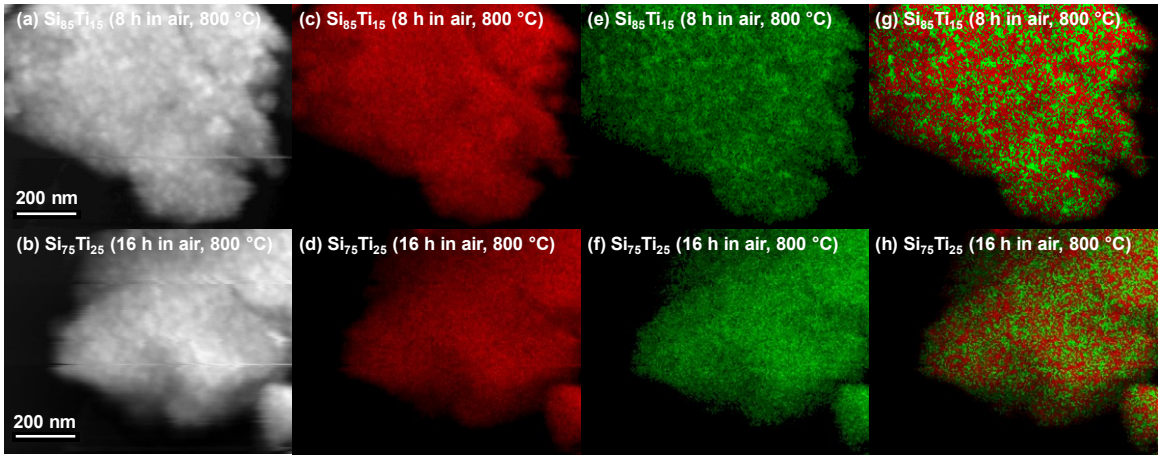

Figure 7.12 (a and b) STEM images, (c and d) Si maps, (e and f) Ti maps, and (g and h) Si-Ti substitution overlays (Si: red, Ti: green) of $Si_{85}Ti_{15}$ (8 h in air, 800 °C) and $Si_{75}Ti_{25}$ (16 h in air, 800 °C).

Figure 7.12 shows STEM images (Figures 7.12(a) and (b)), Si maps (Figures 7.12(c) and (d)), Ti maps (Figures 7.12(e) and (f)), and Si-Ti substitution overlays (Figures 7.12(g) and (h)) for $Si_{85}Ti_{15}$ (8 h in air, 800 °C) and $Si_{75}Ti_{25}$ (16 h in air, 800 °C) samples. A substitution overlay shows a combination of Si and Ti elements, where only the element with the higher intensity at each pixel is displayed. The $Si_{75}Ti_{25}$ (16 h in air, 800 °C) alloy displays homogenous Si and Ti distributions and a fine grain structure within the instrument resolution. For the $Si_{85}Ti_{15}$ (8 h in air, 800 °C) alloy, Ti distribution is a little inhomogeneous as shown in Figure 7.12(e), presumably due to low Ti content and shorter milling time of this sample.

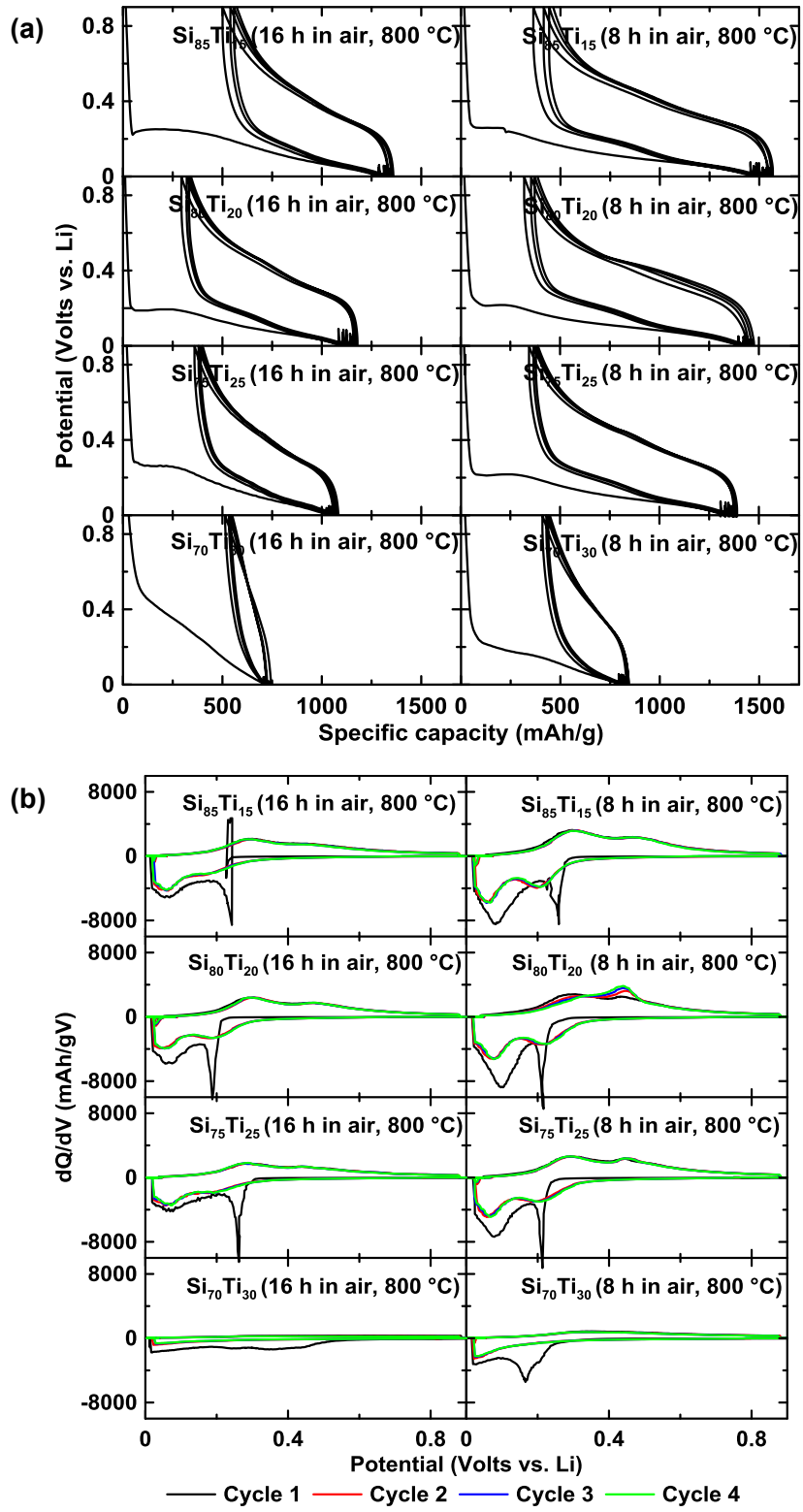

Figure 7.13 The first four cycle potential curves and (b) the corresponding dQ/dV curves of Si-Ti-N-O samples after thermal treatment vs. lithium metal.

Table 7.4 ICE and 200 cycle capacity retention of Si-Ti-N-O samples after thermal treatment vs. lithium metal (for each sample, the error bars were calculated based on 3 duplicate cells).

.

Sample	ICE (%)	Capacity retention (%)
$Si_{85}Ti_{15}$ (8 in air, 800 °C)	75.4 ± 1.9	64.7 ± 2.1
$Si_{80}Ti_{20}$ (8 h in air, 800 °C)	76.2 ± 3.2	61.8 ± 3.3
$Si_{75}Ti_{25}$ (8 h in air, 800 °C)	75.1 ± 1.0	71.3 ± 2.2
$Si_{70}Ti_{30}$ (8 h in air, 800 °C)	48.5 ± 4.8	80.8 ± 1.9
$Si_{85}Ti_{15}$ (16 h in air, 800 °C)	62.3 ± 0.3	71.4 ± 2.7
$Si_{80}Ti_{20}$ (16 h in air, 800 °C)	75.6 ± 0.7	69.8 ± 2.8
$Si_{75}Ti_{25}$ (16 h in air, 800 °C)	65.9 ± 0.8	83.5 ± 0.1

The first four cycle potential profiles and the corresponding dQ/dV curves of Si_xTi_{100-x} ($70 \leq x \leq 85$, $\Delta x = 5$, 8 h and 16 h in air, 800 °C) half cells are shown in Figures 7.13(a) and (b), respectively. In Figure 7.5(a), a high potential initial lithiation plateau (typically ~0.45 V) is present for the Si-Ti-N-O alloys before heat treatment, which probably results from the irreversible reaction of Li with oxygen in the samples. This high potential initial plateau has previously been observed for ball milled SiO_x.[186] However, the high potential initial lithiation plateau cannot be found for the Si-Ti-N-O samples after heat treatment, as shown in Figure 7.13(a). This is also the case for ball milled SiO_x samples, where the high potential initial lithiation plateau was deemed to be present only in SiO_x

with defects, where free radical oxygen is easily available for reaction with lithium. After heating, such defects are eliminated, and their associated high potential plateau disappears.[186] Similarly, for the Si-Ti-N-O alloys, defects were introduced during sample milling, but these defects were reduced during heat treatment. Therefore, the high potential initial lithiation plateau is only present in the Si-Ti-N-O alloys before heat treatment. ICEs of these heated Si-Ti-N-O samples studied here (expecting $Si_{70}Ti_{30}$ (16 h in air, 800 °C) with low active Si content) are listed in Table 7.4, which are typically similar with those of the samples before heat treatment (Table 7.3). The results support that the irreversible reaction between Li and oxygen in these heated Si-Ti-N-O samples still occurred during the initial lithiation. However, the potential for this irreversible reaction shifted negatively for the Si-Ti-N-O samples after heat treatment. During the following lithiation and delithiation displayed in Figure 7.13, the potential profiles and the corresponding dQ/dV curves of the heated Si-Ti-N-O alloys are generally identical to those of a-Si without $Li_{15}Si_4$ formation.[16]

Figure 7.14 exhibits $Li_{15}Si_4$ formation fraction (*f*) during cycling and cycling performance in terms of volumetric capacity for the heated Si-Ti-N-O samples shown in Figure 7.13 (excepting $Si_{70}Ti_{30}$ (16 h in air, 800 °C) with low active Si content). The data in terms of specific capacity is shown in Figure 7.15(a). Significant $Li_{15}Si_4$ formed in $Si_{85}Ti_{15}$ (8 h in air, 800 °C) and $Si_{80}Ti_{20}$ (8 h in air, 800 °C) during cycling, which is accompanied with rapid capacity fade. Some active Si regions unbonded by inactive phases

are likely to be present in these two alloys, because of low Ti contents and relatively coarse microstructure (Figure 7.12), leading to the lack of $Li_{15}Si_4$ suppression. As mentioned in the previous chapters, cr-$Li_{15}Si_4$ formation could be a detrimental factor for Si-based negative electrodes and result in microstructure damage (like particle fracture). The $Si_{85}Ti_{15}$ (8 h in air, 800 °C) electrode coating after cycling became much more fragile compared to the one before cycling as shown in Figure 7.16. This may be due to a combination of electrode mechanical failure because of the large volume expansion of this sample and particle fracture due to significant cr-$Li_{15}Si_4$ formation during cycling. The instability of the electrode structure may be the origin of rapid capacity fade of $Si_{85}Ti_{15}$ (8 h in air, 800 °C) and $Si_{80}Ti_{20}$ (8 h in air, 800 °C).

$Li_{15}Si_4$ formation fractions of $Si_{85}Ti_{15}$ (8 h in air, 800 °C) and $Si_{80}Ti_{20}$ (8 h in air, 800 °C) grow rapidly during cycling reaching up to a maximum value of 31%, then become decreased with more cycles. This may be because $Li_{15}Si_4$ formation could contribute to particle fracture, resulting in more active Si unbonded by inactive phases and more $Li_{15}Si_4$ formation during cycling. Capacity fade because of particle fracture additionally results in an effective "C-rate" increase, which negatively shifts the Si lithiation potential, resulting in $Li_{15}Si_4$ formation suppression (its equilibrium formation potential vs. lithium is ~50 mV for pure Si).[16,97] In this way, the *f* of $Si_{85}Ti_{15}$ (8 h in air, 800 °C) and $Si_{80}Ti_{20}$ (8 h in air, 800 °C) becomes decreased after 31 cycles and 24 cycles, respectively. The other Si-Ti-N-O samples after heat treatment shown in Figure 7.14 display good cr-$Li_{15}Si_4$ suppression.

As shown in Figures 7.14 and 7.15(a), the heated Si-Ti-N-O samples with more Ti or longer air milling time typically have better cycling stability, and the $Si_{75}Ti_{25}$ (16 h in air, 800 °C) sample with a reversible capacity of 1276 ± 4 Ah/L preforms the most stable cycling and the largest 200 cycle capacity retention of 83.5% ± 0.1% (Table 7.4) among the samples studied here. Furthermore, $Si_{75}Ti_{25}$ (16 h in air) after heat treatment has a higher capacity retention than the one before heat treatment (92.1% ± 1.3% vs. 82.4% ± 3.0% after 100 cycles), suggesting cycling performance of this sample is improved via thermal treatment. Thermal treatment has also been found to improve cycling performance of SiO_x.[186]

Figure 7.17 shows SEM secondary electron (SE) (Figures 7.17(a) and (b)) and backscattered electron (BSE) (Figures 7.17(c) and (d)) images of cross sections of $Si_{75}Ti_{25}$ (16 h in air, 800 °C) before and after cycling. After 200 cycles, $Si_{75}Ti_{25}$ (16 h in air, 800 °C) generally keeps its pristine state and just slight surface erosion of Si-based particles can be observed. The microstructure of the $Si_{75}Ti_{25}$ (16 h in air, 800 °C) electrode is highly stable during cycling, which could be attributed to the fine grain structure (Figures 7.11 and 7.12) and good cr-$Li_{15}Si_4$ suppression (Figure 7.14) of this sample, leading to good cycling performance (Figures 7.14 and 7.15(a)). Figure 7.15(b) shows CEs of the heated Si-Ti-N-O alloys studied here, which are generally 99.5%~99.7% and are comparable or even higher than those of the unheated Si-Ti-N-O samples.

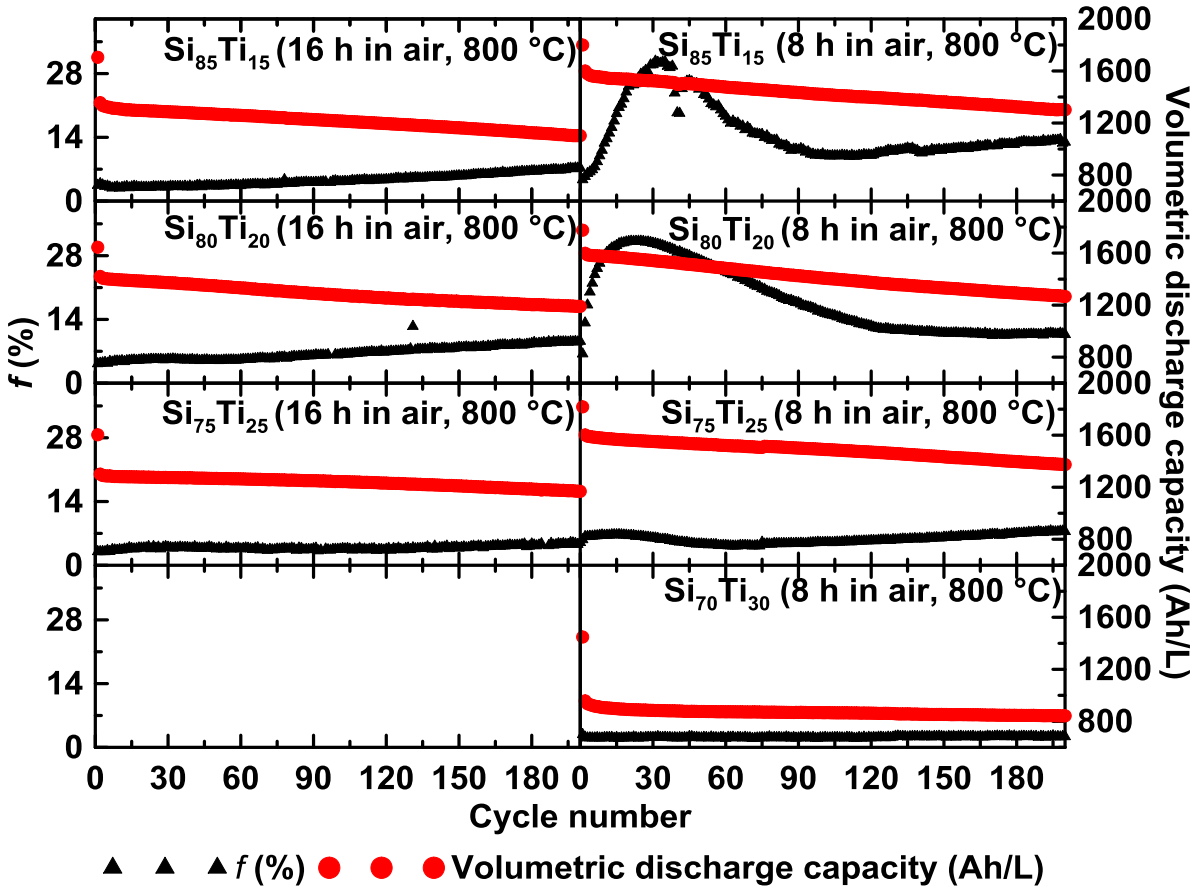

Figure 7.14 Plots of the percent active Si that forms $Li_{15}Si_4$ at full lithiation (*f*) vs. cycle number (the left axis) and volumetric capacity vs. cycle number curves (the right axis) of Si-Ti-N-O alloys after thermal treatment vs. lithium metal.

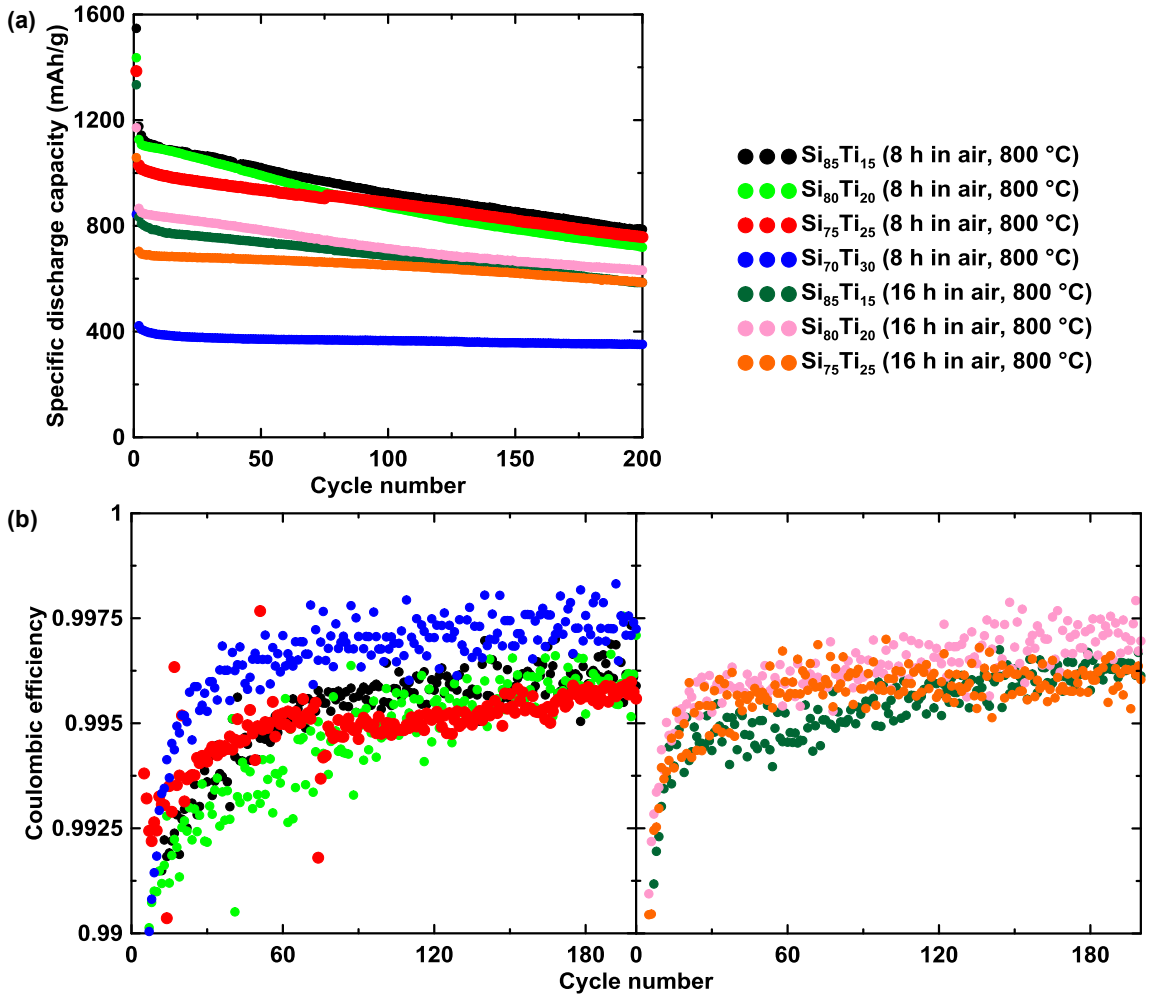

Figure 7.15 (a) Specific capacity and (b) CE of Si-Ti-N-O samples after thermal treatment.

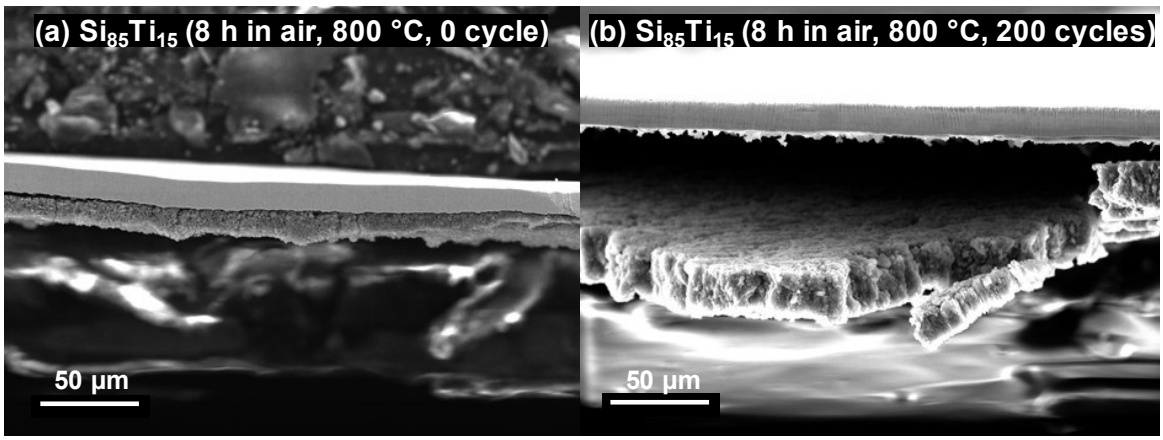

Figure 7.16 SEM SE images of $Si_{85}Ti_{15}$ (8 h in air, 800 °C) electrode (a) before and (b) after 200 cycles.

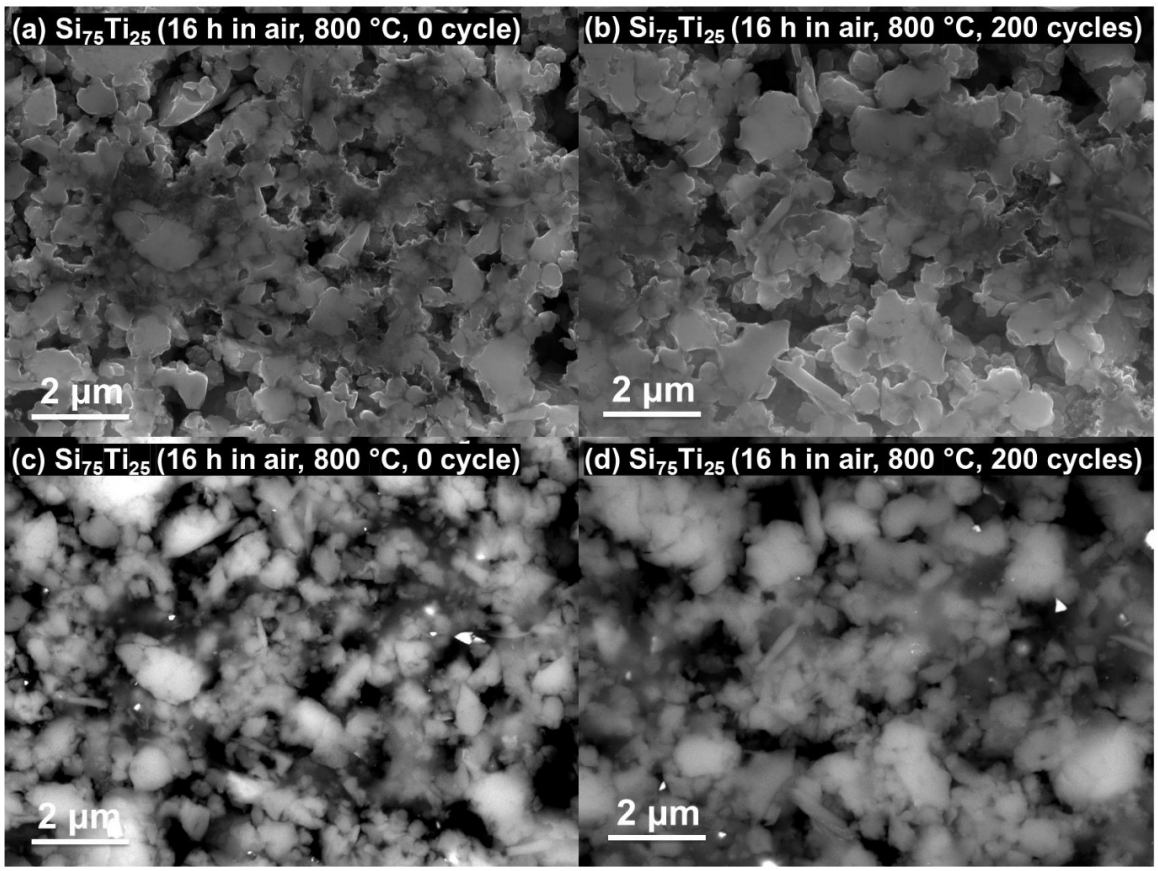

Figure 7.17 SEM (a and b) SE and (c and d) BSE images of cross section of $Si_{75}Ti_{25}$ (16 h in air, 800 °C) before and after 200 cycles.

7.4 Conclusions

In this study, it was found that Si-Ti-N-O alloys can be prepared by simply ball milling Si and Ti powders in air. Longer air milling time and higher Ti content contribute to inducing increased oxygen and nitrogen during air milling. Generally, the Si-Ti-N-O alloys display good cr-$Li_{15}Si_4$ suppression during cycling and relatively stable cycling performance. The Si-Ti-N-O samples with long air milling time or high Ti content typically have good temperature tolerance, evidenced by low crystallization, $Li_{15}Si_4$ formation

suppression during cycling, and stable cell cycling after heat treatment. These alloys can be applied for high-temperature post-processing (e.g. high temperature carbon coating). $Si_{75}Ti_{25}$ (16 h in air, 800 °C) has a reversible capacity of 1276 ± 4 Ah/L and a 200 cycle capacity retention of 83.5% ± 0.1%, which is attractive from a manufacturing standpoint.

Compared to commercial SiO and $SiO_{0.37}$ studied in Reference [186], most of the Si-Ti-N-O samples studied here show higher ICEs (SiO vs. $SiO_{0.37}$ vs. Si-Ti-N-O samples: 55% vs. 70% vs. 71%-78%). As shown in Chapters 5 and 7, the ICEs of these Si-Ti-N-O alloys are lower than those of Si-TiN alloys prepared by N_2 (g) milling (ICEs: > 80%). However, these Si-Ti-N-O alloys typically show better temperature tolerance than Si-TiN (N_2) samples (Chapter 6). Only one Si-TiN (N_2) sample discussed in Chapter 6 ($Si_{70}(TiN)_{30}$ (N_2)) shows low crystallization during heat treatment and good cr-$Li_{15}Si_4$ suppression during cycling after heat treatment, while most of the Si-Ti-N-O alloys studied here with different Si-Ti stoichiometric ratios display high thermal stability and good restriction to cr-$Li_{15}Si_4$ formation during cycling after heat treatment. Moreover, some Si-Ti-N-O samples after heat treatment have larger capacity retentions than the heated Si-TiN (N_2) samples (e.g. $Si_{75}Ti_{25}$ (16 h in air, 800 °C) vs. $Si_{70}(TiN)_{30}$ (N_2, 800 °C): 92.1 ± 1.3% vs. 72.6 ± 3.1% after 100 cycles). Therefore, Si-Ti-N-O alloys may represent a good compromise in obtaining high temperature tolerance, cycle life, while maintaining a high ICE; compared to SiO_x and Si/TiN alloys.

Chapter 8 Preliminary Carbon Coating Results

8.1 Introduction

As discussed in Section 2.3.5.3, making carbon coating is an effective way to improve cell performance of Si-based materials. Carbon contributes to increasing electrical conductivity of Si-based materials. Also, carbon coating as a protective layer of Si-based materials can avoid the exposure of Si-based particles to electrolyte and maintain a stable solid electrolyte interface (SEI) during cell cycling.[111] Pyrolysis of carbon precursors and chemical vapour deposition (CVD) are two commonly used approaches to prepare carbon coating for Si-based materials.[108,112]

Some Si-TiN (N_2 gas milling, Chapters 5 and 6) and Si-Ti-N-O (Chapter 7) samples show good thermal stability in a temperature range that would make them compatible high temperature carbon coating. In this chapter, pyrolysis or CVD was employed to make carbon coatings for the Si-TiN (N_2 gas milling, Chapters 5 and 6) and Si-Ti-N-O (Chapter 7) alloys with high temperature tolerance. Preliminary results and issues with using these two methods to prepare carbon coating for these Si alloys, which will be discussed in this chapter.

8.2 Experimental

A Si-TiN sample ($Si_{70}(TiN)_{30}$ (N_2)) and a Si-Ti-N-O sample ($Si_{85}Ti_{15}$ (16h in air)) were prepared using the preparation methods described in sections 5.2 and 7.2,

respectively. Pyrolysis of a carbon precursor was used for preparing a carbon coating on the $Si_{70}(TiN)_{30}$ (N_2) alloy powder particles. The $Si_{70}(TiN)_{30}$ (N_2) alloy was added into a β-lactose (⩽30% α-anomer basis, ⩾99% total lactose basis, Sigma-Aldrich)/isopropanol solution with an alloy/β-lactose volume ratio of 3:1. The suspension was mixed using planetary mill (Retsch PM200) with 3 tungsten carbide balls (d = 12.7 mm) at 100 rpm for 30 min and was dried at 120 °C in air overnight. Then, the sample was collected and heated at 700 °C for 1 h. Other heating conditions can be found in Section 3.1. The resulting sample is referred to here as C- $Si_{70}(TiN)_{30}$ (N_2). In addition, CVD was used to prepare a carbon coating on the $Si_{85}Ti_{15}$ (16h in air) alloy powder particles. C_2H_4 and Ar were used as a carbon source and a carrier gas, respectively. For this process, the sample was placed in a rotating fluidized bed in flowing Ar, and the temperature was increased from room temperature to 800 °C with a heating rate of 10 °C/min. The sample was heated at 800 °C in flowing C_2H_4/Ar for 3 h and then in Ar for 1.5 h. The sample was naturally cooled to room temperature under flowing Ar. The resulting sample is referred to here as CVD-$Si_{85}Ti_{15}$ (16h in air). Sample cross section and sample morphology were characterized using a Schottky field emission scanning electron microscope (SEM, TESCAN MIRA 3 LMU), which was operated at an accelerating voltage of 5 kV. Sample specific surface area was measured with a surface area analyzer (Micromeritics FlowSorb II 2300).

8.3 Results and Discussion

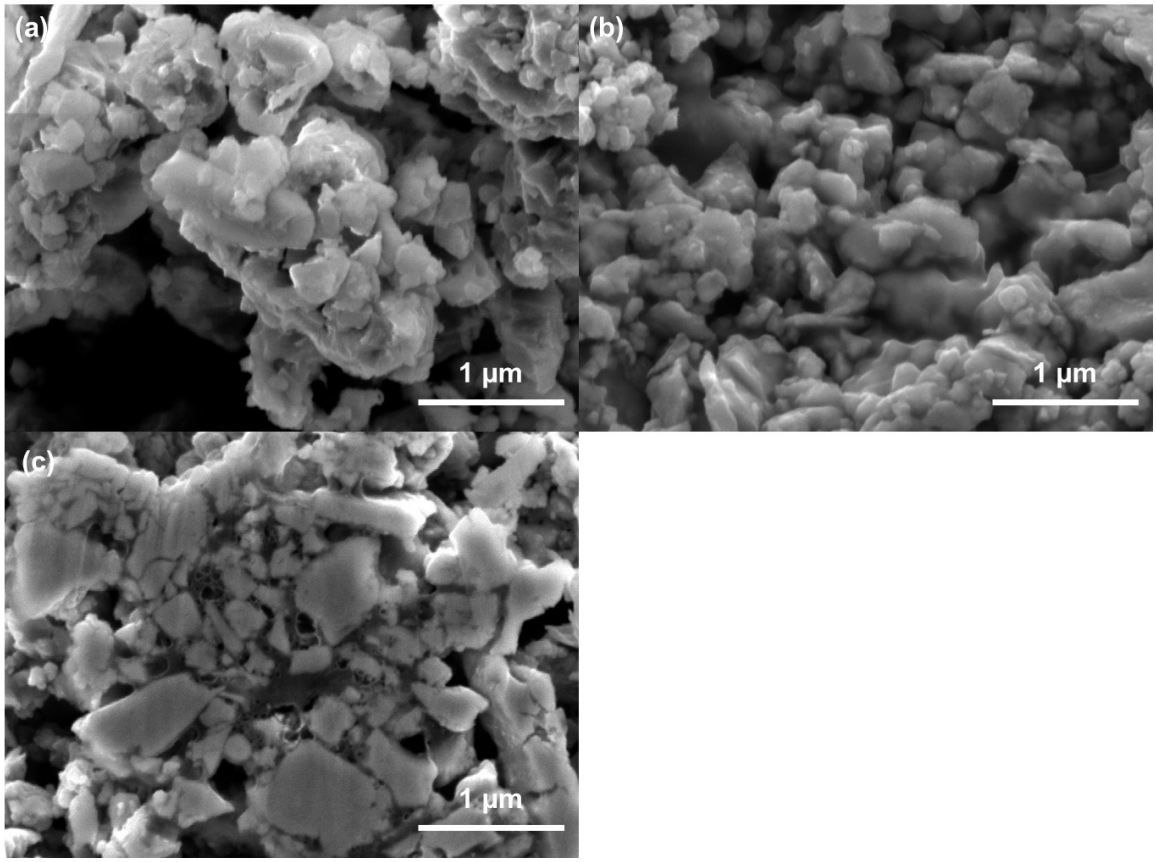

Figure 8.1 SEM SE images of (a) $Si_{70}(TiN)_{30}$, (b) C-$Si_{70}(TiN)_{30}$, and (c) cross section of C-$Si_{70}(TiN)_{30}$.

Figures 8.1(a) and (b) illustrate sample morphology of $Si_{70}(TiN)_{30}$ (N_2) before and after carbon coating. The sample morphology of C-$Si_{70}(TiN)_{30}$ (N_2) is different from that of $Si_{70}(TiN)_{30}$ (N_2). Compared to $Si_{70}(TiN)_{30}$ (N_2), C-$Si_{70}(TiN)_{30}$ (N_2) shows less distinct particle edges, suggesting that $Si_{70}(TiN)_{30}$ (N_2) is successfully carbon coated through β-lactose carbonization. Unfortunately, aggregation and porosity was generated during carbon coating preparation, as illustrated in Figure 8.1(c), which resulted in an

increase in sample specific surface area (11.0 $m^2/g \rightarrow 22.2\ m^2/g$). As shown in Chapter 6, when using phenolic resin as a carbon source, specific surface area growth also occurred during high temperature carbonization. High surface area is detrimental to electrode materials, which can contribute to significant solid electrolyte interface (SEI) formation and low coulombic efficiency (CE) during cycling.

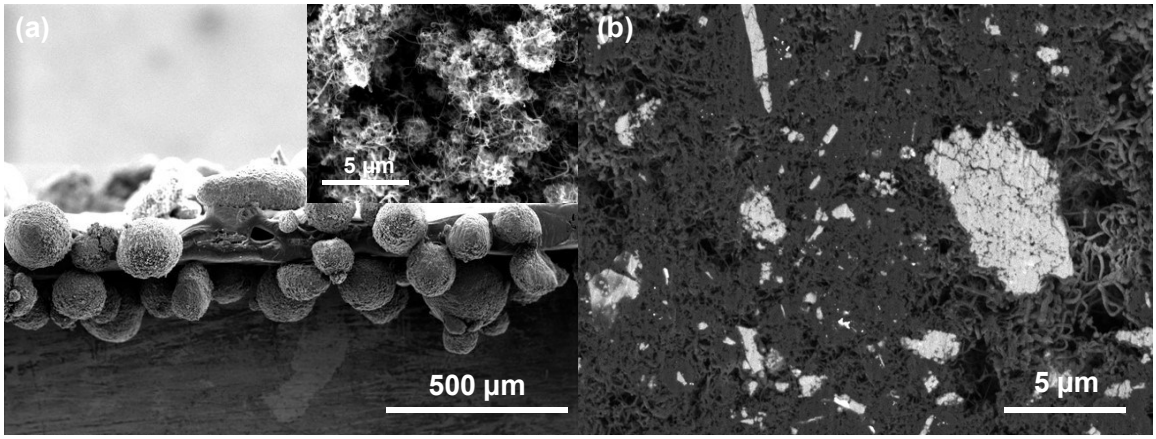

Figure 8.2 (a) SEM SE image and (b) SEM BSE image of cross section of CVD-$Si_{85}Ti_{15}$ (16h in air).

Sample morphology and cross section of CVD-$Si_{85}Ti_{15}$ (16 h in air) are shown in Figure 8.2. The results indicate that a large amount of carbon nanotubes not carbon coating formed on the surface of $Si_{85}Ti_{15}$ (16 h in air) during CVD. Similar phenomena were also observed when using CVD to make carbon coating for other Si-TiN (N_2 gas milling, Chapter 5) and Si-Ti-N-O (Chapter 7) samples (not shown here). This is probably because the transition metal element (Ti) is a catalytically active component, leading to carbon nanotube generation during CVD. Significant carbon nanotubes can lead to large surface area, which is not good for electrode materials as mentioned above. In addition, the samples

are highly agglomerated and highly porous, which would result in volumetric low energy density.

8.4 Conclusions

In this chapter, pyrolysis and CVD were tried for carbon coating preparation of some Si alloys studied in this thesis. Pyrolysis did result in the formation of a carbon coating. However, particle aggregation occurred and the porosity produced during carbonization resulted in high surface area. For Si alloys containing Ti, a carbon coating was not obtained using CVD. Significant carbon nanotube formation occurred instead. This also lead to high surface area, highly aggregated and highly porous particles, which is detrimental for Si-based negative electrode materials. Improved carbon coating preparation methods should be studied in future work.

Chapter 9 Conclusions and Future Work

9.1 Conclusions

This thesis is dedicated to developing new Si-based negative electrode materials for lithium batteries. As discussed in previous chapters, there are still challenges for using Si-based negative electrodes in commercial lithium batteries, such as huge volume expansion, $Li_{15}Si_4$ formation, and unstable solid electrolyte interface (SEI) during cycling. Making Si/inactive materials and Si/C composites (especially carbon coated Si-based materials) have been deemed to be two effective approaches to relieve these difficulties and to improve Si-based negative electrode materials. In this thesis, several new Si/inactive alloy negative electrode materials were prepared and studied. The sample preparation approach is typically mechanical milling in an inert or reactive atmosphere (e.g. N_2(g) or air). Composition, morphology, and electrochemical performance of these Si/inactive alloys were investigated by characterization methods like X-ray diffraction (XRD), LECO analysis, scanning electron microscopy (SEM), energy dispersive spectroscopy (EDS), transmission electron microscopy (TEM), scanning TEM (STEM), and half cell cycling. High temperature carbon coating requires Si-based materials to have high thermal stability. Therefore, the thermal stability of these Si/inactive alloys was also studied by heating these alloys to high temperature and analyzing composition, morphology, and electrochemical performance of these alloys after heat treatment.

Si-Mo alloys synthesized by milling Si and Mo powders in Ar were discussed in Chapter 4. Phase evolution during ball milling, electrochemical properties, and thermal stability were studied for these Si-Mo samples. The phase evolution of these samples during ball milling indicated that nanostructured amorphous Si (a-Si)/$MoSi_2$ alloys can be obtained after only 4 h ball milling. Although $MoSi_2$ has a high melting point (2030 °C), these Si-Mo alloys did not display improvement in thermal stability compared to some other Si-transition metal alloys (e.g. Si-Fe alloys), as evidenced by a-Si crystallization at about 600 °C and $MoSi_2$ crystallization below 600 °C. This crystallization leads to significant $Li_{15}Si_4$ formation during cycling. However, although the Si-Mo samples after heat treatment typically showed a high degree of $Li_{15}Si_4$ formation during cycling, they still provided good cycling performance. Therefore, these Si-Mo alloys still can be regarded as good candidates for being carbon coated at high temperature.

In Chapter 5, Si-TiN alloys were prepared using a novel approach, namely reactive N_2 gas milling of Si and Ti powders. Compared to the conventional Si-TiN preparation method (ball milling Si and TiN powders in Ar), the reactive N_2 gas milling approach without the use of TiN precursor is less costly. It was found that the Si-TiN alloys prepared by the novel and conventional methods have comparable phase compositions. However, the Si-TiN alloys prepared by N_2 gas milling had finer grain structure, leading to better cell performance (such as better $Li_{15}Si_4$ suppression, reduced area surface impedance (ASI) increase, and higher cycling stability). Thermal stability of the Si-TiN alloys synthetized

by N_2 gas milling and Ar milling was investigated in Chapter 6. After heat treatment at 800 °C, the Si-TiN alloys prepared by N_2 gas milling display lower crystallization, finer microstructure, and higher $Li_{15}Si_4$ suppression during cycling than the Si-TiN alloys prepared by Ar milling. A $Si_{70}(TiN)_{30}$ sample synthesized by N_2 gas milling was selected for further improvement by high temperature carbon coating. The carbon coated $Si_{70}(TiN)_{30}$ sample was synthesized by heating a $Si_{70}(TiN)_{30}$/phenolic resin mixture at 800 °C. The resulting sample has a reversible volumetric capacity of 1490 Ah/L and shows an improvement in capacity retention than the original $Si_{70}(TiN)_{30}$ sample (94% vs. 85% after 50 cycles). However, the carbon coated $Si_{70}(TiN)_{30}$ sample has a huge surface area, which can lead to a large amount of SEI formation and low coulombic efficiency during cycling. If Si-TiN alloys prepared by N_2 gas milling can be carbon coated with a more suitable method, better cell performance could be expected.

Si-Ti-N-O alloys prepared by simply ball milling Si and Ti powders in air were studied in Chapter 7. The Si-Ti-N-O alloys typically show good cr-$Li_{15}Si_4$ suppression during cycling and high cycling stability. The thermal stability study results suggest that after heat treatment the Si-Ti-N-O samples with long air milling time or high Ti content typically exhibit low crystallization and good cell performance (good resistance to $Li_{15}Si_4$ formation and high cycling stability), suggesting high temperature tolerance of these samples. High thermal stability allows the Si-Ti-N-O alloys to be modified by high temperature carbon coating for further improvement.

9.2 Future Work

In this thesis, active gas (N_2 and air) milling was discussed, and some reactions involved are as follows:

1. $Si + N_2(g) \rightarrow Si$
2. $Si + Ti + N_2(g) \rightarrow Si + TiN$
3. $Si + air \rightarrow SiO_x$ ($x_{max}=0.37$)[186]
4. $Si + Ti + air \rightarrow Si + TiN + Si\text{-}O\text{-}N + Si\text{-}Ti\text{-}O\text{-}N$

When pure Si or Si-Ti mixtures were ball milled under N_2 gas, no Si-N compound was found to form during milling and only TiN was produced for the Si-Ti mixtures. During milling Si in air, only SiO_x ($x_{max}=0.37$) was observed to form.[186] However, when Si and Ti powders were ball milled in air, much more N (N/Ti >1) and O (O/Si > 0.37) contents were introduced into the samples as shown in Chapter 7. This perhaps indicates that synergistic behavior among Si, Ti, N, and O elements occurs and ternary or quaternary species (e.g. ternary Si-O-N or quaternary Si-Ti-O-N compounds) form. The strange phenomena during milling Si and Ti in air should be studied in a future work.

Pyrolysis of carbon precursors and CVD were used to make carbon coatings for some Si alloys studied in this thesis. Unfortunately, this resulted in major issues, as mentioned above.

As discussed in Chapters 6 and 8, carbon coated Si alloys prepared by high temperature carbonization of carbon precursors usually have high surface area. In future work, optimized parameters (like an appropriate carbon precursor, a proper carbon

precursor/Si alloy mass ratio, and suitable heating steps and temperatures) of the high temperature carbonization method should be found for obtaining carbon coated Si alloys with acceptable surface area.

As shown in Chapter 8, a huge amount of carbon nanotubes formed on the surface of Si alloys containing Ti during CVD, which can lead to high porosity and large surface area. Nevertheless, if an appropriate amount of carbon nanotubes is introduced to Si-based negative electrode materials, it is possible that this might result in an improvement in cell performance because carbon nanotubes could aid in maintaining electrical contact to the Si-based particles during cycling. Carbon nanotube/Si composites, which were synthesized using CVD with Ni-P alloys deposited on the surface of Si as catalysts, have been reported and have shown improved cell performance compared to Si.[188] It is worth mentioning that no extra catalyst needs to be added to the Si-TiN (N_2 gas milling, Chapter 5) or Si-Ti-N-O alloys (Chapter 7) for producing carbon nanotubes during CVD, which suggests simple preparation processes. In future work, CVD parameters (such as heating time and C_2H_4 flow rate) should be optimized for obtaining the carbon nanotube/Si-TiN or carbon nanotube/Si-Ti-N-O samples with good cell performance. Embedding these alloys into graphite may be another way of avoiding carbon nanotube formation.

References

1. M. S. Whittingham, Belgain patent no. 819672 (1975).

2. M. S. Whittingham, *Science*, **192**, 1126–1127 (1976).

3. J. B. Goodenough and K. Mizushima, US patent no. 4,357,215 (1982).

4. K. Mizushima, P. C. Jones, P. J. Wisenman, and J. B. Goodenough, *Mater. Res. Bull.*, **15**, 783–789 (1980).

5. A. Yoshino, K. Sanechika, and T. Nakajima, Japanese patent no. 1989293 (1985).

6. A. Yoshino, K. Sanechika, and T. Nakajima, US patent no. 4,668,595 (1987).

7. Y. Nishi, *Chem. Rec.*, **1**, 406–413 (2001).

8. N. Nitta, F. Wu, J. T. Lee, and G. Yushin, *Mater. Today*, **18**, 252–264 (2015).

9. G. Berckmans, M, Messagie, J. Smekens, N. Omar, L. Vanhaverbeke, and J. V. Mierlo, *Energies*, **10**, 1314 (2017).

10. S. Pacala and R. Socolow, *Science*, **305**, 968–973 (2004).

11. P. G. Bruce, B. Scrosati, and J. M. Tarascon, *Angew. Chem. Int. Ed.*, **47**, 2930–2946 (2008).

12. X. Su, Q. Wu, J. Li, X. Xiao, A. Lott, W. Lu, B. W. Sheldon, and J. Wu, *Adv. Energy Mater*., **4**, 1300882 (2014).

13. M. N. Obrovac and V. L. Chevrier, *Chem. Rev*., **114**, 11444–11502 (2014).

14. Y. Yao, M. T. McDowell, I. Ryu, H. Wu, N. Liu, L. Hu, W. D. Nix, and Y. Cui, *Nano Lett*., **11**, 2949–2954 (2011).

15. U. Kasavajjula, C. Wang, and A. J. Appleby, *J. Power Sources*, **163**, 1003–1039 (2007).

16. M. N. Obrovac and L. Christensen, *Electrochem. Solid-State Lett.*, **7**, A93–A96 (2004).

17. D. S. M. Iaboni and M. N. Obrovac, *J. Electrochem. Soc.*, **163**, A255–A261 (2016).

18. S. Cao, J. C. Bennett, Y. Wang, S. Gracious, M. Zhu, and M. N. Obrovac, *J. Power Sources*, **438**, 2270003 (2019).

19. L. J. Krause, T. Brandt, V. L. Chevrier, and L. D. Jensen, *J. Electrochem. Soc.*, **164**, A2277–A2282 (2017).

20. V. Etacheri, O. Haik, Y. Goffer, G. A. Roberts, I. C. Stefan, R. Fasching, and D. Aurbach, *Langmuir*, **28**, 965–976 (2012).

21. K. Schroder, J. Alvarado, T. A. Yersak, J. Li, N. Dudney, L. J. Webb, Y. S. Meng, and K. J. Stevenson, *Chem. Mater.*, **27**, 5531–5542 (2015).

22. K. Xu, *Chem. Rev.*, **104**, 4303–4417 (2004).

23. P. Arora and Z. Zhang, *Chem. Rev.*, **104**, 4419–4462 (2004).

24. J. Park, *Principles and Applications of Lithium Secondary Batteries* (2012).

25. T. Kim, W. Song, D. Y. Son, L. K. Ono, and Y. Qi, *J. Mater. Chem. A*, **7**, 2942–2964 (2019).

26. S. A. Needham, G. X. Wang, H. K. Liu, V. A. Drozd, and R. S. Liu, *J. Power Sources*, **174**, 828–831 (2007).

27. A. K. Padhi, K. S. Nanjundaswamy, and J. B. Goodenough, *J. Electrochem. Soc.*, **144**, 1188–1194 (1997).

28. S. Y. Chung, J. T. Bloking, and Y. M. Chiang, *Nat. Mater.*, **1**, 123–128 (2002).

29. Y. Ding, Z. P. Cano, A. Yu, J. Lu, and · Z. Chen, *Electrochem. Energy Rev.*, **2**, 1–28 (2019).

30. M. Wagemaker, B. L. Ellis, D. Lutzenkirchen-Hecht, F. M. Mulder, and L. F. Nazar, *Chem. Mater.*, **20**, 6313–6315 (2008).

31. W. J. Zhang, *J. Power Sources*, **196**, 2962–2970 (2011).

32. C. Sun, S. Rajasekhara, J. B. Goodenough, and F. Zhou, *J. Am. Chem. Soc.*, **133**, 2132–2135 (2011).

33. M. M. Thackeray, W. I. F. David, P. G. Bruce, and J. B. Goodenough, *Mater. Res. Bull.*, **18**, 461–472 (1983).

34. G. Xu, Z. Liu, C. Zhang, G. Cui, and L. Chen, *J. Mater. Chem. A*, **3**, 4092–4123 (2015).

35. J. Cho, T. J. Kim, Y. J. Kim, and B. Park, *Chem. Commun.*, 1074–1075 (2001).

36. M. Jo, M. Noh, P. Oh, Y. Kim, and J. Cho, *Adv. Energy Mater.*, **4**, 1301583 (2014).

37. Y. Wang, J. Jiang, and J. R. Dahn, *Electrochem. commun.*, **9**, 2534–2540 (2007).

38. I. Belharouak, W. Lu, D. Vissers, and K. Amine, *Electrochem. commun.*, **8**, 329–335 (2006).

39. H. J. Noh, S. Youn, C. S. Yoon, and Y. K. Sun, *J. Power Sources*, **233**, 121–130 (2013).

40. J. Cho, *J. Power Sources*, **126**, 186–189 (2004).

41. X. B. Cheng, R. Zhang, C. Z. Zhao, and Q. Zhang, *Chem. Rev.*, **117**, 10403–10473 (2017).

42. V. Thangadurai, S. Narayanan, and D. Pinzaru, *Chem. Soc. Rev.*, **43**, 4714–4727 (2014).

43. W. Xu, J. Wang, F. Ding, X. Chen, E. Nasybulin, Y. Zhang, and J. G. Zhang, *Energy Environ. Sci.*, **7**, 513–537 (2014).

44. M. Kotobuki, K. Kanamura, Y. Sato, and T. Yoshida, *J. Power Sources*, **196**, 7750–7754 (2011).

45. S. Wenzel, D. A. Weber, T. Leichtweiss, M. R. Busche, J. Sann, and J. Janek, *Solid State Ionics*, **286**, 24–33 (2016).

46. T. Krauskopf, H. Hartmann, W. G. Zeier, and J. Janek, *ACS Appl. Mater. Interfaces*, **11**, 14463–14477 (2019).

47. J. R. Dahn, T. Zheng, Y. Liu, and J. S. Xue, *Science*, **270**, 590–593 (1995).

48. E. Peled, C. Menachem, D. Bar-Tow, and A. Melman, *J. Electrochem. Soc.*, **143**, L4–L7 (1996).

49. J. S. Kim, *J. Power Sources*, **97–98**, 70–72 (2001).

50. A. Piotrowska, K. Kierzek, P. Rutkowski, and J. Machnikowski, *J. Anal. Appl. Pyrolysis*, **102**, 1–6 (2013).

51. G. Pan, W. Liang, P. Liang, and Q. Chen, *Clean Energy*, **3**, 211–216 (2019).

52. R. Fong, U. von Sacken, and J. R. Dahn, *J. Electrochem. Soc.*, **137**, 2009–2013 (1990).

53. H. O. Pierson, *Handbook of Carbon, Graphite, Diamonds and Fullerenes* (1993).

54. P. Mukhopadhyay and R. K. Gupta, *Graphite, Graphene, and Their Polymer Nanocomposites* (2012).

55. M. S. Seehra, U. K. Geddam, D. Schwegler-Berry, and A. B. Stefaniak, *Carbon*, **95**, 818–823 (2015).

56. Y. Qi and S. J. Harris, *J. Electrochem. Soc.*, **157**, A741–A747 (2010).

57. Z. Zhang, Z. Chen, X. Zhang, Y. Li, Q. Zhang, J. Hart, and J. Li, ECS J. Solid State Sci. Technol., 5, Q3088–Q3094 (2016).

58. L. Madec, J. Xia, R. Petibon, K. J. Nelson, J. P. Sun, I. G. Hill, and J. R. Dahn, J. Phys. Chem. C, 118, 29608–29622 (2014).

59. A. A. Williams, J. Park, S. Byun, M. Ryou, and Y. M. Lee, J. Electrochem. Soc., 163, A2757–A2767 (2016).

60. T. Ohzuku, A. Ueda, and N. Yamamoto, J. Electrochem. Soc., 142, 1431–1435 (1995).

61. S. Scharner, W. Weppner, and P. Schmid-Beurmann, *J. Electrochem. Soc.*, **146**, 857–861 (1999).

62. X. Sun, P. V. Radovanovic, and B. Cui, *New J. Chem.*, **39**, 38–63 (2015).

63. H. Wu and Y. Cui, Nano Today, 7, 414–429 (2012).

64. C. Y. Ouyang, Z. Y. Zhong, and M. S. Lei, *Electrochem. commun.*, **9**, 1107–1112 (2007).

65. Y. Wang, H. Li, P. He, E. Hosono, and H. Zhou, *Nanoscale*, **2**, 1294–1305 (2010).

66. T. F. Yi, H. Liu, Y. R. Zhu, L. J. Jiang, Y. Xie, and R. S. Zhu, J. Power Sources, 215, 258–265 (2012).

67. S. Huang, Z. Wen, Z. Gu, and X. Zhu, *Electrochim. Acta*, **50**, 4057–4062 (2005).

68. H. Li and H. Zhou, Chem. Commun, 48, 1201–1217 (2012).

69. Y. B. He, B. Li, M. Liu, C. Zhang, W. Lv, C. Yang, J. Li, H. Du, B. Zhang, Q. H. Yang, J. K. Kim, and F. Kang, Sci. Rep., 2, 1–9 (2012).

70. M. S. Song, R. H. Kim, S. W. Baek, K. S. Lee, K. Park, and A. Benayad, J. Mater. Chem. A, 2, 631–636 (2014).

71. M. N. Obrovac, L. Christensen, D. B. Le, and J. R. Dahn, *J. Electrochem. Soc.*, **154**, A849–A855 (2007).

72. N. S. Hudak and D. L. Huber, J. Electrochem. Soc., 159, A688–A695 (2012).

73. G. Taillades and J. Sarradin, *J. Power Sources*, **125**, 199–205 (2004).

74. W. Xianming, T. Nishina, and I. Uchida, J. Power Sources, 104, 90–96 (2002).

75. H. Kim, B. Park, H. J. Sohn, and T. Kang, *J. Power Sources*, **90**, 59–63 (2000).

76. J. Wang, P. King, and R. A. Huggins, *Solid State Ionics*, **20**, 185–189 (1986).

77. C. M. Park, S. Yoon, S. I. Lee, J. H Kim, J. H. Jung, and H. J Sohn, *J. Electrochem. Soc.*, **154**, A917–A920 (2007).

78. J. Li and J. R. Dahn, *J. Electrochem. Soc.*, **154**, A156–A161 (2007).

79. J. R. Dahn, I. A. Courtney, and O. Mao, *Solid State Ionics*, **111**, 289–294 (1998).

80. Y. Hwa, J. H. Sung, B. Wang, C. M. Park, and H. J. Sohn, J. Mater. Chem., 22, 12767–12773 (2012).

81. Y. Wang and J. R. Dahn, *J. Electrochem. Soc.*, **153**, A2188–A2191 (2006).

82. B. A. Boukamp, G. C. Lesh, and R. A. Huggins, *J. Electrochem. Soc.*, **128**, 725–729 (1981).

83. C. J. Wen and R. A. Huggins, *J. Solid State Chem.*, **37**, 271–278 (1981).

84. M. N. Obrovac and L. J. Krause, J. Electrochem. Soc., 154, A103–A108 (2007).

85. Y. Kubota, M. C. S. Escao, H. Nakanishi, and H. Kasai, *J. Appl. Phys.*, **102**, 053704 (2007).

86. Y. Wang and J. Dahn, J. Electrochem. Soc., 153, A2314–A2318 (2006).

87. V. L. Chevrier, J. W. Zwanziger, and J. R. Dahn, *Can. J. Phys.*, **87**, 625–632 (2009).

88. P. Limthongkul, Y. I. Jang, N. J. Dudney, and Y. M. Chiang, *Acta Mater.*, **51**, 1103–1113 (2003).

89. P. Limthongkul, Y. I. Jang, N. J. Dudney, and Y. M. Chiang, *J. Power Sources*, **119**, 604–609 (2003).

90. L. Y. Beaulieu, T. D. Hatchard, A. Bonakdarpour, M. D. Fleischauer, and J. R. Dahn, *J. Electrochem. Soc.*, **150**, A1457–A1464 (2003).

91. K. Rhodes, N. Dudney, E. Lara-Curzio, and C. Daniel, *J. Electrochem. Soc.*, **157**, A1354–A1360 (2010).

92. J. O. Besenhard, J. Yang, and M. Winter, J. Power Sources, 68, 87–90 (1997).

93. X. H. Liu, L. Zhong, S. Huang, S. X. Mao, T. Zhu, and J . Y. Huang, *ACS Nano*, **6**, 1522–1531 (2012).

94. M. J. Chon, V. A. Sethuraman, A. McCormick, V. Srinivasan, and P. R. Guduru, *Phys. Rev. Lett.*, **107**, 045503 (2011).

95. K. Zhao, M. Pharr, Q. Wan, W. L. Wang, E. Kaxiras, J. J. Vlassak, and Z. Suo, *J. Electrochem. Soc.*, **159**, A238–A243 (2012).

96. M. T. McDowell, S. W. Lee, J. T. Harris, B. A. Korgel, C. Wang, W. D. Nix, and Y. Cui, *Nano Lett.*, **13**, 758–764 (2013).

97. V. L. Chevrier, L. Liu, D. B. Le, J. Lund, B. Molla, K. Reimer, L. J. Krause, L. D. Jensen, E. Figgemeier, and K. W. Eberman, *J. Electrochem. Soc.*, **161**, A783–A791 (2014).

98. Z. Du, R. A. Dunlap, and M. N. Obrovac, J. Electrochem. Soc., 161, A1698–A1705 (2014).

99. J. Y. Li, Q. Xu, G. Li, Y. X. Yin. L. J. Wan, and Y. G. Guo, *Mater. Chem. Front.*, **1**, 1691–1708 (2017).

100. J. Yang, B. F. Wang, K. Wang, Y. Liu, J. Y. Xie, and Z. S. Wen, *Electrochem. Solid State Lett.*, **6**, A154–A156 (2003).

101. A. Timmons, A. D. W. Todd, S. D. Mead, G. H. Carey, R. J. Sanderson, R. E. Mar, and J. R. Dahn, *J. Electrochem. Soc.*, **154**, A865–A874 (2007).

102. L. Y. Beaulieu, K. C. Hewitt, R. L. Turner, A. Bonakdarpour, A. A. Abdo, L. Christensen, K. W. Eberman, L. J. Krause, and J. R. Dahn, *J. Electrochem. Soc.*, **150**, A149–A156 (2003).

103. T. D. Hatchard, M. N. Obrovac, and J. R. Dahn, *J. Electrochem. Soc.*, **153**, A282–A287 (2006).

104. H. J. Ahn, Y. S. Kim, K. W. Park, and T. Y. Seong, Chem. Commun., 43–45 (2005).

105. T. D. Hatchard, M. N. Obrovac, and J. R. Dahn, *J. Electrochem. Soc.*, **152**, A2335–A2344 (2005).

106. S. J. Lee, H. Y. Lee, Y. Park, H. K. Baik, and S. M. Lee, J. Power Sources, 119, 117–120 (2003).

107. X. Yang, Z. Wen, S. Huang, X. Zhu, and X. Zhang, *Solid State Ionics*, **177**, 2807–2810 (2006).

108. M. L. Terranova, S. Orlanducci, E. Tamburri, V. Guglielmotti, and M. Rossi, *J. Power Sources*, **246**, 167–177 (2014).

109. X. Zhao, X. Rui, W. W. Zhou, L. Tan, Q. Yan, Z. Lu, H. H. Hng, *J. Power Sources*, **250**, 160–165 (2014).

110. B. Wang, X. Li, X. Zhang, B. Luo, Y. Zhang, and L. Zhi, *Adv. Mater.*, **25**, 3560–3565 (2013).

111. Y. S. Hu, R. Demir-Cakan, M. M. Titirici, J. O. Muller, R. Schogl, M. Antonietti, and J. Maier, Angew. Chem. Int. Ed., 47, 1645–1649 (2008).

112. W. R. Liu, J. H. Wang, H. C. Wu, D. T. Shieh, M. H. Yang, and N. L. Wu, *J. Electrochem. Soc.*, **152**, A1719–A1725 (2005).

113. N. Dimov, K. Fukuda, T. Umeno, S. Kugino, and M. Yoshio, *J. Power Sources*, **114**, 88–95 (2003).

114. X. Q. Yang, J. McBreen, W. S. Yoon, M. Yoshio, H. Wang, K. Fukuda, T. Umeno, *Electrochem. commun.*, **4**, 893–897 (2002).

115. M. Liu, G. Lu, and J. Chen, Nanotechnology, 19, 265705 (2008).

116. N. Liu, Z. Lu, J. Zhao, M. T. McDowell, H. W. Lee, W. Zhao, and Y. Cui, *Nat. Nanotechnol.*, **9**, 187–92 (2014).

117. K. M. Lee, Y. S. Lee, Y. W. Kim, Y. K. Sun, and S. M. Lee, *J. Alloys Compd.*, **472**, 461–465 (2009).

118. X. Zhao, R. J. Sanderson, M. A. Al-Maghrabi, R. A. Dunlap, and M. N. Obrovac, *J. Electrochem. Soc.*, **164**, A1165–A1172 (2017).

119. P. Zuo and G. Yin, *J. Alloys Compd.*, **414**, 265–268 (2006).

120. S. J. Kim, H. C. Park, M. C. Kim, D. M. Kim, Y. W. Lee, and K. W. Park, *J. Power Sources*, **273**, 707–715 (2015).

121. S. Kirklin, B. Meredig, and C. Wolverton, *Adv. Energy Mater.*, **3**, 252–262 (2013).

122. W. J. Weydanz, M. Wohlfahrt-Mehrens, and R. A. Huggins, *J. Power Sources*, **81–82**, 237–242 (1999).

123. M. D. Fleischauer, M. N. Obrovac, and J. R. Dahn, *J. Electrochem. Soc.*, **153**, A1201–A1205 (2006).

124. M. D. Fleischauer, J. M. Topple, and J. R. Dahn, *Electrochem. Solid-State Lett.*, **8**, A137–A140 (2005).

125. Z. Du, T. D. Hatchard, P. Bissonnette, R. A. Dunlap, and M. N. Obrovac, J. Electrochem. Soc., 163, A2456–A2460 (2016).

126. Z. Du, T. D. Hatchard, R. a. Dunlap, and M. N. Obrovac, J. Electrochem. Soc., 162, A1858–A1863 (2015).

127. H. Liu, M. Zhu, Z. Du, and M. N. Obrovac, J. Electrochem. Soc., 163, A192–A196 (2016).

128. Z. Du, R. A. Dunlap, and M. N. Obrovac, *J. Electrochem. Soc.*, **163**, A2011–A2016 (2016).

129. Z. Du, H. Liu, S. N. Ellis, R. A. Dunlap, M. Zhu, and M. N. Obrovac, *J. Electrochem. Soc.*, **163**, A1275–A1279 (2016).

130. Z. Du, S. N. Ellis, R. A. Dunlap, and M. N. Obrovac, *J. Electrochem. Soc.*, **163**, A13–A18 (2015).

131. D. Yaakov, Y. Gofer, D. Aurbach, and I. C. Halalay, *J. Electrochem. Soc.*, **157**, A1383–A1391 (2010).

132. T. Kawamura, A. Kimura, M. Egashira, S. Okada, and J. I. Yamaki, J. Power Sources, 104, 260–264 (2002).

133. C. L. Campion, W. Li, and B. L. Lucht, *J. Electrochem. Soc.*, **152**, A2327–A2334 (2005).

134. P. Arora, R. E. White, and M. Doyle, *J. Electrochem. Soc.*, **145**, 3647–3667 (1998).

135. S. F. Lux, I. T. Lucas, E. Pollak, S. Passerini, M. Winter, R. Kostecki, *Electrochem. commun.*, **14**, 47–50 (2012).

136. S. P. Kim, A. C. T. V. Duin, and V. B. Shenoy, J. Power Sources, 196, 8590–8597 (2011).

137. Z. Chen, W. Q. Lu, J. Liu, and K. Amine, *Electrochim. Acta*, **51**, 3322–3326 (2006).

138. S. S. Zhang, *J. Power Sources*, **162**, 1379–1394 (2006).

139. T. D. Hatchard, A. Genkin, and M. N. Obrovac, *AIP Adv.*, **7**, 045201 (2017).

140. C. Suryanarayana and M. G. Norton, *X-Ray Diffraction: A Practical Approach*, pp. 3–19 (1998).

141. B. D. Cullity, *Elements of X-Ray Diffraction*, pp. 3–30 (1978).

142. S. Kobayashi and K. Inaba, *Rigaku J.*, **28**, 8–13 (2012).

143. E. Prince and J. K. Stalick, *Accuracy in Powder Diffraction II: Proceedings of the International Conference*, pp. 26 (1992).

144. M. Kahle, M. Kleber, and R. Jahn, *Geoderma*, **109**, 191–205 (2002).

145. G. Caglioti, A. Paoletti, and F. P. Ricci, *Nucl. Instruments*, **3**, 223–228 (1958).

146. W. Zhou and Z. L. Wang, *Scanning Microscopy for Nanotechnology: Techniques and Applications*,, pp. 1–40 (2007).

147. E. Pretorius, *Microsc. Res. Tech.*, **73**, 225–228 (2010).

148. F. Hrumeich, *https://www.coursehero.com/file/33086929/TEMpdf/* (2018).

149. D. U. Shah and P. J. Schubel, *Polym. Test.*, **29**, 629–639 (2010).

150. M. Doyle, J. Newman, and J. Reimers, *J. Power Sources*, **52**, 211–216 (1994).

151. H. Lee, Y. Kim, M. Hong, and S. Lee, *J. Power Sources*, **141**, 159–162 (2005).

152. J. Yu, J. Yang, X. Feng, H. Jia, J. Wang, and W. Lu, *Ind. Eng. Chem. Res.,* **53**, 12697–12704 (2014).

153. A. B. Gokhale and G. J. Abbaschian, *J. Phase Equilibria*, **12**, 493–498 (1991).

154. Y. Liu, B. Scott, and M. N. Obrovac, *J. Electrochem. Soc.*, **166**, A1170–A1175 (2019).

155. J. P. Maranchi, A. F. Hepp, and P. N. Kumta, *Electrochem. Solid-State Lett.*, **6**, A198–A201 (2003).

156. Y. Cao, B. Scott, R. A. Dunlap, J. Wang, and M. N. Obrovac, *J. Electrochem. Soc.*, **166**, A21–A26 (2019).

157. S. Cao, J. C. Bennett, Y. Wang, S. Gracious, M. Zhu, and M. N. Obrovac, *J. Power Sources*, **438**, 227003 (2019).

158. I. Kim, P. N. Kumta, and G. E. Blomgren, *Electrochem. Solid State Lett.*, **3**, 493–496 (2000).

159. N. Savvides and B. Window, *J. Appl. Phys.*, **64**, 225–234 (1988).

160. Z. Yan and M. N. Obrovac, *J. Power Sources*, **397**, 374–381 (2018).

161. Y. Zhang, Z. W. Fu, and Q. Z. Qin, *Electrochem. commun.*, **6**, 484–491 (2004).

162. K. Hanai, Y. Liu, N. Imanishi, A. Hirano, M. Matsumura, T. Ichikawa, and Y. Takeda, *J. Power Sources*, **146**, 156–160 (2005).

163. Y. Wang, S. Cao, H. Liu, M. Zhu, and M. N. Obrovac, MRS Commun., 8, 1352–1357 (2018).

164. A. Calka, J. S. Williams, and P. Millet, *Scr. Metall. Mater.*, **27**, 1853–1857 (1992).

165. C. Suryanarayana, *Prog. Mater. Sci.*, **46**, 1–184 (2001).

166. Y. Wang, S. Cao, M. Kalinina, L. Zheng, L. Li, M. Zhu, and M. N. Obrovac, *J. Electrochem. Soc.*, **164**, A3006–A3010 (2017).

167. E. G. Barbagiovanni, L. V Goncharova, and P. J. Simpson, *Phys. Rev. B*, **83**, 035112 (2011).

168. S. M. Castanho, R. Moreno, and J. L. G. Fierro, *J. Mater. Sci.*, **32**, 157–162 (1997).

169. R. Huang, Z. Lin, Y. Guo, C. Song, X. Wang, H. Lin, L. Xu, J. Song, and H. Li, *Opt. Mater. Express*, **4**, 205–212 (2014).

170. D. Tang, R. Yi, M. L. Gordin, M. Melnyk, F. Dai, S. Chen, J. Song, and D. Wang, *J. Mater. Chem. A*, **2**, 10375–10378 (2014).

171. J. F. Marco, A. C. Agudelo, J. R. Gancedo, and D. Hanzel, *Surf. interface Anal.*, **27**, 71–75 (1999).

172. M. J. Vasile, A. B. Emerson, and F. A. Baiocchi, *J. Vac. Sci. Technol. A*, **8**, 99–105 (1990).

173. D. Jaeger and J. Patscheider, *J. Electron Spectros. Relat. Phenomena*, **185**, 523–534 (2012).

174. J. B. Price, J. O. Borland, and S. Selbrede, *Thin Solid Films*, **236**, 311–318 (1993).

175. V. L. Chevrier, L. Liu, D. B. Le, J. Lund, B. Molla, K. Reimer, L. J. Krause, L. D. Jensen, E. Figgemeier, and K. W. Eberman, *J. Electrochem. Soc.*, **161**, A783–A791 (2014).

176. M. D. Fleischauer, J. M. Topple, and J. R. Dahn, *Electrochem. Solid-State Lett.*, **8**, A137–A140 (2005).

177. G. X. Wang, J. H. Ahn, J. Yao, S. Bewlay, and H. K. Liu, *Electrochem. commun.*, **6**, 689–692 (2004).

178. J. Wang, C. Wang, Y. Zhu, N. Wu, and W. Tian, *Ionics*, **21**, 579–585 (2015).

179. M. Miyachi, H. Yamamoto, H. Kawai, T. Ohta, and M. Shirakata, *J. Electrochem. Soc.*, **152**, A2089–A2091 (2005).

180. J. H. Kim, C. M. Park, H. Kim, Y. J. Kim, and H. J. Sohn, *J. Electroanal. Chem.*, **661**, 245–249 (2011).

181. M. A. Al-Maghrabi, J. Suzuki, R. J. Sanderson, V. L. Chevrier, R. A. Dunlap, and J. R. Dahn, *J. Electrochem. Soc.*, **160**, A1587–A1593 (2013).

182. L. Shi, C. Pang, S. Chen, M. Wang, K. Wang, Z. Tan, P. Gao, J. Ren, Y. Huang, H. Peng, and Z. Liu, *Nano Lett.*, **17**, 3681–3687 (2017).

183. A. Hohl, T. Wieder, P. A. van Aken, T. E. Weirich, G. Denninger, M. Vidal, S. Oswald, C. Deneke, J. Mayer, H. Fuss, *J. Non. Cryst. Solids*, **320**, 255–280 (2003).

184. H. R. Philipp, *J. Non. Cryst. Solids*, **8**–**10**, 627–632 (1972).

185. G. W. Brady, *J. Phys Chem*, **63**, 1119-1120 (1959).

186. Y. Cao, J. C. Bennett, R. A. Dunlap, and M. N. Obrovac, *Chem. Mater*., **30**, 7418–7422 (2018).

187. C. M. Park, W. Choi, Y. Hwa, J. H. Kim, G. Jeong, and H. J. Sohn, *J. Mater. Chem*., **20**, 4854–4860 (2010).

188. J. Shu, H. Li, R. Yang, Y. Shi, and X. Huang, *Electrochem. commun*., **8**, 51–54 (2006).